Strathclyde Institute of Pharmacy and Biomedical Sciences

Investigating the crystallisation behaviour of pharmaceutical compounds confined within mesoporous materials

A thesis presented for the degree of

Doctor of Philosophy

in the Faculty of Science of the

University of Strathclyde

Eleanor Catherine Laide Jones

Declaration of Author's Right

This thesis is the result of the author's original research. It has been composed by the author and has not been previously submitted for examination which has led to the award of a degree.

The copyright of the thesis belongs to the author under the terms of the United Kingdom Copyright Acts as qualified by University of Strathclyde Regulation 3.50. Due acknowledgment must always be made of the use of any material contained in, or derived from, this thesis.

Signed: E. Jones

Date: 17th November 2022

Acknowledgements

My deepest gratitude goes to Iain Oswald and Martin Ward for all of their support, encouragement and guidance. This PhD pushed me to my limit and without them would have been near impossible. Thank you for allowing me to pursue my interests and turn this PhD into something I am proud of. I owe this PhD to you both. Many thanks also goes to Luis Bimbo for giving me the opportunity to pursue this PhD and introducing me to the world of porous materials. I have had the pleasure of working with the members of two research groups who helped and advised me along the journey: June Kaewchuchuen, Suse Bebiano, Lloyd Farquhar, Julia Gasol Cardona and Dave Ashworth. A special thanks goes to the CMAC technical team for all of their support with the instruments, in particular Alan Martin and all his guidance with the XRD instruments and Deborah Bowering for her support with BET. Thank you to "The Scatterers", my fellow X-ray users who brought humour to the lab and provided me with valuable advice: Michael Devlin, Vijay Srirambhatla and John Mahon. I would like to thank the friends I have made along the way: Alice Turner, Scott Davidson, John Totten, Natalie Maclean and Ivan Hall Barrientos.

I am also grateful for my support network in Glasgow. My cousin Kirsty and Colin for making me feel welcome and at home in Glasgow. Your friendship, support and kind words have not gone unnoticed. To Michael and Ruaridh, thank you for making my time in The North so enjoyable. In you I have found true friendship. My family, Auntie Cathy and Uncle Nigel, who have believed in me even when I doubted myself. Thank you for all of your emotional support, patience and love. This journey would not have been possible without you and I owe you both a great debt. I would also like to thank my sister Mary-Anne, even at a young age you show such interest in what I do. I hope my journey has inspired you to pursue your dreams and ambitions.

Lastly and most importantly to my mum whom I take strength from every day. You showed me what it was to be a strong, brave and determined woman. You told me I was your greatest achievement, so Valerie Jones I dedicate this to you.

Abstract

The research illustrated in this doctoral thesis aims to probe the crystallisation behaviour of pharmaceutical compounds confined in porous materials, when loaded at both ambient and high pressure. Review of the literature shows how the confinement of molecular compounds in porous material can influence their solid-state i.e., the polymorph of the crystalline state or the amorphous form. Prior to confinement, understanding the crystallisation behaviour of the pharmaceutical compound is imperative, in particular investigating their response to pressure and the influence of the solvent on the compound's crystallisation. For this reason, the thesis is split into three sections as briefly detailed below.

Isonicotinamide has been well characterised in literature, with six known polymorphs reported in the Cambridge Structural Database and common reference as a "model compound". Nonetheless, its response to pressure is unknown until now with Chapter 3 investigating the compression of the thermodynamically stable polymorph – Form I isonicotinamide. Super-elastic behaviour is exhibited beyond 4.33 GPa, where a single-crystal to single-crystal phase transition to new polymorph Form I'.

Chapter 4 continues the investigation into the compression of isonicotinamide. This chapter looks to address the significance of hydrogen bonding pattern on the structure as hydrostatic pressure is applied to metastable polymorphs Form II, Form III and Form IV. These polymorphs are structurally similar, with layered structures and head-to-tail hydrogen bonding, differing to the dimeric structure of Form I isonicotinamide. Form II and Form IV exhibit a phase transition beyond 1.49 and 2.01 GPa respectively. Whilst the structure of Form III remains consistent up till the deterioration of the crystal beyond 4.27 GPa, suspected to be due to the additional hydrogen bond.

Chapter 5 looks at the influence of solvent on the structure of pharmaceutical compound nifedipine. With the polymorphism of the compound known to be closely related by temperature, solvents were used in this study to further investigate the polymorph landscape. Two known and seven new solvates were crystallised during the investigation and characterised using low-temperature single-crystal XRD. The solvates were then subjected to variable-temperature XRD to capture the desolvation event, examining if this route could lead to additional polymorphs.

The final experimental chapter utilises both high pressure and the use of solvents when loading isonicotinamide into porous silica, splitting the study into two sections: synthesis of mesoporous silica and loading isonicotinamide into porous silica. Mesoporous silica with pores ranging in diameter and volume are selected with characterisation by nitrogen sorption. Ethanol and chloroform are used as loading solvents due to the difference in binging energy with isonicotinamide, thus the affinity of isonicotinamide to move from the solvent and into the pores. This chapter also highlights difficulties faced when trying to reproduce literature methods.

Table of Contents

List of Figures

List of Tables

Abbreviations

API(s)	Active Pharmaceutical Ingredient(s)	MCF	Mesoscopic Cellular Foam
BET	Brunauer-Emmett-Teller	MeOH	Methanol
BFDH	Bravais, Friedel, Donnay and Harker	MHRA	Medicines and Healthcare products Regulatory Agency (UK)
BJH	Barrett-Joyner-Halenda	MORPH	Morpholine
CPG	Controlled Porous Glass	N	Nifedipine
CSD	Cambridge Structural Database	NMR	Nuclear Magnetic Resonance
DAC	Diamond Anvil Cell	NTE	Negative thermal expansion
DFT	Density Functional Theory	PET	Petroleum Ether
DIO	1,4-Dioxane	pSi	Porous Silicon
DMA	Dimethylacetamide	PSiO	Porous Silica
DMF	Dimethylformamide	PTM	Pressure Transmitting Medium
DMSO	Dimethyl Sulfoxide	PYRI	Pyridine
DSC	Differential Scanning Calorimetry	SC-XRD	Single-Crystal X-ray Diffraction
EoS	Equation of State	STA	Simultaneous Thermal Analysis
FDA	Food and Drug Administration (US)	TEM	Transmission Electron Microscopy
FTIR	Fourier Transform Infra-Red	TGA	Thermal Gravimetric Analysis
GPa	Gigapascal	THF	Tetrahydrofuran
HPLC	High-Performance Liquid Chromatography	VT	Variable-Temperature
IR	Infra-Red	XRD	X-ray Diffraction
K	Kelvin	XRPD	X-ray Powder Diffraction

Chapter 1

Introduction

This chapter has been published, in part, in the journal Pharmaceutics as a review paper.

Jones, E. C. L.; Bimbo, L. M. Crystallisation Behaviour of Pharmaceutical Compounds Confined within Mesoporous Silicon. *Pharmaceutics*. 2020.

Adaptions have been made to accommodate changes to the research carried out during the PhD.

1 Introduction

1.1 Drug crystallisation and amorphisation

Nearly half of all the newly developed compounds entering the drug development pipeline suffer from unfavourable physicochemical properties, affecting their bioavailability and, consequently, the efficacy of the treatment.[1] Poor aqueous solubility is one of the most prevalent issues affecting both the drug's pharmaceutical processability and biodistribution and is intimately tied to the compound's solid-state properties. The solid phase can be subcategorised into two divisions according to their order of molecular packing/arrangement: the crystalline and amorphous states.

Crystalline materials are ordered in a repeating pattern, creating a three-dimensional crystal structure held together by intermolecular forces, including hydrogen bonding and van der Waals forces. The smallest repeating unit is known as the unit cell and, when built up, shows the composition of the crystal (Figure 1.1). Crystalline materials are at their most stable state with atoms packed in a way that reduces their total potential energy.[2] Due to their high stability, a large amount of energy is needed to break the intermolecular forces in the crystal structure. When crystalline solids are melted, they produce a well-defined melting point, determining the energy needed to break down the crystal structure.

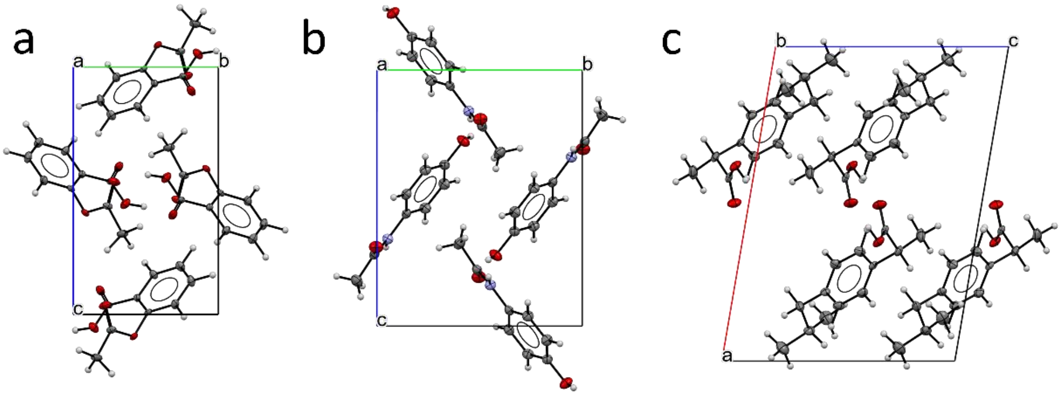

Figure 1.1: Unit cells of commonly used drugs a) aspirin, b) paracetamol and c) ibuprofen.

Crystallisation is a process that allows for the formation and purification of many active pharmaceutical ingredients (APIs), generating solid particles with the desired crystal habit,[3, 4] crystal form[5] and purity,[6] crucial for controlling a compound's physicochemical properties. Pudasaini and authors investigated the optimal crystal shape for downstream processing, identifying 6 crystal habits produced by modifying the crystallisation environment of 5-aminosalicylic acid. The influence of crystal shape on the physical properties of the API were highlighted. Spherical particles provided optimal flowability, whilst tablets comprising of needle-shaped particles demonstrated greater tensile strength, beneficial for packaging and patient usage.[3] Crystallisation can be divided into two subprocesses: nucleation and crystal growth. Nucleation is defined as the formation of small "crystalline entities", nuclei, from a supersaturated solution.[7] According to Ostwald's rule of stages, during solution crystallisation the metastable polymorph should crystallise first, with subsequent transformation to the stable form.[8] The critical nucleus size is said to fall within the range of 100 to 1000 atoms, and once reached, crystal growth can follow with the growth of nuclei into "macroscopic crystals".[9] Nucleation can be classified as primary, occurring in the absence of crystalline material, or secondary, which occurs in the presence of the material being crystallised and often serves as a catalyst for further nucleation. Primary nucleation can be classified as either homogeneous or heterogeneous. Heterogeneous nucleation occurs at the interface of a surface other than the material to be crystallised, whereas homogeneous nucleation occurs in a clear solution.[10] Classical Nucleation Theory (CNT) is one of the simplest theories used to describe homogeneous nucleation.[9] Figure 1.2 depicts CNT, showing the total free energy required for cluster formation and growth (ΔG). ΔG is the sum of two factors; the energy required for the formation of the crystalline phase (ΔG_s) and the energy loss caused by the creation of new surfaces (ΔG_v). Initially a positive ΔG_s is favoured at smaller nuclei size, causing dissolution of the smaller clusters. Once a critical nucleus size (r_c) is reached and ΔG reaches its maximum (ΔG_{crit}), ΔG decreases as the growth of the clusters becomes the favourable factor, resulting in the growth of a crystal. Secondary nucleation can be controlled using a seeding technique, whereby seed crystals of the desired crystal form are suspended in a supersaturated solution.[11] This can enable the formation of specific a polymorph during the manufacturing process, mitigating the crystallisation of an undesired form.[12]

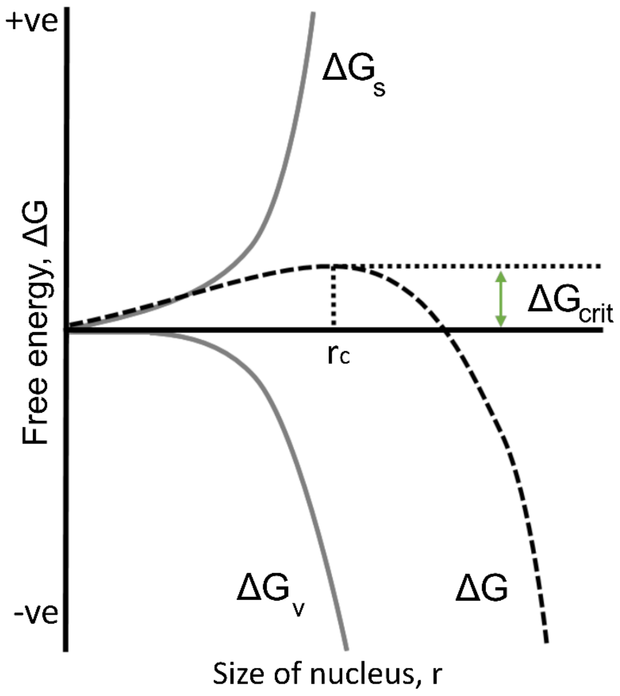

Figure 1.2: Free energy diagram for nucleation.

The crystalline state can be composed of a single component or multiple components, e.g., co-crystals, solvates and hydrates. Polymorphism is the ability of a compound to exist in more than one crystalline form, with molecules arranging themselves differently within the crystal structure, attributing to different physical and mechanical properties between forms. Polymorphism can be divided into two categories: conformational polymorphism and packing polymorphism. The former is when molecules within the solid state present conformational flexibility whilst the latter is defined as the solid state exhibiting different packing of conformational rigid molecules.[5, 13] The reaction product of acetylenedicarboxylic acid and 4-pyridinecarbonitrile in solvent mixtures produced two conformational polymorphs. The position of the hydrogen atom on the carboxylic acid functional groups led to different hydrogen bonding patterns within the crystal structures of (Z)-3-Carboxy-2-(4-cyanopyridin-1-ium-1-yl)-acrylate. Rotation of the protonated oxygen within the acid group led to the cis and trans positions in the α-form and β-form respectively, highlighting their identities as conformational polymorphs.[14] Polymorphs of the same material can exhibit different melting points, crystal habits and solubility, which is of great interest and concern to the pharmaceutical industry. Sorafenib exists in numerous salt forms, with the tosylate form used in pharmaceutical formulations. The polymorphs of sorafenib tosylate have shown a variation in bioavailability which is believed to be due to issues with solubility that is usually due to the change in crystal structure.[15] Wiergowska *et al.,* explored the solubility of two structural polymorphs of sorafenib tosylate, thermodynamically stable Form I and metastable Form III by varying the pH of the dissolution medium. Dissolution only occurred with the addition of surfactant sodium dodecyl sulfate, observing that the medium with a pH of 4.5 was optimum with both polymorphs, 2.404 and 2.355 mg/mL for Form I and III respectively. The thermodynamically stable form (Form I) was stated to have greater solubility at this pH, whilst the metastable polymorph, Form III, displayed a greater solubility in mediums with pH values of 1 and 6.8. Solubility differences between polymorphs can be explained by the difference in lattice energy, i.e., the attractive forces that hold the crystal structure together and repulsive forces that allow the crystal to dissociate in solution.[16] It is understood that metastable polymorphs display greater solubility but can undergo solvent-mediated transformation to a more stable, hence lower, solubility state in order to retain system equilibrium.[16] Unfortunately, due to the nature of metastable polymorphs, pharmaceutical formulations often contain the most stable form. However, understanding the experimental factors that play a role in polymorphism is important hence screening crystalline materials for polymorphism is a fundamental role in drug development.

Amorphous materials also play a role in drug development. They lack the long-range order that crystalline materials possess. The irregular arrangement of molecules leads to unequal intermolecular forces and, hence, physical instability in comparison to their crystalline counterparts. Amorphous compounds possess a greater Gibbs free energy than their crystalline state and are thermodynamically unfavourable, which can lead to their transformation to the stable crystalline state.[17] This instability is advantageous in terms of increased solubility of compounds and, hence, bioavailability. However, it is difficult to determine the solubility of amorphous compounds due to their tendency to recrystallise upon contact with an aqueous environment.[18]

1.2 Drug confinement into porous substrates

Amorphous compounds display the favourable characteristic of greater solubility than their stable crystalline counterparts due to higher free energy and greater molecular mobility. However, their instability and tendency to recrystallise can eliminate this highly desirable property.[19] The vast majority of new and existing drug compounds are crystalline, with their long-range order promoting stability. When confined in pores, however, they tend to lose their long-range order, remaining in a disordered state, thus reducing their thermodynamic stability and improving dissolution from the substrate in aqueous environments.[20] Inorganic mesoporous substrates, i.e., materials with pores ranging between 2 and 50 nm in diameter, have shown promise for stabilising drugs in the amorphous state due to their exceptional properties, such as: a large pore volume, which confers the ability to host large quantities of drug compound; a high surface area, allowing great potential for drug adsorption; and tuneable pore size with a uniform distribution, allowing a reproducible loading and release of drugs.[21, 22] The amorphisation of pore-loaded compounds is hypothesised to be related to the limited space available within a pore, amongst other properties. The limited space can prevent nucleation and subsequent crystal growth leading to the confinement and stabilisation of the drug in its amorphous form.[23-25] The confinement of drug compounds inside the pores of mesoporous materials additionally enables the attainment of local high-drug concentrations and even drug supersaturation, leading to an increase in drug permeation and subsequent net absorption.[26] This has allowed drug confinement into mesoporous materials to emerge as an attractive strategy to improve the dissolution behaviour of poorly water-soluble compounds. Thus, understanding the crystallisation (or lack of) behaviour of drug compounds confined within these substrates at a molecular level is of critical importance in the formulation of amorphous systems.[27]

The polymorphism of crystalline compounds with the aid of porous substrates has been investigated with a view to manipulating the nucleation process.[28, 29] One of the ways the nucleation process can be altered is by changing the pore size to dimensions close to that of the critical nucleus size. This has the potential to regulate polymorphism if each form has a different critical nucleus size. It has also been stated that pore sizes should be approximately 20 times the molecular radius of the compound for crystallisation to occur in confinement;[30] an observation supported by Dwyer *et al.,* who investigated fenofibrate confinement in nanoporous silica. Amorphous fenofibrate was solidified in pores less than 20 nm, but was crystalline in pore sizes greater than 20 nm.[31] The molecular radius of fenofibrate is ~1.27 nm hence the drug would not have enough space in the 20 nm pore to crystallise and would therefore be amorphous.

Further confinement studies have focussed on porous and nonporous glass as crystallisation templates for the crystallisation of anthranilic acid (AA). AA crystallises in three polymorphs. Form I was mixed with nonporous glass beads and controlled pore glass (CPG) and heated above the melting point of the acid. Form II was dominant in pores of 7.5 nm, with the nanoscale crystals depicted by the decrease in melting point of anthranilic acid and broadening of the X-ray diffraction (XRD) peaks (Figure 1.3). Confinement led to the stabilisation of the metastable polymorph, with storage studies conducted for one month at room temperature. The authors suggested that the confinement of metastable Form II was due to the critical nucleus size being suitable for the smaller pore sizes.[28] Form III, the metastable polymorph known to crystallise from the melt, was also discovered to crystallise on the surface of the nonporous glass and confined within a controlled pore glass of 55 nm.

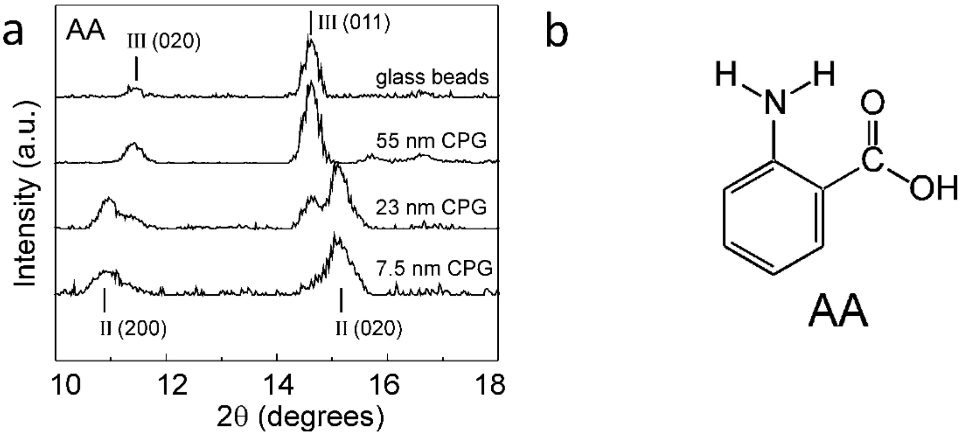

Figure 1.3: a) X-ray powder diffraction (XRPD) data for anthranilic acid crystallised by cooling of its melt on nonporous glass beads and within controlled pore glasses (CPGs) of various pore sizes. b) Structure of anthranilic acid – AA.[28]

Among pharmaceutically relevant compounds, indomethacin has been extensively employed as a model drug when investigating the influence of confinement on drug molecules, due to its array of polymorphs and limited aqueous solubility. Nartowski and collaborators investigated the influence of pore size and drug-loading method on the polymorphism of indomethacin.[32] The controlled porous glass (CPG) and mesoscopic cellular foam (MCF) were used as the substrates due to their varying pore sizes of 55 and 30 nm respectively. Indomethacin is known to form a glassy amorphous solid on cool of the unconfined melt.[32] Loading from the melt also led to the identification of amorphous indomethacin within the porous materials, displaying an amorphous "halo" in the X-ray powder diffraction (XRPD) patterns. Solid-state nuclear magnetic resonance (NMR) was also used, with the broadening of indomethacin peaks in the spectra indicating the many orientations of carbon atoms and differences in environments within the amorphous sample. The smaller pore size of MCF prevented the thermally induced recrystallisation of indomethacin beyond the glass transition of amorphous indomethacin at *ca.* 40 °C; however, the larger pore size of CPG allowed thermally induced recrystallisation. CPG showed concentration dependent thermally induced recrystallisation behaviour, with drug concentrations of 30 wt.% and above showing recrystallisation beyond the glass transition temperature to both the α and γ polymorphs. This highlights the importance of drug concentration when loading the porous material, as well as pore dimensions.[33] Solvent induced crystallisation of 15-25 wt.% loaded molten-IMC in CPG was investigated using three solvents: methanol, ethanol and acetonitrile. Recrystallisation of the γ-form was identified when ethanol and acetonitrile were used, however methanol induced the recrystallisation of either a methanol solvate, which desolvated to Form V or a mixture of both the γ-form and Form V.

The influence of pore volume and surface area on drug-loading capacity was also investigated by Bavnhøj *et al.,* using three model drugs with good glass-forming capabilities: celecoxib, cinnarizine and paracetamol.[23] Loading capacity was defined as: monomolecular loading capacity (MLC), whereby a single layer of drug molecules covers the surface of the porous material; or pore-filling capacity (PFC), which involves the filling of the pores. Hempel *et al.,* produced a method to overcome problems faced with difference in drug loading methods, when determining the MLC.[34] Differential scanning calorimetry (DSC) was used to determine the heat capacity of drugs loaded into porous materials at varying weight percentages of drug to substrate. The linear fit of heat capacity against drug fraction was plotted with the x-intercept providing the experimental MLC value (Figure 1.4). Drug loads below the experimentally determined MLC were reported to result in the stable amorphous form of the drug. Pore volume was determined to be the limiting factor to drug-loading capacity in this case. Increase in surface area from 559 to 682 m^2/g did not increase the experimental MLC value, as greater surface area was produced at the expense of pore volume (0.80 and 0.44 cm^3/g respectively), leading to spatial limitation. The theoretical MLC suggested the general trend to be an increase in MLC with an increase in surface area, which assumed the entire silica surface to be covered by drug molecules and did not account for the blocking of pores due the molecular size of the drugs. By plotting the experimental MLC along with the theoretical MLC and PFC as a function of surface area and pore volume, the authors were able to identify their influence on drug-loading fraction, with four zones describing loading within the pores or on the surface of the mesoporous silica, which could prove beneficial to future investigations looking into compound-loading onto mesoporous materials.

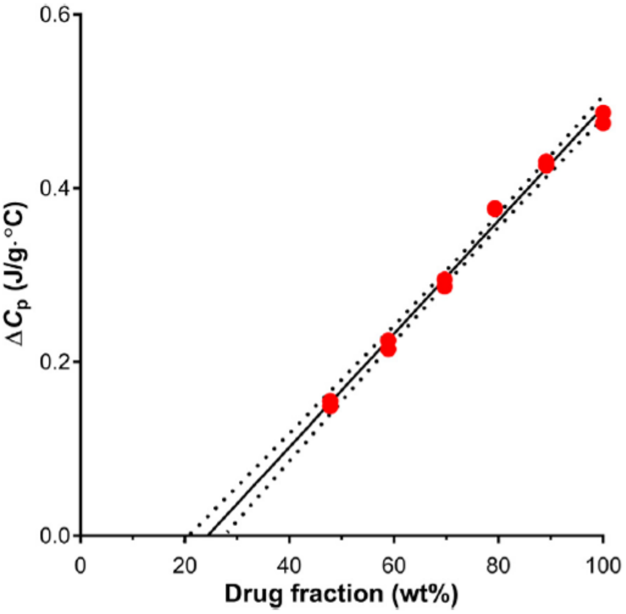

Figure 1.4: Heat capacity (△Cp) plotted as a function of drug fraction for celecoxib loaded into porous material with surface area, pore diameter and pore volume of 268 m^2/g, 21 nm, and 1.60 cm^3/g respectively, after thermal manipulation. The data is extrapolated to zero △Cp through linear extrapolation (solid line, r2=0.995) including the 95% confidence interval (dashed lines).[23]

1.3 Crystallisation characterisation techniques

Thermal evaluation of the effect of confinement on drug compounds can be provided by DSC, whilst also offering fast benchtop analysis. This technique can be used to quantify and differentiate between drug molecules confined in porous materials and that on the surface of the material.[35] It can also differentiate between crystalline and amorphous material. Kiwilsza and collaborators used DSC to determine the surface crystallisation of nimodipine in porous silica.[22] The endotherm indicated the melting of crystalline nimodipine on the surface of the porous silica when unwashed. Washing the loaded silica removed the surface crystalline material, which was indicated by the lack of endotherm. As no melting peak was observed for the washed samples, it was inferred that the confined nimodipine was amorphous. To confirm that the washed particles were loaded with nimodipine, the authors carried out a drug dissolution study. More than 60% of the drug was reported to dissolve and be released within the first three minutes of the study. Dwyer and collaborators took a similar approach, using DSC in the analysis of confined fenofibrate.[31] The sharp single melting endotherm indicated crystalline fenofibrate, but the lack of melting point for the smallest pore size indicated amorphous fenofibrate, which was confirmed by solid-state NMR. Double peaks in the DSC thermograph would speculate surface crystallisation in addition to confined crystals.

The XRPD offers a complementary way of assessing the crystallinity of confined compounds.[24, 28, 31, 33, 36-38] Like DSC, XRPD can be used to determine if the confined drug is in its crystalline or amorphous state. If the drug is crystalline, diffraction peaks will be observed in the pattern, and if well-defined, they can be used to determine the crystal structure present using crystallographic software. It can also illustrate if a mixture of crystal systems are present when dealing with polymorphs.[36] One of the disadvantages of XRPD is the decrease in peak intensity at greater angles. A way to overcome this is through neutron powder diffraction, which relies on the same principles as XRPD. Whilst X-rays interact with the electrons in the sample, neutrons interact with the nuclei. This means that neutron diffraction is better at resolving the hydrogen positions of a drug compound, for example, or can be used to investigate surface interactions between the drug and the pores it is confined within. Unfortunately, powder neutron diffraction requires the drug compounds to be deuterated, where the hydrogen atoms are replaced with the isotope deuterium, which may not always be technically feasible. Analysis by neutron powder diffractioncan only be carried out in specialised research facilities: for example, ISIS Neutron and Muon Source in the UK and the Institut Laue-Langevin located in France.

Aside from DSC and XRPD methods, neutrons and synchrotron X-rays have shown promise as techniques used to investigate porous substrates. Webber and Dore used neutron diffraction cryoporometry to assess the crystallisation behaviour of water and ice in porous silica. They were able to differentiate between the different states, observing that the signal produced was proportional to the quantity of the liquid or solid crystalline state, hence, were able to track the ratio as a function of temperature. From this, the Gibbs-Thomson equation could be applied to interpret structural information of the compound's state when confined in SBA-15, a type of mesoporous silica nanoparticle.[39] The Gibbs-Thomson equation is used to describe the melting point depression (Δ Tm) of small spherical crystals and is dependent on the properties of the material in its solid and liquid form and the interfacial interaction between them (Equation 1).

Equation 1

$$\Delta Tm = T_m^{\infty} - Tm(x) = \frac{4\sigma cl\, T_m^{\infty}}{x\Delta H_f \rho s}$$

Where Tm$^{\infty}$ *is the melting point of crystals of an infinite size (bulk melting temperature); Tm(x) is the melting point of the crystals with a diameter of x; σcl is the interfacial energy between the crystalline and liquid phases;* ΔH_f *is the bulk enthalpy of fusion and ρs is the density of the solid.*

When crystals are confined in pores, the interactions between the compound and pore wall need to be accommodated in the equation and additional terms are required (Equation 2).

Equation 2

$$\Delta Tm = \frac{kGT}{x} = \frac{k_g \cdot k_s \cdot k_i}{x}$$

Where k_g is a geometric constant; k_s is a constant specific to the solid's thermodynamic behaviour and k_i is the interfacial energy constant.

The confinement of proteins in mesoporous silica was also investigated using small-angle neutron scattering (SANS), assessing their arrangement within the pores. SBA-15 was chosen for its well-defined geometrical pores, and KIT-6 mesoporous silica was chosen for the contorted nature of the pores, allowing for the comparison of protein arrangement with regards to pore morphology.[40] The authors first charged the proteins to allow for electrostatic attraction with the silica substrates. They then observed that lower protein concentrations showed lower signal amplitudes from additional protein adsorbed on the walls of the silica matrix or free inside the pores, which distorted the scattering and, hence, substantiated that the information produced from SANS was reliable. Further research detailed the use of deep inelastic neutron scattering (DINS) to investigate mesoporous silica, due to its sensitivity for the investigation of the local environment of protons, complementing diffraction studies on atomic spatial distributions.[41] Water molecules were confined within hexagonally arranged porous silica with pore sizes of 4.3 nm. This led to the conclusion that hydrogen bonding between the water molecules and the silanol groups was much stronger than the hydrogen bonds within unconfined water, supporting the hypothesis of a difference in proton environment.

Pair distribution function (PDF) has also been used to probe the local atomic ordering of SBA-15 porous silica by investigating the relationship between porous structure and thermal stability of the substrate. Atomic pair distribution is the sine Fourier transform of the structure function that is determined experimentally by X-ray or neutron diffraction and can be used to study materials at an atomic scale.[42] Pair distribution function (PDF) has also been used in combination with small-angle X-ray diffraction (SAX) to probe the local atomic ordering of SBA-15 porous silica by investigating the relationship between porous structure and thermal stability of the substrate. Rantanen *et al.,* used SAX to determine the distance between the pores, using experimental data to estimate the pore wall thickness (W) using Equation 3.

Equation 3

$$W = a - D$$

Where D is the pore diameter, determined by nitrogen sorption analysis and a represents the pore distance calculated using the following equation where d_{100} *is the distance between lattice planes for the (100) diffraction peak.*

Equation 4

$$a = 2d_{100}/\sqrt{3}$$

The SAX diffraction data further showed that, with decreasing pore size, the position of the (100) peak of silica shifted to a lower 2θ (Figure 1.5). Decrease in pore size also showed an increase in wall thickness, with irregular ordering of wall structure. The measured structure function showed differences between pore sizes, with greater separation between peaks for the samples with larger pore sizes (9.69 and 12.05 nm average diameter), suggesting that the ordering of SiO4 tetrahedra was more regular. There was also an indication that silicon atom pairs were separated by a lesser distance, causing the structure to be more tightly packed, resulting in a greater density at the pore walls, which could influence the stability of the porous structure as a whole.[42] The PDF analysis has also been used to investigate the changes in short- to medium-range structures of nanoporous silica, characterising pore morphology as well as pore wall thickness and atomic structure within the pore walls.[42, 43]

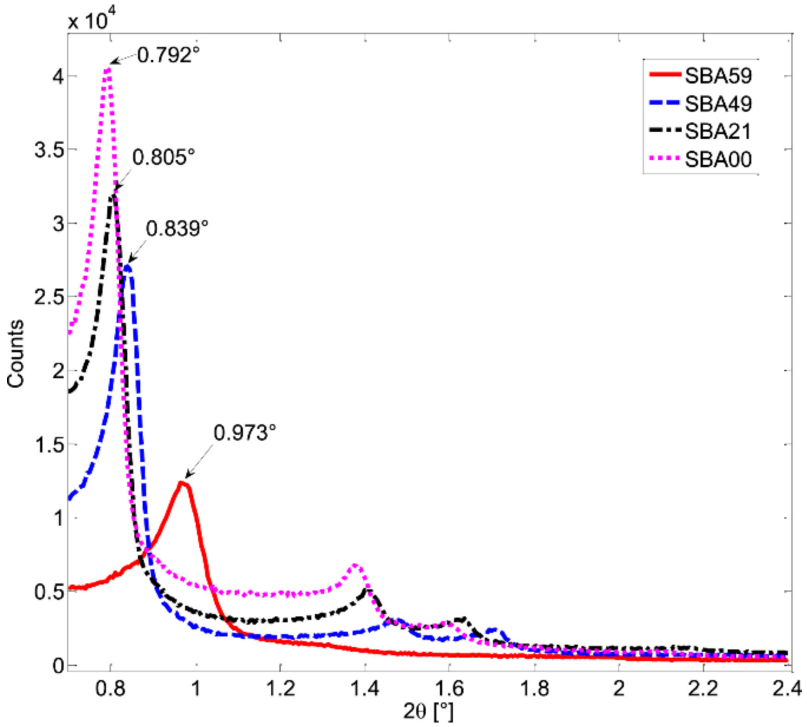

Figure 1.5: Diffraction patterns from small-angle X-ray diffraction samples SBA59, SBA49, SBA21 and SBA00 with pore diameters of 5.24, 8.12, 9.69 and 12.05 nm respectively. Locations of the 100 peaks are pointed out.[42]

Detailed structural information can also be gained from using X-ray total scattering coupled to atomic PDF and solid-state NMR. Atomic PDF is well-suited for structural characterisation of crystalline materials, as well as nano-sized and amorphous materials. It has been stated that PDF is a representation of "total scattered X-ray intensities and reflects both long-range atomic structure, manifested in the sharp Bragg peaks, and the local structural imperfections, manifested in the diffuse components of the total scattering pattern".[44] The structural information that PDF provides persists over long distances and can therefore describe structural properties at varying orders of scale. However, structural studies based on PDFs obtained from total X-ray scattering data of amorphous organic-inorganic nanocomposites can prove challenging due to their weak scattering power.

An application of such principles was explored by Hsieh and collaborators, where they investigated mononitrosyl complexes in porous silica matrices to determine a structural characterisation strategy to apply to another compound, sodium nitroprusside. As with any investigation, complementary methods of analysis are needed, and in this study, short-range NMR and long-range XRD provided the orthogonal approach. Thus, PDF can be used to bridge the gap between the two methods. The XRD data of loaded and unloaded silica showed amorphous features within the diffraction patterns with a characteristic peak at Q ~1.64 Å. Change in scattering contrast was witnessed between unloaded and loaded samples, with the principal peak within the loaded diffraction pattern displaying a broader nature with a lower intensity.[44] In a study by Nartowski and collaborators, ^{19}F solid-state NMR together with terahertz spectroscopy was used to detect the presence of confined molecules of flufenamic acid (FFA) in different environments and vibration motions.[45] This enabled the authors to gain in situ mechanistic insight into the molecular self-assembly at different length scales by taking advantage of the higher sensitivity of ^{19}F nuclei to changes in the local environments of molecules confined in the porous hosts. The authors reported for the first time the presence of a liquid-like layer of drug molecules on the porous scaffold's surface, which affected the nucleation and crystallisation behaviour of the drug (Figure 1.6).

Figure 1.6 shows the mechanisms by which FFA was confined in three porous silica structures with pore diameters ranging from 3.2 to 29 nm. Figure C and D show the confinement and stabilisation of amorphous FFA in pore sizes 3.2 and 7.1 nm respectively. The mechanism described in C is the formation of a plug followed by growth of the amorphous form, whereas D shows the surface saturation of the porous silica by a highly mobile species of FFA prior to plug formation and growth. Figure E shows porous silica with a pore diameter of 29 nm, highlighting the mechanism and formation of crystalline Form I FFA, by surface saturation by a highly mobile species followed by the nucleation and growth of the crystalline form.

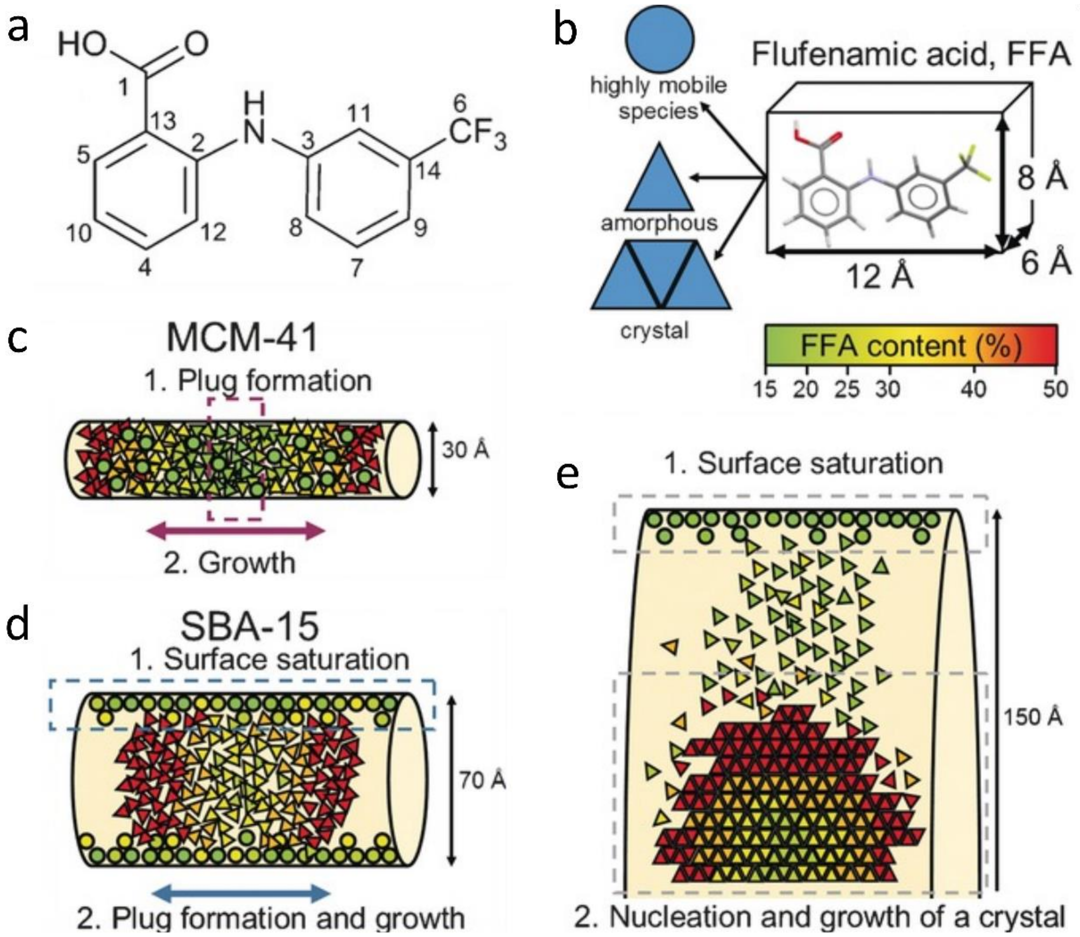

Figure 1.6: a) Structure of flufenamic acid (FFA) with labelling of the carbon atoms. b) Average dimensions of the FFA molecule and the three different states of FFA species inside the pores. c, d) Different mechanisms for FFA adsorption and stabilisation of the amorphous state. e) Mechanism of the formation of crystalline FFA form I in mesoscopic cellular foam.[45]

NMR has also been utilised to characterise the porous structure of hydrogels. Average pore diameter and pore volume are usually determined using mercury porosimetry and gas adsorption, but due to the nature of the hydrogel, NMR provides an alternative that is not impeded by the liquid phase. Low-field NMR—pulsed gradient spin echo was employed to understand the pore characteristics of a hydrogel composed of bacterial cellulose and acrylic acid, with high diffusion times indicating the interconnected nature of hydrogel pores.[46] NMR relaxation times have also been used to determine pore radius distribution profiles of hydrogels quickly without destroying the sample. NMR measurements rely on the excitation of targeted nuclei spins in the aqueous phase and subsequent measurement of the proton spins returning to equilibrium.[47] The relaxation rate of proton spins near the pore's surface is faster than in the bulk, providing a difference which can be measured. Sørland and collaborators used NMR to investigate pore size distribution of porous rocks, further concluding that NMR was more sensitive to pore size distributions than the mercury intrusion technique, as mercury underestimates larger cavities.[48]

1.4 Porous silicon

One of the materials that has shown great promise for the confinement of drugs is porous silicon (pSi). When pores are introduced into the structure of the chemical element silicon, rendering a large surface-to-volume ratio, we obtain the pSi form. The discovery of pSi was made fortuitously in 1956 while trying to develop a method for shaping and polishing the surfaces of silicon and germanium.[49] At the time their porous nature was not reported and only several years later in 1971 a procedure conducive to obtaining highly microporous silicon was published.[50] However, it was not until the early 1990's when Leigh Canham, concurrently with Lehmann and Göselle, hypothesised that the thin silicon filaments created when the pores become large and numerous enough to overlap, might display quantum confinement effects, leading to the demonstration that silicon wafers could emit light if subjected to chemical and electrochemical dissolution.[51] These discoveries soon instigated a substantial amount of research focused on Si-based lasers, displays, and optoelectronic switches. Nonetheless, due to the material's mechanical and chemical instability, as well as its low electroluminescence efficiency, most of the research in that area subsequently faded. In addition to its electronic properties, pSi was later found to act as a bioactive material,[52] which rekindled its study for biomedical applications.[53, 54]

There are over 40 different fabrication routes for pSi, using both “top-down” and bottom-up” approaches. “Top-down” methods rely on generating voids in monocrystalline silicon wafers using chemical and/or physical removal of atoms from the silicon substrate to create highly directional porosity. “Bottom-up” approaches, on the other hand, depend on assembling silicon clusters together in a way that, while establishing a crystalline form, leaves voids behind so that a porous structure can be synthesized.[55] Most processes for obtaining pSi over the last 50 years have relied on electrochemical anodisation of monocrystalline silicon wafers in aqueous electrolytes comprised of ethanol and hydrofluoric acid (HF).[56, 57] In electrochemical etching, the solid silicon wafer functions as an anode while a platinum (Pt) plate functions as a cathode, when both are submerged in the HF-ethanol electrolyte (Figure 1.7). The intrinsic properties of the pSi obtained through this route, such as pore size and shape, pore layer thickness, and porosity, are mainly determined by the manufacturing conditions. These conditions include current density, wafer type, resistivity, HF concentration, chemical composition of the electrolytes, crystallographic orientation, temperature, time, electrolyte stirring, illumination intensity and wavelength. While complete control over all of these process parameters is a major challenge for the fabrication of pSi, most of them are somehow related and can be kept constant, thereby achieving a satisfactory degree of reproducibility during the whole process.[58]

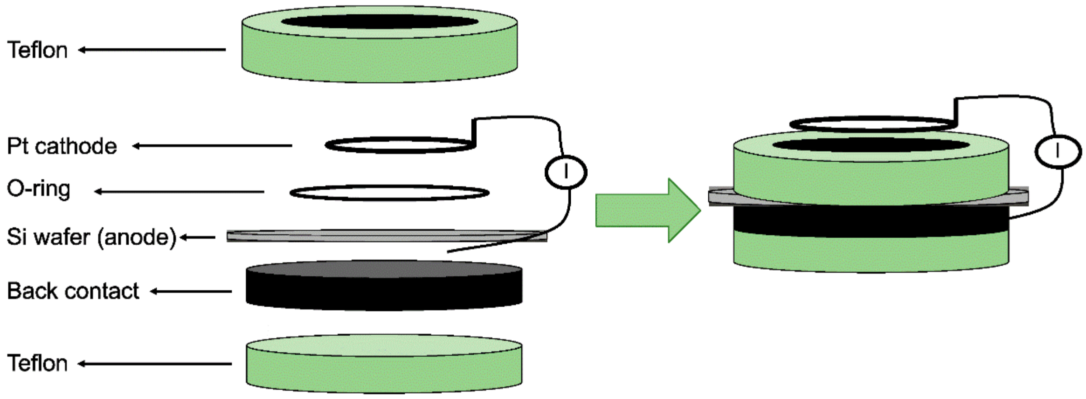

Figure 1.7: Schematic representation of a one-side etching setup for pSi fabrication. The Pt is the cathode and the Si wafer the anode in a HF ethanoic solution.[57]

1.4.1 Porous silicon surface stabilisation

Following annodisation, the pSi surface becomes hydrogen terminated (Si–H_x) and displays a certain degree of environmental chemical reactivity. The bonds at the surface can be Si–H, Si–H_2 and Si–H_3 hybrids and render the silicon surface prone to oxidation even in dry ambient conditions.[57, 59] In addition to the native oxidation of pSi, the extent and rate of oxidation is dependent on the storage conditions, with the transition from hydrophobic hydrogen termination to the hydrophilic oxidized surface taking place over the course of months at room temperature. Complete native oxidation, however, occurs over a much longer time period.[60]

The silicon hydride species present in the as-anodised surface of pSi can promote reactivity towards any compound potentially loaded within the pores of pSi,[61, 62] and thus a stable non-reactive surface is essential to replace the unstable hydrogen terminated surface of the freshly etched pSi. The conversion of the reactive groups at the surface into more stable oxidized, hydrosilylated or (hydro) carbonized forms allows for further modification of the pSi surface (Figure 1.8), which can include radiotracers such as ^{18}F.[63]

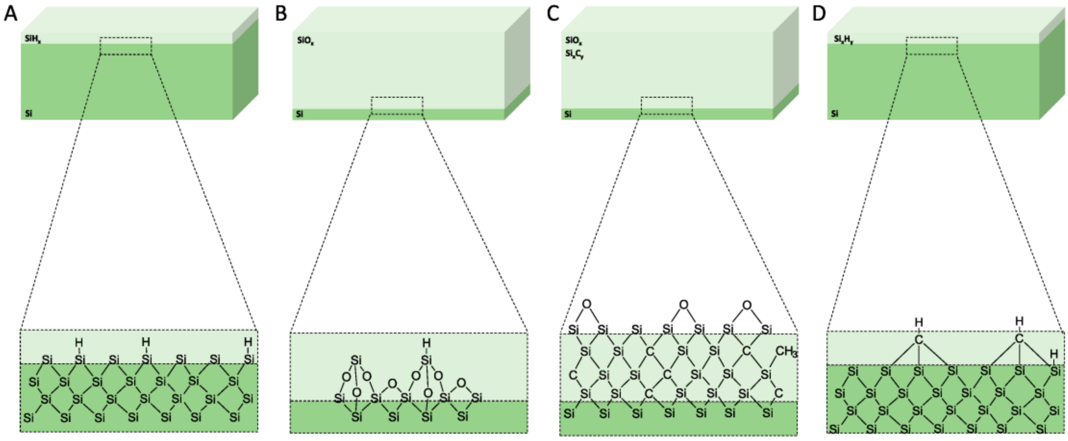

Figure 1.8: Schematics of the surface chemistry of the mesoporous materials after anodisation and after surface treatments. (A) as-anodized; (B) oxidized; (C) carbonized; and (D) hydrocarbonized.[63]

1.4.2 Thermal oxidation

One of the most straightforward methods to oxidise pSi surfaces is through thermal oxidation, which gives rise to thermally oxidized pSi (TOpSi).[64] The thermal oxidation of the pSi surface occurs at a threshold temperature of around 250 °C under ambient air conditions where the loss of hydrogen from the pSi surface is first detected, and where the Si dangling bond sites generated are able to chemisorb O_2 dissociatively, leading to the first stage of surface oxidation. This initial oxidation promotes further insertion of oxygen into the Si–Si back-bonds, giving rise to $-O_ySiH_x$ species. Concurrently, the oxidation process also leads to the formation of surface Si–OH species as a result of the oxygen insertion into the Si–H bonds.[65] The conversion of the native Si_ySiH_x surface to O_ySiH, O_ySiOH and SiOSi through thermal oxidation has been amply reported in the literature, especially due to its effect on pSi photoluminescence.[65, 66]

1.4.3 Hydrosilylation

Hydrosilylation is another process of passivating the silicon surface and can summarily be described as a radical-induced reaction which can be initiated either by free radical initiators, ultraviolet light (UV), or thermal energy to produce covalent linkage of alkyl chains to the hydrogen-terminated pSi surface, using unsaturated compounds such as terminal alkenes and alkynes as substrates. The first reports of a covalent linkage of densely packed, long alkyl chains directly to a silicon surface were published by Linford and Chidsey, where they employed pyrolysis of diacyl peroxides in the presence of hydrogen-terminated silicon. The authors used the thermal decomposition of diacyl peroxides to produce alkyl radicals, $CH_3(CH_2)_n^\bullet$ *via* $CH_3(CH_2)_nCOO^\bullet$ which were then reacted with the silicon surface. They also concluded that a large number of the linkages formed using this process were C to Si direct bonds. However, it was also noted the presence of some carbonyl groups which indicated that these monolayers were not comprised solely of alkyl chains. This was attributed to the presence of hydrolysable acyloxy bonds to the silicon surface (Si—O—C(O)—CH_2—) for one third of the chains, whereas the more robust alkyl bonds to the silicon surface (Si—CH2—) comprised the remaining fraction of the chains.[67] The same group later reported an optimised method for obtaining chains packed at approximately 90% the density of crystalline *n*-alkanes using pyrolysis of mixtures of either 1-alkenes or 1-alkynes and diacyl peroxides.[68] The presence of stable Si—O bonds at the surface decreases the number of reaction centres since these bonds cannot be broken by UV light or the thermal energies typically used in hydrosilylation reactions. By employing hydrogenated amorphous silicon (a—Si:H), a material known to be more resistive against oxide formation than crystalline silicon for the fabrication of hydrosilylated silicon surfaces,[69] the additional benefit of allowing the substrate to be treated under ambient conditions during surface functionalisation could be achieved.[70] Lewis acid-mediated hydrosilylation of alkynes and alkenes on non-oxidized hydride-terminated porous silicon has also been reported, where $EtAlCl_2$ acts upon terminal, cis- and trans-disubstituted, trisubstituted, and tetrasubstituted alkenes and terminal and internal alkynes to promote the covalent attachment of organic functionalities to the silicon surface *via* Si—C bonds resulting in alkenyl- or alkyl-terminated surfaces.[71, 72] A hydrosilylation approach towards the formation of Si—C bonds on silicon surfaces, which yielded surface bound vinyl and alkyl groups respectively has also been described. The authors employed a Pt catalysed reaction between 3,4,-dichlorobutene and hydrogen-terminated silicon surfaces, where after an initial step involving adsorption of Pt on the hydrogen-terminated silicon, an oxidative addition of the SiH to the coordination sphere of the Pt(0) complex to form $(dichlorobutene)_3Pt^{2+}$ (H)(Si) occurs. Subsequently, hydride addition to dichlorobutene takes place during the migratory insertion step which is followed by the reductive elimination of the alkylsilane.[73] The pSi surface can also be hydrosilylated by reductive electrolysis of organohalides, where the pSi is immersed in a solution containing an organohalide (RX, X=I or Br) and then passing cathodic current through the solution. The hydrosilylation occurs either by direct reaction between the Si radical and the alkyl radical, or by reduction of the Si radical to an anion followed by nucleophilic attack of the organohalide.[74] This hydrosilylation route has been reported to functionalize 20–80% of the Si—H bonds on the pSi surface, which still leaves the remaining Si—H bonds vulnerable to attack and oxidation. However, by following the organohalide functionalisation with a CH_3I methylation of the remaining Si—H bonds, it is possible to achieve a larger Si—C surface coverage.[75]

1.4.4 Thermal carbonisation

Thermal carbonisation is another process employed for stabilising the silicon surface which also involves chemical derivatisation of the pSi surface with organic compounds and formation of Si—C bonds.[76] It was first described in the late 1990's as an attempt to stabilise the photoluminescence of pSi and although the treatment does indeed produce a stable non-stoichiometric silicon carbide layer on the pSi surface, it also completely quenches its initial photoluminescence.[77] Early efforts relied on reactions involving heating of pSi single-crystals, which in turn proved potentially damaging to the fragile nanoscale structure of the substrate. Several research groups have subsequently investigated the formation of Si—C bonds on pSi at room temperature using one- or two-step methods.[71, 78, 79] The pSi surface produced via this route is remarkably stable to boiling alkali solutions, which indicates a sufficient degree of coverage to fully protect the exposed surface, whereas the Si—H terminated pSi dissolves quickly under these conditions.[78] Stability studies of differently stabilised pSi samples have shown that the thermal carbonisation of pSi (TCpSi) is an even more efficient stabilising method than thermal oxidation.[80] Functionalisation of TCpSi by radical coupling of sebacic acid has been also reported, as well as their capability to further modify the pSi surface using standard bioconjugate chemistry methods. The surface was stable and comparable to a non-functional thermal oxide, but superior to the widely used carboxy-terminated surface prepared by the thermal hydrosilylation route.[81]

1.4.5 Thermal hydrocarbonisation

Thermal decomposition of acetylene is another method that can be used to generate a hydrocarbon terminated surface.[82] This surface treatment allows functionalisation to be carried out at a lower temperature, as there is a threshold temperature which changes the thermal functionalisation of pSi into carbonisation. This temperature, nonetheless, allows for acetylene to be continuously circulated without the problem of graphitisation. Below 700 °C, the hydrogen atoms remain on the pSi surface rendering it hydrophobic (Si—C—H bonds; thermally hydrocarbonized pSi, THCpSi). Temperatures above 700 °C, on the other hand, allow the dissociation of hydrogen from the surface, rendering the surface more hydrophilic than the material produced at lower temperatures. One of the advantages of using small gaseous molecules of acetylene includes the faster and improved diffusion into the pores, which further improves the efficiency of surface coverage. The hydrocarbon terminated surface Si—C—H can be present in several configurations, with three silicon atoms bonded to a C atom presenting as the most common. This surface treatment has several advantages over the carbonization treatment including: the pSi surface remaining hydrophobic; the treated layer is thinner; and the gas adsorption properties are different from those found in the carbonized pSi. This treatment also enables further functionalisation of the pSi for cell targeting and antifouling purposes.[83]

1.4.6 Metalothermic reduction

Other than etching, chemical conversion of silica is nowadays one of the most prevalent routes for obtaining pSi.[84] Nanostructured silica can be reduced to pSi with the assistance of reducing agents such as magnesium and aluminium at moderate temperatures (400–800 °C). The milder reduction temperatures offer a desirable alternative for producing silicon when compared with the industrial blast furnace carbothermic reduction method (over 1400 °C).[85] Magnesiothermic reduction of silica was first described in the early 80's in India when researchers tried to obtain solar-grade silicon from rice husks.[86] The process of magnesiothermic reduction can be briefly detailed as follows: starting at a temperature of 400-600 °C in an inert atmosphere or vacuum, magnesium gas reacts with silicon dioxide to yield silicon and magnesium oxide according to the chemical reaction depicted in Equation 5.

Equation 5

$$SiO_2\ (s) + 2\ Mg\ (g) \rightarrow Si(s) + 2\ MgO\ (s)$$

The magnesia (MgO) can be easily removed afterwards with HCl, leaving behind a silicon replica with higher surface area than the starting template. The exothermic nature of the reduction reaction allows for utilisation of the heat produced aiding the process further, lowering the cost of the reaction.[87]

It is, however, noteworthy to point out that a side reaction can reduce the yield of silicon through the formation of magnesium silicide (Mg_2Si) as depicted in Equation 6. The Mg_2Si is obtained when the gaseous magnesium reacts with silica on the surface and, consequently, the formed Si product prevents access of magnesium to silica in the interior, causing a mismatch of the stoichiometric ratio of magnesium and silica, thus resulting in an undesired side reaction that produces magnesium silicide.[88] The formation of Mg_2Si reduces the yield of Si formed and impacts on the morphology of the final product upon removal, which occurs concurrently with the MgO removal with the HCl wash.[89]

Equation 6

$$Si\ (s) + 2Mg\ (g) \rightarrow Mg_2Si(s)$$

The greatest advantages of the magnesiothermic reduction of silica are the inexpensive silica feedstock that can be employed (sand, rice husk ash, etc.), as well as the lower required amounts of HF or organic solvents throughout the process.

Another reducing agent that has been given increasing attention is aluminium. Aluminium is an inexpensive metal which has long been known to react rapidly with silica to yield silicon according to Equation 7.

Equation 7

$$3SiO_2(s) + 4Al(l) \rightarrow 3Si(s) + 2Al_2O_3(s)$$

The advantages of using aluminium, besides its lower cost compared with magnesium, are the avoidance of minor silicide by-products (such as the Mg_2Si described earlier) and the alumina passivation of the silicon structure.[90]

The magnesiothermic reduction of silica nanoparticles has been reported to increase the surface area from 8.2 m^2g^{-1} to 386 m^2g^{-1} after a 12-hour reaction time at 500 °C. Pore volume also increased from 0.07 cm^3g^{-1} to 1.7 cm^3g^{-1} which were the highest values obtained from all samples. The surface area of silicon particles produced by aluminothermic reduction was a magnitude smaller than that of the magnesium reduced product, with the greatest surface area reported as 37 m^2g^{-1} after 24 hours at 650 °C. Pore volume was determined to be 0.51 cm^3g^{-1} after 12 hours at 650 °C. TEM images of the porous substrate showed aluminothermic reduction to produce a less porous substrate than magnesiothermic reduction, with the porous silicon composed of layers.[91]

1.5 Drug loading and release from pSi

There are many advantages of confining pharmaceutical compounds into mesoporous materials. To leverage this, in the case of pSi, drugs need to be loaded into a mesoporous matrix in a reproducible fashion and in high yield. The most common methods for drug loading in the context of pSi materials are solvent loading, where the mesoporous matrix is immersed into a saturated solution of the drug,[92-94] melt intrusion, where the mesoporous matrix is put into contact with the molten drug substance which facilitates complete pore-filling through capillary action,[95] or even by supercritical drying of ultrahigh porosity (90%) pSi.[96] When assessing the degree of drug loading, it is critical to distinguish the fraction of drug within the pores from the drug on the external surface of the material. Several methods have been employed to quantify drug loading, such as calorimetry,[35, 97] high-performance liquid chromatography (HPLC),[93, 94] atomic force microscopy (AFM) together with Time-of-Flight Secondary Ion Mass Spectroscopy (ToF-SIMS),[98] gas sorption,[62] and XRPD. While there is not a single method that could discern between loaded and surface-bound drugs in pSi, a suite of thermoanalytical and spectroscopic techniques has been proved to provide valuable information on the physical state of the drug molecules.

Surface modification of pSi makes the substrate adaptable for the confinement of many compounds, both hydrophilic and hydrophobic. Loading capacity can increase if the pore surface is tailored to suit the functional groups of the loaded molecule. It has been reported that hydrophobic drugs load better into hydrophobic pores, but the drugs could prove difficult to wet in physiological conditions.[99] To try and address this, a three-step pSi functionalisation method was employed. Firstly, the pSi films were hydrosilylated with 1-dodecene, followed by etching of the surface and a further hydrosilylation stage using (3-aminopropyl)triethoxysilane (APTES). This process provided the outer surface with hydrophilic functional groups and the inner pore surfaces with hydrophobic groups, which suited the hydrophobic drug camptothecin. An additional layer of polymer was attached to the loaded pSi surface to further control the release of the drug. Modification of the pSi doubled the drug-loading concentration, and the external polymer coat improved the drug release profile with a slower, steadier release than the control (Figure 1.9).[100]

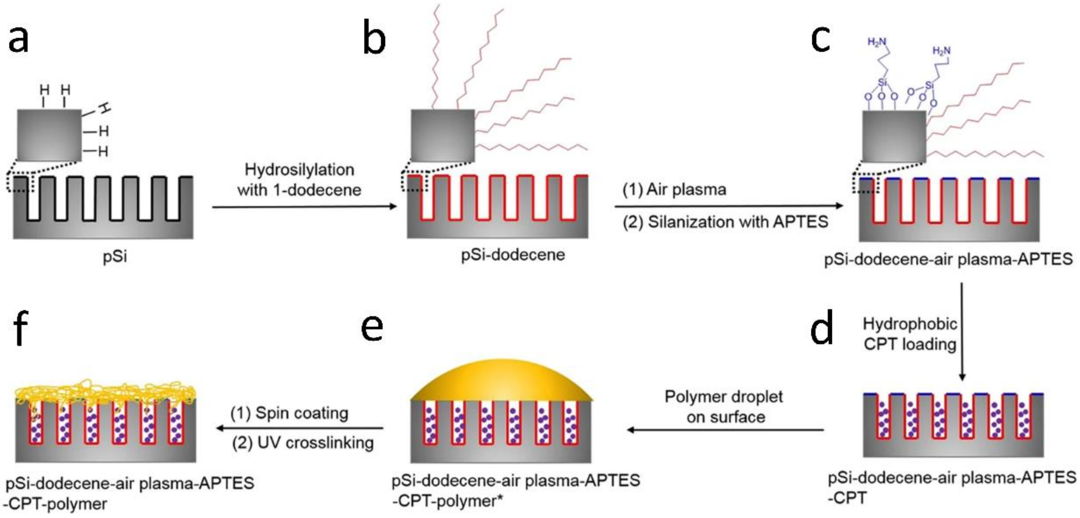

Figure 1.9: Schematic diagram showing the differential functionalisation of interior and exterior surfaces of pSi films to allow improved camptothecin (CPT) drug loading and release and CPT release.[100]

Nanoparticles of pSi have also been employed for drug delivery using polymer coatings, forming porous silicon-polymer composites. Krepker and Segal detailed the many designs of pSi-polymer composites and their fabrication, endowing the surface of the pSi with a wide range of surface chemistries for a variety of applications.[101] Porous silicon polymer nanocomposites have been used for the delivery of peptide nucleic acids (PNA) due to their large loading capacities.[102] However, pSi alone does not allow the release of the nucleic acid from the endo-lysomal vesicles into the cytoplasm and, therefore, requires additional modifications. Oxidised pSi nanoparticles were loaded with PNA before the application of a polymer coating, poly((ethylene glycol)–block–(2-(dimethylamino)ethyl methacrylate–co–butyl methacrylate)) (PEGDB). The PEGDB allowed for the systemic delivery of negatively charged nucleic acids, facilitating endosomal release of the nucleic acid.[103] The modified surface of the pSi nanoparticles led to increased stability and reduction in particle aggregation in comparison to the uncoated pSi nanoparticles. It was stated that the increased stability witnessed was due to the polymer-blocking surface adsorption of proteins and ions, therefore preventing aggregation.[104]

Salonen and collaborators looked at ibuprofen confined within thermally carbonised pSi to assess the loaded drug in comparison to drug crystallised on the surface by DSC.[35] Ibuprofen loaded onto nonporous silicon showed a melting peak (endotherm) at 74 °C, close to that of the bulk drug (76 °C). Ibuprofen loaded in pSi and washed in a solution of water and ethanol displayed two endotherms in the thermograph: the suppressed melting point of confined crystalline material and a small amount of surface crystals with a melting peak close to that of bulk ibuprofen. Washing the loaded pSi in pure ethanol showed no surface crystallisation. Depression of the melting point is often observed for confined crystalline compounds due to the reduced size of the crystals.[105] The confinement and increased drug dissolution has been further confirmed with studies which included the poorly water-soluble drugs indomethacin and griseofulvin, with the amorphous state of the confined compounds enhancing the drug dissolution or drug permeation rate.[24, 93, 106] In these studies, the loading degree of both drugs ranged between 6 to 29 wt.% for indomethacin and 6 to 17 wt.% for griseofulvin, depending on surface chemistry and pore size of the pSi substrate and highlighted the potential impact of these physicochemical parameters in further pharmaceutical processing. The loading of poorly water-soluble antiviral compounds, such as saliphenylhalamide, has also been conducted, in which a 2.88% drug loading was reported.[94] The authors attributed the low loading values to the drug's partition coefficient (a measure of the lipophilicity of a compound) and its molecular radius.

The application of pSi to deliver the anti-cancer drug doxorubicin to transferrin receptor-overexpressing tumour cells across a blood-brain barrier (BBB) model has also been reported.[107] The pSi particles were first functionalised using undecylenic acid to produce particles with carboxyl terminations and further conjugated to transferrin to target cell surface markers. The hypothesis of this study was that the transferrin-coupled pSi particles would be able to cross the BBB and, furthermore, bind to transferrin receptors found on the surface of tumour cells to deliver the drug. Unlike many other studies involving the use of pSi as a drug delivery system, the focus of this investigation was not to increase the solubility of a poorly aqueous soluble drug but to achieve targeted drug delivery using functionalised pSi particles. The functionalisation of the silicon surface increased the particles' colloidal stability, as demonstrated by a decrease in hydrodynamic radius measured by dynamic light scattering. Loading was determined to be 87.90 ± 2.16 μg/mg pSi particles, with drug release dependent on the pH of the environment. The release of the drug was studied to simulate endolysosomal and physiological conditions (pH 5 and 7.4, respectively). Stable hydrogen bonds were formed between the pSi surface and doxorubicin in a neutral pH, limiting the drugs release. Hydrogen bonds weakened in an acidic environment, leading to a greater drug release, with up to 90% in 12 h. Furthermore, brain tumour tissue is known to have a lower pH than normal tissue; therefore, a pH-dependent rate would be beneficial for improved drug release at the target site.[107]

The successful confinement of crystalline and amorphous small drug molecules has led to research into the confinement or adsorption of proteins to mesoporous substrates, an area of increasing promise to the pharmaceutical industry.[38, 40, 93, 108] The loading of metformin into pSi for extended drug release has also been investigated. Metformin is routinely administered in high and frequent doses, which can cause side effects within the gastrointestinal tract. Attempts to increase the bioavailability of the drugs have been employed, including research into the encapsulation of metformin into chitosan-poly(lactide-co-glycolide) nanoparticles only producing low encapsulation efficiency values.[109] The pSi offered the sustained release needed due to a combination of morphological features and surface chemistry. The aim of the work was to investigate the bonding between drug and carrier, an area which many other studies had failed to address. The pSi was fabricated from electrochemical etching of silicon wafers with surface passivation via thermal oxidation to promote the adsorption of the drug. The largest dimension of the pore was determined to be 8 nm ± 2 nm. Due to the irregular shape of the pores, the average pore diameter was not conclusive. Albeit, the pores were large enough to facilitate the free movement of the drug into the pores and through the porous network. Interestingly, the authors analysed the distribution of charge within the drug-loaded pSi and found that metformin was protonated in media with a pH less than 2.8, monoprotonated between pH 2.8 and 11.5, and neutral above pH 11.5. The pH of the media also influenced the surface chemistry of the oxidised pSi, which therefore influenced its drug-loading capacity. Particles displayed a positive surface charge at a pH of 2.2 or lower and negative charge above that value. A zeta potential of less than 30 mV indicates particle instability, which was determined to be at a pH less than 7. This provided an optimum pH of 7, with the negatively charged surface of the pSi (Si-O⁻) favouring the loading of the positively charged metformin molecules, with electrostatic forces enabling the interaction between the drug molecules and the carriers' surface (Figure 1.10). Overall, this study found thermally oxidised pSi to be advantageous as a carrier of metformin, with prolonged release over a period of 26 h.[110]

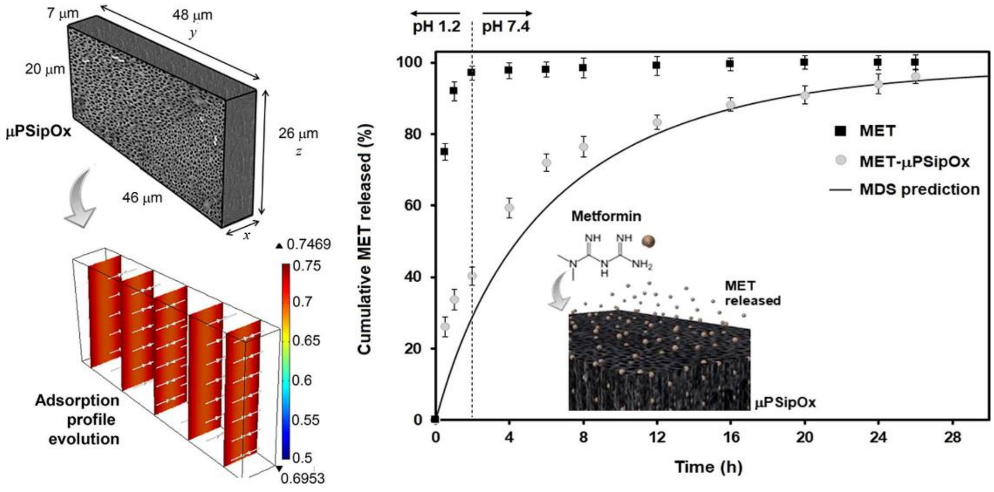

Figure 1.10: Representative geometry used for modelling the loading kinetics during the adsorption of metformin (MET) onto porous silicon microparticles (μpSip), dimensionless concentration profiles inside the μpSipOx during the adsorption of MET, and in vitro release profiles of pure MET and MET-μpSipOx (oxidised porous silicon microparticles).[110]

The use of pSi as an aid in the crystallisation of proteins has also been investigated due to the limited success of protein nucleation on other modified surfaces. The pSi was used as a substrate on the basis that the pores would enable the confinement of protein molecules, which would lead to nucleation and crystal growth. The average pore size of the material was between 5 and 10 nm with a solution-loading method employed. The pSi induced the nucleation of five out of the six proteins (lysozyme, trypsin, catalase, thaumatin, and phycobiliprotein) with hydrodynamic radii ranging from 2 to 5 nm, with crystals either growing on the silicon fragments or growing within the oil droplet which suspended the silicon and protein solution, decreasing in size the further away they were from the silicon fragment. This could have been due to nuclei diffusing away from the nucleation site or nucleation taking place on smaller fragments of pSi. An explanation as to why concanavalin A, one of the proteins, did not crystallise in the presence of the pSi substrate was not discussed. Further to this, the influence of smaller pore sizes on crystallisation was investigated using other porous materials, which did not prove successful. This has supported the hypothesis of the dependency of pore size on the crystallisation of proteins. The crystallisation of proteins usually depends on the pH of the system; however, using pSi as a nucleation surface removed this dependency with confinement of the molecules, leading to localised supersaturation—hence, enabling crystallisation.[38]

The use of pSi as a carrier for fatty acid α-linolenic acid has also been reported.[111] The aim of the study was to load compounds of nutritional benefit into a drug carrier in order to stimulate the secretion of gut hormone glucagon-like peptide 1 (GLP-1). Nutrients such as fatty acids have been known to aid the regulation of appetite and blood glucose levels, which is beneficial in the treatment of obesity.[112] The pSi particles were first thermally hydrocarbonised to aid the loading of the hydrophobic fatty acid and delay its release. Two drug-loading ratios were used within the study: 3% and 9.2%; however, 49.4% ± 6.29% and 25.7% ± 1.53% of the confined α-linolenic acid remained unreleased, respectively. It was stated that the empty pSi did not stimulate the expression of GLP-1 from the STC-1 cell line, but the fatty acid-loaded substrate increased GLP-1 secretion by 1.5% compared to buffer alone. The detectable amount of α-linolenic acid was reduced with increased incubation time and acidity of the buffer, which may have been due to the accelerated oxidation of fatty acid in an acidic environment.[113] However, the time in which fatty acids remain within the acidic environment of the human stomach depends on many factors, including the type of food and how often it is consumed.

Microparticles of pSi loaded with GLP-1 were also reported to lower the blood glucose levels after a single subcutaneous injection in mice, but none of the microparticles were able to prolong the glucose-lowering effect, as compared to the GLP-1 solution.[114] In this study, the authors loaded and released the GLP-1 peptide from negatively charged TOpSi and TCpSi microparticles and from positively charged amine modified microparticles, designated as TOpSi-NH2-D (isolelectric point 8.8) and TCpSi-NH2-D (isoelectric point 8.8), respectively. They found that the adsorption of GLP-1 onto the pSi microparticles could be increased 3–4-fold by changing the pSi surface charge from negative to positive, indicating that the positive surface charge of pSi promoted an electrostatic interaction between the negatively charged peptide. The adsorption and desorption kinetics of the GLP-1 peptide were also subject to study, where the authors concluded that, albeit electrostatic attraction between the peptide and the pSi surface is relevant, at low concentrations, the hydrophobic interaction seems to have a higher impact, even though the effect is less important for most hydrophilic nanoparticles.[115]

Molecular modelling has been used to identify the intermolecular interactions that characterise physicochemical factors, influencing the release of a drug from a dosage form.[116] Polkovnikova and collaborators aimed to investigate the activation energy required for drug desorption from silicon and silicon–dioxide surfaces. Desorption and dissolution of the drug from the surface was observed when the van der Waals interaction energy reached zero. The activation energy was defined as the difference between the average energy of the desorbed and adsorbed state in water. The change in electronic energy was relative to the initial state, with the drug either in its ionised or unionised state when adsorbed to the surface.

The unionised drug molecules were positioned flat on the surface of the silicon. Desorption of the drug from the surface was said to occur in two stages: first, the separation of the polar part of the molecule, followed by the separation of the hydrophobic phenyl radical, which was stated to have a greater affinity for the silicon. Desorption energy profiles showed evidence of these two stages with a two-stage energy increase. The ionised drug desorbed quicker than the unionised drug, also occurring in two stages; firstly, the hydrophobic phenyl group attached to the SiH and SiOH groups of the silicon surface and then, the subsequent removal of the hydrophilic section of the drug. Bonding between the drug and adsorbent surface was also investigated, with the hydrogen bond between the surface OH group of the SiOH and the nitrogen atom of the drug breaking during desorption for both ionised and unionised surfaces.

Estimations of the activation energies for the dissolution of the drug from the surface of the adsorbent into water were calculated by using the difference between the electronic energies of the system dissolved in water and the initial adsorbed state. The energy required for desorption of the drug from the ionised SiO2 surface was overall the greatest, with 1218.33 ± 305.41 kJ/mol required for the dissolution of the drug. Desorption of the drug cation was the lowest, lower than that of the drug in its unionised state (110.66 and 347.30 kJ/mol, respectively). Estimations of the activation energy of drug desorption in aqueous solutions of different pH values were also investigated. Drug desorption from the SiO2 surface at pH 6.8 and 7 showed the greatest significance, with activation energies of 1049.96 ± 244.98 kJ/mol and 1076.96 ± 239.24 kJ/mol respectively, which is significant if dissolution was to occur in the large intestine.

The ability to load and release drug molecules trapped within its pores has led to discussions over the possibility of employing pSi as a nanoscale delivery system but also raised concerns about their toxicological profile in a biological setting.[117] Ever since pSi was first reported as a bioactive material,[52] many studies have been devoted to study its biocompatibility and biomedical applications.[118] It has been reported that pSi biodegradation can be controlled by the overall porosity, pore size, shape, surface, and bulk properties,[119] which in turn can be modulated by controlling the material fabrication parameters of the matrix.[120] For instance, pSi with a porosity >70% dissolves in all the simulated body fluids (except gastric fluids), whereas pSi with a porosity <70% is bioactive and slowly biodegradable.[54] The fact that pSi degrades mainly into monomeric silicic acid, Si(OH)4, the most natural form of Si in the environment and very important in human physiology in protecting against the poisonous effects of aluminium,[121] is an important feature that contributes even further to the pSi apparent biocompatibility. It has been reported that the average intake of Si is approximately 25–40 mg/day and that Si is an essential nutrient for the human body.[122] Silicic acid does not accumulate within the human body and has been shown to be absorbed readily by the gastrointestinal tract of humans and rapidly excreted via the urinary pathway.[123]

Porous materials show many advantages as a drug carrier due to their large loading capacity, tuneable pore size and controlled drug release. They can influence the polymorphic form of the confined crystalline state or stabilise the disordered amorphous state confined within them, which shows promise as a way of improving the dissolution rate of poorly water-soluble drugs. Protein crystallisation has also successfully utilised porous materials for heterogeneous nucleation, using porous silicon as a templating surface. From this, we have been able to identify the issues faced by many researchers in their investigations into the confinement of drug compounds in mesoporous materials; for example, crystallisation on the surface of the porous substrate limiting the overall drug dissolution. A clear understanding is needed of how external factors such as temperature and pH influence crystallisation, as well as the pore structure and surface chemistry of the substrate before translation to the pharmaceutical industry. The nucleation of the crystalline state in porous silicon needs to be evaluated, including the influence of pore diameter and pore volume, as well as the interactions between drug molecules and the surface of the substrate. Neutron and synchrotron X-ray diffraction, as well as solid-state NMR, are emerging as advanced characterisation techniques that are now beginning to be utilised to tackle this, along with the conventional methods such as DSC and XRPD.

These fundamental issues need to be addressed continuously in order for research to turn to the scale-up of these processes and make drug confinement in mesoporous materials feasible for pharmaceutical development.

1.6 Outline of Thesis

The aim of this research is to work towards understanding the crystallisation behaviour of pharmaceutical compounds confined in porous materials, at both ambient and high-pressure. Porous materials are known to influence the polymorphic form of the crystalline state or stabilise the amorphous form of the confined compound. To fully understand this behaviour, a clear understanding of the crystallisation behaviour of a pharmaceutical compound is required in order to fully understand the role of confinement. This thesis is split into three sections: investigating how crystalline structures react to high pressure, how their structures are influenced by re-crystallisation in various solvents and finally their behaviour when confined in porous material. Isonicotinamide is a model compound whose behaviour is well understood and characterised, with six known polymorphs deposited in the Cambridge Structural Database. Structural characterisations of the isonicotinamide polymorphs at high-pressure are detailed in Chapter 3 and 4, with investigations into how differences in hydrogen-bonding motifs influence the compression and polymorphic behaviour. When using a solvent mediated loading method, it is important to understand how the solvent influences the polymorphism of the compound. Nifedipine has six known polymorphs, crystallised through the thermal manipulation of the thermodynamically stable form, however little has been reported on polymorphism via solvent-induced crystallisation. Chapter 5 explores the polymorphic behaviour of nifedipine through solvation and thermal desolvation. The final experiment detail the confinement of isonicotinamide in porous silica, looking at the influence of solvent and the differences in outcome when loaded at ambient and high pressure, and concluding this thesis on the crystallisation behaviour of crystallisation behaviour of pharmaceutical compounds confined within porous materials.

1.7 References

1. Singh, A.; Worku, Z. A.; Van Den Mooter, G. Oral formulation strategies to improve solubility of poorly water-soluble drugs. In *Expert Opinion on Drug Delivery*, 2011.
2. Seto, J.; Romero, P. A. 1 - Shaping it up: Design and engineering of biominerals and crystalline materials from the bottom up. In *Biomineralization and Biomaterials*, Aparicio, C., Ginebra, M.-P. Eds.; Woodhead Publishing, 2016; pp 3-50.
3. Pudasaini, N.; Upadhyay, P. P.; Parker, C. R.; Hagen, S. U.; Bond, A. D.; Rantanen, J. Downstream Processability of Crystal Habit-Modified Active Pharmaceutical Ingredient. *Organic Process Research & Development* **2017**, *21* (4), 571-577. DOI: 10.1021/acs.oprd.6b00434.
4. Salvatori, F.; Mazzotti, M. Manipulation of Particle Morphology by Crystallization, Milling, and Heating Cycles: Experimental Characterization. In *Industrial & Engineering Chemistry Research*, American Chemical Society: 2018; Vol. 57, pp 15522-15533.
5. Lee, A. Y.; Erdemir, D.; Myerson, A. S. Crystal Polymorphism in Chemical Process Development. In *Annual Review of Chemical and Biomolecular Engineering*, Annual Reviews: 2011; Vol. 2, pp 259-280.
6. Tanoury, G. J.; Hett, R.; Kessler, D. W.; Wald, S. A.; Senanayake, C. H. Taking Advantage of Polymorphism To Effect an Impurity Removal: Development of a Thermodynamic Crystal Form of (R,R)-Formoterol Tartrate. In *Organic Process Research & Development*, American Chemical Society: 2002; Vol. 6, pp 855-862. Urwin, S. J.; Yerdelen, S.; Houson, I.; ter Horst, J. H. Impact of Impurities on Crystallization and Product Quality: A Case Study with Paracetamol. In *Crystals*, 2021; Vol. 11.
7. Briuglia, M. L.; Sefcik, J.; Horst, J. H. T. Measuring Secondary Nucleation through Single Crystal Seeding. In *Crystal Growth and Design*, American Chemical Society: 2019; Vol. 19, pp 421-429. Lynch, M. B.; Lawrence, S. E.; Nolan, M. Predicting Nucleation of Isonicotinamide from the Solvent-Solute Interactions of Isonicotinamide in Common Organic Solvents. In *Journal of Physical Chemistry A*, American Chemical Society: 2018; Vol. 122, pp 3301-3312.
8. Ferrari, E. S.; Davey, R. J.; Cross, W. I.; Gillon, A. L.; Towler, C. S. Crystallization in polymorphic systems: The solution-mediated transformation of β to α glycine. In *Crystal Growth and Design*, 2003; Vol. 3, pp 53-60.
9. Erdemir, D.; Lee, A. Y.; Myerson, A. S. Nucleation of Crystals from Solution: Classical and Two-Step Models. In *Accounts of Chemical Research*, American Chemical Society: 2009; Vol. 42, pp 621-629.
10. Ter Horst, J. H.; Schmidt, C.; Ulrich, J. Fundamentals of Industrial Crystallization. In *Handbook of Crystal Growth: Bulk Crystal Growth: Second Edition*, 2015; Vol. 2, pp 1317-1349.
11. McGinty, J.; Yazdanpanah, N.; Price, C.; ter Horst, J. H.; Sefcik, J. CHAPTER 1 Nucleation and Crystal Growth in Continuous Crystallization. In *The Handbook of Continuous Crystallization*, The Royal Society of Chemistry: 2020; pp 1-50.
12. Parambil, J. V.; Heng, J. Y. Y. Seeding in Crystallisation BT - Engineering Crystallography: From Molecule to Crystal to Functional Form. Roberts, K. J., Docherty, R., Tamura, R., Eds.; Springer Netherlands: Dordrecht, 2017; pp 235-245. Zhang, F.; Shan, B.; Wang, Y.; Zhu, Z.; Yu, Z.-Q.; Ma, C. Y. Progress and Opportunities for Utilizing Seeding Techniques in Crystallization Processes. In *Organic Process Research & Development*, American Chemical Society: 2021; Vol. 25, pp 1496-1511.
13. Yu, L.; Reutzel-Edens, S. M.; Mitchell, C. A. Crystallization and Polymorphism of Conformationally Flexible Molecules: Problems, Patterns, and Strategies. In *Organic Process Research & Development*, American Chemical Society: 2000; Vol. 4, pp 396-402. Cruz-Cabeza, A. J.; Bernstein, J. Conformational Polymorphism. In *Chemical*

Reviews, American Chemical Society: 2014; Vol. 114, pp 2170-2191. Nangia, A. Conformational Polymorphism in Organic Crystals. In *Accounts of Chemical Research*, American Chemical Society: 2008; Vol. 41, pp 595-604.
14. Lombard, J.; Haynes, D. A.; le Roex, T. Polymorphic Behavior of Two Organic Zwitterions: Two Rare Cases of No Observable Conversion between Polymorphs. In *Crystal Growth & Design*, American Chemical Society: 2017; Vol. 17, pp 6625-6633.
15. Wiergowska, G.; Stasiłowicz, A.; Miklaszewski, A.; Lewandowska, K.; Cielecka-Piontek, J. Structural Polymorphism of Sorafenib Tosylate as a Key Factor in Its Solubility Differentiation. In *Pharmaceutics*, 2021; Vol. 13.
16. Nicoud, L.; Licordari, F.; Myerson, A. S. Estimation of the Solubility of Metastable Polymorphs: A Critical Review. In *Crystal Growth & Design*, American Chemical Society: 2018; Vol. 18, pp 7228-7237.
17. Chen, J.; Sarma, B.; Evans, J. M. B. B.; Myerson, A. S. Pharmaceutical crystallization. In *Crystal Growth and Design*, 2011; Vol. 11, pp 887-895.
18. Grohganz, H.; Löbmann, K.; Priemel, P.; Jensen, K.; Graeser, K.; Strachan, C.; Rades, T. Amorphous drugs and dosage forms. In *Journal of Drug Delivery Science and Technology*, 2013; Vol. 23, pp 403-408.
19. Garcia-Bennett, A. E.; Lau, M.; Bedford, N. Probing the Amorphous State of Pharmaceutical Compounds Within Mesoporous Material Using Pair Distribution Function Analysis. In *Journal of pharmaceutical sciences*, 2018; Vol. 107, pp 2216-2224.
20. Hancock, B. C.; Parks, M. What is the True Solubility Advantage for Amorphous Pharmaceuticals? In *Pharmaceutical Research*, 2000; Vol. 17, pp 397-404. Hancock, B. C.; Zografi, G. Characteristics and Significance of the Amorphous State in Pharmaceutical Systems. In *Journal of Pharmaceutical Sciences*, Elsevier: 2002; Vol. 86, pp 1-12.
21. Vallet-Regí, M.; Balas, F.; Arcos, D. Mesoporous Materials for Drug Delivery. In *Angewandte Chemie International Edition*, 2007; Vol. 46, pp 7548-7558. Brás, A. R.; Merino, E. G.; Neves, P. D.; Fonseca, I. M.; Dionísio, M.; Schönhals, A.; Correia, N. T. Amorphous ibuprofen confined in nanostructured silica materials: A dynamical approach. In *Journal of Physical Chemistry C*, 2011; Vol. 115, pp 4616-4623. Uejo, F.; Limwikrant, W.; Moribe, K.; Yamamoto, K. Dissolution improvement of fenofibrate by melting inclusion in mesoporous silica. In *Asian Journal of Pharmaceutical Sciences*, Elsevier: 2013; Vol. 8, pp 329-335.
22. Kiwilsza, A.; Milanowski, B.; Drużbicki, K.; Coy, L. E.; Grzeszkowiak, M.; Jarek, M.; Mielcarek, J.; Lulek, J.; Pajzderska, A.; W\kasicki, J. Mesoporous drug carrier systems for enhanced delivery rate of poorly water-soluble drug: nimodipine. In *Journal of Porous Materials*, 2015; Vol. 22, pp 817-829.
23. Bavnhøj, C. G.; Knopp, M. M.; Madsen, C. M.; Löbmann, K. The role interplay between mesoporous silica pore volume and surface area and their effect on drug loading capacity. In *International Journal of Pharmaceutics: X*, 2019; Vol. 1, p 100008.
24. Mäkilä, E.; Ferreira, M. P. A. A.; Kivelä, H.; Niemi, S. M.; Correia, A.; Shahbazi, M. A.; Kauppila, J.; Hirvonen, J.; Santos, H. A.; Salonen, J. Confinement effects on drugs in thermally hydrocarbonized porous silicon. In *Langmuir*, 2014; Vol. 30, pp 2196-2205.
25. Qian, K. K.; Bogner, R. H. Application of mesoporous silicon dioxide and silicate in oral amorphous drug delivery systems. In *Journal of Pharmaceutical Sciences*, 2012; Vol. 101, pp 444-463.
26. Kaukonen, A. M.; Laitinen, L.; Salonen, J.; Tuura, J.; Heikkilä, T.; Limnell, T.; Hirvonen, J.; Lehto, V. P. Enhanced in vitro permeation of furosemide loaded into thermally carbonized mesoporous silicon (TCPSi) microparticles. In *European Journal of Pharmaceutics and Biopharmaceutics*, 2007. Brouwers, J.; Brewster, M.

E.; Augustijns, P. Supersaturating drug delivery systems: The answer to solubility-limited oral bioavailability? In *Journal of Pharmaceutical Sciences*, 2009.

27. Mellaerts, R.; Aerts, C. A.; Humbeeck, J. V.; Augustijns, P.; Den Mooter, G. V.; Martens, J. A. Enhanced release of itraconazole from ordered mesoporous SBA-15 silica materials. In *Chemical Communications*, 2007; Vol. d, pp 1375-1377. Van Speybroeck, M.; Barillaro, V.; Thi, T. D.; Mellaerts, R.; Martens, J.; Van Humbeeck, J.; Vermant, J.; Annaert, P.; Van Den Mooter, G.; Augustijns, P. Ordered mesoporous silica material SBA-15: A broad-spectrum formulation platform for poorly soluble drugs. In *Journal of Pharmaceutical Sciences*, 2009; Vol. 98, pp 2648-2658.

28. Ha, J.-M.; Wolf, J. H.; Hillmyer, M. A.; Ward, M. D. Polymorph Selectivity under Nanoscopic Confinement. In *Journal of the American Chemical Society*, American Chemical Society: 2004; Vol. 126, pp 3382-3383.

29. Choi, K.-M.; Kuroda, K. Polymorph Control of Calcium Carbonate on the Surface of Mesoporous Silica. In *Crystal Growth & Design*, American Chemical Society: 2012; Vol. 12, pp 887-893.

30. Sliwinska-Bartkowiak, M.; Dudziak, G.; Gras, R.; Sikorski, R.; Radhakrishnan, R.; Gubbins, K. Freezing behavior in porous glasses and MCM-41. In *Colloids and Surfaces A: Physicochemical and Engineering Aspects*, 2001; Vol. 187, pp 523-529.

31. Dwyer, L. M.; Michaelis, V. K.; O'Mahony, M.; Griffin, R. G.; Myerson, A. S. Confined crystallization of fenofibrate in nanoporous silica. In *CrystEngComm*, The Royal Society of Chemistry: 2015; Vol. 17, pp 7922-7929.

32. Fukuoka, E.; Makita, M.; Yamamura, S. Some Physicochemical Properties of Glassy Indomethacin. In *Chemical & Pharmaceutical Bulletin*, 1986; Vol. 34, pp 4314-4321. Borka, L. The polymorphism of indomethacine. New modifications, their melting behavior and solubility. In *Acta pharmaceutica Suecica*, 1974; Vol. 11, pp 295-303.

33. Nartowski, K. P.; Tedder, J.; Braun, D. E.; Fábián, L.; Khimyak, Y. Z. Building solids inside nano-space: from confined amorphous through confined solvate to confined 'metastable' polymorph. In *Physical Chemistry Chemical Physics*, The Royal Society of Chemistry: 2015; Vol. 17, pp 24761-24773.

34. Hempel, N.-J.; Brede, K.; Olesen, N. E.; Genina, N.; Knopp, M. M.; Löbmann, K. A fast and reliable DSC-based method to determine the monomolecular loading capacity of drugs with good glass-forming ability in mesoporous silica. In *International Journal of Pharmaceutics*, 2018; Vol. 544, pp 153-157.

35. Salonen, J.; Paski, J.; Vähä-Heikkilä, K.; Heikkilä, T.; Björkqvist, M.; Lehto, V.-P. Determination of drug load in porous silicon microparticles by calorimetry. In *physica status solidi (a)*, John Wiley & Sons, Ltd: 2005; Vol. 202, pp 1629-1633.

36. Santana, M.; Estevez, J. O.; Agarwal, V.; Herrera-Becerra, R. Room Temperature Crystallization of Hydroxyapatite in Porous Silicon Structures. In *Nanoscale Research Letters*, 2016; Vol. 11, p 497.

37. Kalluri, J. R.; West, J.; Akkaraju, G. R.; Canham, L. T.; Coffer, J. L. Plant-Derived Tandem Drug/Mesoporous Silicon Microcarrier Structures for Anti-Inflammatory Therapy. In *ACS Omega*, American Chemical Society: 2019; Vol. 4, pp 8359-8364.

38. Chayen, N. E.; Saridakis, E.; El-Bahar, R.; Nemirovsky, Y. Porous silicon: an effective nucleation-inducing material for protein crystallization. In *Journal of Molecular Biology*, 2001; Vol. 312, pp 591-595.

39. Webber, J. B. W.; Dore, J. C. Neutron Diffraction Cryoporometry—A measurement technique for studying mesoporous materials and the phases of contained liquids and their crystalline forms. In *Nuclear Instruments and Methods in Physics Research Section A: Accelerators, Spectrometers, Detectors and Associated Equipment*, 2008; Vol. 586, pp 356-366.

40. Siefker, J.; Biehl, R.; Kruteva, M.; Feoktystov, A.; Coppens, M.-O. Confinement Facilitated Protein Stabilization As Investigated by Small-Angle Neutron Scattering.

In *Journal of the American Chemical Society*, American Chemical Society: 2018; Vol. 140, pp 12720-12723.

41. Pantalei, C.; Senesi, R.; Andreani, C.; Sozzani, P.; Comotti, A.; Bracco, S.; Beretta, M.; Sokol, P. E.; Reiter, G. Interaction of single water molecules with silanols in mesoporous silica. In *Physical Chemistry Chemical Physics*, The Royal Society of Chemistry: 2011; Vol. 13, pp 6022-6028.

42. Rantanen, J.; Majda, D.; Riikonen, J.; Lehto, V.-P. The atomic local ordering of SBA-15 studied with pair distribution function analysis, and its relationship to porous structure and thermal stability. In *Acta Materialia*, 2019; Vol. 175, pp 341-347.

43. Rimsza, J. M.; Du, J. Structural and Mechanical Properties of Nanoporous Silica. In *Journal of the American Ceramic Society*, John Wiley & Sons, Ltd (10.1111): 2014; Vol. 97, pp 772-781.

44. Hsieh, K.-Y.; Bendeif, E.-E.; Gansmuller, A.; Pillet, S.; Woike, T.; Schaniel, D. Structure and dynamics of guest molecules confined in a mesoporous silica matrix: Complementary NMR and PDF characterisation. In *RSC Advances*, The Royal Society of Chemistry: 2013; Vol. 3, pp 26132-26141.

45. Nartowski, K. P.; Malhotra, D.; Hawarden, L. E.; Sibik, J.; Iuga, D.; Zeitler, J. A.; Fábián, L.; Khimyak, Y. Z. 19F NMR Spectroscopy as a Highly Sensitive Method for the Direct Monitoring of Confined Crystallization within Nanoporous Materials. In *Angewandte Chemie - International Edition*, 2016; Vol. 55, pp 8904-8908.

46. Halib, N.; Mohd Amin, M. C. I.; Ahmad, I.; Abrami, M.; Fiorentino, S.; Farra, R.; Grassi, G.; Musiani, F.; Lapasin, R.; Grassi, M. Topological characterization of a bacterial cellulose–acrylic acid polymeric matrix. In *European Journal of Pharmaceutical Sciences*, 2014; Vol. 62, pp 326-333.

47. Chui, M. M.; Phillips, R. J.; McCarthy, M. J. Measurement of the Porous Microstructure of Hydrogels by Nuclear Magnetic Resonance. In *Journal of Colloid and Interface Science*, 1995; Vol. 174, pp 336-344.

48. Sørland, G. H.; Djurhuus, K.; Widerøe, H. C.; Lien, J. R.; Skauge, A. Absolute pore size distributions from NMR. 2007.

49. Uhlir, A. Electrolytic Shaping of Germanium and Silicon. In *Bell System Technical Journal*, 1956; Vol. 35, pp 333-347.

50. Watanabe, Y.; Sakai, T. Application of a thick anode film to semiconductor devices. In *Rev Elec Commun Lab (Tokyo)*, 1971; Vol. 19, pp 899-903.

51. Canham, L. T. Silicon quantum wire array fabrication by electrochemical and chemical dissolution of wafers. In *Applied Physics Letters*, 1990; Vol. 57, pp 1046-1048. Lehmann, V.; Gösele, U. Porous silicon formation: A quantum wire effect. In *Applied Physics Letters*, 1991; Vol. 58, pp 856-858.

52. Canham, L. T. Bioactive silicon structure fabrication through nanoetching techniques. In *Advanced Materials*, 1995; Vol. 7, pp 1033-1037.

53. Stewart, M. P.; Buriak, J. M. Chemical and biological applications of porous silicon technology. In *Advanced Materials*, 2000; Vol. 12, pp 859-869. Canham, L. Porous silicon as a therapeutic biomaterial. In *1st Annual International IEEE-EMBS Special Topic Conference on Microtechnologies in Medicine & Biology, Proceedings*, Dittmar, A., Beebe, D., Eds.; IEEE: Lyon, 2000; pp 109-112. Bayliss, S. C.; Buckberry, L. D.; Fletcher, I.; Tobin, M. J. The culture of neurons on silicon. In *Sensors and Actuators A: Physical*, 1999; Vol. 74, pp 139-142. Tahvanainen, M.; Rotko, T.; Mäkilä, E.; A. Santos, H.; Neves, D.; Laaksonen, T.; Kallonen, A.; Hämäläinen, K.; Peura, M.; Serimaa, R.; et al. Tablet preformulations of indomethacin-loaded mesoporous silicon microparticles. In *International Journal of Pharmaceutics*, Elsevier B.V.: 2012; Vol. 422, pp 125-131. Santos, H. A.; Bimbo, L. M.; Herranz, B.; Shahbazi, M.-A.; Hirvonen, J.; Salonen, J. Nanostructured porous silicon in preclinical imaging: Moving from bench to bedside. In *Journal of Materials Research*, 2013; Vol. 28.

54. Salonen, J.; Kaukonen, A. M.; Hirvonen, J.; Lehto, V.-P. Mesoporous silicon in drug delivery applications. In *Journal of Pharmaceutical Sciences*, 2008; Vol. 97, pp 632-653.
55. Canham, L. Routes of formation for porous silicon. In *Handbook of Porous Silicon: Second Edition*, 2018; Vol. 1-2, pp 3-11.
56. Salonen, J.; Björkqvist, M.; Laine, E.; Niinistö, L. Effects of fabrication parameters on porous p+-type silicon morphology. In *Physica Status Solidi (A) Applied Research*, 2000; Vol. 182, pp 249-254.
57. Salonen, J.; Lehto, V. P. Fabrication and chemical surface modification of mesoporous silicon for biomedical applications. In *Chemical Engineering Journal*, 2008; Vol. 137, pp 162-172.
58. Lehmann, V.; Stengl, R.; Luigart, A. On the morphology and the electrochemical formation mechanism of mesoporous silicon. In *Materials Science and Engineering B: Solid-State Materials for Advanced Technology*, 2000; Vol. 69-70, pp 11-22.
59. Burrows, V. A.; Chabal, Y. J.; Higashi, G. S.; Raghavachari, K.; Christman, S. B. Infrared spectroscopy of Si(111) surfaces after HF treatment: Hydrogen termination and surface morphology. In *Applied Physics Letters*, 1988; Vol. 53, pp 998-1000. Canham, L. T.; Houlton, M. R.; Leong, W. Y.; Pickering, C.; Keen, J. M. Atmospheric impregnation of porous silicon at room temperature. In *Journal of Applied Physics*, 1991; Vol. 70, pp 422-431.
60. Loni, A.; Simons, A. J.; Calcott, P. D. J.; Newey, J. P.; Cox, T. I.; Canham, L. T. Relationship between storage media and blue photoluminescence for oxidized porous silicon. In *Applied Physics Letters*, 1997; Vol. 71, pp 107-109. Hossain, S. M.; Chakraborty, S.; Dutta, S. K.; Das, J.; Saha, H. Stability in photoluminescence of porous silicon. In *Journal of Luminescence*, 2000; Vol. 91, pp 195-202.
61. Shabir, Q.; Webb, K.; Nadarassan, D. K.; Loni, A.; Canham, L. T.; Terracciano, M.; De Stefano, L.; Rea, I. Quantification and Reduction of the Residual Chemical Reactivity of Passivated Biodegradable Porous Silicon for Drug Delivery Applications. In *Silicon*, 2018; Vol. 10, pp 349-359.
62. Salonen, J.; Laitinen, L.; Kaukonen, A. M.; Tuura, J.; Björkqvist, M.; Heikkilä, T.; Vähä-Heikkilä, K.; Hirvonen, J.; Lehto, V. P. Mesoporous silicon microparticles for oral drug delivery: Loading and release of five model drugs. In *Journal of Controlled Release*, 2005; Vol. 108, pp 362-374.
63. Sarparanta, M.; Mäkilä, E.; Heikkilä, T.; Salonen, J.; Kukk, E.; Lehto, V.-P.; Santos, H. A.; Hirvonen, J.; Airaksinen, A. J. 18F-Labeled Modified Porous Silicon Particles for Investigation of Drug Delivery Carrier Distribution in Vivo with Positron Emission Tomography. In *Molecular Pharmaceutics*, American Chemical Society: 2011; Vol. 8, pp 1799-1806.
64. Petrova-Koch, V.; Muschik, T.; Kux, A.; Meyer, B. K.; Koch, F.; Lehmann, V. Rapid-thermal-oxidized porous Si-The superior photoluminescent Si. In *Applied Physics Letters*, 1992; Vol. 61, pp 943-945. Salonen, J.; Lehto, V. P.; Laine, E. Thermal oxidation of free-standing porous silicon films. In *Applied Physics Letters*, 1997; Vol. 70, pp 637-639.
65. Mawhinney, D. B.; Glass, J. A.; Yates, J. T. FTIR study of the oxidation of porous silicon. In *Journal of Physical Chemistry B*, 1997; Vol. 101, pp 1202-1206.
66. Kumar, R.; Kitoh, Y.; Hara, K. Effect of surface treatment on visible luminescence of porous silicon: Correlation with hydrogen and oxygen terminators. In *Applied Physics Letters*, 1993; Vol. 63, pp 3032-3034. Takazawa, A.; Tamura, T.; Yamada, M. Photoluminescence mechanisms of porous Si oxidized by dry oxygen. In *Journal of Applied Physics*, 1994; Vol. 75, pp 2489-2495.
67. Linford, M. R.; Chidsey, C. E. D. Alkyl Monolayers Covalently Bonded to Silicon Surfaces. In *Journal of the American Chemical Society*, 1993; Vol. 115, pp 12631-12632.

68. Linford, M. R.; Chidsey, C. E. D.; Fenter, P.; Eisenberger, P. M. Alkyl Monolayers on Silicon Prepared from 1-Alkenes and Hydrogen-Terminated Silicon. In *Journal of the American Chemical Society*, 1995; Vol. 117, pp 3145-3155.
69. Ponpon, J. P.; Bourdon, B. Oxidation of glow discharge a-Si:H. In *Solid State Electronics*, 1982; Vol. 25, pp 875-876.
70. Lehner, A.; Steinhoff, G.; Brandt, M. S.; Eickhoff, M.; Stutzmann, M. Hydrosilylation of crystalline silicon (111) and hydrogenated amorphous silicon surfaces: A comparative x-ray photoelectron spectroscopy study. In *Journal of Applied Physics*, 2003; Vol. 94, pp 2289-2294.
71. Stewart, M. P.; Buriak, J. M. Photopatterned hydrosilylation on porous silicon. In *Angewandte Chemie - International Edition*, 1998; Vol. 37, pp 3257-3260.
72. Buriak, J. M.; Stewart, M. P.; Geders, T. W.; Allen, M. J.; Choi, H. C.; Smith, J.; Raftery, D.; Canham, L. T. Lewis acid mediated hydrosilylation on porous silicon surfaces. In *Journal of the American Chemical Society*, 1999; Vol. 121, pp 11491-11502. Holland, J. M.; Stewart, M. P.; Allen, M. J.; Buriak, J. M. Metal Mediated Reactions on Porous Silicon Surfaces. In *Journal of Solid State Chemistry*, 1999; Vol. 147, pp 251-258.
73. Zazzera, L. A.; Evans, J. F.; Deruelle, M.; Tirrell, M.; Kessel, C. R.; Mckeown, P. Bonding organic molecules to hydrogen-terminated silicon wafers. In *Journal of the Electrochemical Society*, 1997; Vol. 144, pp 2184-2188.
74. Gurtner, C.; Wun, A. W.; Sailor, M. J. Surface modification of porous silicon by electrochemical reduction of organo halides. In *Angewandte Chemie - International Edition*, 1999; Vol. 38, pp 1966-1968.
75. Lees, I. N.; Lin, H.; Canaria, C. A.; Gurtner, C.; Sailor, M. J.; Miskelly, G. M. Chemical stability of porous silicon surfaces electrochemically modified with functional alkyl species. In *Langmuir*, 2003; Vol. 19, pp 9812-9817.
76. Salonen, J.; Kaasalainen, M.; Rauhala, O. P.; Lassila, L.; Hakamies, M.; Jalkanen, T.; Hahn, R.; Schmuki, P.; Mäkilä, E. Thermal carbonization of porous silicon: The current status and recent applications. In *ECS Transactions*, 2015; Vol. 69, pp 167-176.
77. Kostishko, B. M.; Atazhanov, S. R.; Mikov, S. N.; Koltsova, L. V.; Puzov, I. P. Photoluminescence and Degradation Properties of the Carbonized Porous Silicon. In *Physics of Low-Dimensional Structures*, 1999; Vol. 1999, pp 155-162. Seo, Y. J.; Cheon, H. J.; Choi, D. J. Enhancement of the thermal stability of photoluminescence by the carbonization of porous silicon. In *Journal of Materials Science Letters*, 1998; Vol. 17, pp 313-315.
78. Buriak, J. M.; Allen, M. J. Lewis Acid Mediated Functionalization of Porous Silicon with Substituted Alkenes and Alkynes. In *Journal of the American Chemical Society*, 1998; Vol. 120, pp 1339-1340.
79. Kim, N. Y.; Laibinis, P. E. Derivatization of porous silicon by Grignard reagents at room temperature. In *Journal of the American Chemical Society*, 1998; Vol. 120, pp 4516-4517.
80. Björkqvist, M.; Salonen, J.; Paski, J.; Laine, E. Characterization of thermally carbonized porous silicon humidity sensor. In *Sensors and Actuators, A: Physical*, 2004; Vol. 112, pp 244-247.
81. Sciacca, B.; Alvarez, S. D.; Geobaldo, F.; Sailor, M. J. Bioconjugate functionalization of thermally carbonized porous silicon using a radical coupling reaction. In *Dalton Transactions*, 2010; Vol. 39, pp 10847-10853.
82. Salonen, J.; Björkqvist, M.; Laine, E.; Niinistö, L. Stabilization of porous silicon surface by thermal decomposition of acetylene. In *Applied Surface Science*, North-Holland: 2004; Vol. 225, pp 389-394.
83. Wang, C. F.; Mäkilä, E. M.; Bonduelle, C.; Rytkönen, J.; Raula, J.; Almeida, S.; Närvänen, A.; Salonen, J. J.; Lecommandoux, S.; Hirvonen, J. T.; et al.

Functionalization of alkyne-terminated thermally hydrocarbonized porous silicon nanoparticles with targeting peptides and antifouling polymers: Effect on the human plasma protein adsorption. In *ACS Applied Materials and Interfaces*, 2015; Vol. 7, pp 2006-2015. Liu, Z.; Balasubramanian, V.; Bhat, C.; Vahermo, M.; Mäkilä, E.; Kemell, M.; Fontana, F.; Janoniene, A.; Petrikaite, V.; Salonen, J.; et al. Quercetin-Based Modified Porous Silicon Nanoparticles for Enhanced Inhibition of Doxorubicin-Resistant Cancer Cells. In *Advanced Healthcare Materials*, 2017; Vol. 6, pp 1-11.
84. Canham, L. Porous silicon formation by porous silica reduction. In *Handbook of Porous Silicon: Second Edition*, 2018; pp 1-8.
85. Filsinger, D. H.; Bourrie, D. B. Silica to Silicon: Key Carbothermic Reactions and Kinetics. In *Journal of the American Ceramic Society*, 1990; Vol. 73, pp 1726-1732.
86. Banerjee, H. D.; Sen, S.; Acharya, H. N. Investigations on the production of silicon from rice husks by the magnesium method. In *Materials Science and Engineering*, 1982. Bose, D. N.; Govindacharyulu, P. A.; Banerjee, H. D. Large grain polycrystalline silicon from rice husk. In *Solar Energy Materials*, 1982.
87. Haouli, S.; Boudebane, S.; Slipper, I. J.; Lemboub, S.; Gębara, P.; Mezrag, S. Combustion synthesis of silicon by magnesiothermic reduction. In *Phosphorus, Sulfur, and Silicon and the Related Elements*, Taylor & Francis: 2018; Vol. 193, pp 280-287.
88. Kim, K. H.; Lee, D. J.; Cho, K. M.; Kim, S. J.; Park, J. K.; Jung, H. T. Complete magnesiothermic reduction reaction of vertically aligned mesoporous silica channels to form pure silicon nanoparticles. In *Scientific Reports*, 2015; Vol. 5, pp 1-7.
89. Barati, M.; Sarder, S.; McLean, A.; Roy, R. Recovery of silicon from silica fume. In *Journal of Non-Crystalline Solids*, Elsevier B.V.: 2011; Vol. 357, pp 18-23.
90. Xu, K.; Zhang, Z.; Su, W.; Wei, Z.; Zhong, G.; Wang, C.; Huang, X. Alumina coated nano silicon synthesized by aluminothermic reduction as anodes for lithium ion batteries. In *Functional Materials Letters*, 2017.
91. Lai, Y.; Thompson, J. R.; Dasog, M. Metallothermic Reduction of Silica Nanoparticles to Porous Silicon for Drug Delivery Using New and Existing Reductants. In *Chemistry – A European Journal*, 2018; Vol. 24, pp 7913-7920.
92. Riikonen, J. Solvent Loading of Porous Silicon BT - Handbook of Porous Silicon. Canham, L., Ed.; Springer International Publishing: Cham, 2018; pp 913-925.
93. Bimbo, L. M.; Mäkilä, E.; Raula, J.; Laaksonen, T.; Laaksonen, P.; Strommer, K.; Kauppinen, E. I.; Salonen, J.; Linder, M. B.; Hirvonen, J.; et al. Functional hydrophobin-coating of thermally hydrocarbonized porous silicon microparticles. In *Biomaterials*, 2011; Vol. 32, pp 9089-9099.
94. Bimbo, L. M.; Denisova, O. V.; Mäkilä, E.; Kaasalainen, M.; De Brabander, J. K.; Hirvonen, J.; Salonen, J.; Kakkola, L.; Kainov, D.; Santos, H. A. Inhibition of influenza A virus infection in vitro by saliphenylhalamide- loaded porous silicon nanoparticles. In *ACS Nano*, 2013; Vol. 7, pp 6884-6893.
95. Loni, A. Melt Intrusion in Porous Silicon BT - Handbook of Porous Silicon. Canham, L., Ed.; Springer International Publishing: Cham, 2018; pp 945-950.
96. Nadarassan, D. K.; Loni, A.; Shabir, Q. Q.; Kelly, C.; O'Brien, H.; Caffull, E.; Webb, K.; Canham, L. T.; Maniruzamman, M.; Trivedi, V.; et al. Ultrahigh drug loading and release from biodegradable porous silicon aerocrystals. In *Controlled Release Society Meeting*, CRS: 2015; Vol. 825, pp 42-43.
97. Lehto, V.-P.; Vähä-Heikkilä, K.; Paski, J.; Salonen, J. Use of thermoanalytical methods in quantification of drug load in mesoporous silicon microparticles. In *Journal of Thermal Analysis and Calorimetry*, Akadémiai Kiadó, co-published with Springer Science+Business Media B.V., Formerly Kluwer Academic Publishers B.V.: Budapest, Hungary, 2005; Vol. 80, pp 393-397.

98. Prestidge, C. A.; Barnes, T. J.; Mierczynska-Vasilev, A.; Kempson, I.; Peddie, F.; Barnett, C. Peptide and protein loading into porous silicon wafers. In *physica status solidi (a)*, John Wiley & Sons, Ltd: 2008; Vol. 205, pp 311-315.
99. Wang, M.; Hartman, P. S.; Loni, A.; Canham, L. T.; Bodiford, N.; Coffer, J. L. Influence of Surface Chemistry on the Release of an Antibacterial Drug from Nanostructured Porous Silicon. In *Langmuir*, American Chemical Society: 2015; Vol. 31, pp 6179-6185.
100. Zhang, D.-X.; Yoshikawa, C.; Welch, N. G.; Pasic, P.; Thissen, H.; Voelcker, N. H. Spatially Controlled Surface Modification of Porous Silicon for Sustained Drug Delivery Applications. In *Scientific Reports*, 2019; Vol. 9, p 1367.
101. Krepker, M. A.; Segal, E. Porous Silicon Polymer Composites BT - Handbook of Porous Silicon. Canham, L., Ed.; Springer International Publishing: Cham, 2018; pp 269-280.
102. Beavers, K. R.; Werfel, T. A.; Shen, T.; Kavanaugh, T. E.; Kilchrist, K. V.; Mares, J. W.; Fain, J. S.; Wiese, C. B.; Vickers, K. C.; Weiss, S. M.; et al. Porous Silicon and Polymer Nanocomposites for Delivery of Peptide Nucleic Acids as Anti-MicroRNA Therapies. In *Advanced materials (Deerfield Beach, Fla.)*, 2016/07/06 ed.; 2016; Vol. 28, pp 7984-7992.
103. Nelson, C. E.; Kintzing, J. R.; Hanna, A.; Shannon, J. M.; Gupta, M. K.; Duvall, C. L. Balancing cationic and hydrophobic content of PEGylated siRNA polyplexes enhances endosome escape, stability, blood circulation time, and bioactivity in vivo. In *ACS nano*, 2013/09/23 ed.; 2013; Vol. 7, pp 8870-8880.
104. Adolph, E. J.; Nelson, C. E.; Werfel, T. A.; Guo, R.; Davidson, J. M.; Guelcher, S. A.; Duvall, C. L. Enhanced Performance of Plasmid DNA Polyplexes Stabilized by a Combination of Core Hydrophobicity and Surface PEGylation. In *Journal of materials chemistry. B*, 2014; Vol. 2, pp 8154-8164.
105. Xu, W.; Riikonen, J.; Lehto, V. P. Mesoporous systems for poorly soluble drugs. In *International Journal of Pharmaceutics*, Elsevier: 2013; Vol. 453, pp 181-197.
106. Bimbo, L. M.; Mäkilä, E.; Laaksonen, T.; Lehto, V.-P.; Salonen, J.; Hirvonen, J.; Santos, H. A. Drug permeation across intestinal epithelial cells using porous silicon nanoparticles. In *Biomaterials*, 2011; Vol. 32, pp 2625-2633. Bimbo, L. M.; Sarparanta, M.; Mäkilä, E.; Laaksonen, T.; Laaksonen, P.; Salonen, J.; Linder, M. B.; Hirvonen, J.; Airaksinen, A. J.; Santos, H. A. Cellular interactions of surface modified nanoporous silicon particles. In *Nanoscale*, 2012; Vol. 4, pp 3184-3192. Liu, D.; Bimbo, L. M.; Mäkilä, E.; Villanova, F.; Kaasalainen, M.; Herranz-Blanco, B.; Caramella, C. M.; Lehto, V.-P.; Salonen, J.; Herzig, K.-H.; et al. Co-delivery of a hydrophobic small molecule and a hydrophilic peptide by porous silicon nanoparticles. In *Journal of Controlled Release*, 2013; Vol. 170, pp 268-278.
107. Luo, M.; Lewik, G.; Ratcliffe, J. C.; Choi, C. H. J.; Mäkilä, E.; Tong, W. Y.; Voelcker, N. H. Systematic Evaluation of Transferrin-Modified Porous Silicon Nanoparticles for Targeted Delivery of Doxorubicin to Glioblastoma. In *ACS Applied Materials & Interfaces*, American Chemical Society: 2019; Vol. 11, pp 33637-33649.
108. Nanev, C. N.; Saridakis, E.; Chayen, N. E. Protein crystal nucleation in pores. In *Scientific Reports*, The Author(s): 2017; Vol. 7, p 35821.
109. Gundogdu, N.; Cetin, M. Chitosan-poly (lactide-co-glycolide) (CS-PLGA) nanoparticles containing metformin HCl: Preparation and in vitro evaluation. In *Pakistan Journal of Pharmaceutical Sciences*, 2014; Vol. 27, pp 1923-1929.
110. S. García-Briones, G.; Ocampo, R.; F.A. Gómez-Durán, C.; Neri-Gómez, T.; Palestino, G. Porous silicon microcarriers for extended release of metformin: Design, biological evaluation and 3D kinetics modeling. In *Chemical Engineering Journal*, 2019; Vol. 365.
111. Kamakura, R.; Kovalainen, M.; Riikonen, J.; Nissinen, T.; Shere Raza, G.; Walkowiak, J.; Lehto, V.-P.; Herzig, K.-H. Inorganic mesoporous particles for

controlled α-linolenic acid delivery to stimulate GLP-1 secretion in vitro. In *European Journal of Pharmaceutics and Biopharmaceutics*, 2019; Vol. 144, pp 132-138.

112. Karhunen, L. J.; Juvonen, K. R.; Huotari, A.; Purhonen, A. K.; Herzig, K. H. Effect of protein, fat, carbohydrate and fibre on gastrointestinal peptide release in humans. In *Regulatory Peptides*, 2008; Vol. 149, pp 70-78.

113. Nettleton, J. A. Omega-3 fatty acids: comparison of plant and seafood sources in human nutrition. In *Journal of the American Dietetic Association*, 1991; Vol. 91, pp 331-337.

114. Huotari, A.; Xu, W.; Mönkäre, J.; Kovalainen, M.; Herzig, K. H.; Lehto, V. P.; Järvinen, K. Effect of surface chemistry of porous silicon microparticles on glucagon-like peptide-1 (GLP-1) loading, release and biological activity. In *International Journal of Pharmaceutics*, Elsevier B.V.: 2013; Vol. 454, pp 67-73.

115. Kaasalainen, M.; Rytkönen, J.; Mäkilä, E.; Närvänen, A.; Salonen, J. Electrostatic interaction on loading of therapeutic peptide GLP-1 into porous silicon nanoparticles. In *Langmuir*, 2015; Vol. 31, pp 1722-1729.

116. Polkovnikova, Y. A.; Len'shin, A. S.; Slivkin, A. I. Quantum-Chemical Modeling of Vinpocetine Desorption from Silicon and Silicon-Dioxide Particle Surfaces. In *Pharmaceutical Chemistry Journal*, 2019; Vol. 53, pp 170-174.

117. M. Bimbo, L.; Peltonen, L.; Hirvonen, J.; A. Santos, H. Toxicological Profile of Therapeutic Nanodelivery Systems. In *Current Drug Metabolism*, 2012; Vol. 13, pp 1068-1086.

118. Bhatia, S. N.; Park, J.-H.; Ruoslahti, E.; Sailor, M. J.; Gu, L.; von Maltzahn, G. Biodegradable luminescent porous silicon nanoparticles for in vivo applications. In *Nature Materials*, Nature Publishing Group: 2009; Vol. 8, pp 331-336. Low, S. P.; Voelcker, N. H.; Canham, L. T.; Williams, K. A. The biocompatibility of porous silicon in tissues of the eye. In *Biomaterials*, 2009; Vol. 30, pp 2873-2880. Low, S. P.; Voelcker, N. H. Biocompatibility of Porous Silicon BT - Handbook of Porous Silicon. Canham, L., Ed.; Springer International Publishing: Cham, 2018; pp 533-545. Shahbazi, M.-A.; Hamidi, M.; Mäkilä, E. M.; Zhang, H.; Almeida, P. V.; Kaasalainen, M.; Salonen, J. J.; Hirvonen, J. T.; Santos, H. A. The mechanisms of surface chemistry effects of mesoporous silicon nanoparticles on immunotoxicity and biocompatibility. In *Biomaterials*, 2013; Vol. 34, pp 7776-7789. Liu, D.; Shahbazi, M.-A.; Bimbo, L. M.; Hirvonen, J.; Santos, H. A. Biocompatibility of porous silicon for biomedical applications. Santos, H. A. B. T.-P. S. f. B. A., Ed.; Woodhead Publishing: 2014; pp 129-181. Tölli, M. A.; Ferreira, M. P. A.; Kinnunen, S. M.; Rysä, J.; Mäkilä, E. M.; Szabó, Z.; Serpi, R. E.; Ohukainen, P. J.; Välimäki, M. J.; Correia, A. M. R.; et al. In vivo biocompatibility of porous silicon biomaterials for drug delivery to the heart. In *Biomaterials*, 2014; Vol. 35, pp 8394-8405. Bimbo, L. M.; Sarparanta, M.; Santos, H. A.; Airaksinen, A. J.; Mäkilä, E.; Laaksonen, T.; Peltonen, L.; Lehto, V.-P.; Hirvonen, J.; Salonen, J. Biocompatibility of Thermally Hydrocarbonized Porous Silicon Nanoparticles and their Biodistribution in Rats. In *ACS Nano*, 2010; Vol. 4, pp 3023-3032.

119. Shabir, Q. Biodegradability of Porous Silicon BT - Handbook of Porous Silicon. Canham, L., Ed.; Springer International Publishing: Cham, 2018; pp 547-554. Decuzzi, P.; Godin, B.; Tanaka, T.; Lee, S.-Y.; Chiappini, C.; Liu, X.; Ferrari, M. Size and shape effects in the biodistribution of intravascularly injected particles. In *Journal of Controlled Release*, 2010; Vol. 141, pp 320-327.

120. Anglin, E. J.; Schwartz, M. P.; Ng, V. P.; Perelman, L. A.; Sailor, M. J. Engineering the Chemistry and Nanostructure of Porous Silicon Fabry-Pérot Films for Loading and Release of a Steroid. In *Langmuir*, American Chemical Society: 2004; Vol. 20, pp 11264-11269. Tasciotti, E.; Liu, X.; Bhavane, R.; Plant, K.; Leonard, A. D.; Price, B. K.; Cheng, M. M.-C.; Decuzzi, P.; Tour, J. M.; Robertson, F.; et al. Mesoporous silicon

particles as a multistage delivery system for imaging and therapeutic applications. In *Nature Nanotechnology*, 2008; Vol. 3, pp 151-157.
121. Popplewell, J. F.; King, S. J.; Day, J. P.; Ackrill, P.; Fifield, L. K.; Cresswell, R. G.; Di Tada, M. L.; Liu, K. Kinetics of uptake and elimination of silicic acid by a human subject: a novel application of 32Si and accelerator mass spectrometry. In *Journal of Inorganic Biochemistry*, Elsevier: 1998; Vol. 69, pp 177-180.
122. Jugdaohsingh, R.; Anderson, S. H. C.; Tucker, K. L.; Elliott, H.; Kiel, D. P.; Thompson, R. P. H.; Powell, J. J. Dietary silicon intake and absorption. In *The American journal of clinical nutrition*, Oxford University Press: 2002; Vol. 75, pp 887-893. Jugdaohsingh, R.; Tucker, K. L.; Qiao, N.; Cupples, L. A.; Kiel, D. P.; Powell, J. J. Dietary silicon intake is positively associated with bone mineral density in men and premenopausal women of the Framingham Offspring cohort. In *Journal of Bone and Mineral Research*, Wiley Online Library: 2004; Vol. 19, pp 297-307.
123. Reffitt, D. M.; Jugdaohsingh, R.; Thompson, R. P. H.; Powell, J. J. Silicic acid: its gastrointestinal uptake and urinary excretion in man and effects on aluminium excretion. In *Journal of Inorganic Biochemistry*, Elsevier: 1999; Vol. 76, pp 141-147.

Chapter 2

Methodology

2 Methodology

2.1 Investigating crystallisation behaviours: Techniques

2.1.1 X-ray generation

X-rays are electromagnetic waves of radiation produced by accelerating electrons, using a voltage, from a cathode towards a metal anode, within a vacuum known as an X-ray tube (Figure 2.1). On collision with the metal target, an electron will be displaced, and light will be emitted in the wavelength region of 0.1-10 nm - X-rays.

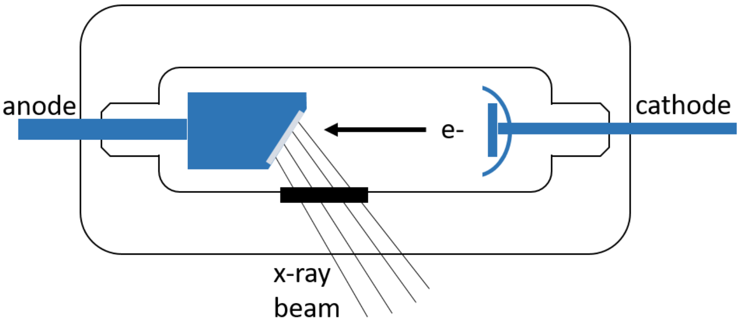

Figure 2.1: Simplistic diagram of an X-ray tube.

X-rays can be categorised into Bremsstrahlung and characteristic radiation. Bremsstrahlung, also known as continuous X-rays, occurs when an electron is accelerated towards the metal atoms, deaccelerating as it passes the protons of the metal atom. The closer the electron gets to these protons, the more it is decelerated and the greater the energy released as X-ray photons. Characteristic radiation occurs when an incident electron has enough energy to excite an inner electron of the metal atom, ejecting it from the atom. Electrons from the outer shells replace this electron, emitting X-ray photons in the process which have energies equivalent to the difference between energy levels. If the electron drops from the L- to the K-orbital, the resultant photon is termed $K\alpha_1$ or $K\alpha_2$, the former being higher in energy. The movement of electrons from the M- to the K-orbital results in $K\beta$ photons. Characteristic radiation has a lower occurrence than Bremsstrahlung. The wavelength of the resultant X-ray can be varied according to the chemistry of the sample to be analysed. Copper sources produce X-rays with a wavelength of 1.54 Å. Longer wavelengths of lower energy interact more strongly with atoms, in particular lighter atoms that scatter weakly, i.e., carbon, oxygen and nitrogen atoms found in organic pharmaceutical compounds. The lower energy of the wavelength also results in higher flux, which defines the intensity of the X-rays. Copper is also advantageous in determining the absolute structure for chiral compounds. Molybdenum and silver produce shorter wavelengths, 0.71 and 0.56 Å respectively. The shorter wavelengths are absorbed less strongly than copper and are therefore suited to the heavier atoms found in metallocompounds.

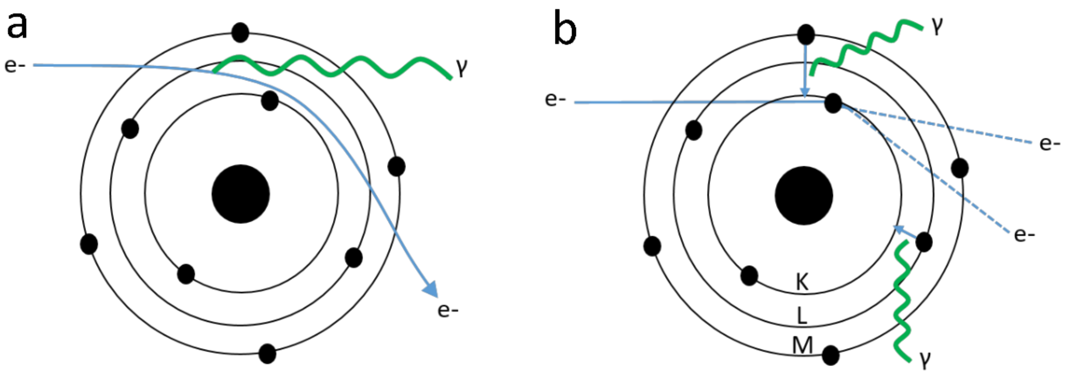

Figure 2.2: Generation of X-rays by a) Bremsstrahlung and b) characteristic radiation.

2.1.2 X-ray diffraction and crystallography

2.1.2.1 Single crystal X-ray diffraction (SX-XRD)

This section provides a brief outlook on how data was collected using X-ray diffraction. More information can be found in the following books: Pharmaceutical Crystallography: A Guide to Structure and Analysis,[1] Modern X-Ray Analysis on Single Crystals: A Practical Guide,[2] and Crystal Structure Analysis: Principles and Practice.[3]

When characterising crystalline solids, X-ray diffraction is 'Gold Standard'. X-rays have been utilised for over a century, first observed by physicist and 1901 Nobel Prize Winner Wilhelm Röntgen in 1895 during an investigation into the transmittance of cathode rays through glass, also discovering that X-rays could pass through human tissue, but not the high-density bone, making them visible of photographic plates underneath.

If a material possesses long range order it can be defined as crystalline. Max von Laue was awarded the Nobel Prize in 1914 for his discovery of X-ray diffraction in crystals. Crystalline material was placed in the beam of X-rays, with diffraction producing a pattern of regularly spaced dots on photographic paper. Laue's work paved the way for father and son duo William Henry Bragg and William Lawrence Bragg, who were awarded the Nobel prize for their analysis of crystal structures using X-rays and the birth of crystallography, the understanding of the arrangement of atoms in a crystalline solid. Their research led to the understanding of the relationship between the wavelength of the incident X-ray and the distance between planes of atoms (d-spacing) in a crystal. When X-rays encounter an object with a size comparable to their wavelength, interference occurs known as diffraction. This can be used to measure the distance between the atoms in a crystalline material. Alignment of the waves amplifies the signal produced and is termed as constructive interference, whereas waves out of alignment destroys the signal and are termed as destructive. For constructive interference to occur, the Bragg condition needs to be satisfied and can be equated as:

Equation 8

$$n\lambda = 2dsin\theta$$

Where nλ is an integer number of wavelengths is proportional to two times the spacing between atomic planes (d) and the angle of incidence (ϑ).

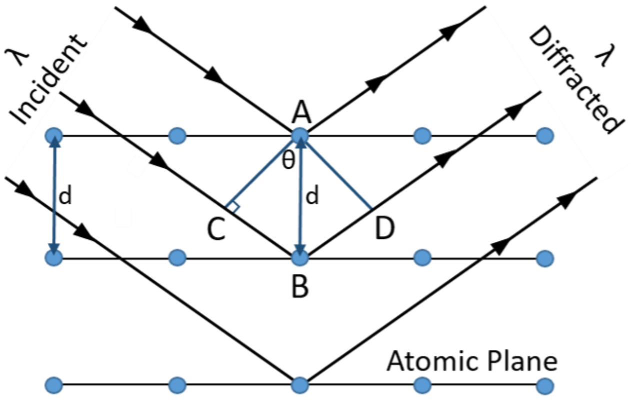

Figure 2.3: Bragg's Law diagram showing X-ray diffraction from crystal if conditions for constructive interference are met.

Suitable crystals need to be chosen prior to XRD analysis. This is usually carried out visually under a microscope, ensuring crystals of a good quality are selected, with no visible flaws in the crystal faces. A translucent crystal is usually a good indicator of a quality crystal and can be observed by rotating crystals under crossed polarisers which should result in optical extinction. Opaque crystals indicate a crystal are of poor quality or are amorphous. The crystal should have well-defined edges and should be no bigger than 75% of the beam to account for issues with absorption.

Once a suitable crystal has been chosen, analysis proceeds firstly by capturing enough diffraction to establish the unit cell parameters of the crystal. This is usually termed as a matrix collection. Upon the collection of data, the diffraction frames are converted into a list of reflections which are harvested based on a measure of the signal (intensity) they produce versus the background noise (Mean I/ sigma).

Indexing the crystal provides each reflection that was harvested with a hkl value or Miller Indices which shows how atoms are arranged in 3D space and identifying the planes that make up a crystal structure, related to the unit cell by Bragg's Law. These planes intercept the unit cell axis i.e., the (100) plane only intercepts the *a*-axis at *a* = 1 but does not intercept the *b*- or *c*-axis (Figure 2.4).

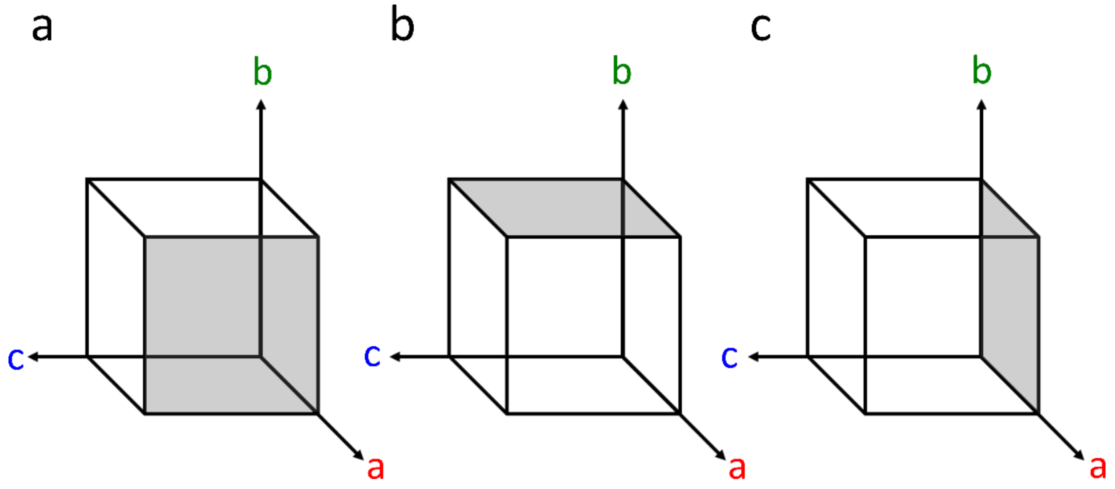

Figure 2.4: Miller Indices for planes indicated in grey: a) (100), b) (010) and c) (001).

The relative position of diffracted X-rays or reflections allows for analysis of the unit cell, the smallest volume unit of a crystal, in particular, the dimensions and shape of the unit cell. The shape a unit cell takes is known as the crystal system and is used to describe the symmetry of a structure. There are seven crystal systems, which vary in level of symmetry, from triclinic with the lowest level of symmetry to cubic with the highest level of symmetry. This preliminary analysis can lead to the identification of polymorphs as each polymorph will have a unique unit cell.

Table 2.1: Bravais Lattice parameters associated with the seven crystal systems.

	Bravais Lattices					
Crystal System	Axes	Angles	Simple (P)	Body Centred (I)	Face Centred (F)	Base Centred (C)
Triclinic	a ≠ b ≠ c	α ≠ β ≠ γ	x			
Monoclinic	a ≠ b ≠ c	α = γ = 90° ≠ β	x	x		
Orthorhombic	a ≠ b ≠ c	α=β=γ=90°	x	x	x	x
Tetragonal	a = b ≠ c	α=β=γ=90°	x	x		
Trigonal	a = b = c	α = β = γ ≠ 90°	x			
Hexagonal	a = b ≠ c	α = β = 90° γ = 120°	x			
Cubic	a = b = c	α = β = γ = 90°	x	x		x

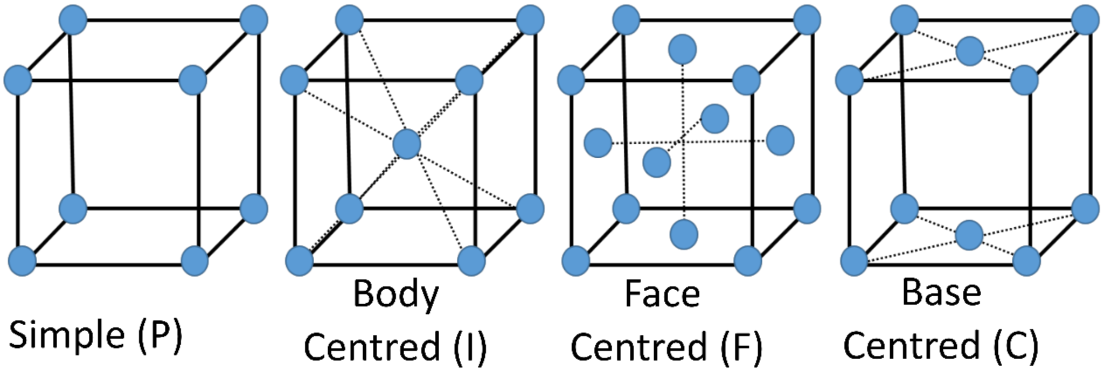

Figure 2.5: Four types of Crystal Lattice.

Reflections also provide information on the intensity of diffracted X-rays and along with the hkl values can be converted into electron density which is used for structure analysis via Fourier Transform methods. This will be discussed in the structural solution section.

Indexing a crystal and identifying the crystal system further indicates how much data is needed to be collected for structural solution and a strategy can be calculated. The higher the crystal symmetry the less data that needs to be collected. Data collected in triclinic (lowest possible symmetry) will afford more unique reflections, therefore more data is needed to determine the structure. Triclinic systems require a hemisphere, monoclinic systems require a quadrant and orthorhombic systems require an octant of data to determine the molecular structure of the crystal.[2] It is possible to collect a full sphere of data, which is necessary for chiral systems, however this requires more time. An issue with this is calculating a strategy for data collection based on the assumption that the crystal has a higher symmetry whereas in reality the system is lower in symmetry i.e., assuming the crystal is orthorhombic will not provide enough reflections if the symmetry is in fact triclinic. The only time a full sphere is required is when the crystal is chiral.

Reflections can either be unique, whereby only one is collected, or duplicated whereby more than one equivalent reflection is collected. Duplicating the number of equivalent reflections calculated adds to the redundancy of the data, providing an average and reducing statistical error (Andrew Bond). When calculating the strategy, the redundancy of the data can be set, selecting on average how many times all reflections will be collected. Redundancy must be greater than 5 to produce the absolute structure. An orientation matrix provides a relationship between the crystal system and the diffractometers geometry, providing the diffractometer with positions as where to collect data.

2.1.2.2 Structure Solution - Intensity and structure factor

As previously mentioned, each reflection is assigned a hkl value, but the intensity of each reflection is also required for structure solution and refinement. Equation 9 demonstrates the summation of the scattering from all atoms to give the intensity. Each atom will take a different position (xyz) in the unit cell hence the scattering from each atom may not be in phase with each other, known as the phase problem. Accurate intensities relate to the atomic position by a structure factor which needs to consider two factors: the amplitude and phases of scattered X-rays (Equation 9). However, intensity can only provide information on the amplitude which is given by an atomic scattering factor related to the number of electrons in the atom. The relative phase relationship between the scattering from each atom is unknown and is the phase problem that needs to be solved to identify the electron density.

The structure factor relates to the Fourier Transform of the electron density with units of electrons per unit volume (Equation 10). Where electron density is concentrated, it can be concluded that it is the location of an atom, which can then be used to build up the atomic contents of the unit cell.

To solve the structure, information is required regarding the phases. X-rays scattered by the atoms have different pathlength due to the different positions of atoms in a unit cell, which causes a difference in phase between scattered waves. This is known as the phase problem and can be resolved using Direct and Dual-Space methods. These methods then determine how the space group is assigned to the structure.

Equation 9

$$F(hkl) = \sum_{n=1}^{N} f_n \, exp\{2\pi i \, (hx_n + ky_n + lz_n)\}$$

Where f_n is the atomic scattering factor for the n^{th} atom in the unit cell at position (xyz)n.

Equation 10

$$\rho \, (xyz) = \frac{1}{V_{cell}} \sum_{hkl} F \, (hkl) \, exp\{-2\pi i \, (hx_n + ky_n + lz_n)\}$$

Where ρ (xyz) is the value of the electron density at position x, y, z.

The intensity of reflections can also be affected by physical issues including absorption. Absorption of X-rays by a crystal is affected by its chemistry – its atomic make-up. Heavier atoms absorb strongly leading to larger reflections. In this case radiation with a shorter wavelength should be used to minimise this i.e., molybdenum. Larger crystals also absorb X-rays more strongly. Shape also influences absorption. Needle-shaped crystals prove challenging as the intensity differs with the path taken leading to anisotropic absorption. Spherical crystals would be ideal, minimising absorption effects, but this is not practical.

Absorption by the crystals can be corrected for using two methods: multi-scan correction and face indexing. Multi-scan correction aims to minimise the differences between the multiple measurements with different intensities which should be equivalent. High-redundancy data is required to provide multiple measurements for comparison. Multi-scan can also correct intensities for systematic absences which arise due to the absence of certain reflections in the diffraction pattern due to the effect of the space group symmetry. These absences occur when the lattice is centred, or translational symmetry is present (glide planes and screw axes).

Face indexing can also be used to correct for absorption, which takes the morphology of the crystal into consideration, important for needle and plate crystals which display anisotropic absorption. The crystal is rotated in view of a camera to produce a model of the crystal shape. Path lengths can be determined for each reflection.

The next stage in solving the crystal structure is to develop a structural model, with the aim to produce an image of the electron density. This involves a cycle where the observed structure factor and calculated phase values are used to determine an image of the electron density whereby atoms can be assigned, and new phase values can be calculated from the model. The new phase can be fed back into the cycle until the correct phase value has been calculated and the electron density is accounted for. Least-squares methods are used to refine the model produced, minimising the difference between the observed and calculated structure factors, known as the residual, and adapting the model to match the best fit until any changes are negligible. Measured intensities have varying degrees of uncertainty therefore a weighting scheme is applied to each residual measurement.

The R factor (R1) and weighted R factor (wR2) quantify how well the model matches the data. For good data, they are typically < 5% and between 10-20 % respectively.

Equation 11

$$R1 = \frac{\sum\{||F(hkl)_{obs}| - |F(hkl)_{calc}||\}}{\sum\{|F(hkl)_{obs}|\}}$$

Equation 12

$$wR2 = \left[\frac{\sum w(hkl)\{|F(hkl)_{obs}|^2 - |F(hkl)_{calc}|^2\}^2}{\sum w(hkl)\{|F(hkl)_{obs}|^2\}^2}\right]^{\frac{1}{2}}$$

During this process parameters are also applied to the atoms, however as the symmetry has previously been defined, it is only necessary to treat atoms within the asymmetric unit. Early stages of structure refinement involve heavy atom refinement, which in the case of organic drug molecules is primarily carbon, oxygen, and nitrogen i.e., non-hydrogen atoms. Anisotropic refinement is conducted for non-hydrogen atoms due to the thermal motion associated with them and the difference in atomic position. Atomic positions are averaged for the entire crystal into one asymmetric unit. Both factors lead to displacement of the atoms, producing an ellipsoid. Residual electron density can be used to assign atoms (i.e., missing solvent or water molecules). Hydrogen atoms have one electron and therefore diffract X-rays weakly. This being said hydrogen atoms are placed onto their parent atoms, with crystallographic software (e.g. Olex2) calculating the most likely positions.[4] Further ways to improve data are to apply restraints and constraints, which work to produce a comprehensive structure. Restraints provides additional information that limit parameters to specified values within a range, e.g., a DFIX restraint fixes a bond length between two atoms with a given estimated standard deviation. RIGU restraints can be applied to high-pressure data sets, later discussed, restraining the displacement parameters of the atoms to be a similar value. Constraints specify an exact value for a parameter, e.g., AFIX constrains are applied to cyclic groups of atoms, making them rigid.

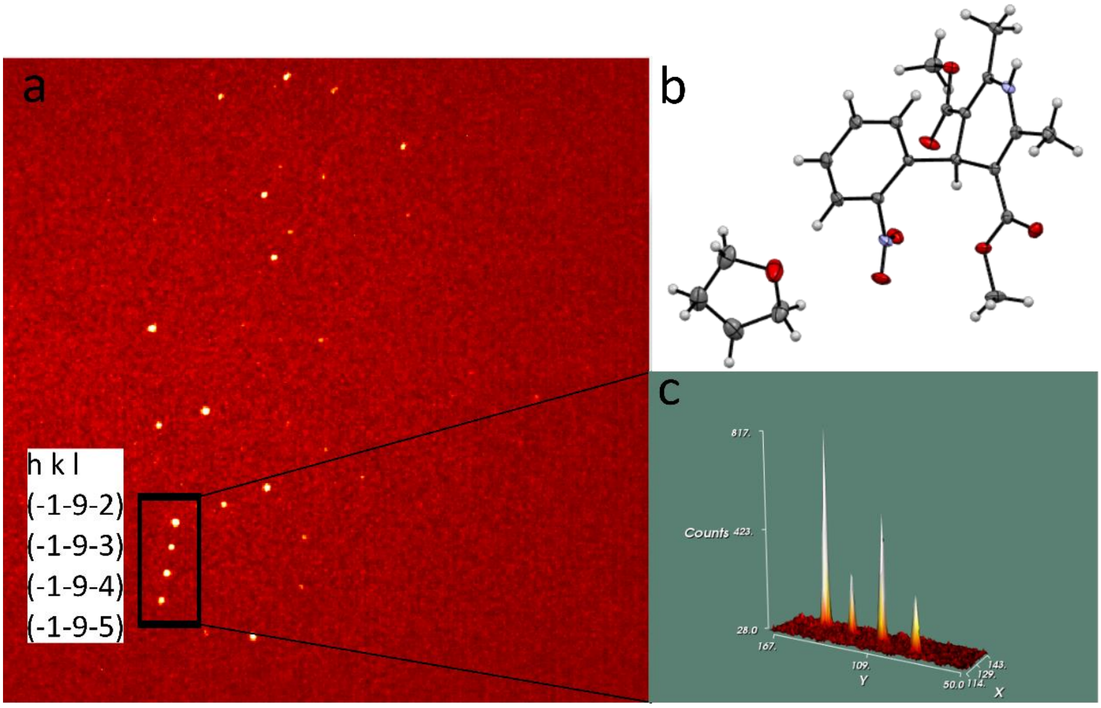

Figure 2.6: a) A diffraction frame from the collection of b) nifedipine-THF. Figure c) shows the 3D-profile peaks of the highlighted diffractionss wirh specified hkl values defined in Figure a).

2.1.2.3 X-ray powder diffraction (XRPD)

Crystallising a single-crystals of an ideal size and quality for single-crystal X-ray diffraction is not always possible, in which case powder samples can be assessed using X-ray powder diffraction. XRPD obtains a pattern for bulk material, collecting measurements from numerous crystals in varying orientations with respect to the incident X-ray beam, outputting a diffractogram or pattern with peaks corresponding to a 2θ value which related to the spacing between crystallographic planes (d-spacing). It is ideal for users who want to identify or confirm the phase of the material by comparison to a powder pattern from a database or reference material, assess the purity of a sample and distinguish between crystalline and amorphous material. Amorphous material lacks long range order and does not satisfy Bragg's Law; therefore, diffraction peaks are not present and results in an 'amorphous' halo. However, unlike SC-XRD, XRPD only provides 1-dimensional data which makes interpretation challenging and requires high-resolution data for structure analysis. For example, separate reflections may have similar d-spacing values yet cannot be easily resolved in the pattern leading to difficulties in assigning the correct intensity.

After collection of the data, the diffraction pattern is indexed, and a unit cell suggested from the identification of peak positions. For this process, the first 20 peaks are typically selected in this process, and are assigned hkl values (Miller indices).[5] As a measure of success, the potential unit-cell volume can be used as an indicator as to which unit-cell parameters best fits the expected molecular contents. Using the 18 Å^3 rule, which implies that each non-hydrogen atom occupies 18 Å^3 within the unit cell, the volume of the molecule can be roughly calculated and then multiplied by the expected number of molecules given a particular symmetry. This rule is only successful for typical organic materials and if the user knows how the sample has been prepared. There is an assumption as to the solid-state form of the sample i.e., if the sample is a solvate, hydrate or pure API.

Potential unit cells can be tested against the data, using Pawley refinement, where the unit cell parameters are refined against the data. This is the only method to definitively prove the successful indexing. Pawley refinement uses a least-square approach to fit the diffraction pattern. Parameters that are adjusted along with the refinement of the unit cell parameters (peak positions) are the peak shape and background to the data. The peak intensities are taken from the diffraction pattern hence do not contain any information on the structure of the material. The fit can be assessed using a difference curve – observed intensity minus calculated intensity

(Figure 2.7). Pawley refinements require the data to be of high resolution for sufficient fitting, using the an R-factor (R) as a measure to assess how well the calculated model fits the observed data fits (Equation 13).[6]

Equation 13

$$R = \frac{\Sigma\,||F_{obs}| - |F_{calc}||}{\Sigma|F_{obs}|}$$

If the structure is known the Rietveld refinement can be used to assess the solid.[7] Rietveld refinement optimises the structural model against the data. Much like Pawley Refinement, Rietveld looks at the difference between calculated pattern and experimental data. The diffracted intensities are calculated from the crystal structure, taking preferred orientation into consideration, and determining structural parameters including atomic type and positions.

This study used SC-XRD and XRPD complementary. Powder patterns were simulated from single-crystal data to assess whether solvated crystals of nifedipine crystallised used for single-crystal analysis matched the bulk material slurried from the respective solvent, characterised by powder diffraction. Mercury software uses lattice parameters from imported CIF files to calculate the d-spacing values for each hkl value. Using the Bragg equation, d-spacing's can be converted to 2θ values, plotted against intensity.

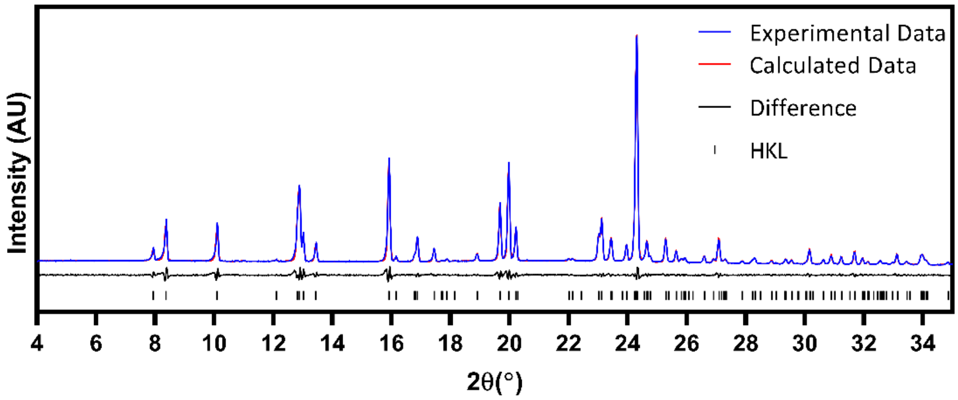

Figure 2.7: Pawley refinement of 1,4-dioxane-nifedipine solvate XRPD data.

2.1.3 High-pressure

High pressure is an efficient way of altering the solid state landscape of a compound, with the ability to generate conformational changes in molecules, polymorphic transitions and exploring the relationship between structures and their properties.[8] The type of system used to generate pressure is dependent on the sample type, whether it be a single crystal or powder and the maximum pressure required. In this thesis, two systems were used to generate pressure.

Diamond anvil cells (DAC) were first introduced in 1958 by Jamieson and Weir with continuous developments to date. High-pressure studies of single crystals require a diamond anvil cell. The Merrill-Bassett design, used in the following chapters, consists of two steel plates, each of which houses a tungsten carbide backing seat and a diamond anvil.[9] Diamonds provide low absorption of X-rays and transparency which allows electromagnetic radiation to pass through to the sample it houses as well as visual observation using optical microscopy. They are the hardest natural material, able to mechanically transmit a large force. The table face provides a larger surface which force can be transmitted through. The width of the culet faces dictates how much pressure can be generated as according to Equation 14.

Equation 14

$$Pressure = \frac{Force}{Area}$$

Whereby the pressure generated is dictated by the force applied to a given area, i.e., a smaller culet face generates a larger pressure. A metal gasket with a thickness of *ca.* 300 μm, including tungsten and steel, is placed between the diamonds and indented till it reaches a thickness between 80 and 100 μm.[10] A hole is then drilled into this indentation with a diameter that suits the size of the diamonds culet of (in the case of this study *ca.* 250 μm) providing a chamber for the sample and also preventing the diamonds from touching and breaking under the force. A single crystal is loaded into the sample chamber along with an internal pressure calibrant, typically a ruby chip or sphere. The ruby fluorescence line shifts with change in pressure and can be measured spectroscopically, using a Raman spectrometer and compared to a reference ruby at ambient pressure.[11] A pressure transmitting medium (PTM) is used to maintain hydrostatic pressure within the sample chamber, as well as preventing the gasket from collapsing as force is applied, filling any volume that is not occupied. The PTM used in the following studies was petroleum ether (PET) which provided a hydrostatic environment up to a maximum pressure of 6 GPa.[12] Methanol-ethanol mixtures (4:1) can provide a hydrostatic environment up to 10.4 GPa,[13] however this PTM is often incompatible with organic material, causing dissolution of the sample in the gasket e.g. isonicotinamide used in this study.

2.1.3.1 High-Pressure Data Collection

Diamond anvil cells produce many issues when it comes to the data collection of the sample they house. The steel body of the DAC limits the orientations of the crystal within the X-ray beam in comparison to a crystal on the end of a fibre, reducing the amount reciprocal space that can be observed.

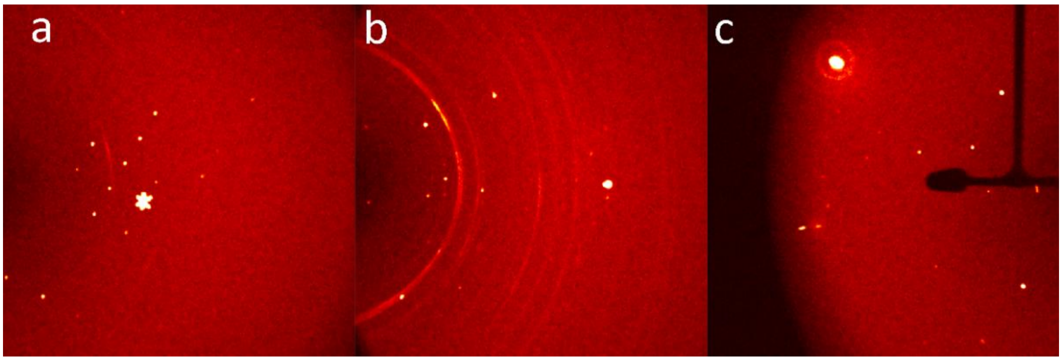

Figure 2.8: Diffraction frames taken from the collection of a high-pressure data set highlighting diffraction from a) the loaded isonicotinamide crystal and b) the tungsten gasket (observed as powder rings). Figure c) shows shading of the diffraction frame by the steel body of the DAC and beam stop.

Reflections from both diamond and ruby also contaminate the diffraction frames, observed in Figure 2.8a, b and c as a large reflection, and must be eliminated during the harvesting stage of the data collection, prior to indexing (Figure 2.9a and b). Diffraction from the gasket presents itself as powder rings (Figure 2.8b), whilst shading from the cell wall and beam stop present as shadows in the frames (Figure 2.8c). All of these combined, limit the completeness of the data collected, especially if the crystal system is low in symmetry, where we typically observe 30% completion of the diffraction sphere for monoclinic and triclinic systems. To improve data completeness, shorter wavelength X-rays are employed, i.e., molybdenum or silver, contracting diffraction to lower Bragg angles and accessing a larger range of reciprocal space. During structure refinement restraints and constraints are also applied to high-pressure structures due to the reduced data.

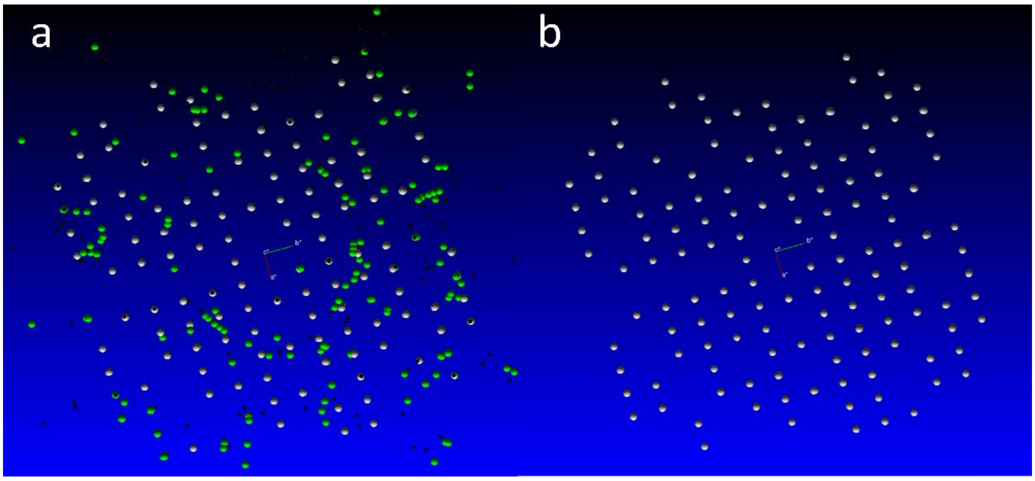

Figure 2.9: Reciprocal space of a high pressure isonicotinamide collection before and after reciprocal lattice clean-up.

2.1.4 Raman spectroscopy

Raman spectroscopy, named for its founder and 1930 Nobel Prize winner Chandrasekhara Venkata Raman, is a light scattering technique used to measure vibrational information contained within a molecule upon interaction with a laser. When an incident beam of laser light hits a molecule it can be excited to a virtual energy state, a transient process, which results in the molecule re-emitting the energy by either elastic or inelastic scattering. The most dominant type is elastic Rayleigh scattering, whereby the wavelength of the incident beam is equivalent to the wavelength of the scattered beam, therefore no energy is lost and no useful information provided. Stokes and Anti-Stokes inelastic scattering are rare, occurring approximately 1 in 10^6 events, resulting in a loss or gain of energy due to the interaction with the molecules energy levels that are involved with vibrational and rotational transitions. Stokes scattering occurs when the molecule returns to a higher vibrational energy level after absorbing energy from the laser, therefore the light scattered is lower than energy. If a molecule starts in a higher vibrational energy level and returns to the vibrational ground state, the light scattered is greater in energy, known as Anti-Stokes Raman Scattering; this is a rarer occurrence. Raman scattering is governed by a Boltzmann distribution, determining the population of each energy level at a given temperature. At thermal equilibrium the ground state is more populated, but as the temperature increases the higher vibrational energy levels can be populated. This increases the likelihood for Anti-Stokes Scattering as more molecules are in higher vibrational energy levels that can be moved to lower vibrational levels.

A limitation to Raman spectroscopy is the fluorescence that can occur, which is highly efficient in comparison to Raman scattering and can therefore hinder any useful signal. Fluorescence occurs when a molecule is hit by a laser causing excitation to a higher electronic energy level. The absorption of a photon by a molecule causes it to vibrate and drop to ground state, emitting a photon of light in the process – fluorescence. Highly coloured compounds are known to fluoresce when exposed to laser light, for example salmeterol xinafoate, caffeine and nifedipine.[14] Addressing fluorescence of materials when subjected to laser light can be done by using a laser with lower energy, as seen with *N*-methyl-3,4-methylenedioxyamphetamine.[15] Using a laser with higher wavelength can prevent excitation to a higher electronic level i.e. using a 785 nm laser rather than one at 532 nm. The drawback to this is the higher the wavelength, the less efficient the Raman scattering.

Raman spectra are graphically displayed as intensity or counts of the scattered light detected at a particular frequency. The difference in wavelength between vibrational modes of a molecule is small therefore the frequency is depicted as Raman shift, wavelengths shifted from that of the initial laser or Rayleigh scattered line. The amount of energy lost from the laser depends on the active vibrational modes that can take place within a molecule. These vibrations are Raman active if there is a change in polarizability occurring during the symmetrical vibrations, unlike IR where only asymmetric vibrations are active, making the two techniques complementary.

2.1.5 Infra-red spectroscopy (IR)

The principles of IR spectroscopy are similar to Raman spectroscopy, whereby irradiation of a sample using infrared light causes vibrations of atoms within the molecules. Changes in dipole moment give rise to IR activity whilst changes in polarisability are required for Raman activity. Transitions that are strong in an IR spectrum are often weak or absent in a Raman spectrum and vice versa, making them complementary techniques. IR spectroscopy emphasises the functional groups within a sample and the molecular vibration and frequency at which IR light is absorbed is influenced by atom size and bond strength.

Molecular vibrations caused by IR light can be classified as stretching or bending. Stretching is a result of changing distances of interatomic bonds, whilst bending is the change in angle between two atoms. Various types of vibrations absorb IR light at different frequencies resulting in unique spectral fingerprint for each compound.

The energy of IR light that is absorbed is recorded as a percentage of the light that reaches the detector i.e., wavenumber versus percentage transmittance. Figure 2.10 shows the FTIR spectrum of nifedipine. The stretches of the ester groups, highlighted in the figure, transmit a low percentage of light to the detector due to it being absorbed by that particular functional group. The N-H and C-H stretches at higher wavenumbers do not absorb a high percentage of IR light and therefore a larger percentage of light reaches the detector.

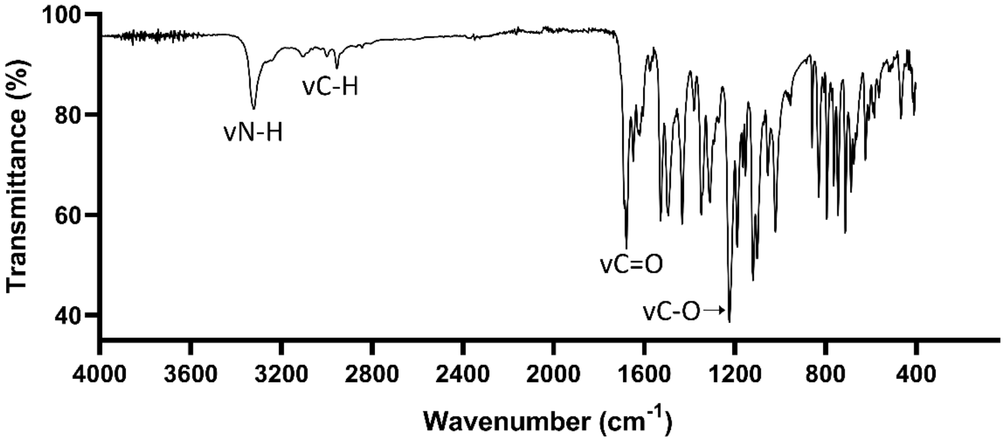

Figure 2.10: FTIR spectrum of nifedipine Form A, highlighting regions of interest.

2.1.6 Thermal Analysis

2.1.6.1 Differential Scanning Calorimetry (DSC)

Enthalpy (H) is defined by the sum of the internal energy of a system (E) and the energy required to accommodate the systems pressure (P) and volume (V) as shown in Equation 15.

Equation 15

$$H = E + PV$$

Change in enthalpy (ΔH) is a much more valuable concept, describing the loss or gain of heat (q) in a chemical reaction at a constant pressure (Equation 16).

Equation 16

$$\Delta H = q$$

If q is positive, the reaction absorbs heat from its surroundings and is termed endothermic; negative and the reaction is exothermic, releasing heat to its surroundings. Change in enthalpy allows the determination of the amount of energy contained within a compound. Using calorimetry, the temperature change can be measured during a chemical reaction, using a closed system to separate the sample from the outer environment, and thus can be used to measure change in enthalpy.

Differential scanning calorimetry (DSC) measures the heat flow of a sample in comparison to a reference, typically an empty pan, as a function of temperature and time (Figure 2.11). Heat flux DSC systems measures this difference in heat flow, whilst a thermocouple connects the sample and reference for simultaneous analysis. As the signal produced for the reference linearly increases with time, the DSC signal produced by the sample exhibits similar behaviour until the thermocouples detect a difference in temperature due to the start of a chemical reaction. Once complete the DSC signal of the sample begins to linearly increase along with the reference. The temperature difference recorded is related to the enthalpy change in a sample; in the melt process heat is required, providing the energy to break molecular bonds, and is therefore an endothermic event. If heat is released by the sample and less energy is required to maintain the temperature difference between sample and reference, the change in enthalpy is negative and is therefore an exothermic event. For example, crystallisation is an event which releases energy, therefore if a polymorphic transition or recrystallisation occurs on the application of heat, it is seen in a DSC thermograph as an exothermic event.

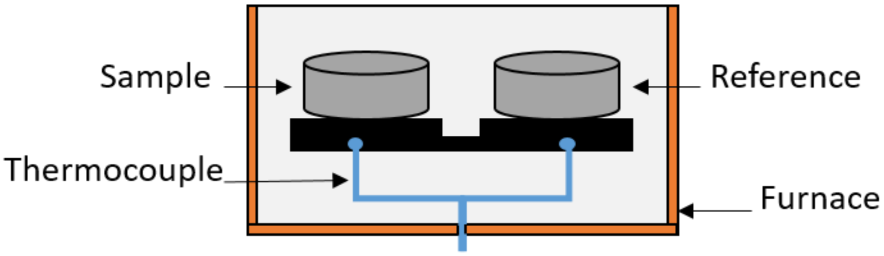

Figure 2.11: Schematic diagram of a Heat Flux DSC system.

Thermographs are used to plot the resultant heat flow data against temperature. There are three typical thermal events to look out for when analysing the thermograph of a crystalline material, two of which are displayed in the thermograph of nifedipine (Figure 2.12). Event 1 is negative and is therefore an exothermic event, which relates to the re-crystallisation of nifedipine. Event 2 relates to the heat required to melt the material and is endothermic in nature. Integration of the peaks shown in Figure 2.12 can be used to calculate the associated enthalpies with a unit of J/g. The final event appears as a step in the baseline of the thermograph, usually caused by a glass transition in the material. Glass transitions occur when the properties of a material (usually amorphous or semi-crystalline) change from a brittle 'glassy' state to a state with more flexibility on increase in temperature.

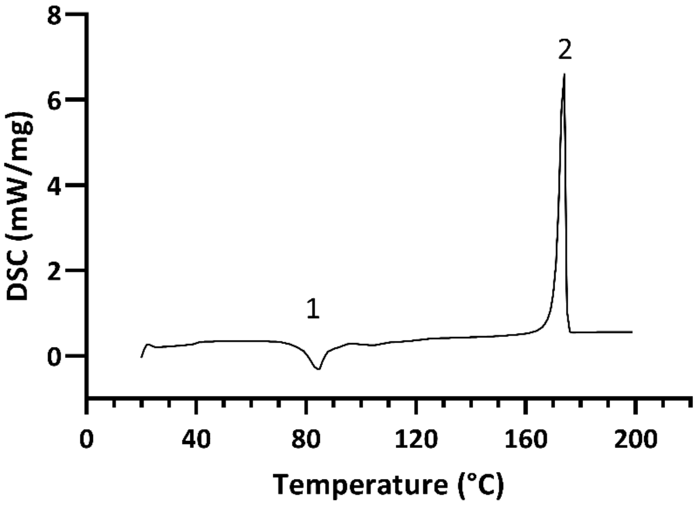

Figure 2.12: DSC thermograph of nifedipine Form A, highlighting an exothermic (1) and endothermic event (2).

2.1.6.2 Thermal Gravimetric Analysis (TGA)

Thermal gravimetric analysis (TGA) was carried out simultaneously to DSC using the Netzsch STA449 F1 Jupiter. TGA is used to monitor the mass of a substance as a function of temperature or time, whilst subjected to a controlled temperature program in a controlled environment, quantifying the loss of water or solvent and decomposition of a sample. Thermal gravimetric analysis can provide information regarding the chemical reaction of a material as it is subjected to elevated temperatures. A balance is used to monitor the mass change as a function of time and temperature, typically given as a percentage of the initial mass. TGA was predominantly used to study the desolvation of nifedipine solvates in Chapter 5. The technique was used to quantify the stoichiometric ratio of solvent to API and investigate the removal of solvent from the crystal structures. TGA was also used to confirm the loading of isonicotinamide in porous silica particles. Silica remains stable beyond 1000 °C, therefore any mass loss observed between 200 and 300 °C can be ascertained as the decomposition of isonicotinamide.

2.2 Characterisation of surfaces and mesoporous materials

2.2.1 Gas sorption

Surface adsorption can be categorised as either physical interaction using gas (physisorption) or chemical bonding (chemisorption). Chemisorption is a process which involves a chemical reaction between adsorbate and specific active sites located on the surface of the sample; typically used in the characterisation of catalysts.

Gas adsorption can either be characterised as volumetric, whereby the adsorbed amount of gas is calculated by the difference between the amount of gas admitted and the amount of gas in the void space; or gravimetric which relies on a microbalance and pressure gauge to determine the adsorbed gas. These techniques can be used to characterise various types of micro- and mesoporous solids: metal organic frameworks (MOFs), zeolites, foods, and pharmaceuticals. The IUPAC definition of micropores is < 2 nm, with mesopores ranging from 2 to 50 nm. Pore size analysis for gas sorption techniques ranges from 0.3 to 500 nm. Gas or vapour is used as the absorptive, forming physical bonds (van der Waals) with the sample which are both weak and reversible. Nitrogen gas is most commonly used for gas adsorption as it is common and relatively inexpensive. There are many drawbacks to using nitrogen including the surface charge of the molecules having an impact on the packing of the molecules within the pores of the samples.

Gas sorption is used within the pharmaceutical industry to calculate the surface area of particles, with it being used on APIs and excipients alike. Differences in surface area can have a big impact on how a material behaves during the formulation processes such as blending and tabletting of powders is affected by their surface area. Larger surface areas are desired for APIs, due to there being greater area for the dissolution medium to interact with, which in turn influences the bioavailability of the drug. The addition of pores to a material also increases the surface area of a particle.

For optimal adsorption, the sample needs to be degassed to remove any water trapped in the pores or impurities on the surface of the particles. To do this, a high temperature is applied to the sample under vacuum. Porous silica and silicon can withstand high temperatures, so degassing can take place between 200 and 300 °C. Next the sample is exposed to the absorptive gas for analysis. Pressure in the sample chamber is increased to facilitate the adsorption of the gas molecules, until a monolayer is formed (a single layer of molecules covering the surface of the sample); thus, allowing for calculation of the surface area by the Brunauer-Emmett-Teller method. Additional gas molecules adsorb forming a multilayer which can be used to calculate pore size distribution and total pore volume. Pores will then fill by capillary condensation, smaller pores filling before larger ones; once the pores are full the adsorbed amount will plateau.

Pressure transducers record the pressure of the adsorptive gas and quantitatively determine the amount of gas adsorbed and desorbed. An adsorption isotherm can then be plotted.

2.2.1.1 Brunauer-Emmett-Teller (BET)

The surface area of a solid material is the means by which it interacts with its environment. We can increase the surface area of solid material by making it porous and can be calculated using the BET. The calculation can be applied in the relative pressure range of 0.05 to 0.3 as this is the region in which the monolayer is formed. The surface area of microporous particles can be difficult to determine using BET as it is difficult to distinguish between the monolayer formation and micropore filling.

Equation 17

$$\frac{1}{W\left(\left(\frac{P_0}{P}\right)-1\right)}=\frac{1}{WmC}+\frac{C-1}{WmC}\left(\frac{P}{P_0}\right)$$

Where W is the weight of gas adsorbed at relative pressure P/P_0*. Wm is the weight of the adsorbate that forms a monolayer on the surface of the material. C is the constant related to the energy of the adsorption in the monolayer.*

2.2.1.2 Pore size Analysis

Gas sorption also characterises the pores that make up the surface of a solid. Barrett-Joyner-Halenda (BJH) analysis is a macroscopic thermodynamic technique based on the Kelvin equation which describes the change in vapour pressure when in the presence of a curved interface. When vapour enters a confined space i.e., a pore or capillary, less pressure is needed for condensation to occur, occurring below the saturation pressure of the bulk fluid and van der Waals forces of attraction become stronger between each vapour particle. The vapour phase particles adsorb to the pore walls leading to multilayer adsorption till a meniscus forms at the liquid vapour interface. This process is termed ‘capillary (or pore) condensation’.

Equation 18

$$ln\frac{P_v}{P_{sat}} = -\frac{2H\,\gamma Vl}{RT}$$

Where P_v is the equilibrium vapour pressure; P_{sat} is the saturation vapour pressure; H equals the mean curvature of the meniscus; γ is the liquid/vapour surface tension; V_l is the liquid molar volume; R is the ideal gas constant and T is the temperature.

Although BJH is linked to pore condensation, it is known to fail in its characterisation of micropores and narrow mesopores, underestimating them by 20 to 30%. BJH also assumes that fluid in the pores behaves in a similar manner to fluid in the bulk.

Density Functional Theory (DFT) correctly takes into the account the behaviour of fluids inside the pores, with the outcome being a more accurate micro- and mesopore size distribution. This theory is based on molecular simulation, describing the conformation of the adsorbed fluid phase at a molecular level. DFT allows for the calculation of the equilibrium density profile of the fluid particles located on the surface and in the pores, based on intermolecular interactions between fluid-fluid particles and fluid-solid particles, providing a more comprehensive study of the pores.

2.3 Analytical determination methods for drug loading

2.3.1 High-Performance Liquid Chromatography (HPLC)

High-performance liquid chromatography (HPLC) is an analytical separation technique used to identify and quantify components from a mixture, working on the principle of separating compounds based on their polarity and affinity for a mobile and stationary phase. A mobile phase, typically consisting of a mixture of solvents such as water, methanol or acetonitrile is pumped through the system at high pressure in which a sample is injected into. This leads to a column, termed the stationary phase. The column contains solid particles which interact with the analyte carried in the mobile phase, separating the components depending on their polarity, resulting in varying retention time hence separation.

HPLC can be categorised into multiple types, with the most common being normal phase HPLC and reverse phase HPLC; the later used in the research carried out in Chapter 6. A polar mobile phase is used to carry the analyte through the column, which consists of surface functionalised silicon. Hydrocarbon chains make the column non-polar, retaining compounds with non-polar functional groups for a longer time due to interactions. Compounds with a lower affinity for the non-polar phase are carried in the mobile phase, eluting from the column earlier. The application of HPLC is to quantify isonicotinamide loaded in porous silica. Quantitative analysis uses a calibration curve, whereby a series of known concentrations are analysed, and their response (area under the peak) assigned to that concentration. A linear relationship is established between the concentration and peak area allowing for quantification of an unknown concentration.

2.4 References

1. Bond, A. Pharmaceutical Crystallography. The Royal Society of Chemistry: 2019.
2. Luger, P. Modern X-Ray Analysis on Single Crystals: A Practical Guide. De Gruyter: 2014.
3. Clegg, W.; Blake, A. J.; Cole, J. M.; Evans, J. S. O.; Main, P.; Parsons, S.; Watkin, D. J. Crystal Structure Analysis: Principles and Practice. In *Crystal Structure Analysis: Principles and Practice*, Clegg, W., Blake, A. J., Cole, J. M., Evans, J. S. O., Main, P., Parsons, S., Watkin, D. J., Eds.; Oxford University Press: 2009; Vol. 9780199219, pp 1-408.
4. Dolomanov, O. V.; Bourhis, L. J.; Gildea, R. J.; Howard, J. A. K.; Puschmann, H. OLEX2: A complete structure solution, refinement and analysis program. In *Journal of Applied Crystallography*, 2009; Vol. 42, pp 339-341.
5. Pawley, G. S. Unit-cell refinement from powder diffraction scans. In *Journal of Applied Crystallography*, International Union of Crystallography (IUCr): 1981; Vol. 14, pp 357-361.
6. Toby, B. H. R factors in Rietveld analysis: How good is good enough? In *Powder Diffraction*, 2012/03/01 ed.; Cambridge University Press: 2006; Vol. 21, pp 67-70.
7. Rietveld, H. M. A profile refinement method for nuclear and magnetic structures. In *Journal of Applied Crystallography*, 1969; Vol. 2, pp 65-71.
8. Katrusiak, A. High-pressure crystallography. In *Acta Crystallographica Section A*, 2008; Vol. 64, pp 135-148.
9. Moggach, S. A.; Allan, D. R.; Parsons, S.; Warren, J. E. Incorporation of a new design of backing seat and anvil in a Merrill{--}Bassett diamond anvil cell. In *Journal of Applied Crystallography*, 2008; Vol. 41, pp 249-251.
10. Miletich, R.; Allan, D. R.; Kuhs, W. F. High-Pressure Single-Crystal Techniques. In *Reviews in Mineralogy and Geochemistry*, 2000; Vol. 41, pp 445-519.
11. Forman, R. A.; Piermarini, G. J.; Barnett, J. D.; Block, S. Pressure Measurement Made by the Utilization of Ruby Sharp-Line Luminescence. In *Science*, American Association for the Advancement of Science: 1972; Vol. 176, pp 284-285.
12. Barnett, J. D.; Bosco, C. D. Viscosity Measurements on Liquids to Pressures of 60 kbar. In *Journal of Applied Physics*, American Institute of Physics: 1969; Vol. 40, pp 3144-3150.
13. Klotz, S.; Chervin, J.-C.; Munsch, P.; Le Marchand, G. Hydrostatic limits of 11 pressure transmitting media. In *Journal of Physics D: Applied Physics*, IOP Publishing: 2009; Vol. 42, p 75413.
14. Ali, H. R. H.; Edwards, H. G. M.; Hargreaves, M. D.; Munshi, T.; Scowen, I. J.; Telford, R. J. Vibrational spectroscopic characterisation of salmeterol xinafoate polymorphs and a preliminary investigation of their transformation using simultaneous in situ portable Raman spectroscopy and differential scanning calorimetry. In *Analytica Chimica Acta*, 2008; Vol. 620, pp 103-112. Pavel, I.; Szeghalmi, A.; Moigno, D.; Cîntă, S.; Kiefer, W. Theoretical and pH dependent surface enhanced Raman spectroscopy study on caffeine. In *Biopolymers - Biospectroscopy Section*, 2003; Vol. 72, pp 25-37. Grooff, D.; Liebenberg, W.; De Villiers, M. M. Preparation and Transformation of True Nifedipine Polymorphs: Investigated with Differential Scanning Calorimetry and X-Ray Diffraction Pattern Fitting Methods. In *Journal of Pharmaceutical Sciences*, Elsevier: 2011; Vol. 100, pp 1944-1957.
15. Bell, S. E. J.; Burns, D. T.; Dennis, A. C.; Speers, J. S. Rapid analysis of ecstasy and related phenethylamines in seized tablets by Raman spectroscopy. In *Analyst*, The Royal Society of Chemistry: 2000; Vol. 125, pp 541-544.

Chapter 3

Pressure-induced superelastic behaviour of isonicotinamide

This chapter has been published in the journal Chemical Communications.

Jones, E. C. L.; Bebiano, S. S.; Ward, M. R.; Bimbo, L. M.; Oswald, I. D. H. Pressure-Induced Superelastic Behaviour of Isonicotinamide. Chem. Commun. 2021, 57 (89), 11827–11830.

3 Pressure-induced superelastic behaviour of isonicotinamide

3.1 Abstract

The thermodynamically stable form of Isonicotinamide (Form I) exhibits superelastic behaviour on application of pressure in excess of 4.33 GPa. There is a distinct change in crystal morphology on transition that is reversible once pressure is released. An investigation into the single-crystal to single-crystal phase transition of Form I isonicotinamide to previously unknown polymorph Form I' at a pressure of 4.98 GPa provides molecular information from which a mechanism for the transition is proposed. Pixel energy calculations provide intermolecular information that indicates that the repulsion in the secondary interlayer interactions is relieved by the transition.

3.2 Introduction

Materials that convert energy into a mechanical response have a wealth of potential applications in, for example electronics, energy harvesting, gating and even in simulation of muscle contractions.[1] For the materials to be of use, there is a requirement to remain flexible and resilient when strain is applied, whether it be thermal or driven by shear stress. Crystals that exhibit a mechanical response when subjected to external perturbation can be defined as dynamic. These effects can either be restorative (i.e. bending or twisting) or disintegrative (i.e. cracking or fragmentation of the crystal).[1] Previous studies have witnessed changes in shape during polymorphic transitions, attributed to martensitic transitions.[2, 3] Martensitic transitions are a form of cooperative structure transition, by which there is a coordinated displacement of molecules in a crystalline material. An example of this type of transition was the single crystal transition in [1]benzothieno[3,2-b]benzothiophene (diBu-BTBT). Chung *et al.*, demonstrated that diBu-BTBT undergoes a reversible transition on heating to 345 K but with some hysteresis on cooling (331 K).[2] One of the remarkable features was the observation of a boundary line propagating across the crystal with a reversible colour change from blue to yellow.[2] The authors were able to identify that the high temperature phase displayed disorder of the tertiary butyl side groups adopting three different conformations, that impacts on the molecular packing leading to a small change in crystal shape.

Martensitic transitions have also been witnessed in a simpler molecular system hexamethylbenzene (HMB).[3] In their paper, Li *et al.*, discuss the potential application of HMB as an actuator utilising the transition between Form II and Form I on heating. The authors showed via single-crystal diffraction that the expansion in HMB is caused by the increased separation between the layers that causes the elongation along the *a*-direction in the structure hence the crystal. More significantly, they observed that the crystal is capable of providing a mechanical force of 10,000 time its own weight, places it firmly in the realm of thermal actuators.[3] The authors do note that the transition is slow but powerful, with the propagation of new phase at 6.36 mm s^{-1} in comparison to thermosalient transitions of compounds which occur at a rate two orders of magnitude faster than that of HMB.[4] There are few studies to compare the magnitude, however, in their recent review, Naumov *et al.,* have highlighted the potential of thermally actuated organic crystals in comparison to other materials, possessing a greater maximum force per work output than nano-muscles or ceramic piezoelectrics.[1]

Not all single-crystal to single-crystal transitions, where changes in crystal dimensions are observed, are martensitic transformations. The phase transition of 7,7,8,8-tetracyanoquinodimethane-p-bis(8-hydroxyquinolinato)copper(II) (CuQ_2-TCNQ) Form II to Form I using mechanical stimulation resulted in a 100% increase in crystal length. The authors reveal that during the transition the main crystal face changes from the (001) to the (11-1) face, relating the change in structure to a rotation of the layered structure by approximately 28° with respect to the dominant face. This cooperative movement is one of the classifications of a martensitic transition. However, the timescales of the transition, i.e. not instantaneous (0.01mm/s movement in wavefront in contrast to the 2.5mm/s boundary transfer seen in a single crystal of 3,5-difluorobenzoic acid upon removal of shear stress), discounted this definition in favour of a nucleation and growth mechanism of Form I.[5] The authors propose that the nucleation event is initiated by the use of the external probe, which creates a number of nuclei that alters the molecular arrangement culminating in the rearrangement in the layers to the new phase. The authors also observed that the transition could occur on increasing temperature where the change is accompanied by a broad exothermic event between 220-240 K. By careful selection of the sample with a defined crystallite size they were able to narrow the endothermic event to a 5 K interval at 230 K.

In each of these cases, a large change in the intermolecular interactions is observed between molecules through a change in temperature, however this is not the only method by which a system can be perturbed. Phase transitions in organic or organometallic materials can be explored using the application of pressure. The application of pressure to crystalline materials can strongly impart changes to the intermolecular interactions that hold the molecules together into the crystal structure, e.g. hydrogen bonding, but also the packing of molecules hence could be used as a tool to explore the changes imparted in the studies above.[6, 7] Of particular interest, is how smaller molecules can exhibit pressure-induced phase transformations. The previous study by Takamizawa and Takasaki investigated the effect of pressure as well as temperature on the martensitic transition of tetrabutyl-*n*-phosphonium tetraphenylborate. They were able to quantify the response to pressure on particular faces of the crystal, during transformation from the α to β form.[8]

Isonicotinamide is commonly investigated in solid-state studies due to its hydrogen bonding behaviour, with two hydrogen bond acceptors and one hydrogen bond donor. It has been known to enhance the physicochemical properties of pharmaceutical compounds by acting as a coformer in co-crystallisation, readily bonding to many APIs, enhancing solubility and bioavailability without affecting the drugs therapeutic effect. One example is the co-crystallisation between isonicotinamide and the dihydropyridine drug nifedipine. The photostability of nifedipine has been of concern of manufacturers, with a photoreaction occurring when the drug is exposed to daylight. Yu and colleagues investigated how altering the electron environment of the dihydropyridine ring, increasing the distance between the oxygen on the nitro group and hydrogen of the dihydropyridine ring would prevent or slow down this reaction.[9] A synthon between isonicotinamide nifedipine led to an increase in the forementioned contact thus increasing the stability of nifedipine within the co-crystal. After 10 hours' exposure to UV light, 98% of nifedipine was present in the co-crystal sample in comparison to 83% in the control sample. The pyridine carboxamide compound has over 200 reported entries in the CSD, making it well characterised and an exciting prospect to investigate under high-pressure conditions.[10] There are six known polymorphs, each possessing different bonding patterns, but of particular interest is the fact that the most thermodynamically stable (Form I) is the only structure that forms dimers using the amide moieties in a $R^2_2(8)$ dimer (Figure 3.1a).[11, 12] Dimers are created by hydrogen bonds between two neighbouring amide groups (NH···O) extending in the direction of the *a*-axis. Dimers are connected to form chains via a second hydrogen bond (NH···O) parallel to the *b*-axis.

Forms II through to VI all possess a chain structure with interactions involving the pyridine, and amide functionality (NH···N). Form II has two molecules in the asymmetric unit leading to two independent chains repeating throughout the structure, ABB’A’, where the apostrophe denotes symmetry equivalent layer (Figure 3.1d). Form IV has three molecules in the asymmetric unit forming chains of symmetry related molecules (Figure 3.1e). Form VI resembles Form II isonicotinamide, however the two independent molecules are arranged to form chains ABA’B’ (Figure 3.1d and f, respectively). Chain structures Form III and Form V both possess slightly different structures to the previously mentioned polymorphs (Figure 3.1b and c). Both have one molecule in the asymmetric unit with weak CH···O bonds providing a slightly different orientations of molecules. Every second molecule in the chain structure of Form V is rotated by 61.73 °, making it almost perpendicular to its hydrogen-bonded neighbours that prevents the interaction of the aromatic CH with the carbonyl group of the next chain as observed in Form III. Form III is the only structure possessing the additional weak hydrogen bond which leads to the flat layers, whilst the other chain polymorphs possess a pleated sheet structure.

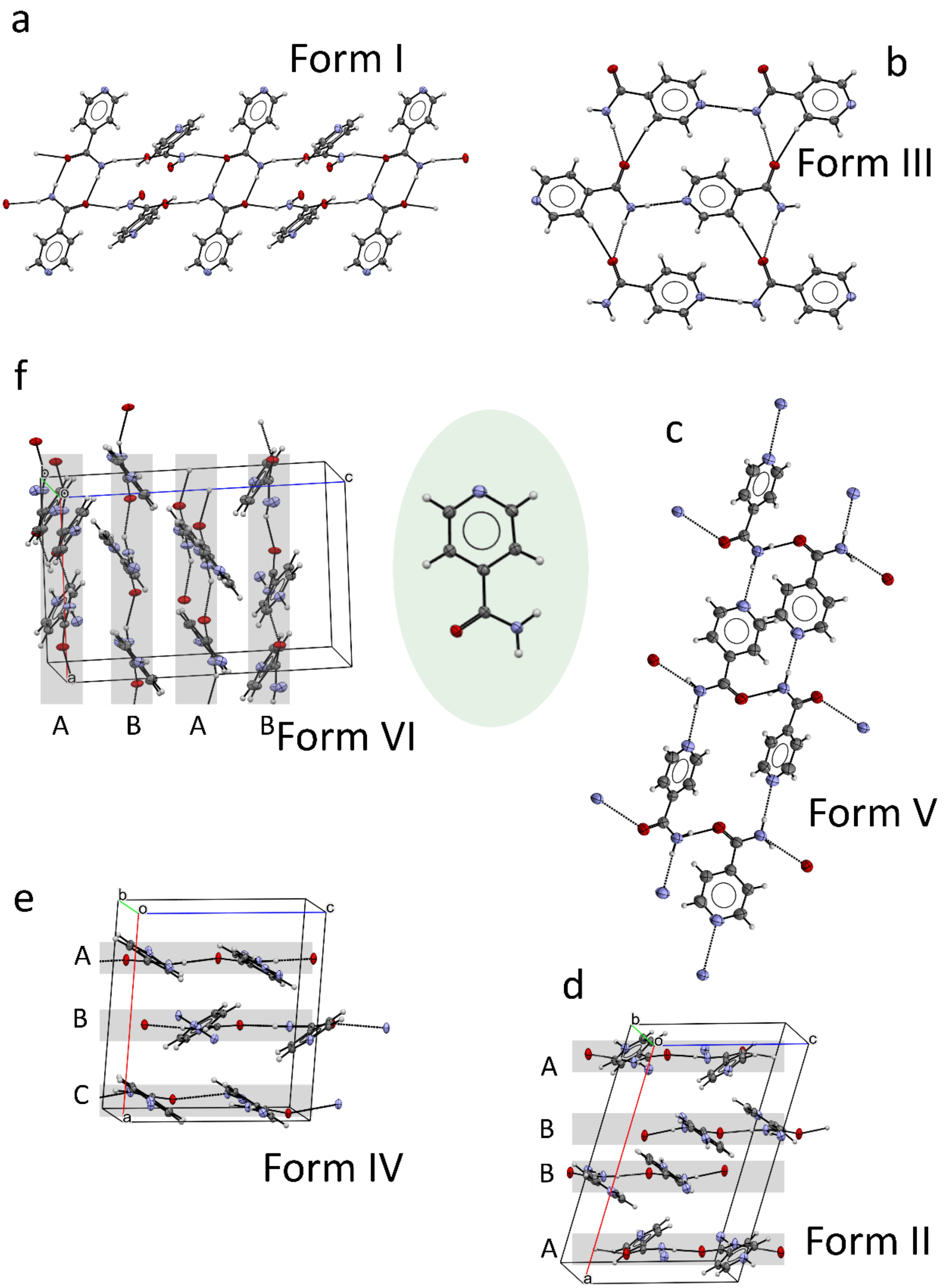

Figure 3.1: Crystal structures of the isonicotinamide polymorphs; a) Form I is the only polymorph with a dimeric structure. b and c) show Forms III and V respectively, with one molecule in the asymmetric unit forming chains. d), e) and f) shows Forms II, IV and VI respectively, viewed along the *b*-axis which form layers of symmetry independent molecules.

3.3 Experimental

3.3.1 Crystal formation

Form I was recrystallised from a solution of isonicotinamide (Sigma Aldrich, 99% purity) in ethanol (80 mg/mL, Fisher Scientific, 99.8% purity) at 22 °C. The solution was stirred for 60 minutes and filtered into a clean vial using PTFE syringe filter (0.2 μm). Colourless block crystals were produced by slow evaporation of the solvent and characterised using X-ray diffraction and Raman spectroscopy before loading into a diamond anvil cell.

3.3.2 Diamond anvil cell

Merrill-Bassett diamond anvil cells (DAC) were used to apply pressure to single crystals of isonicotinamide during the X-ray and Raman studies. A pre-indented tungsten foil gasket (99.95 %, Hollinbrow, Telford, UK) was placed between two diamonds with 600 μm culets. The gasket, 250 μm in thickness, was pre-indented to approximately 100 μm before a 250 μm hole was drilled through the foil to serve as a sample chamber. Petroleum ether (PET 35/60, Alfa Aesar) was used as the hydrostatic medium.[13] The pressure of the cell was monitored using fluorescent R-line of crushed ruby spheres within the chamber of the cell, compared to those at ambient pressure.[14]

3.3.3 Single-crystal X-ray diffraction (SC-XRD)

Single crystal X-ray diffraction data were collected for crystals at ambient pressure using a Bruker D8 Venture diffractometer with a Photon II Pixel Array detector and Incoatec IμS microfocus Cu X-ray source (Kα1 λ = 1.54178 Å). Data were reduced using SAINT within the Apex3 suite of software.[15] SADABS was used to correct for absorption.[16] OLEX2 v1.2 software was used to refine the structures, with coordinates taken from EHOWIH01 (Cambridge Structural Database, CSD).[10, 11, 17]

High-pressure diffraction data was collected using Bruker APEX-II diffractometer with Incoatec IμS microfocus Mo X-ray source (Kα1 λ = 0.71073 Å) and CCD detector. Data were reduced using SAINT within APEX3 using the dynamic masking procedures.[15] SADABS was used for absorption correction.[16] The structures were refined in OLEX2 v1.2.[17]

Refinement against the pressure data were conducted using the coordinates of the ambient form, collected from the CSD (ref code: EHOWIH01).[10, 11] The refined atomic coordinates at each pressure were used as the input for each subsequent data set. Non-hydrogen atoms were treated using anisotropic displacement parameters. RIGU restraints were applied to all non-hydrogen atoms. 10 data sets were collected between 1.58 and 5.65 GPa for Form I using two different crystals. Crystal 1 was collected at 1.90, 2.40, 3.23, 4.00 and 5.65 GPa. Crystal 2 was collected at 1.58, 3.46, 3.99, 4.33 and 4.98 GPa.

Crystallographic data can be found in Appendix A (Table A1).

3.3.4 Raman spectroscopy

Raman spectra were collected using a Horiba Scientific Raman XploRA™ PLUS microscope with a 523 nm laser source. Acquisition parameters including accumulation, acquisition time, grating, slit, and hole were varied to maximise the signal for each data collection. Raman spectra were taken in the region of 50 to 3500 cm^{-1}. The diamond peak at 1300-1350 cm^{-1} is omitted for clarity in Figure 3.2.

3.3.5 Periodic DFT calculations

Geometry optimisations of isonicotinamide were performed by periodic Density Functional Theory (DFT) using the DMOL3 code found in Materials Studio v8 by my supervisor, Dr Iain Oswald, to provide computational verification of the high pressure structures due to the lack of data in high-pressure datasets and subsequent problems that impact on the refinements.[18, 19] The DNP numerical basis set[18] was used together with the PBE functional[20] with dispersion correction applied.[21] The parameters used in the DFT calculations followed those of previous work in the research group and elsewhere.[22] The models from the single crystal refinements were used and the unit cell dimensions were fixed at the values obtained from the experimental data and the atomic coordinates were allowed to optimise. Convergence was defined when the maximum changes in total energy, displacement and gradient were 10^{-5} Ha, 5×10^{-3} Å and 2×10^{-3} Ha Å^{-1}, respectively. Brillouin zone integrations were performed by Monkhorst-Pack[23] *k*-point sampling at intervals of 0.07 Å^{-1}.

3.3.6 Pixel calculations

Pixel calculations were performed on each dataset from ambient to 5.65 GPa using the MrPIXEL v3.1 program using the geometry optimised structures to account for any variation in the refinements due to data or the modelling over the pressure series.[24] Molecular electron densities were calculated using Gaussian09W at the B3LYP/6-31G** level.[25] The condensation level was set to 4 and cluster radius was 14Å. Interactions in the first molecular coordination sphere of Form I isonicotinamide can be found in Appendix A (Table A2). The most energetic intermolecular interactions of Form I and Form I' are displayed in Table A3 found in Appendix A and relationship between molecular pairs visualised using Mercury (Figure 3.9).[26]

3.4 Results and Discussion

The initial investigations of isonicotinamide at high pressure used Raman spectroscopy to identify any molecular (e.g., conformation) or environmental changes around the isonicotinamide molecules, e.g., hydrogen bonding (Figure 3.2). During this investigation it was observed that isonicotinamide Form I exhibits pressure-induced deformation beyond 4.3 GPa. Crystals that were square became thinner and more elongated whilst maintaining their single crystal-like nature. Due to crystal confinement in the gasket and between two diamonds, change to the third dimension was not observed, hence bending of the crystal on compression seen in other systems cannot be ruled out.[27] The initial Raman spectra indicated that the environment of the pyridine ring was altered as the crystal changed. The out-of-plane (oop) bending (400 cm^{-1})[28] and in-plane bending (ip; 660, 663 and 664 cm^{-1}) show distinct changes where the oop bend splits into two peaks with an additional band at 374 cm^{-1} appearing. The ip bends all soften to lower frequencies which is indicative of a potential phase transition (Figure 3.2a and b). Further evidence of the change is observed around the N-H stretch (3072 cm^{-1}) where splits into three separate peaks (3075, 3113 and 3127 cm^{-1}). From the discontinuities in the Raman behaviour, it suggests that the phase transition between 4.33 and 4.98 GPa alters the environment of the pyridine ring system such that it perturbs the internal vibration of the molecule.

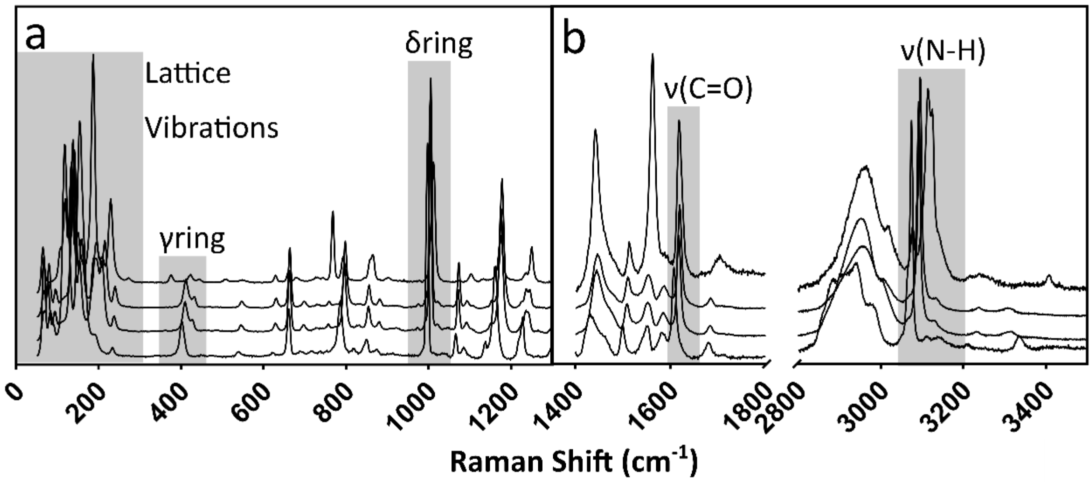

Figure 3.2: Raman spectra of Form I isonicotinamide on increasing pressure from bottom to top: 1.58, 3.99, 4.33 and 4.98 GPa. a) 50-1300 cm^{-1} and b) 1400-3500 cm^{-1}. The diamond peak at 1300 cm^{-1} and between 1800-2800 cm^{-1} were excluded for clarity. The region prior to 3000 cm^{-1} displays a broad band indicative of the aliphatic hydrocarbons in the pressure transmitting medium, petroleum ether. γ, out-of-plane bending; δ, in-plane bending; ν, stretching.

The crystals exhibit an elastic behaviour with the crystals regaining their original shape as pressure is released. From this behaviour, isonicotinamide can be defined as possessing superelastic properties, rarely witnessed in organic crystals.[1] One example of an organic material possessing this characteristic is terepthalamide, where the application of shear stress transforms the α-form to the β-form via the bending of the crystal. The molecules interact via an amide dimer at both ends to form chains, and through the second amide hydrogen, form sheets with other dimers through side-by-side hydrogen bonding. As the external stimuli is applied, the molecules rotate to accommodate the change in the external form of the crystal.[29] Notably, the hydrogen bonding motif remained the same in the new phase, with the recovery of the α-form after removal of the stressor. Molecular arrangement changed from AAAA to A'BA'B, with differences observed in the stacking of the phenyl rings resulting in a denser phase.

In isonicotinamide, the observation of the superelasticity in the crystal was not limited to one observation. A further nine crystals of varying dimensions were loaded into a membrane-driven Diamond Anvil Cell (mDAC) to see whether the aspect ratio of the crystals would have an impact on the superelastic behaviour (Figure 3.3, Table 3.1). The pressure of the cell was increased from ambient to 5.29 GPa holding for 2 minutes at each 2-bar increase of the membrane. Five out of nine crystals showed an increase in aspect ratio on compression with one indicating a reduction in aspect ratio (crystal 8) and a further 3 crystals that showed no change. During this process, a slight delay of the phase transformation was noted, indicating that kinetics will be playing a part in the transformation between the low pressure and high-pressure phase. On decompression, the crystals regained their original form albeit the impact of the phase transition was apparent on visual inspection of the crystals. Each of the crystals showed markings on the surface of the crystal. As shown in Figure 3.3, the diameter of the gasket at 5.29 GPa is larger than at ambient pressure. As pressure increases, the hole should decrease in size – as force is applied to the gasket the pressure increases and area decreases as according to Equation 19. When the area of the gasket begins to increase, the upper pressure limit has been met and the pressure pushing outwards is greater than the pressure pushing inwards – as shown in Figure 3.3b.

Equation 19

$$P = \frac{F}{A}$$

Pressure (P) is defined as the force applied (F) to a given area (A) and has units of Pascal or Newton's per square meter (N/m²).

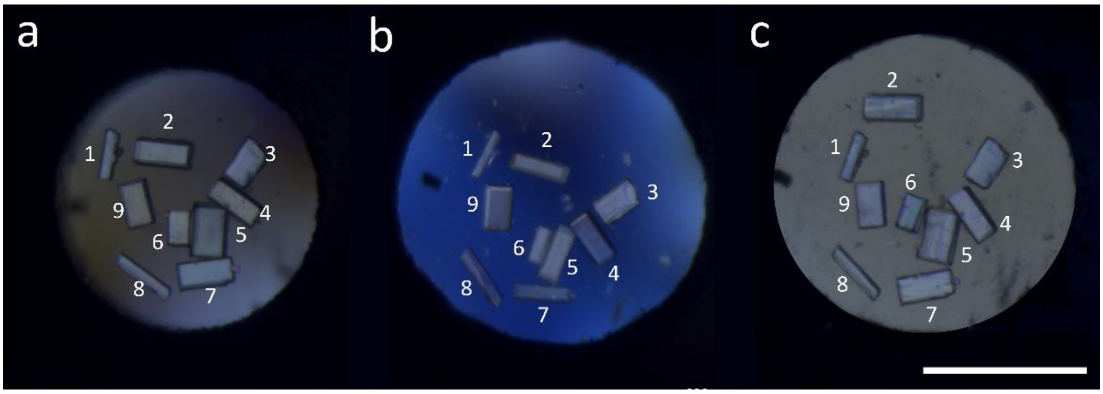

Figure 3.3: Microscopy image of isonicotinamide Form I loaded in a gas membrane cell at a) ambient pressure and b) after the phase transition 5.29 GPa showing changes to crystal dimensions. c) shows the crystals back at ambient, with restoration back to their original dimensions. Scale bar represents 200 µm.

Table 3.1: Crystal dimensions and aspect ratios of Form I isonicotinamide crystals during compression to 5.29 GPa and decompression.

Crystal No.	**Dimensions (µm)**		**Aspect Ratio**		**Dimensions (µm)**	**Aspect Ratio**
	Ambient	**5.29 GPa**	**Ambient**	**5.29 GPa**	**Ambient (after decompression)**	
1	16.8	11.7	3.5	5.4	19	3.1
	59	63.1			59	
2	30.9	19.8	2.1	3.4	32.3	2.1
	64.2	68.3			68.1	
3	32	33	1.6	1.6	36.1	1.6
	51.6	51.3			56.6	
4	24.8	28.2	2.5	2.2	28.9	2.3
	63.2	61.3			65.3	
5	39.8	24.7	1.7	2.5	39.6	1.6
	67.2	62.4			64	
6	27.6	12.2	1.5	3.3	27.4	1.5
	41.8	40.5			42	
7	33.2	17	2.0	3.9	33.7	1.9
	67.8	66.7			62.9	
8	15	17.6	5.2	4.2	15.4	5.0
	77.4	73.5			77	
9	32.1	31.5	1.7	1.7	34	1.7
	54.6	54.4			58.2	

The single crystal to single crystal phase transition opened the possibility of studying the transition using diffraction techniques to gain a molecular understanding of this remarkable physical change. To perform the diffraction experiment, a single crystal of isonicotinamide Form I was loaded into a Merrill-Bassett DAC equipped with Boehler-Almax diamonds, a steel gasket (250 µm hole), ruby as the pressure marker and petroleum ether 35:60 as the pressure-transmitting medium. Form I isonicotinamide crystallises with one molecule in the asymmetric unit in monoclinic $P2_1/c$ with unit cell dimensions: a = 10.229(3) Å, b = 5.7538(16) Å, c = 10.095(3) Å, β = 97.277(18)° (Table A1).[11] Upon application of pressure, isonicotinamide displays anisotropic behaviour with respect to the cell lengths and decrease monotonically with each dimension decreasing by 10.25%, 1.50% and 5.44% for the *a*-, *b*-, and *c*-axis, respectively to 4.33 GPa. (Figure 3.4).[30] The anisotropic behaviour of the compression is similar to other simple organic systems e.g. aniline and α-PABA.[6, 31] The data is fit to a 3rd order Birch-Murnaghan Equation of State (Figure 3.5).[32] This gave a bulk modulus (K_0) of 10.6(7) GPa, V_0 = 589(5) and K' = 7(15) which is typical for this type of organic solid.

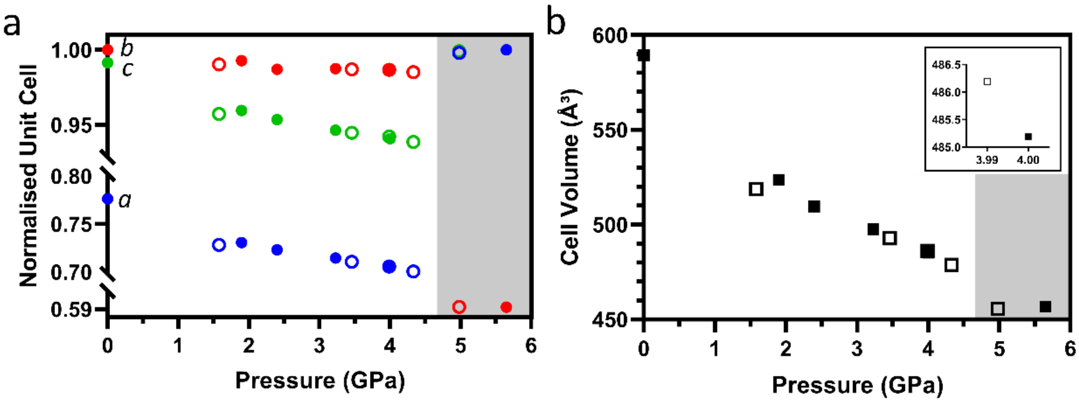

Figure 3.4: Variation in a) unit cell lengths and b) unit cell volume of isonicotinamide Form I as a function of pressure. Different symbols in b) indicate the two different crystallites used in the pressure study. Area highlighted in grey shows data collected after the transition at 4.98 GPa. Inset shows the cell volumes at 3.99 and 4.00 GPa where the overlap occurs on the main Figure.

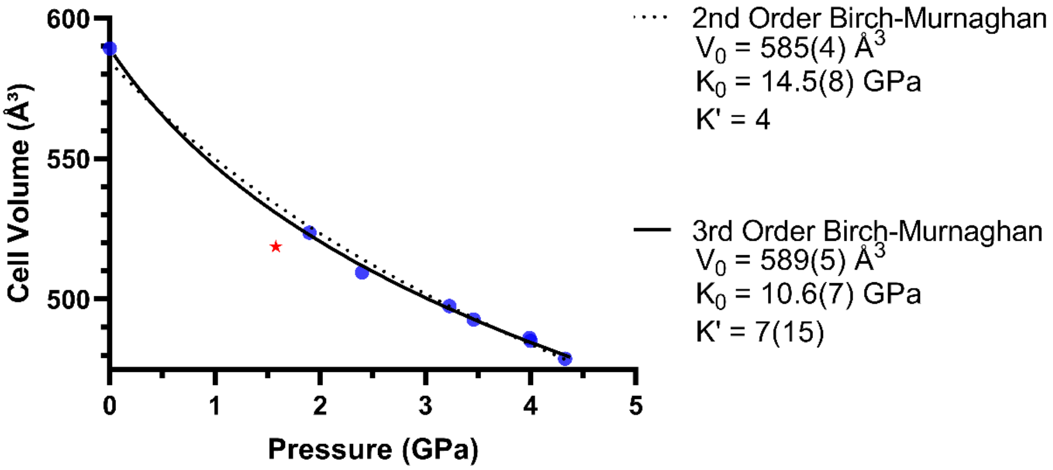

Figure 3.5: 3rd Order Birch-Murnaghan Equation of State for Form I isonicotinamide from ambient pressure to 4.33 GPa. Data point at 1.58 GPa was not used in the calculation due to poor fit (red star).

There are clear changes in unit cell parameters between 4.33 and 4.98 GPa. The new phase was solved using the high-pressure data and remains as monoclinic $P2_1/c$. The cell parameters for the new phase (designated Form I') are: a = 13.149(8) Å, b = 3.4103(10) Å, c = 10.173(2) Å, β = 93.11(4) °. The quality of the diffraction pattern was not as good as the data before the transition however, it provided the molecular level detail of the changes over the phase transition. The new phase indicates a major structural rearrangement where molecules in every second layer of the chain rotate substantially causing a change to the environment of the pyridine ring (Figure 3.6), confirming the difference shown in the Raman spectra (Figure 3.2a). Figure 3.6c shows a comparison between the structure of Form I before the transition at 4.33 GPa and the new phase at 4.98 GPa. The structures have been superimposed to show the differences between the packing of the molecules. The Crystal Packing Similarity function in Mercury identified three molecules out of fifteen were in common with each other, with a root mean square of 0.422, signifying a substantial difference in structures.[33]

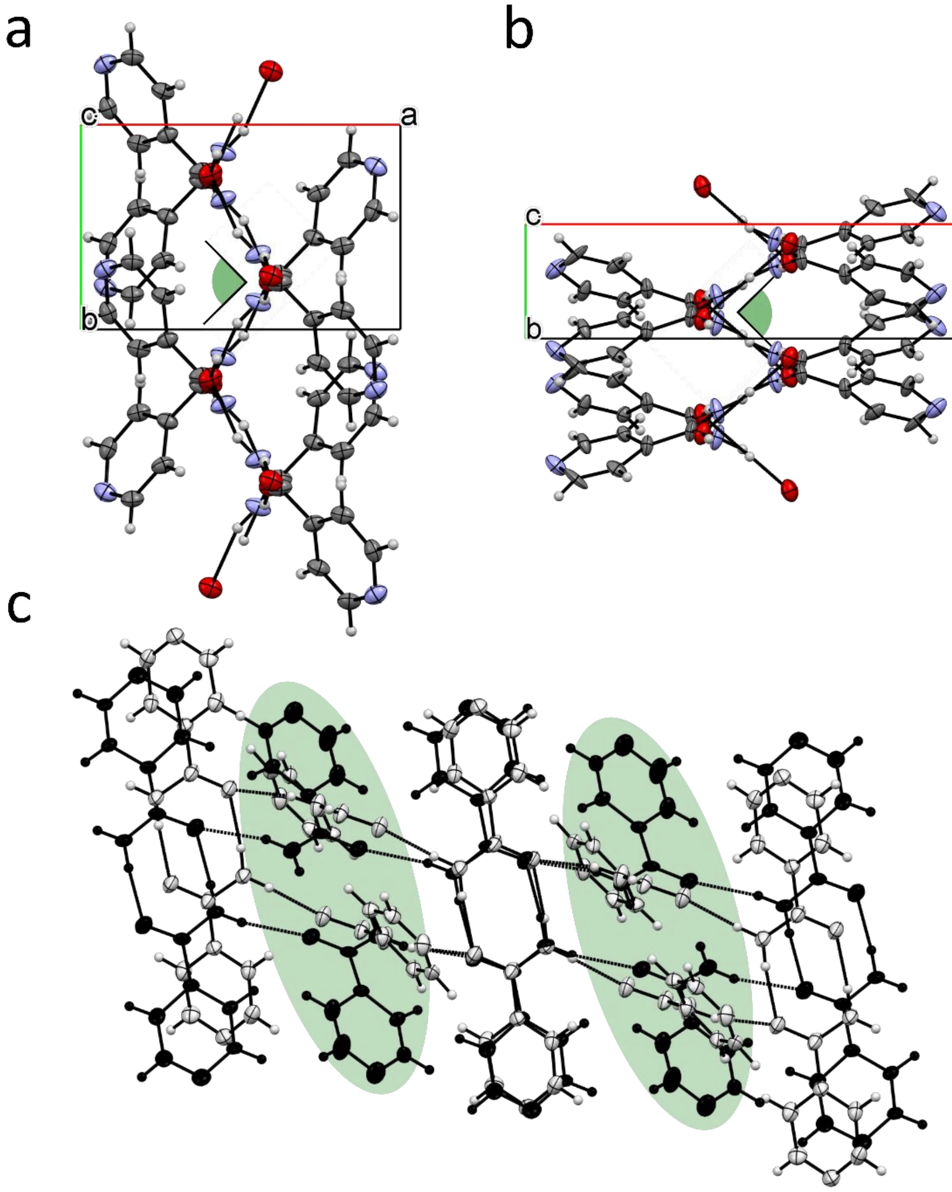

Figure 3.6: Crystal structures of isonicotinamide Form I and Form I’ are shown in Figures a) and b) respectively. The structures are shown looking down the crystallographic *c*-axis. Neighbouring dimers are rotated by 57.80° at 4.33 GPa and 59.16° after the transition. c) The structural difference between Form I at 4.33 GPa (grey) and the new phase at 4.98 GPa (black). The rotational differences in every other layer is highlighted in green.

To understand what has to happen to the structure to cause this change, a mechanism is proposed as detailed in Figure 3.7. On compression, the principle axis of strain, as calculated by PASCal,[34] indicates that greatest compression is predominantly between the *a*- and *c*-axis as shown by the indicatrix (Figure 3.7a) which corresponds to the direction perpendicular to the hydrogen bonded sheets (Figure 3.7b). From the perspective of the phase transition, this compression will affect the hydrogen-bonded chains and, in particular, the inter-dimer interactions. In Figure 3.7c and d, the orientation of the top and bottom dimers is maintained which enables the comparison between the orientations of the central sets of dimers. In Form I, the direction of interactions of the central dimers are into the plane of the page whilst in Form I' they are substantially more across the page. Moving over the transition, a lateral shift to the right of the upper dimer molecules relative to the bottom dimer is observed (indicated by the wire frame). It is speculated that this movement induces a rotation of the molecules in every second dimer that forces a change in hydrogen bonded partner for those molecules. The molecules highlighted in green rotate (about an axis though the N–C–O atoms of the molecule) and hydrogen bond to each other forming a new dimer. In Figure 3.7c and d, an orange and blue molecule rotate anticlockwise allowing the formation of a hydrogen bond between them; essentially swapping the hydrogen-bonding partners. This exchange of partners elongates the hydrogen-bonded network, hence extending the length of the crystal (Figure 3.8).

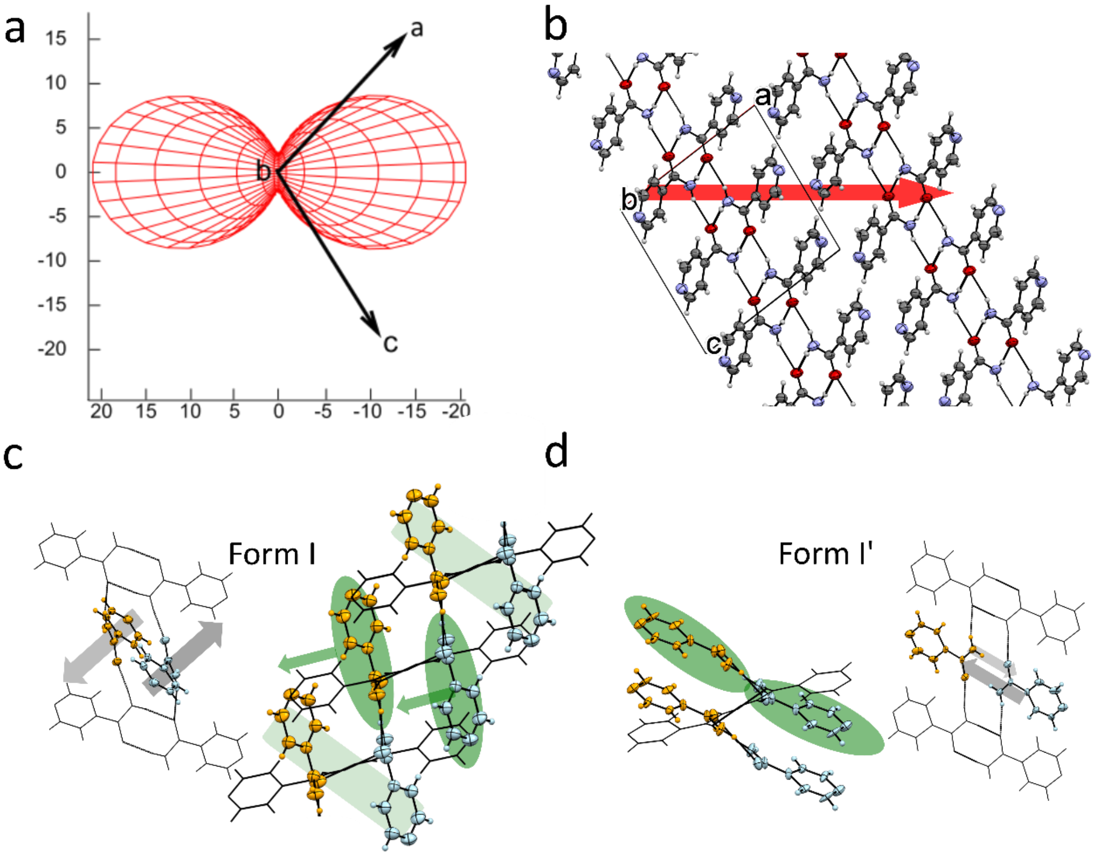

Figure 3.7: a) Compressibility of Form I isonicotinamide as calculated by PASCal. b) Compression occurs between the a- and c-axis. c & d) Structural differences between Form I and Form I' isonicotinamide at 4.33 and 4.98 GPa, respectively. The focus is on dimers coloured in blue and orange and their movement on compression to the new phase, as indicated by the green arrows. After the transition, molecules highlighted in green hydrogen bond to each other forming a new dimer. Grey arrows represent the direction of the dimer into and out of the plane of the paper.

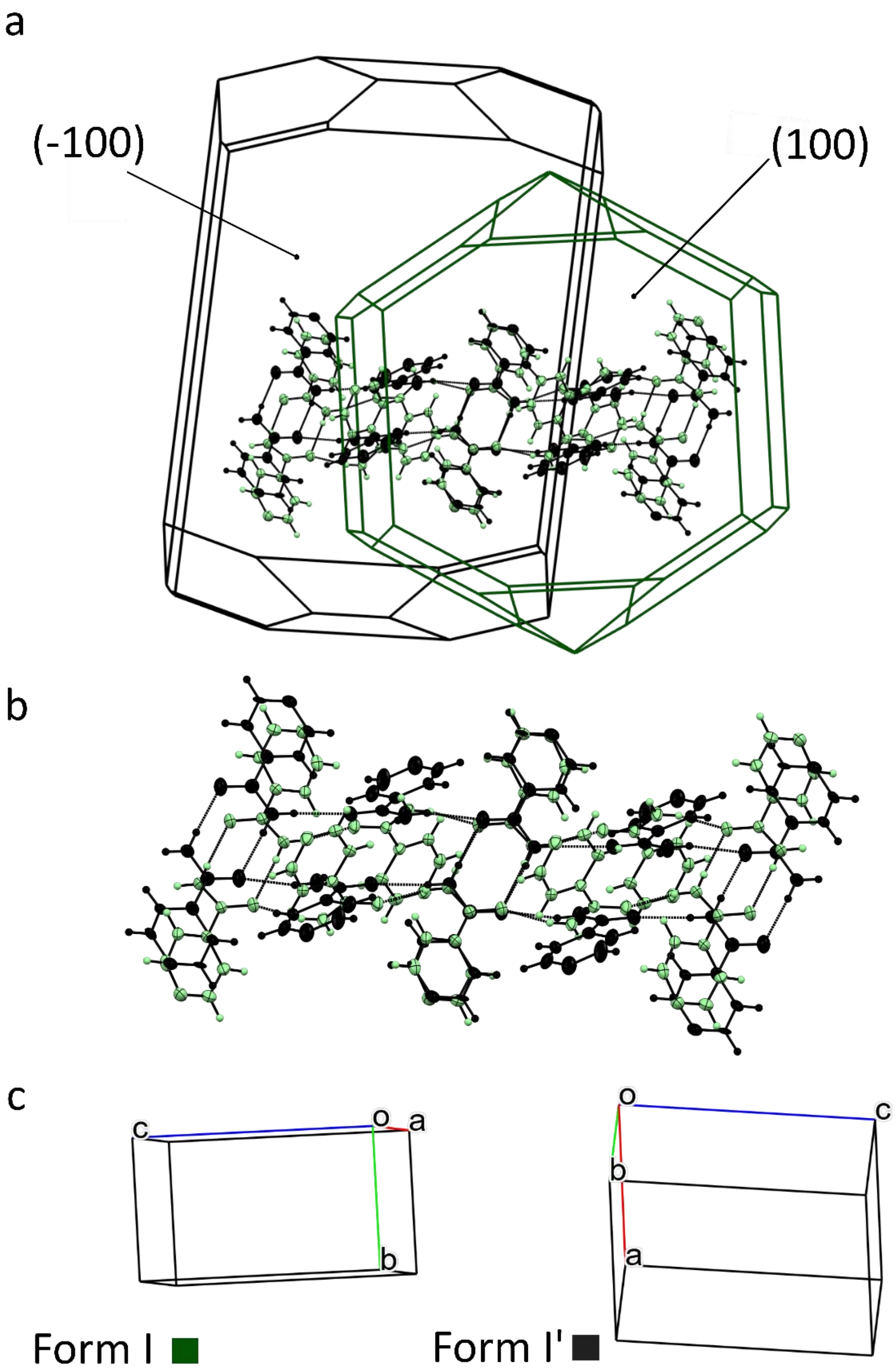

Figure 3.8: a) Bravais, Friedel, Donnay and Harker (BFDH) model of the crystal morphology of Form I isonicotinamide at 4.33 GPa (green) and Form I’ at 4.98 GPa (black), with b) crystal structures overlaid to show rotation of the molecules after the transition. c) Unit cell of isonicotinamide before and after the transition to indicate the relative orientation.

So, what instigates the change in the structure? Pixel calculations have been used to follow the changes in energy of different intermolecular interactions in the structures. A summary of the interaction energies at each pressure is detailed Appendix A (Table A2). In both Form I and I', isonicotinamide forms dimers that interact through the amide groups (N-H···O) and are positioned over an inversion centre.[14] This interaction is the strongest with a total energy of -62.4 kJmol^{-1} in Form I and -58.4 kJmol^{-1} in Form I' (Figure 3.9a, Table A3; Int.1). This reduction in favourability is due to the increased repulsion at these higher pressures. The dimers link through hydrogen bonds involving the second hydrogen of the amide to the oxygen of the neighbouring molecule to form chains in the structure along the *c*-axis and *b*-axis, respectively for Forms I and I' (Figure 3.9a, Table A3; Int 2). The dimers are rotated by 68.73° with respect to each other in Form I whilst this changes to be 74.99° in Form I'. Overall, the energy of these interactions are similar however the distribution of each of the terms changes to be slightly more dispersive in character that reflects the need for better packing to the detriment of hydrogen bonding (Table A3 in Appendix A).

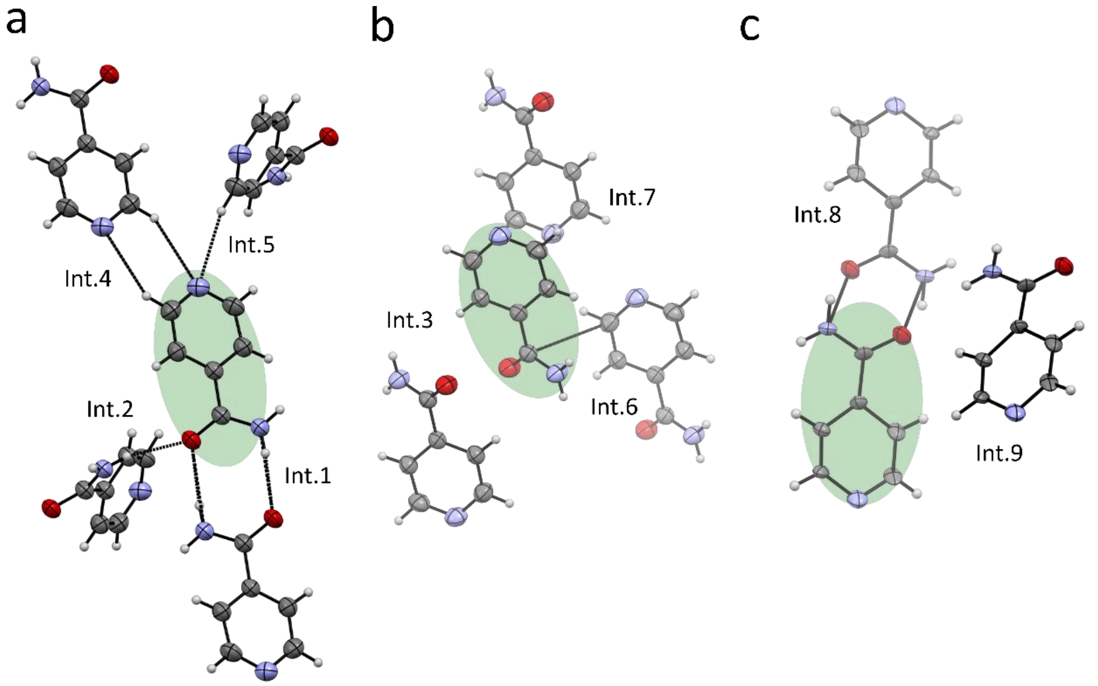

Figure 3.9: Highest energy interactions of a) Form I and Form I' isonicotinamide, b) Form I only and c) Form I' only as calculated by Pixel. The central molecule is highlighted in green. Depth cue is used to show difference in layers between central and interacting molecule.

In both forms, the interaction between the layers is via weaker hydrogen bonding through dispersive CH···N interactions. (Figure 3.9a, Table A3; Int. 4 and Int. 5) and it is here that a change in the interaction energies is observed, providing a clue to the phase transition. The pyridine dimer interaction (Int.4) provides some stability to the structure (-13.6 kJmol^{-1}), but this interaction becomes repulsive as pressure is applied such that the total energy is reduced to -10.4 kJmol^{-1}. Over the phase transition, a relieving of the repulsive energy contribution to this interaction is observed from 44.3 to 19.6 kJmol^{-1}, which is a significant change relative to the other intermolecular interactions present and is the result of better packing of the new phase. In addition to this, Interaction 5 also shows a considerable change in the repulsive contribution from 27.1 to 19 kJmol^{-1}. Therefore, it appears that these two interactions and the repulsion between the molecules causes this phase transition to occur but how does the crystal remains intact over the phase transition?

In solid-state polymerisation reactions, it has been speculated by Kaupp that the ability of a molecule to undergo a reaction is dependent the ability of the molecule to move in the crystal structure.[35] From void analysis of Form I isonicotinamide, observations can be made of where there is space for the molecules to move given a particular probe radius (0.5 Å) (Figure 3.10).[33] When viewed down the *b*-axis, the void space is between the pyridine moieties of the molecules. This is important because the location of these voids will facilitate the rotation of the molecules during the phase transformation. As with many observations of phase transitions at pressure,[36] the driver for the transition is the reduction in the volume of the solid which can be verified by the calculation of the Lattice enthalpy as a function of pressure (Figure 3.11). These data hint that the enthalpy ($H = U+pV$) is marginally lower than the trend of the enthalpies at lower pressures. This is subtle but these small changes in enthalpy have been observed in L-serine, with stabilisation of the high pressure phase caused by the reduction in volume upon reorientation of the hydroxyl groups and change in molecular orientation.[37]

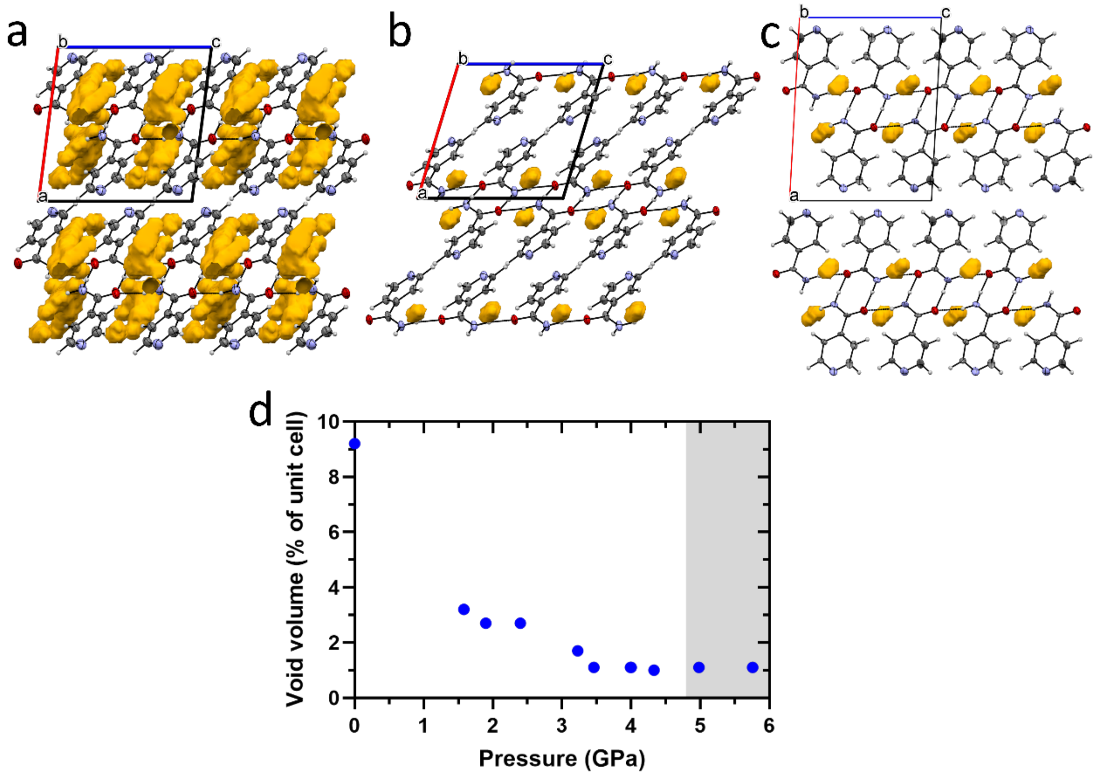

Figure 3.10: Void analysis of isonicotinamide Form I with a probe radius of 0.5 Å and approximate grid spacing of 0.2 Å at a) ambient pressure; b) 4.33 GPa and c) Form I' at 4.98 GPa. All structures are viewed down the b-axis. d) Void volume of isonicotinamide Form I and Form I' (highlighted in grey).

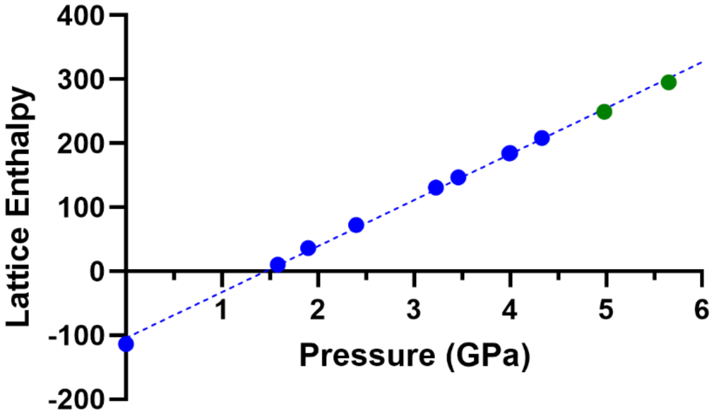

Figure 3.11: Enthalpy of Form I isonicotinamide and Form I' are shown in blue and green respectively, as a function of pressure. Enthalpy values (H) are calculated by $H = U + PV$, where U is the internal energy (kJ mol^{-1}), P is pressure (Pa) and V is the volume (m^3).

3.5 Conclusion

In conclusion, the reversible pressure-induced superelastic behaviour of the thermodynamically stable Form I isonicotinamide has been investigated. The crystal undergoes a single-crystal to single-crystal transition at 4.98 GPa that enabled the proposal of a possible molecular mechanism by which the transition occurs, rationalised using PIXEL calculations that provide intermolecular energies. This was accompanied by obvious elongation and contraction of the crystal dimensions at 4.98 GPa. This new polymorph has been designated Form I'. The transition between the two phases is reversible on decompression and the original crystal dimensions were restored. Comparison of the two structures showed that molecules in every second layer of the new polymorph are rotated, causing a lateral shift in molecules and elongation of the crystal. The nature of the hydrogen-bonding and void space in the crystal structure poses a question as to how universal a mechanism like this is. At the time of investigation there were five structures that possessed the necessary hydrogen bonding and packing that could exhibit pressure-induced superelastic behaviour, including the isostructural iota-form of nicotinamide.[38] Despite exceeding a practically relevant pressure regime, the insights provided here may, in the future, be used to design organic solids through crystal engineering to exhibit superelastic properties.

3.6 References

1. Naumov, P.; Karothu, D. P.; Ahmed, E.; Catalano, L.; Commins, P.; Mahmoud Halabi, J.; Al-Handawi, M. B.; Li, L. The Rise of the Dynamic Crystals. In *Journal of the American Chemical Society*, American Chemical Society: 2020; Vol. 142, pp 13256-13272.

2. Chung, H.; Dudenko, D.; Zhang, F.; D'Avino, G.; Ruzié, C.; Richard, A.; Schweicher, G.; Cornil, J.; Beljonne, D.; Geerts, Y.; et al. Rotator side chains trigger cooperative transition for shape and function memory effect in organic semiconductors. In *Nature Communications*, 2018; Vol. 9, p 278.

3. Li, L.; Commins, P.; Al-Handawi, M. B.; Karothu, D. P.; Halabi, J. M.; Schramm, S.; Weston, J.; Rezgui, R.; Naumov, P. Martensitic organic crystals as soft actuators. In *Chem. Sci.*, The Royal Society of Chemistry: 2019; Vol. 10, pp 7327-7332.

4. Panda, M. K.; Runčevski, T.; Chandra Sahoo, S.; Belik, A. A.; Nath, N. K.; Dinnebier, R. E.; Naumov, P. Colossal positive and negative thermal expansion and thermosalient effect in a pentamorphic organometallic martensite. In *Nature Communications*, 2014; Vol. 5, p 4811. Panda, M. K.; Runčevski, T.; Husain, A.; Dinnebier, R. E.; Naumov, P. Perpetually Self-Propelling Chiral Single Crystals. In *Journal of the American Chemical Society*, American Chemical Society: 2015; Vol. 137, pp 1895-1902.

5. Liu, G.; Liu, J.; Liu, Y.; Tao, X. Oriented Single-Crystal-to-Single-Crystal Phase Transition with Dramatic Changes in the Dimensions of Crystals. In *Journal of the American Chemical Society*, American Chemical Society: 2014; Vol. 136, pp 590-593.

6. Funnell, N. P.; Dawson, A.; Marshall, W. G.; Parsons, S. Destabilisation of hydrogen bonding and the phase stability of aniline at high pressure. In *CrystEngComm*, The Royal Society of Chemistry: 2013; Vol. 15, pp 1047-1060. Yan, T.; Xi, D.; Ma, Z.; Wang, X.; Wang, Q.; Li, Q. Pressure-induced phase transition in N–H···O hydrogen-bonded crystalline malonamide. In *RSC Advances*, The Royal Society of Chemistry: 2017; Vol. 7, pp 22105-22111.

7. Yan, T.; Wang, K.; Duan, D.; Tan, X.; Liu, B.; Zou, B. p-Aminobenzoic acid polymorphs under high pressures. In *RSC Adv.*, The Royal Society of Chemistry: 2014; Vol. 4, pp 15534-15541. Nobrega, M. M.; Temperini, M. L. A.; Bini, R. Probing the Chemical Stability of Aniline under High Pressure. In *The Journal of Physical Chemistry C*, American Chemical Society: 2017; Vol. 121, pp 7495-7501.

8. Takamizawa, S.; Takasaki, Y. Shape-memory effect in an organosuperelastic crystal. In *Chemical Science*, The Royal Society of Chemistry: 2016; Vol. 7, pp 1527-1534.

9. Yu, Q.; Yan, Z.; Bao, J.; Wang, J.-R.; Mei, X. Taming photo-induced oxidation degradation of dihydropyridine drugs through cocrystallization. In *Chemical Communications*, The Royal Society of Chemistry: 2017; Vol. 53, pp 12266-12269.

10. Groom, C. R.; Bruno, I. J.; Lightfoot, M. P.; Ward, S. C. The Cambridge Structural Database. In *Acta Crystallographica Section B*, 2016; Vol. 72, pp 171-179.

11. Aakeröy, C. B.; Beatty, A. M.; Helfrich, B. A.; Nieuwenhuyzen, M. Do Polymorphic Compounds Make Good Cocrystallizing Agents? A Structural Case Study that Demonstrates the Importance of Synthon Flexibility. In *Crystal Growth & Design*, American Chemical Society: 2003; Vol. 3, pp 159-165.

12. Li, J.; Bourne, S. A.; Caira, M. R. New polymorphs of isonicotinamide and nicotinamide. In *Chemical Communications*, The Royal Society of Chemistry: 2011; Vol. 47, pp 1530-1532. Eccles, K. S.; Deasy, R. E.; Fábián, L.; Braun, D. E.; Maguire, A. R.; Lawrence, S. E. Expanding the crystal landscape of isonicotinamide: concomitant polymorphism and co-crystallisation. In *CrystEngComm*, The Royal Society of Chemistry: 2011; Vol. 13, pp 6923-6925. Vicatos, A. I.; Caira, M. R. A new

polymorph of the common coformer isonicotinamide. In *CrystEngComm*, The Royal Society of Chemistry: 2019; Vol. 21, pp 843-849.
13. Tateiwa, N.; Haga, Y. Evaluations of pressure-transmitting media for cryogenic experiments with diamond anvil cell. In *Review of Scientific Instruments*, American Institute of Physics: 2009; Vol. 80, p 123901.
14. Piermarini, G. J.; Block, S.; Barnett, J. D.; Forman, R. A. Calibration of the pressure dependence of the R1 ruby fluorescence line to 195 kbar. In *Journal of Applied Physics*, American Institute of Physics: 1975; Vol. 46, pp 2774-2780.
15. Inc., B. A. *SAINT*; 2017. Inc., B. A. *APEX3*; 2018.
16. Sheldrick, G. M. *SADABS, Program for Absorption Correction for Data from Area Detector Frames*; 2008.
17. Dolomanov, O. V.; Bourhis, L. J.; Gildea, R. J.; Howard, J. A. K.; Puschmann, H. OLEX2: A complete structure solution, refinement and analysis program. In *Journal of Applied Crystallography*, 2009; Vol. 42, pp 339-341.
18. Delley, B. An all-electron numerical method for solving the local density functional for polyatomic molecules. In *The Journal of Chemical Physics*, American Institute of Physics: 1990; Vol. 92, pp 508-517.
19. Software, A. *In Materials Studio Release Notes*; 2011.
20. Perdew, J. P.; Chevary, J. A.; Vosko, S. H.; Jackson, K. A.; Pederson, M. R.; Singh, D. J.; Fiolhais, C. Atoms, molecules, solids, and surfaces: Applications of the generalized gradient approximation for exchange and correlation. In *Physical Review B*, American Physical Society: 1992; Vol. 46, pp 6671-6687.
21. Tkatchenko, A.; Scheffler, M. Accurate Molecular Van Der Waals Interactions from Ground-State Electron Density and Free-Atom Reference Data. In *Physical Review Letters*, American Physical Society: 2009; Vol. 102, p 73005.
22. Delori, A.; Hutchison, I. B.; Bull, C. L.; Funnell, N. P.; Urquhart, A. J.; Oswald, I. D. H. Reaction of Acetylenedicarboxylic Acid Made Easy: High-Pressure Route for Polymerization. In *Crystal Growth & Design*, American Chemical Society: 2018; Vol. 18, pp 1425-1431. Marshall, W. G.; Urquhart, A. J.; Oswald, I. D. H. Investigation of Methacrylic Acid at High Pressure Using Neutron Diffraction. In *Journal of Physical Chemistry B*, 2015; Vol. 119, pp 12147-12154. Johnston, B. F.; Marshall, W. G.; Parsons, S.; Urquhart, A. J.; Oswald, I. D. H. Investigation of Acrylic Acid at High Pressure Using Neutron Diffraction. In *The Journal of Physical Chemistry B*, American Chemical Society: 2014; Vol. 118, pp 4044-4051.
23. Monkhorst, H. J.; Pack, J. D. Special points for Brillouin-zone integrations. In *Physical Review B*, American Physical Society: 1976; Vol. 13, pp 5188-5192.
24. Reeves, M. G.; Wood, P. A.; Parsons, S. MrPIXEL: Automated execution of Pixel calculations via the Mercury interface. In *Journal of Applied Crystallography*, 2020; Vol. 53, pp 1154-1162. Gavezzotti, A. Calculation of lattice energies of organic crystals: the PIXEL integration method in comparison with more traditional methods. In *Zeitschrift für Kristallographie - Crystalline Materials*, 2005; Vol. 220, pp 499-510. Gavezzotti, A. Molecular Aggregation: Structure Analysis and Molecular Simulation of Crystals and Liquids. Oxford University Press: Oxford, UK, 2007. Gavezzotti, A. Efficient computer modeling of organic materials. The atom–atom, Coulomb–London–Pauli (AA-CLP) model for intermolecular electrostatic-polarization, dispersion and repulsion energies. In *New Journal of Chemistry*, The Royal Society of Chemistry: 2011; Vol. 35, pp 1360-1368. Maschio, L.; Civalleri, B.; Ugliengo, P.; Gavezzotti, A. Intermolecular Interaction Energies in Molecular Crystals: Comparison and Agreement of Localized Møller–Plesset 2, Dispersion-Corrected Density Functional, and Classical Empirical Two-Body Calculations. In *The Journal of Physical Chemistry A*, American Chemical Society: 2011; Vol. 115, pp 11179-11186.

25. Frisch, M. J.; Trucks, G. W.; Schlegel, H. B.; Scuseria, G. E.; Robb, M. A.; Cheeseman, J. R.; Scalmani, G.; Barone, V.; Mennucci, B.; Petersson, G. A.; et al. *Gaussian 09W, Revision C.01*; 2009.
26. Macrae, C. F.; Bruno, I. J.; Chisholm, J. A.; Edgington, P. R.; McCabe, P.; Pidcock, E.; Rodriguez-Monge, L.; Taylor, R.; Van De Streek, J.; Wood, P. A. Mercury CSD 2.0 - New features for the visualization and investigation of crystal structures. In *Journal of Applied Crystallography*, 2008; Vol. 41, pp 466-470.
27. Takamizawa, S.; Takasaki, Y. Superelastic Shape Recovery of Mechanically Twinned 3,5-Difluorobenzoic Acid Crystals. In *Angewandte Chemie International Edition*, John Wiley & Sons, Ltd: 2015; Vol. 54, pp 4815-4817. Sasaki, T.; Sakamoto, S.; Takamizawa, S. Twinning-Based Organosuperelasticity and Chirality in a Single Crystal of an Achiral Donor–Acceptor Type Schiff Base Induced by Charge-Transfer Interactions. In *Crystal Growth & Design*, American Chemical Society: 2020; Vol. 20, pp 8079-8083. Engel, E. R.; Takamizawa, S. Versatile Ferroelastic Deformability in an Organic Single Crystal by Twinning about a Molecular Zone Axis. In *Angewandte Chemie International Edition*, John Wiley & Sons, Ltd: 2018; Vol. 57, pp 11888-11892. Panda, M. K.; Ghosh, S.; Yasuda, N.; Moriwaki, T.; Mukherjee, G. D.; Reddy, C. M.; Naumov, P. Spatially resolved analysis of short-range structure perturbations in a plastically bent molecular crystal. In *Nature Chemistry*, 2015; Vol. 7, pp 65-72. Sasaki, T.; Sakamoto, S.; Takasaki, Y.; Takamizawa, S. A Multidirectional Superelastic Organic Crystal by Versatile Ferroelastical Manipulation. In *Angewandte Chemie International Edition*, John Wiley & Sons, Ltd: 2020; Vol. 59, pp 4340-4343. Sakamoto, S.; Sasaki, T.; Sato-Tomita, A.; Takamizawa, S. Shape Rememorization of an Organosuperelastic Crystal through Superelasticity–Ferroelasticity Interconversion. In *Angewandte Chemie International Edition*, John Wiley & Sons, Ltd: 2019; Vol. 58, pp 13722-13726.
28. Bakiler, M.; Bolukbasi, O.; Yilmaz, A. An experimental and theoretical study of vibrational spectra of picolinamide, nicotinamide, and isonicotinamide. In *Journal of Molecular Structure*, 2007; Vol. 826, pp 6-16. Castro, J. L.; Arenas, J. F.; Lopez-Ramirez, M. R.; Soto, J.; Otero, J. C. Surface-enhanced Raman scattering of picolinamide, nicotinamide, and isonicotinamide: Unusual carboxamide deprotonation under adsorption on silver nanoparticles. In *Journal of Colloid and Interface Science*, 2013; Vol. 396, pp 95-100.
29. Takamizawa, S.; Miyamoto, Y. Superelastic Organic Crystals. In *Angewandte Chemie International Edition*, John Wiley & Sons, Ltd: 2014; Vol. 53, pp 6970-6973.
30. Sharma, B. B.; Murli, C.; Sharma, S. M. Hydrogen bonds and polymerization in acrylamide under pressure. In *Journal of Raman Spectroscopy*, John Wiley & Sons, Ltd: 2013; Vol. 44, pp 785-790.
31. Cruz-Cabeza, A. J.; Davey, R. J.; Oswald, I. D. H.; Ward, M. R.; Sugden, I. J. Polymorphism in p-aminobenzoic acid. In *CrystEngComm*, The Royal Society of Chemistry: 2019; Vol. 21, pp 2034-2042.
32. Angel, R.; Gonzalez-Platas, J.; Alvaro, M. EosFit7c and a Fortran module (library) for equation of state calculations. In *Zeitschrift für Kristallographie - Crystalline Materials*, 2014; Vol. 229, pp 405-419.
33. Macrae, C. F.; Sovago, I.; Cottrell, S. J.; Galek, P. T. A.; McCabe, P.; Pidcock, E.; Platings, M.; Shields, G. P.; Stevens, J. S.; Towler, M.; et al. Mercury 4.0: from visualization to analysis, design and prediction. In *Journal of applied crystallography*, 2020; Vol. 53, pp 226-235.
34. Cliffe, M. J.; Goodwin, A. L. PASCal: A principal axis strain calculator for thermal expansion and compressibility determination. In *Journal of Applied Crystallography*, 2012; Vol. 45, pp 1321-1329.

35. Kaupp, G.; Naimi-Jamal, M. R. Mechanically induced molecular migrations in molecular crystals. In *CrystEngComm*, The Royal Society of Chemistry: 2005; Vol. 7, pp 402-410.
36. Ostrowska, K.; Kropidłowska, M.; Katrusiak, A. High-Pressure Crystallization and Structural Transformations in Compressed R,S-Ibuprofen. In *Crystal Growth & Design*, American Chemical Society: 2015; Vol. 15, pp 1512-1517. Giordano, N.; Beavers, C. M.; Kamenev, K. V.; Marshall, W. G.; Moggach, S. A.; Patterson, S. D.; Teat, S. J.; Warren, J. E.; Wood, P. A.; Parsons, S. High-pressure polymorphism in l-threonine between ambient pressure and 22 GPa. In *CrystEngComm*, The Royal Society of Chemistry: 2019; Vol. 21, pp 4444-4456. Novelli, G.; Maynard-Casely, H. E.; McIntyre, G. J.; Warren, M. R.; Parsons, S. Effect of High Pressure on the Crystal Structures of Polymorphs of l-Histidine. In *Crystal Growth & Design*, American Chemical Society: 2020; Vol. 20, pp 7788-7804. Tan, X.; Wang, K.; Li, S.; Yuan, H.; Yan, T.; Liu, J.; Yang, K.; Liu, B.; Zou, G.; Zou, B. Exploration of the Pyrazinamide Polymorphism at High Pressure. In *The Journal of Physical Chemistry B*, American Chemical Society: 2012; Vol. 116, pp 14441-14450. Oswald, I. D. H.; Lennie, A. R.; Pulham, C. R.; Shankland, K. High-pressure structural studies of the pharmaceutical, chlorothiazide. In *CrystEngComm*, The Royal Society of Chemistry: 2010; Vol. 12, pp 2533-2540.
37. Moggach, S. A.; Parsons, S.; Wood, P. A. High-pressure polymorphism in amino acids. In *Crystallography Reviews*, Taylor & Francis: 2008; Vol. 14, pp 143-184.
38. Li, X.; Ou, X.; Wang, B.; Rong, H.; Wang, B.; Chang, C.; Shi, B.; Yu, L.; Lu, M. Rich polymorphism in nicotinamide revealed by melt crystallization and crystal structure prediction. In *Communications Chemistry*, 2020; Vol. 3, p 152. Skelton, B. W.; Pakawatchai, C.; White, A. H. Experimental Crystal Structure Determination. In *CSD Communication*, 2017; Vol. CCDC 64266. Kennedy, A. R. Experimental Crystal Structure Determination. In *CSD Communication*, 2017; Vol. CCDC 15768. Cohen-Addad, C.; Cohen-Addad, J.-P. Crystal structure of isobutyramide and comparison with its conformation in chloroform solution as observed from lanthanide-induced nuclear magnetic resonance shifts. In *Journal of the Chemical Society, Perkin Transactions 2*, The Royal Society of Chemistry: 1978; pp 168-171.

Chapter 4

Compression of isonicotinamide continued – Forms II, III and IV

4 Compression of isonicotinamide continued – Forms II, III and IV

4.1 Abstract

It is vital to understand the polymorphism of compounds used within the pharmaceutical industry. Many formulation methods involve the use of solvents, heat, or compaction, all of which could induce a phase transition of the drug. Investigating the behaviour of polymorphic systems could prevent an unwanted phase transition prior to manufacture into a medicinal product. Following on from Chapter III, this study uses pressure to investigate the metastable polymorphs of isonicotinamide and compares with Form I isonicotinamide. Forms II, III and IV isonicotinamide were exposed to hydrostatic conditions in a Diamond Anvil Cell (DAC) and compressed to 1.61, 4.27 and 2.01 GPa respectively. All the polymorphs are layered structures and exhibit the greatest compression perpendicular to these. A single-crystal-to-single-crystal phase transition was observed for Form II at 1.49 GPa, with a change in symmetry from monoclinic $P2_1/c$ to triclinic $P1$ (Z’ = 4 to Z’ = 8) due to a significant movement in the layers with respect to one another. Form III isonicotinamide remained stable up to a pressure of 4.27 GPa, beyond which the quality of the X-ray diffraction data deteriorated. An additional hydrogen bond provided the structure with flexibility during the compression of Form III, allowing for molecules to rotate into the void space and providing an additional element of stability. X-ray Diffraction and Raman spectroscopy of Form IV indicates that a phase transition occurred between 2.01 and 2.70 GPa, where the diffraction pattern deteriorates significantly with the vibrational spectra indicating a change in the environment of the pyridine ring.

4.2 Introduction

Polymorphism is a concept defined by crystals with identical molecular compositions but different crystalline structures, which in turn alters the physicochemical properties of the solid. Pressure is a valuable tool to explore polymorphism in small organic molecules, whether using it to investigate conformational changes between ambient and high-pressure structures of a compound or how a series of polymorphs react to pressure. The advantage to investigating polymorphs of a compound is that the molecule remains the same (albeit that there may be some subtle conformational changes) but the hydrogen-bonding and packing of the materials is different so that these elements of intermolecular interactions can be evaluated. For example, polymorphs of pyrazinamide exhibit different hydrogen-bonding. The α, β and δ polymorphs all exhibit dimeric structures (as with Form I isonicotinamide). α is composed of ribbons of pyrazinamide molecules, which are positioned planar with respect to one another. Neighbouring ribbons are not connected, with pyrimidine rings lying at 43 ° angle, repeating along the c-axis. The structure of the β form resembles that of Form I isonicotinamide. Consecutive dimer pairs interact via the amide functionality, with every other dimer rotated by 49.5 °, which Tan *et al.,* explains facilitates closer packing of the molecules in comparison to the alpha form. δ also forms dimers of pyrazinamide molecules through head-to-head hydrogen bonds via the amide. Chains form between the dimer pairs via bonding between pyrimidine groups, extending perpendicular to the *ac*-direction. γ is the only polymorph to exhibit head-to-tail hydrogen bonding, forming layers of molecules. Every other molecule is rotated by 49.3 °, forming pleated sheets that extend parallel to the *c*- and *a*-axis, stacking perpendicular the *b*-axis. At high pressure, the α and δ forms are resistant to any phase transitions on compression up to 13 GPa, with the α polymorph becoming amorphous at 13.2 GPa. The amorphisation of the α polymorph was attributed to the molecules rotating, distorting the hydrogen bonds to achieve closer packing. The δ-polymorph remained crystalline to 13 GPa, *ca.* 3 GPa beyond the pressure limit of the methanol: ethanol (4:1) used as the pressure transmitting medium.[1] The flat nature of the layered structure allowed for compression up to the high-pressure without destruction of the sample. XRPD examination during the compression of the γ polymorph showed the onset of transition from *ca.* 4 GPa, with completion at 8 GPa. The high-pressure phase was confirmed to be the β polymorph of pyrazinamide. Although the two polymorphs have different hydrogen bonding motifs, they are structurally similar enabling the transition to occur. Compression of the γ phase, caused rotation of the molecules and reconstruction of hydrogen bonds to form the dimer motif of the β form.[2] Interestingly, the beta form is only known to exist in the presence of the gamma form, at a ratio of 80:20 respectively, from 1,4-dioxane and toluene and chloroform mixtures.[3] This study demonstrates the impact of the type of hydrogen-bonding patterns on the ability of a material to undergo a transition or not. From the perspective of industrial processes, it is important to know how pharmaceutical compounds react on compression, as localised pressure can be applied to pharmaceuticals during their formulation i.e., milling and tabletting so that potential phase transitions in materials can be circumvented or explored in more detail. Paracetamol is a typical example where the packing of the materials has a significant impact on the compaction properties.[4] Form I is the thermodynamically stable form at ambient conditions and is therefore the polymorph of paracetamol found in commercially available formulations of the drug.[5] With this being said, the structure of Form I hinders its ability to be directly compressed into tablets, requiring the use of additives during a wet granulation process, prior to tabletting. Form II, however, exhibits plastic deformation and can be directly compressed into a tablet without the use of further excipients.[6] Compaction of Form I pellets led to them breaking upon impact, whilst Form II pellets remained intact.[7] The differences here are attributed to the presence of the slip planes perpendicular to the *c*-axis in Form II and their absence in Form I. The behaviour of other polymorphic systems under pressure includes piracetam,[8] L-serine,[9] L-histidine,[10] and pyridine[11] indicate that even simple polymorphic materials can exhibit a wide variety of behaviour under pressure.

The overall aim of this PhD is to understand the crystallisation behaviour of pharmaceutical compounds confined within porous materials after loading under ambient and elevated pressures. As part of this process, isonicotinamide was selected as the small molecule candidate. Isonicotinamide is a well characterised small organic molecule widely used in crystallisation and solid-state research: nucleation[12], polymorphism,[13-16] and co-crystallisation.[17] It is a model compound, providing a wide range of information regarding its solid-state behaviour in the unconfined state, making it a suitable candidate for investigation of confinement of organic materials. A solvent mediated method will be used to load isonicotinamide into porous material and could prove challenging due to the uncertainty as to which polymorph would crystallise out. The secondary studies loading under high pressure conditions will add a further dimension to this study. Therefore, it is vital to understand the behaviour of these compounds in their unconfined state under a range of pressure conditions to follow unit cell parameters (that may indicate local pressures with pores) or to elucidate any changes that may occur and characterise the new phases.

Isonicotinamide has 6 known polymorphs, each reported to be crystallised from different solvents using an array of crystallisation methods. Research by Aakeröy *et al.,* reported Form I (monoclinic, $P2_1/c$) to be recrystallised from nitromethane or nitrobenzene whilst Form II (monoclinic $P2_1/c$) crystallised from ethanol, water, tetrahydrofuran and dioxane.[13] Later, Form III isonicotinamide (orthorhombic, *Pbca*) was crystallised from a slow cooling crystallisation experiment in chloroform.[14] More recently, evaporation from acetone led to the concomitant crystallisation of Forms IV and V (monoclinic, Pc and $P2_1/c$ respectively), along with Forms I and II.[15] One of the interesting characteristics of this model compound is the difference in the hydrogen-bonding of the different forms. As discussed in Chapter 3, the thermodynamically stable polymorph Form I crystallises with a dimer motif that enables the cohesive molecular movement and culminates in a macroscopic, superelastic change in the crystal. Forms II to VI possess a catemeric hydrogen bonding motif where the hydrogen bonding is between the amide and pyridine moieties. All of these forms possess a layered structure but there are differences in the way in which these layers interact with one another.

In this chapter, the packing and effect of three polymorphs will be individually explored: Forms II, III and IV, through Raman spectroscopy and X-ray diffraction techniques. Energy calculations were performed using PIXEL software to gain an in-depth understanding of how the intermolecular interactions in Form II isonicotinamide react to compression. Finally, a comparison will be made on how the structure of each polymorph respond to the external stimuli.

4.3 Experimental

4.3.1 Crystal formation

Isonicotinamide was purchased from Sigma Aldrich (99% purity).

Form II was crystallised from an acetone solution (54.1 mg/mL), via a cooling crystallisation method. Isonicotinamide was dissolved in acetone at 50 °C until no visible material was present. The solution was left to cool to ambient temperature until crystals were observed.

Excess liquor was removed from the vial, leaving a layer to prevent the crystals from drying out until crystals were analysed using single-crystal X-ray diffraction. Storing the crystals in excess solution has been observed to lead to the transition to Form I isonicotinamide after several days.

Form III was crystallised from a solution of isonicotinamide in chloroform (2.5 mg/mL, anhydrous ≥99%) at 22 °C. The solution was stirred until all the solid was dissolved before filtering the solution into a clean vial using PTFE syringe filter (0.2 μm). The lid of the vial was pierced 5 times with a 21-gauge needle and solution left to evaporate in a fumehood. Colourless, lathe crystals were produced on slow evaporation of the solvent over three days.

Form IV was also crystallised from a chloroform solution (19 mg/mL) by heating at 45 °C, whilst being magnetically stirred for 10 minutes. The hot solution was filtered using a PTFE syringe filter (0.2 μm) and cooled from 45 to 10 °C over 36 hours using a Lauda Eco 630 cooling thermostat to control the temperature of samples.

Isonicotinamide suffers from concomitant polymorphism hence for each polymorph, crystals were characterised using single-crystal X-ray diffraction and Raman spectroscopy before individually loading into a diamond anvil cell. Despite following literature procedures, the resulting solids were largely mixed phase. The method used to crystallise Form IV isonicotinamide also crystallised Form I, II and III; identification of the polymorphs by crystal habit was impossible due to the polymorphs possessing similar morphology.

4.3.2 Diamond anvil cell

Merrill-Bassett diamond anvil cells (DAC) were used to apply pressure to single crystals of isonicotinamide during the X-ray and Raman studies. A tungsten foil gasket (99.95 %, Hollinbrow, Telford, UK) was placed between two diamonds with 600 µm culets.

The gasket, 250 µm in thickness, was pre-indented to approximately 100 µm before a 250 µm hole was drilled through the foil to serve as a sample chamber. Petroleum ether (PET 35/60, Alfa Aesar) was used as the hydrostatic medium.[18] The pressure of the cell was monitored using fluorescent R-line of crushed ruby spheres within the chamber of the cell, compared to those at ambient pressure.[19]

4.3.3 Single-crystal X-ray diffraction

Single crystal X-ray diffraction data were collected for Form II and Form IV ambient crystals using a Bruker D8 Venture diffractometer with a Photon II CCD detector and Incoatec IµS microfocus Cu X-ray source (Kα1 λ = 1.54178 Å). Data were reduced using SAINT within the Apex3 suite of software.[20] SADABS was used to correct for absorption.[21] OLEX2 v1.2 software was used to refine the structures using EHOWIH02 and EHOWIH04 coordinates as the starting models and ensure the atom labels were consistent between datasets.[13, 22, 23] The ambient structure of Form III isonicotinamide (EHOWIH03) was collected on a Bruker Kappa APEX II with IµS Microfocus Source (Mo Kα1 – 0.71073Å) and APEX II CCD detector. Data were reduced using similar procedures as above.

High pressure diffraction data were collected using Bruker APEX-II diffractometer with Incoatec IµS microfocus Mo X-ray source (Kα1 λ = 0.71073 Å) and CCD detector. Data were reduced using SAINT within APEX3 using the dynamic masking procedures.[20] SADABS was used for absorption correction.[21] The structures were refined in OLEX2 v1.2.[22] Refinement against the pressure data was conducted using the coordinates of each ambient polymorph, collected from the CSD (ref codes: EHOWIH02, EHOWIH03 and EHOWIH04 for Form II, III and IV respectively).[13-15, 23] The refined atomic coordinates at each pressure were used as the input for each subsequent dataset. Non-hydrogen atoms were treated using anisotropic displacement parameters. RIGU restraints were applied to all non-hydrogen atoms.

7 data sets were collected for Form II between 0.39 and 1.61 GPa using two different crystals. Crystal 1 was collected at 0.39, 0.50, 0.94 and 1.61 GPa. At 1.61 GPa the crystal deteriorated; therefore, a new crystal was loaded, and data taken at 0.78, 1.09 and 1.49 GPa. Crystallographic data for Form II can be found in Appendix B, Table B1.

One crystal was used to collect data on Form III isonicotinamide at seven pressure points: 1.40, 2.28, 2.64, 3.01, 4.08, 4.20 and 4.27 GPa. Crystallographic data for Form III is found in Appendix B, Table B5.

7 data sets were collected for Form IV using three different crystals. Crystal 1 was collected at 0.35 GPa. Due to deterioration of crystal I, a second crystal was collected at 0.77, 1.24, 1.40, 1.62 and 2.01 GPa. A third crystal was collected at 0.91 GPa. Crystallographic data for Form IV isonicotinamide is displayed in Table B6 in Appendix B.

4.3.4 Raman spectroscopy

Raman spectra were collected using a Horiba Scientific Raman XploRA™ PLUS microscope with a 523 nm laser source. Acquisition parameters including accumulation, acquisition time, grating, slit, and hole were varied to maximise the signal for each data collection. Raman spectra were taken in the region of 50 to 3500 cm^{-1}. The diamond peak at 1300-1350 cm^{-1} is omitted for clarity.

4.3.5 Pixel

Pixel calculations were performed on each Form II isonicotinamide dataset from ambient to 1.61 GPa using the MrPIXEL v3.1 program.[24] MrPIXEL facilitates the use of Pixel, developed by Gavezzotti,[25] using the Mercury interface.[34] Molecular electron densities were calculated using Gaussian09W at the B3LYP/6-31G** level.[26] The condensation level was set to 4 and cluster radius was 14 Å. Pixel calculations were only conducted for all Form II datasets and the ambient dataset of Form III isonicotinamide. Interactions in the first molecular coordination sphere of Form II from ambient to 1.09 GPa are displayed in Table B2 in Appendix B. The most energetic intermolecular interactions of Form II are displayed in Table B3. in Appendix B and relationship between molecular pairs visualised using Mercury (Figure 4.2a and b).[26]

4.4 Results and Discussion

This study follows on from Chapter 3 - "Pressure-induced superelastic behaviour of isonicotinamide". Here, the structural changes of Form II, Form III, and Form IV isonicotinamide are investigated using pressure. These polymorphs of isonicotinamide have chain structures, with head-to-tail synthons (NH···O), opposed to thermodynamically stable Form I, which forms dimers between the amide moieties. As highlighted in pyrazinamide example, the dimer or chain hydrogen pattern can have an impact on the behaviour of the solid which was the rationale behind investigating these polymorphs together.[2]

4.4.1 Form II isonicotinamide

Form II is the second reported polymorph of isonicotinamide and crystallises in $P2_1/c$.[13] It has two molecules in the asymmetric unit, which form two independent chains of symmetry equivalent molecules, aligned in a head-to-tail orientation along the *b*-axis, via NH···N hydrogen bonds (Figure 4.1). Noticeably, hydrogen bonds between molecules in Form II involve the pyridine ring, as well as the amide functionality (Figure 4.1a). This interaction between molecules is the most stable within the structure, as calculated by Pixel, with the interaction having an overall energy of -33.1 and -33.5 kJmol^{-1} for molecules A and B respectively (Int.1 and 2; Figure 4.2 and Table B4 in Appendix B3. in Appendix B).[30] Neighbouring chains connect via hydrogen bonds between the amide functional groups (NH···O), forming 2D-sheets within the structure. This interaction has an energy comparative that of the hydrogen bond mentioned previously (-31.5 and -30,4 kJmol^{-1} for molecules A and B respectively, Int. 3 and 4, Figure 4.2 and Table B3.). The two-fold rotation about the b-axis leads to the chains of molecules stacking in an ABBA motif, as shown in Figure 4.1b. Hydrogen bonding is not present between these layers with the molecules only interacting via van der Waals forces (-12.9 and -12.5 kJmol^{-1} for A and B respectively, Int. 5 and 6, Figure 4.2 and Table B3).

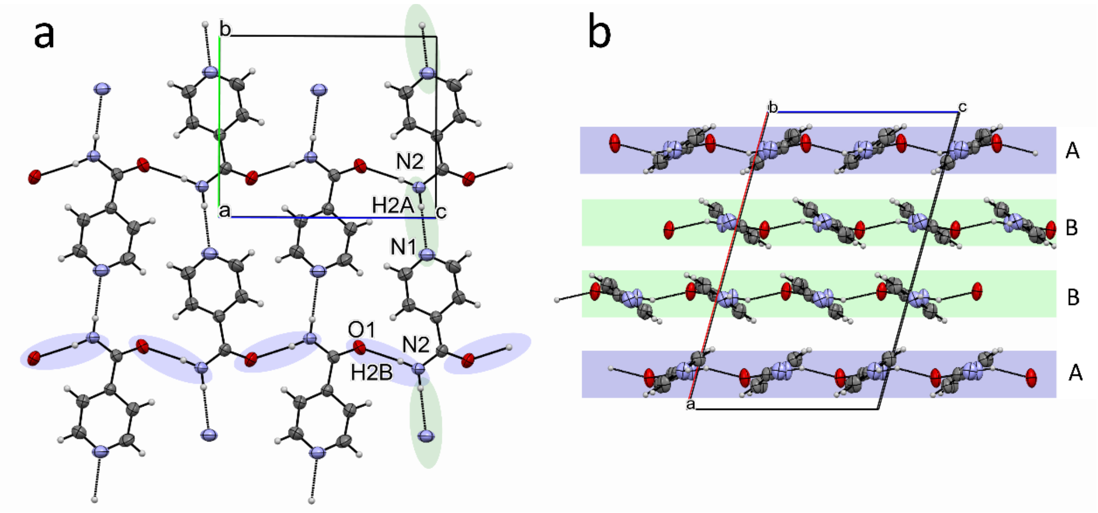

Figure 4.1: a) Structure of Form II isonicotinamide viewed along the *a*-axis. Hydrogen bonds extending along the *b*-axis are highlighted in green whereas hydrogen bonds along the *c*-axis are highlighted in blue. The Figure shows one layer of isonicotinamide molecules which is repeated perpendicular to the *a*-axis forming the ABBA motif. b) Structure of isonicotinamide viewed along the *b*-axis. Layers A and B are highlighted in blue and green respectively.

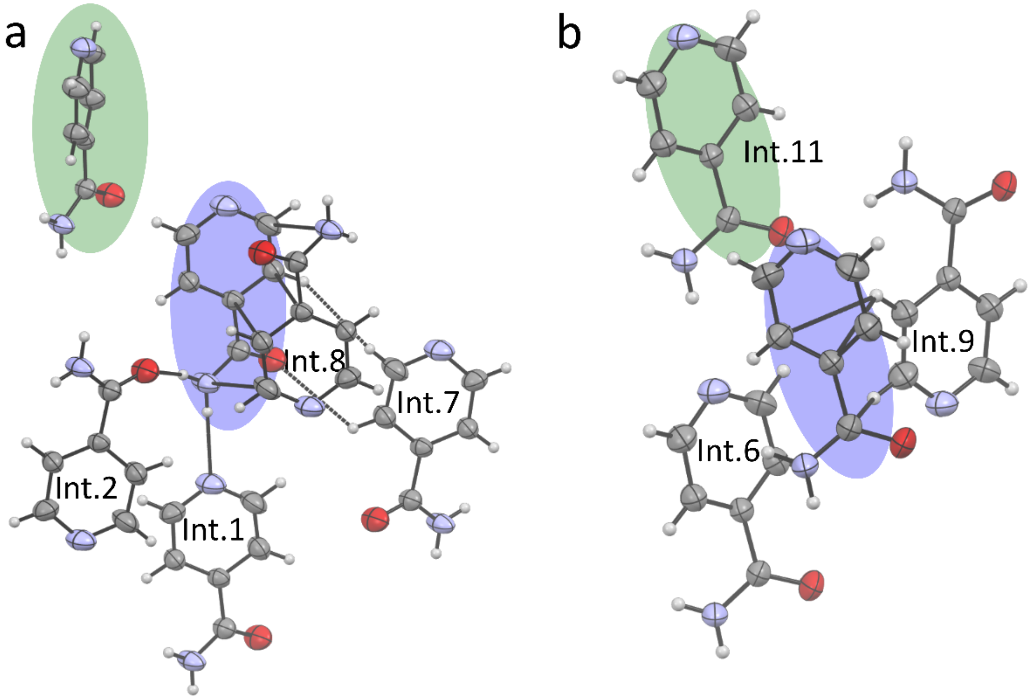

Figure 4.2: Highest energy interactions of Molecule B in Form II isonicotinamide. Molecule A and B are highlighted in green and blue respectively. a) Interactions are displayed between symmetry equivalent molecules, B-B. b) Interactions between Molecules A and B.

The fragile nature of the crystals meant two crystals were used during the study. Most of the data were collected below 1 GPa in a region where the ruby pressure gauge is known to be less sensitive.[19] The *a*-axis significantly decreases on application of pressure from ambient up to 1.09 GPa (6.95 %), in comparison to the b- and c-axes (1.18 and 1.23% respectively, Figure 4.3a). The *a*-axis is perpendicular to the 2-D layers of isonicotinamide and lacks hydrogen bonding between the layers. Data up to this point is fit using a 2nd order Birch-Murnaghan Equation of State (EoS) with a bulk modulus (K_o) of 7.4(12) GPa, V_0 of 1233(14) and K' = 4 (Figure 4.3b).[35] At 1.49 GPa, the *a*-axis decreases further, but slight increases can be observed in the *b*- and *c*-axes (Figure 4.3a). The XRD data at indicates a phase transition, with a reduction in symmetry from monoclinic ($P2_1/c$) to a triclinic system (P1). The Raman spectra at 1.61 GPa shows a difference in lattice vibrations between 50 and 300 cm^{-1}, confirming the transition of Form II isonicotinamide (Figure 4.4). The ABBA motif still applies to the structure after the phase transition, however chains parallel to the *c*-axis now compose of two symmetry independent molecules repeating throughout. Chains parallel to the *b*-axis are composed of symmetry equivalent molecules (Figure 4.5).

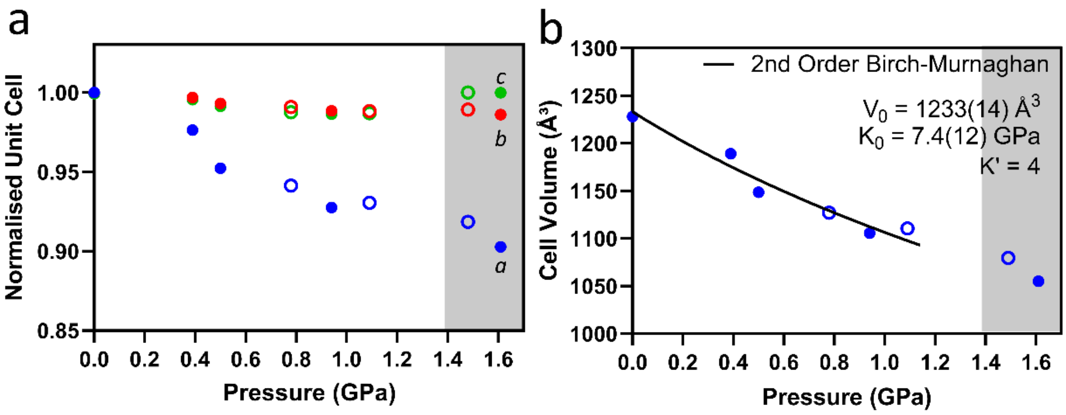

Figure 4.3: Variation in a) unit cell lengths and b) unit cell volume fitted with 2nd Order Birch-Murnaghan Equation of State for Form II, as a function of pressure. Open symbols and closed symbols represent the two different crystallites used in the pressure study. The highlighted area shows data collected after the transition at 1.49 GPa.

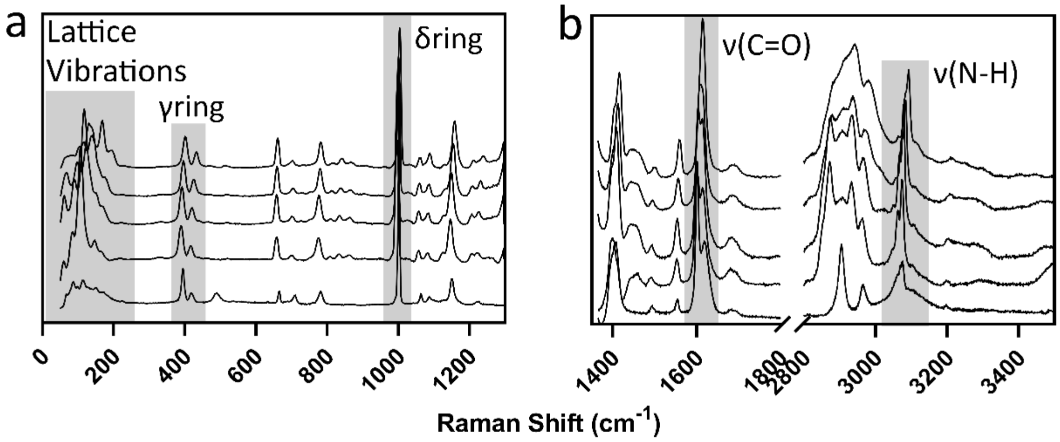

Figure 4.4: Raman spectra of Form II isonicotinamide at various pressures during compression a) 50-1300 cm^{-1} and b) 1400-3500 cm^{-1}. Pressure increases from bottom to top: ambient, 0.39, 0.50, 0.94 and 1.61 GPa. The ambient pressure spectrum of isonicotinamide Form II was collected on a glass microscope slide coated with silicone oil, to prevent the crystal from deteriorating under atmospheric conditions apparent in the spectra with a peak at 487 cm^{-1} corresponding to the Si-O-Si stretch. The diamond peak at 1300 cm^{-1} and between 1800-2800 cm^{-1} are excluded. The region prior to 3000 cm^{-1} displays a broad band indicative of the aliphatic hydrocarbons in the pressure transmitting medium, petroleum ether. γ, out-of-plane bending; δ, in-plane bending; ν, stretching.

As with Form I isonicotinamide, PIXEL calculations can provide an understanding as to what happens to the structure as pressure is applied leading up to the phase transition. Figure 4.2a and Figure 4.2b show 11 significant interactions between molecules A-A, A-B and B-B calculated using the refined Form II crystal structures. Hydrogen bonding between molecules in each layer remains consistent throughout, leading these interactions to be the strongest during the compression (Int. 1-4, Table B3). To explain the phase transition, we look to interaction 11 in Table B3. in Appendix B. Interaction 11 is between the two independent molecules in the asymmetric unit i.e., molecular interactions between the A-B layers, and is predominantly dispersive in nature. Coulombic forces present between these two molecules are relatively unstable, ranging from 4.7 to 3.2 kJmol^{-1} with increase in pressure, and along with repulsive forces, make the overall energy of the interaction much lower in comparison to

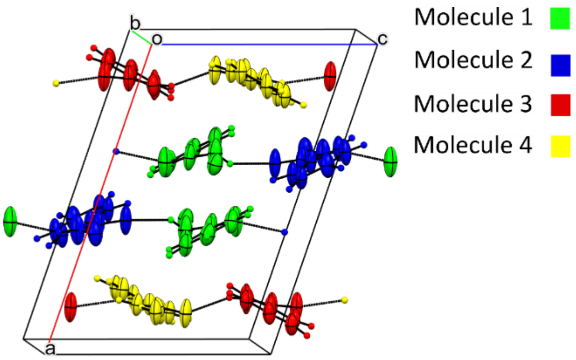

Figure 4.5: Form II isonicotinamide after the phase transition at 1.49 GPa, viewed along the *b*-axis. Molecules are coloured by symmetry equivalence.

interactions 1 to 10. Moving over the transition, this interaction becomes more complex, with four symmetry independent molecules now in the unit cell, highlighted in Figure 4.5. From the energy calculation perspective, the move to Z' = 4 alters the way in which Pixel calculations are performed. For Z'≤ 2, energy calculations are performed on the crystal to a set radius, e.g., 14 Å, and molecule-molecule interactions are calculated between molecules within this radius, For Z' > 2, the calculations are performed on a dimer basis. The effect of this is that the total energy of the crystal is not calculated. The equivalent interactions to Interaction 11 has a prominent stabilising effect on the structure after the transition, with the total energy ranging from -9 to -17.2 kJmol^{-1} at 1.49 GPa, and -8.8 to -18 kJmol^{-1} at 1.61 GPa. Dispersive forces predominantly make up this interaction, as no hydrogen bonding is present between chains. As shown in Figure 4.6, the layers have moved significantly with respect to one another over the phase transition which accounts for increase in the dispersive interactions to leading to a more stabilising interaction between the layers in comparison to the low-pressure phase. Assessment of this interaction is made between molecule pairs in opposite chains: molecules 1 and 3, molecules 1 and 4, and molecules 2 and 4. The pair consisting of molecules 2 and 3 have a low energetic value (-3.0 kJ mol^{-1}) due to the distance of 9.258 Å between them at 1.61 GPa and therefore lack of interaction, so will not be discussed. The differences seen in this interaction indicate a change in relationship between layers of symmetry independent molecules.

Deterioration of Form II crystals are observed beyond their transition; therefore, no further structural information was obtained beyond 1.49 and 1.61 GPa for each separate crystal. The layers in Form II, parallel to the (100) plane, slip on compression and due to the weak interactions between them leads to plastic deformation of the crystal. Figure 4.6 shows the difference between the two structures and provides insight into the destructive nature of the transition. The hydrogen-bonded layers remain intact but the relationship between them changes which has an impact on the symmetry of the solid. Over the transition the layers move so that there is greater overlap between the molecules in neighbouring layers. This greater overlap increases the dispersive component of the interaction energy between these molecules that contributes to the stability of the new high-pressure phase (Figure 4.6) however the significant movement of the layers has a negative impact on the structural integrity of the single crystal.

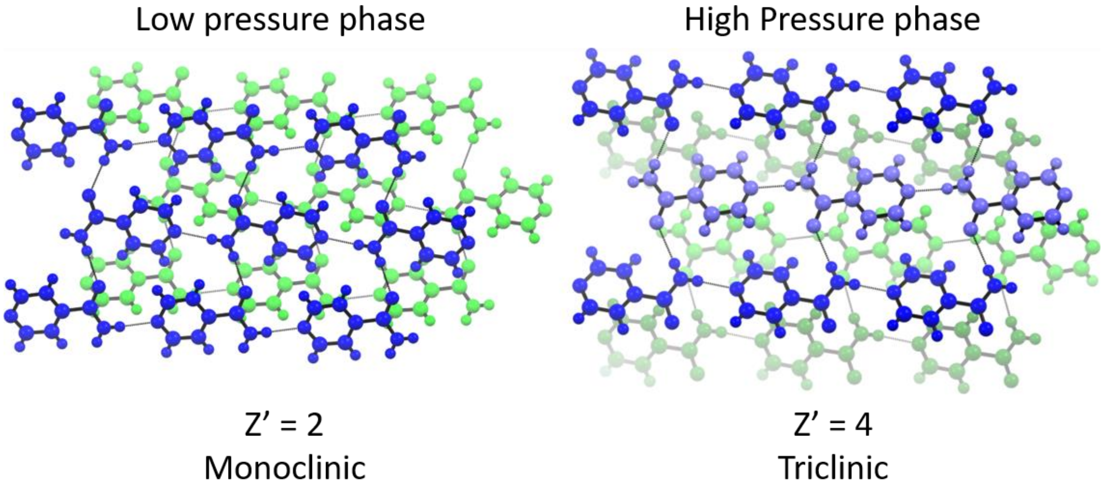

Figure 4.6: Low- and high-pressure phases of Form II isonicotinamide viewed down the *a*-axis (*c*-axis is vertical). Molecules are coloured in varying shades of blue and green to highlight the number of molecules in the asymmetric unit.

Form II isonicotinamide highlights a pseudo-reconstructive phase transition that still enables the single-crystal to single-crystal transition to be characterised. This was observed in the high-pressure study of pyrazinamide during the phase transition of γ phase (the Pc) to the β form ($P2_1/n$), indicated by Raman spectroscopy between 3.6 and 4.5 GPa.[2] The γ polymorph is the preferred phase at high temperature (≥165 °C) and can remain stable at ambient temperature for up to 6 months, where it converts to the α phase. XRD showed the high- and low-pressure phases to coexist between 4 and 8 GPa. Conversion back to the original phase was observed only at ambient pressure leading to a hysteresis caused by an energy barrier. 4-iodobenzonitrile also displayed a reconstructive phase transition, from a monoclinic $I2/a$ system to a triclinic $P1$, at 5.5 GPa.[27] Giordano *et al.*, discuss the destabilising effect of the π··· π stacking of the phenyl rings. The total energy changes from -6.8 kJmol^{-1} at ambient, to 28.1 kJmol^{-1} prior to the transition at 5 GPa, becoming sensitive to the pressure and a destabilising interaction. After the transition at 5.5 GPa, this interaction splits into two due to a shift in layers in the structure. They both remain unstable due to their repulsive nature, but less so than prior to the transition.

4.4.2 Form III isonicotinamide

First discovered by Li *et al.*, Form III was reported to be crystallised by cooling a solution of isonicotinamide in chloroform at a slow rate, similar to that of Form IV described in the experimental section of this chapter.[14] Replication of this method led to the concomitant crystallisation of four of the known polymorphs: Form I, Form II, Form III and Form IV. The slow-evaporation method used in this study solely produced single crystals of Form III isonicotinamide.

Orthorhombic Form III crystallises in the *Pbca* space group with 8 molecules in the unit cell (Z' = 1). At ambient temperature and pressure, the unit cell parameters are: a = 10.1655(14), b = 7.4539(12), c = 15.9218(19) Å (Table B5. in Appendix B). Molecules are arranged in two independent layers, A and A', related by inversion centre, with no hydrogen bonding between layers similar to Form II (Figure 4.7d). Isonicotinamide molecules form chains via hydrogen bonds through NH···N interactions, with adjacent chains connected via NH···O interactions with the secondary hydrogen of the amide group (Figure 4.7c). In contrast to Form II the pyridine moieties in the NH···O chain are related by a c-glide resulting in the pyridine moieties being rotated by 62.45° (Figure 4.7b), in comparison to the 5.95° rotation isonicotinamide molecules in Form II where the molecules were related by a 2_1-screw axis. Weak hydrogen bonds are also present between the pyridine and the amide oxygen of a neighbouring molecule as shown in Figure 4.7b (C1H1···O1). The NH···O hydrogen bonded network that extends in the direction of the a-axis, along with C1H1···O1 contribute to the strongest energy intermolecular interaction of Form III, with a total energy of -33.9 kJmol^{-1}. Symmetry operation 0.5+x, 0.5-y, 2-z relates the two molecules via the glide operation along the a-axis.

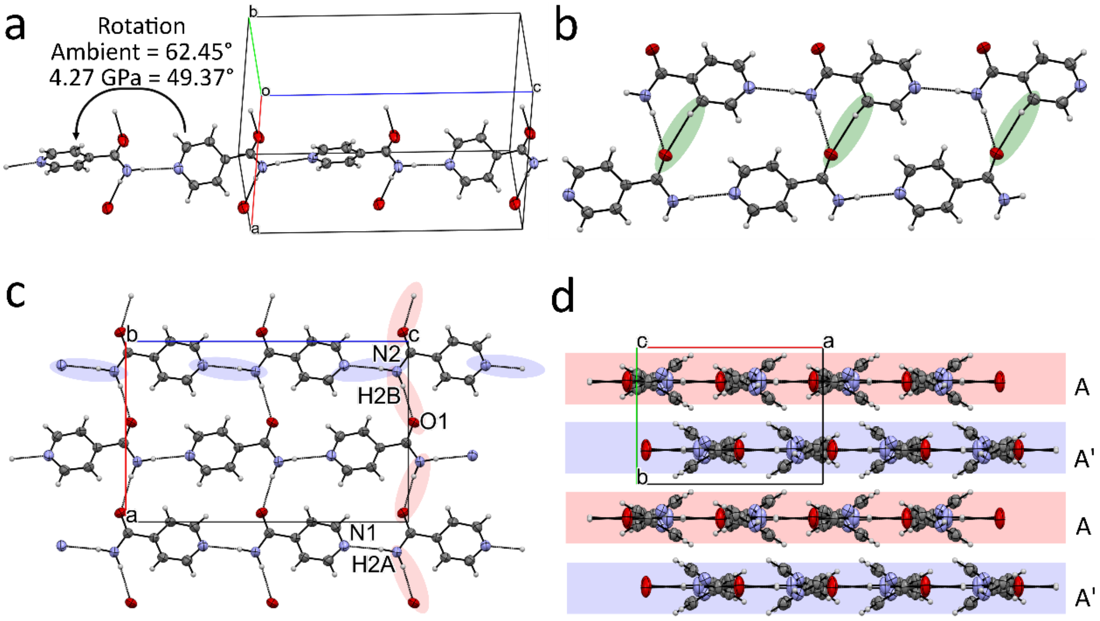

Figure 4.7: Form III isonicotinamide. a) Chains are aligned along the c-axis; the plane of the pyridine ring rotates by 62.45° at ambient pressure to 49.37° at 4.27 GPa. b) Weak hydrogen bonds between isonicotinamide molecules are highlighted in green. c) Structure of Form III isonicotinamide viewed along the *b*-axis. Hydrogen bonds extending along the *a*-axis are highlighted in red whereas hydrogen bonds extending along the *c*-axis are highlighted in blue. d) Structure of Form III viewed along the *c*-axis. Layers A and A' are highlighted in red and blue respectively.

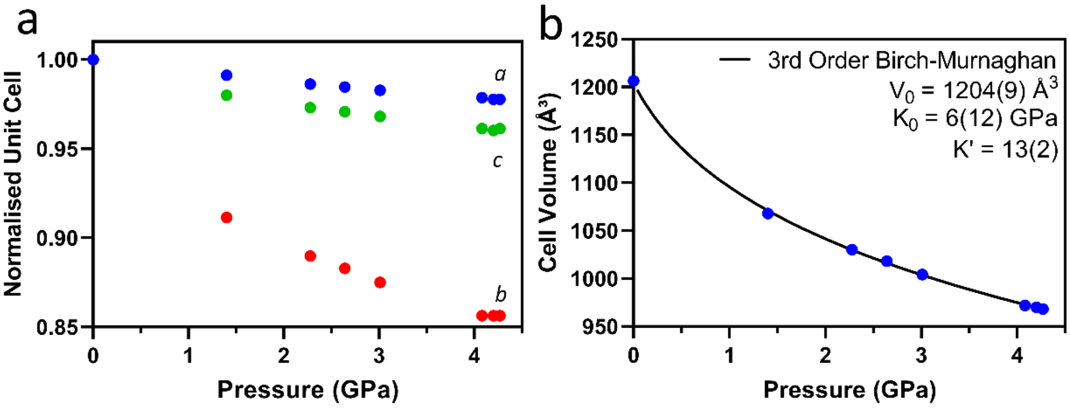

Figure 4.8: Variation in a) unit cell lengths and b) unit cell volume fitted with 3rd Order Birch-Murnaghan Equation of State for Form III isonicotinamide, as a function of pressure.

On compression, Form III remains in the same phase up to 4.27 GPa where the SC-XRD data deteriorates beyond usability. The data from ambient up to 4.27 GPa can be fit using a 3rd order Birch-Murnaghan Equation of State, with bulk modulus (K_o) of 6.0(12) GPa, V_o = 1204(10) and K' = 13(2) (Figure 4.8).[35] Similar to Form II, the unit cell is compressed to the greatest extent perpendicular to the layers. As this is an orthorhombic system the strain tensor aligns to the unit cell axes. The length of the *b*-axis decreases by 14.55 % between ambient pressure and 4.27 GPa, whereas the *a*- and *c*-axis decrease by 2.24 and 3.96% respectively (Figure 4.8). Void space is located between the layers, perpendicular to the *b*-axis (Figure 4.9). The voids decrease from 15.6 % to 3.6% of the unit cell volume as the structure is compressed up to 4.20 GPa (0.5 Å probe radius, 0.2 Å approximate grid spacing). The structure 4.27 GPa shows an increase in void space to 3.8% of unit cell volume. As the layers move closer together, signified by a reduction in void volume, the molecules rotate to enable the continued compression. The molecules aligned along the *c*-axis rotate by 13.08 °, positioning themselves more in plane with one another and perpendicular to the *b*-axis at the higher pressure of 4.27 GPa, which opens up the void space causing the slight increase in the void volume.

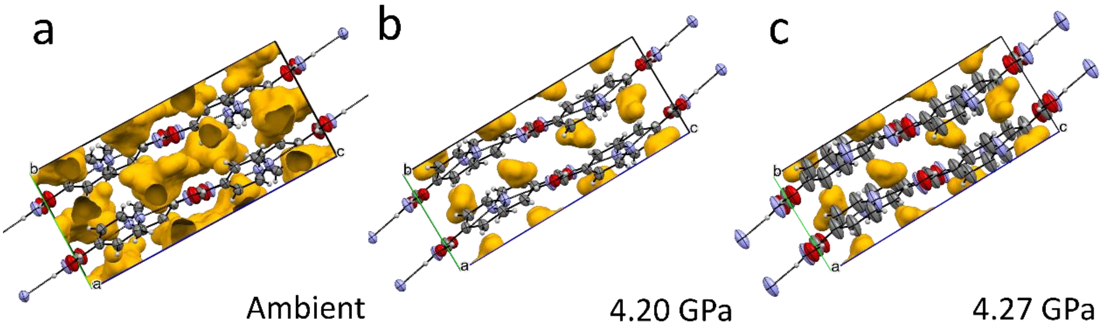

Figure 4.9: Voids in the structure of Form III isonicotinamide are located between layers of isonicotinamide perpendicular to the b-axis at a) ambient, b) 4.20 and c) 4.27 GPa.

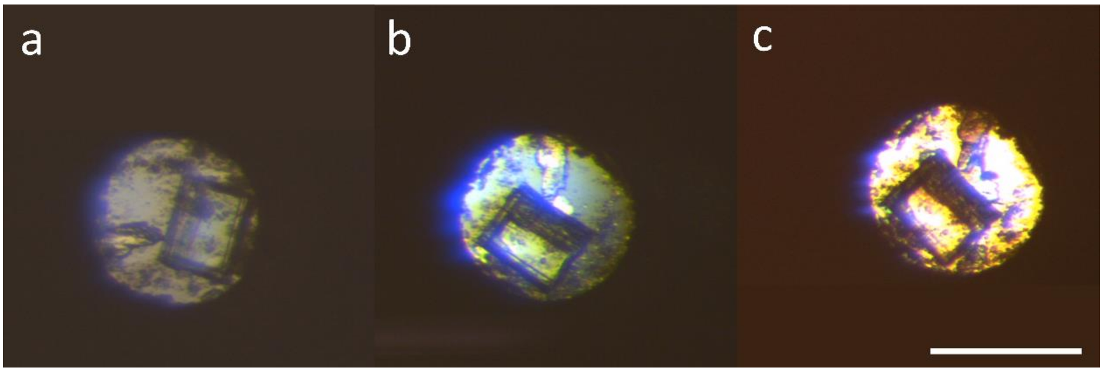

Figure 4.10: Microscope images of the Form III crystals used in the compression study at a) 1.49, b) 4.20 and c) 4.27 GPa. Scale bar represents 200 μm.

The deterioration of the crystal begins earlier in the compression than we expected of the sample. The quality indicators from the integration e.g., R_{int} were still reasonable for a pressure dataset at 4.27 GPa however the next dataset was poor. Petroleum ether remains stable as a pressure transmitting medium up to 6 GPa, ruling out a change to a non-hydrostatic environment.[18] Figure 4.10 shows the microscope images of the crystal taken at 1.40, 4.20 and 4.27 GPa respectively. From these images it appears that the crystal delaminates at the higher-pressures, shown by the lines that run through the length of the crystal, which would cause a deterioration in the data. Delamination tends to be through uniaxial force whereas in this instance the pressure is hydrostatic. This could have occurred if the crystal bridged between the two diamond culets but evidence of this is difficult to observe. The change in the crystal could be attributed to a phase transition. Raman spectroscopy provided information beyond the last XRD collection at 4.27 GPa (Figure 4.11). The spectra at 4.62 GPa shows minimal difference to the previous spectra, in terms of peak positioning, indicating that this is unlikely. The only difference seen in the spectra is the raised background which may be due to the positioning of the sample with respect to the laser, or deterioration of the sample between 4.27 and 4.62 GPa. Neutron powder diffraction beamtime at ISIS Neutron and Muon Source will allow for a definitive answer as to whether a phase transition occurs beyond this pressure.

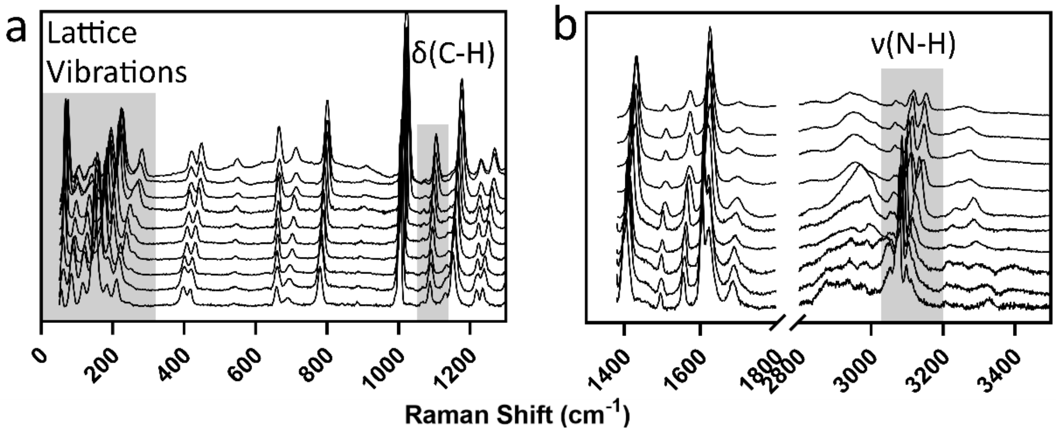

Figure 4.11: Raman spectra of Form III isonicotinamide on increasing pressure from bottom to top: ambient, 0.52, 1.02, 2.28, 2.64, 3.01, 4.08, 4.20, 4.27 and 4.62 GPa. a) 50-1300 cm^{-1} and b) 1400-3500 cm^{-1}. The diamond peak at 1300 cm^{-1} and between 1800-2800 cm^{-1} are excluded for clarity. The region prior to 3000 cm^{-1} displays a broad band indicative of the aliphatic hydrocarbons in the pressure transmitting medium, petroleum ether. δ , in-plane bending; ν , stretching.

4.4.3 Form IV isonicotinamide

Form IV is the final polymorph of isonicotinamide to be studied at high pressure. Monoclinic Form IV has a structure similar to Form II, but with three molecules in the asymmetric unit, crystallising with a *Pc* space group. Comparison of Form II and Form IV isonicotinamide show that 15 out of 15 molecules match when using Mercury's packing similarity wizard however they are distinct polymorphs.[26] Unit cell parameters for the ambient structure are: a = 11.4132(6) Å, b = 8.0036(4) Å, c = 10.0234(5) Å and β = 94.167(3) °. The length of the a-axis is shorter in Form IV, as there are three distinct layers compared with the four layers observed in Form II (*ca.* a = 16.0124(6) Å).

Chains of isonicotinamide molecules extend parallel to the c-axis via amide-amide interactions and form 2-D sheets by extending parallel to the b-axis via amide-pyridine interactions, identical to Form II. Layers of symmetry equivalent molecules stack perpendicular to the a-axis forming the 3D structure, with the motif ABC (Figure 4.12). The pyridine ring of molecules in layer A are rotated by 66.62 ° with respect to layer B, whilst pyridine rings in layer B are rotated by 68.42 ° with respect to layer C. In Form II, the rotation between the rings in layers A and B is 70.27 °, not dissimilar to Form IV.

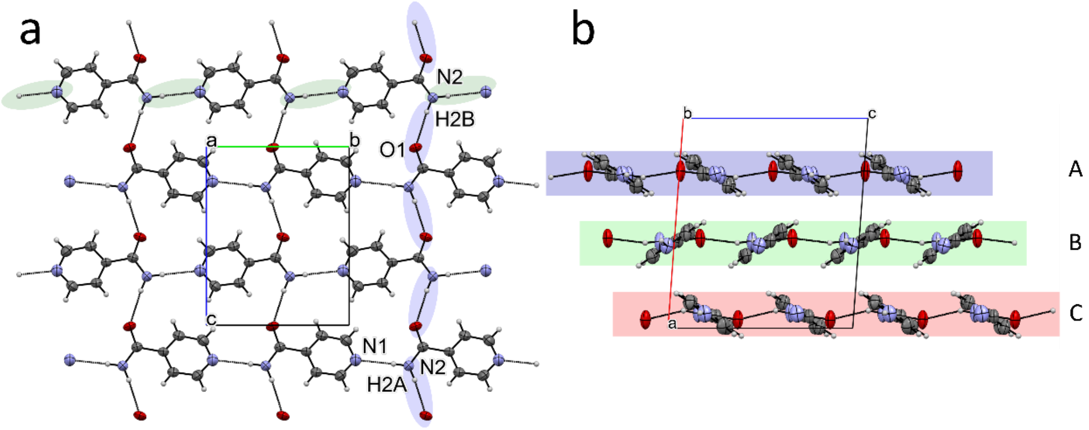

Figure 4.12: Structure of Form IV isonicotinamide viewed along the a-axis. Hydrogen bonds extending along the b-axis are highlighted in green whereas hydrogen bonds along the c-axis are highlighted in blue. The Figure shows one layer of isonicotinamide molecules which is repeated perpendicular to the a-axis forming the ABC motif. b) Structure of isonicotinamide viewed along the b-axis. Layers A, B and C are highlighted in blue, green and red respectively.

As Form IV is compressed, its behaviour is similar to that of Form II isonicotinamide, with a significant decrease in the *a*-axis, the direction in which no hydrogen bonds are present. Data from ambient pressure to 1.4 GPa can be fit using a 3rd order Birch-Murnaghan Equation of State, with bulk modulus (K_0) of 6.8(18) GPa, V_0 = 912(6) Å^3 and K' = 9(4).[28] Data points at 1.62 and 2.01 GPa were omitted from the calculations due to poor fit. Diffraction data for the two points is of consistent quality to the previous data, with R_{int} values of 6.2% and 8.1% for 1.62 and 2.01 GPa respectively, however their unit cell volumes indicate that they may not be in the same phase. The neutron powder diffraction experiment that is planned will be able to provide a robust Equation of state for all the polymorphs and whether there are phase transitions during the compression of each polymorph. From ambient to 2.01 GPa the *a*, *b*, and *c*-axes, decrease by 10.86%, 1.83% and 1.45% respectively, showing anisotropic behaviour (Table B6. in Appendix B). Unit cell parameters show a slight increase in the length of the *a*-axis at 2.01 GPa, which could be due to repulsive interactions acting between the layers of molecules as they are pushed together, in particular the π···π contacts, as seen in Form II and other high-pressure studies of small organic molecules.[2, 27] The increase in *a*-axis could also attribute a change in phase, however Raman spectroscopy shows no changes in the spectra that would suggest a phase transition took place. Compression beyond 2.01 GPa caused deterioration of the data produced from SC-XRD, however Raman spectroscopy of the crystal was still possible, and a spectrum was collected at 2.70 GPa (Figure 4.14 a). The only difference observed was at *ca.* 400 cm^{-1}, where peaks merged to form a broad frequency (Figure 4.14a). This suggests differences in the in-plane bending of the pyridine ring, which may signify a reconstructive phase transition, however the in-plane-bending of the ring at *ca.* 1000 cm^{-1} shows no distinct changes during the compression.

The reason behind the failure at 2.01 GPa is not clear. This pressure is below the limit at which petroleum ether fails as a hydrostatic medium (*ca.* 6 GPa).[18] The first crystal shown in Figure 4.14c, collected at 0.35 and 0.91 GPa, failed at 1.49 GPa. Crystallisation of Form IV isonicotinamide from chloroform produced crystals of a poor quality, often brittle in nature, hence only two pressure point could be collected before it deteriorated. The second larger crystal reached the higher pressures of 1.62 and 2.01 GPa (Figure 4.14d). Its larger dimensions may have caused the crystal to bridge, but the deterioration of the diffraction data of the first crystal indicates that a phase transition is more likely.

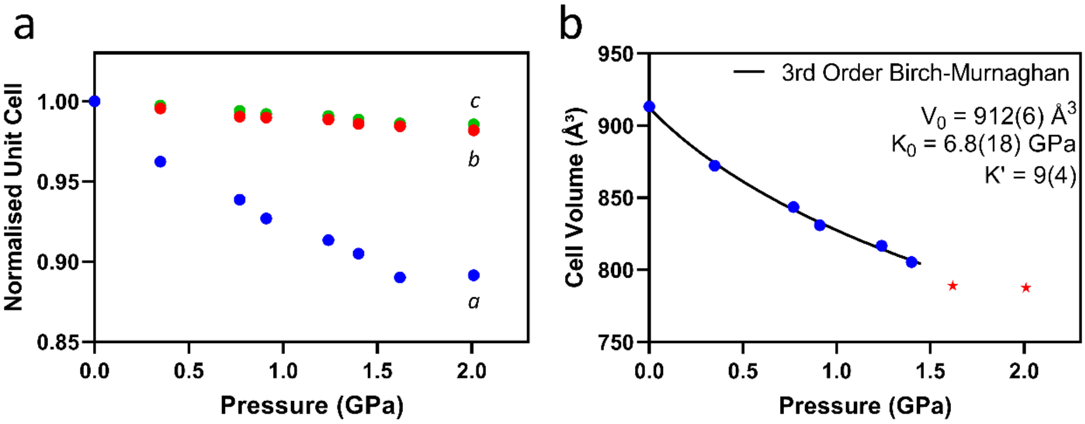

Figure 4.13: Variation in a) unit cell lengths and b) unit cell volume fitted with 3rd Order Birch-Murnaghan Equation of State for Form IV isonicotinamide, as a function of pressure. Data points at 1.62 and 2.01 GPa were not used in the calculation due to poor fit (red stars).

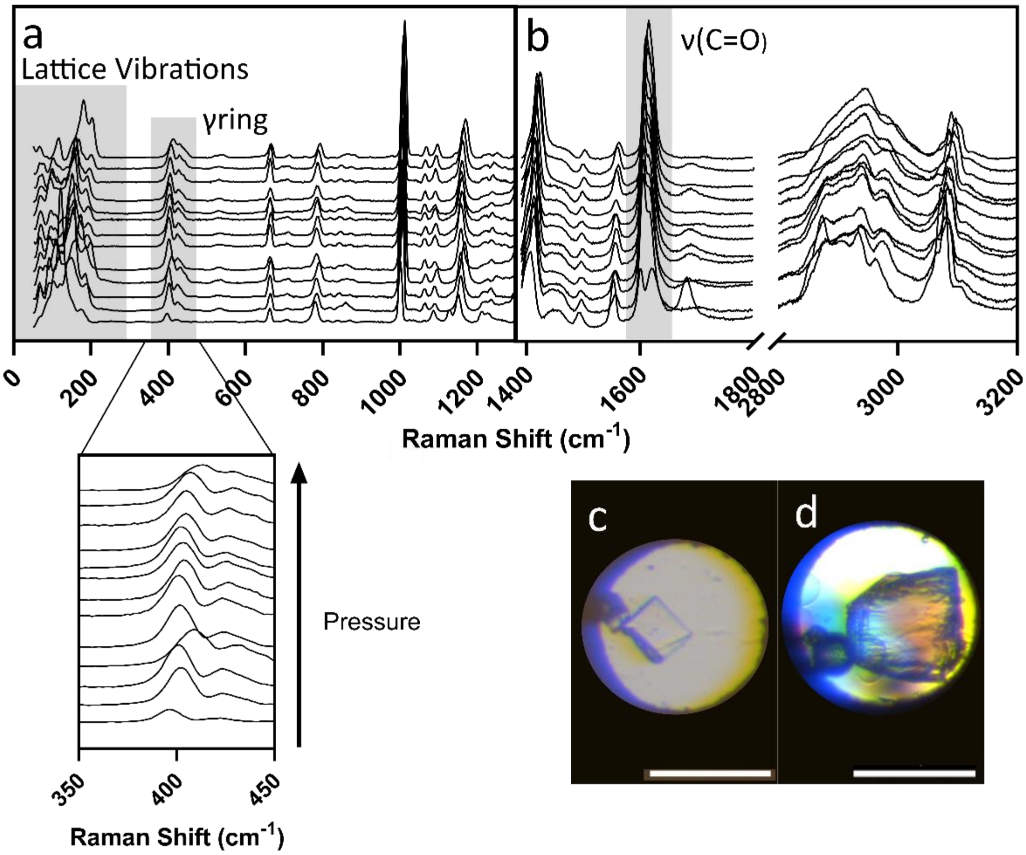

Figure 4.14: Raman spectra of Form IV isonicotinamide on increasing pressure from bottom to top: 0.77, 0.91, 0.93, 1.24 (crystal 1), 1.24 (crystal 2), 1.32, 1.40, 1.49, 1.51, 1.62, 1.71, 2.01 and 2.70 GPa. a) 50-1300 cm^{-1} and b) 1400-3500 cm^{-1}. The diamond peak at 1300 cm^{-1} and between 1800-2800 cm^{-1} are excluded for clarity. The region prior to 3000 cm^{-1} displays a broad band indicative of the aliphatic hydrocarbons in the pressure transmitting medium, petroleum ether. The inset highlights the region where out-of-plane bending of the pyridine ring is observed. c and d) Microscope images of the Form IV crystals used in the Raman study (crystal 1 and 2 respectively). Scale bar represents 200 μm.

4.4.4 Overall comparison of the isonicotinamide polymorphs

The influence of pressure on four polymorphs of isonicotinamide has been studied, each showing distinct behaviour. Out of the four polymorphs, two exhibited a single-crystal to single-crystal transition: Form I (Chapter 3) and Form II. Form III showed no evidence of a phase transition whilst Form IV requires further work to determine whether a phase transition was the cause of the deterioration of the data. With this being said, a successful application has been made to further study Forms II, III and IV at high pressure using neutron diffraction at ISIS Neutron and Muon Source.

As discussed, Form I is the only polymorph with a dimer motif, with its rotation leading to the transition and to Form I' at 4.98 GPa and its super-elastic behaviour, explaining the significantly higher bulk modulus value. The bulk modulus defines how well a material can withstand pressure, i.e., how compressible it is. Lower values represent softer materials. In the two studies of isonicotinamide, each polymorph is observed to react differently during compression, with bulk moduli for Forms I, II, III and IV of 10.6(7), 7.4(12), 6.0(12) and 6.8(18) GPa respectively. As displayed, the errors associated with the bulk modulus for the polymorphs in this chapter are substantially high, but the proposed powder diffraction measurements will enable a much more accurate Equation of State therefore whether these differences are significant. What is clear is that the layered structures seem to be more compressible. Form II features layers within the structure that move with respect to one another during the phase transition that stabilises the structure using dispersive interactions. From the calculations, Form III is indicated to be the most compressible of the three polymorphs in this chapter, which can be seen from its compression up to 4.27 GPa. The molecular orientations in each layer in Form III are different to II and IV. Due to the glide operation, molecules in a layer are rotated with respect to each other that enables additional hydrogen bond between molecules in the same layer which appears aid the rotation of the molecules during the compression. The rotation of the molecules during compression provides extra movement so that the phase remains stable up to 4.27 GPa. There is, however, delamination of the crystal that made XRD data collection beyond this point impossible. Form IV crystal remained structurally sound up to 2.01 GPa which is slightly higher than the phase transition in Form II. Although the structure of Form IV is near identical to that of Form II, different behaviour was observed during its compression. When looking at the high-pressure structure of Form II, the packing shows layers B and B' to be edge to edge, whilst the layers in Form IV are arranged in a herring-bone pattern. This subtle change in the structure and the ability to withstand pressure enables the higher pressure achieved. Over all the polymorphs, whilst the structure of each polymorph is different and they display different behaviour on compression, the molecular volume for each shows a consistency in the rate of compression (Figure 4.15).

The study into the compression of L-histidine polymorphs looked to the density of the two forms to explain the differences in bulk moduli. Form II L-histidine was calculated to have the lower bulk moduli and lower density of the two polymorphs; 11.6(6) GPa and 1.439 g/cm^3 respectively, concluding the less dense material is the softest and therefore most compressible.[10]

5-Methyl-2-[(2-nitrophenyl) amino]-3-thiophenecarbonitrile, more commonly known as ROY, has an extensive number of polymorphs. The compression of the yellow monoclinic polymorph was carried out up to a pressure of 5.2 GPa, with an observed colour change but no phase transition. The 3rd order Birch Murnaghan equation of state was used to determine the bulk modulus to be 6.0 (7) GPa. The density of the ambient structure was determined to be 1.448 g/cm^3.[29] Further studies showed the orange-plate polymorph to have an ambient density of 1.415 g/cm^3 and a bulk modulus of 4.3 (3) GPa,[30] whilst the orange-needle polymorph had an ambient density of 1.434 g/cm^3 and a bulk modulus of 5.9 (14) GPa,[31] both calculated using the 3rd order Birch Murnaghan equation of state. The densest polymorphs mentioned here, the yellow-monoclinic form, also has the greatest bulk modulus, making it the most difficult to compress of the three, following the conclusion by Novelli *et al.* The measurements collected in the investigations ROY were performed using neutron diffraction, producing precise bulk modulus values, which is the aim for isonicotinamide.

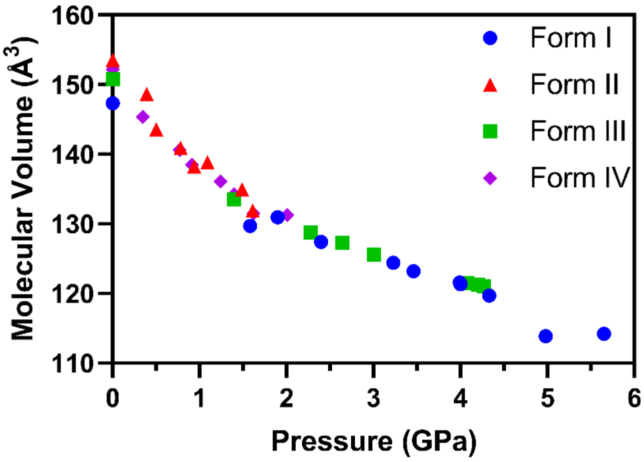

Figure 4.15: Molecular volume of isonicotinamide polymorphs plotted against pressure.

Table 4.1 compares the density and bulk modulus of the four polymorphs of isonicotinamide studied in Chapter 3 and Chapter 4, at ambient pressure. Form I has a bulk modulus of 10.6(7) GPa and a density of 1.376 g/cm^3, making it the densest and the most difficult to compress the polymorphs, matching the behaviour of L-Histidine, discussed by Novelli *et al.*[10] When looking at the layered structures of isonicotinamide, Form III is the densest of the three, at 1.345 g/cm^3, but has a bulk modulus of 6.0(12) GPa, which does not match the statement that compounds with a greater density value are more compressible. A more extensive data set, to be collected at ISIS Neutron and Muon Source, will allow for confirmation of the bulk modulus and therefore the relationship between it and the density of the isonicotinamide polymorphs.

Table 4.1: Calculated densities and bulk modulus values for isonicotinamide polymorphs.

Polymorph	**Density (g/cm^3)**	**Bulk Modulus (GPa)**
Form I	1.376	10.6(7)
Form II	1.321	7.4(12)
Form III	1.345	6.0(12)
Form IV	1.332	6.8(18)

4.5 Conclusion

To conclude the high-pressure investigation of isonicotinamide polymorphs, a single-crystal to single-crystal transition was observed on compression of Form II at 1.49 GPa. The resultant high-pressure structure was solved with a lower symmetry and an increase in molecules in the asymmetric unit from two to four. PIXEL calculations provided information as to why the transition occurred, suggesting the stabilising effect of dispersive interactions between symmetry independent molecules were associated with the transition. The structure of Form III isonicotinamide remained stable up to 4.27 GPa, with no phase transition observed, confirmed by Raman spectroscopy. Form III is the only chain polymorph of isonicotinamide to possess an additional hydrogen bond between molecules in the same layer, which aided the rotation of the molecules and stabilisation of structure at high pressure. Form IV is structurally similar to Form II and was expected to show similar behaviour when pressure was applied to the system. Anisotropic compression of the system was observed up to a pressure of 2.01 GPa, where it was assumed from the XRD data that the quality of the crystal had deteriorated, however, the Raman spectra showed there to be a phase transition between 2.01 and 2.70 GPa, highlighting differences in the region assigned to the in-plane-bending of the pyridine ring. Each polymorph displayed distinct behavioural differences during compression, although similarities are seen in their structures at ambient pressure. To further investigate these differences, neutron diffraction will be employed in the near future to characterise the compression of the metastable polymorphs of isonicotinamide at ISIS Neutron and Muon Source.

4.6 References

1. Piermarini, G. J.; Block, S.; Barnett, J. D. Hydrostatic limits in liquids and solids to 100 kbar. In *Journal of Applied Physics*, American Institute of Physics: 1973; Vol. 44, pp 5377-5382.
2. Tan, X.; Wang, K.; Li, S.; Yuan, H.; Yan, T.; Liu, J.; Yang, K.; Liu, B.; Zou, G.; Zou, B. Exploration of the Pyrazinamide Polymorphism at High Pressure. In *The Journal of Physical Chemistry B*, American Chemical Society: 2012; Vol. 116, pp 14441-14450.
3. Cherukuvada, S.; Thakuria, R.; Nangia, A. Pyrazinamide Polymorphs: Relative Stability and Vibrational Spectroscopy. In *Crystal Growth & Design*, American Chemical Society: 2010; Vol. 10, pp 3931-3941.
4. Boldyreva, E. V.; Shakhtshneider, T. P.; Ahsbahs, H.; Sowa, H.; Uchtmann, H. Effect of High Pressure on the Polymorphs of Paracetamol. In *Journal of Thermal Analysis and Calorimetry*, 2002; Vol. 68, p 437.
5. Haisa, M.; Kashino, S.; Kawai, R.; Maeda, H. The Monoclinic Form of p-Hydroxyacetanilide. In *Acta Crystallographica Section B Structural Crystallography and Crystal Chemistry*, 1976; Vol. 32, pp 1283-1285.
6. Di Martino, P.; Guyot-Hermann, A.-M.; Conflant, P.; Drache, M.; Guyot, J.-C. A new pure paracetamol for direct compression: The orthorhombic form. In *International Journal of Pharmaceutics*, 1996; Vol. 128, pp 1-8.
7. Nichols, G.; Frampton, C. S. Physicochemical Characterization of the Orthorhombic Polymorph of Paracetamol Crystallized from Solution. In *Journal of Pharmaceutical Sciences*, 1998; Vol. 87, pp 684-693.
8. Fabbiani, F. P. A.; Allan, D. R.; David, W. I. F.; Davidson, A. J.; Lennie, A. R.; Parsons, S.; Pulham, C. R.; Warren, J. E. High-Pressure Studies of Pharmaceuticals: An Exploration of the Behavior of Piracetam. In *Crystal Growth & Design*, American Chemical Society: 2007; Vol. 7, pp 1115-1124.
9. Wood, P. A.; Francis, D.; Marshall, W. G.; Moggach, S. A.; Parsons, S.; Pidcock, E.; Rohl, A. L. A study of the high-pressure polymorphs of L-serine using ab initio structures and PIXEL calculations. In *CrystEngComm*, The Royal Society of Chemistry: 2008; Vol. 10, pp 1154-1166.
10. Novelli, G.; Maynard-Casely, H. E.; McIntyre, G. J.; Warren, M. R.; Parsons, S. Effect of High Pressure on the Crystal Structures of Polymorphs of l-Histidine. In *Crystal Growth & Design*, American Chemical Society: 2020; Vol. 20, pp 7788-7804.
11. Giordano, N.; Beavers, C. M.; Campbell, B. J.; Eigner, V.; Gregoryanz, E.; Marshall, W. G.; Peña-Álvarez, M.; Teat, S. J.; Vennari, C. E.; Parsons, S. High-pressure polymorphism in pyridine. In *IUCrJ*, 2020; Vol. 7, pp 58-70.
12. Lynch, M. B.; Lawrence, S. E.; Nolan, M. Predicting Nucleation of Isonicotinamide from the Solvent-Solute Interactions of Isonicotinamide in Common Organic Solvents. In *Journal of Physical Chemistry A*, American Chemical Society: 2018; Vol. 122, pp 3301-3312. Kulkarni, S. A.; McGarrity, E. S.; Meekes, H.; ter Horst, J. H. Isonicotinamide self-association: the link between solvent and polymorph nucleation. In *Chemical Communications*, The Royal Society of Chemistry: 2012; Vol. 48, pp 4983-4985. Frisch, M. J.; Trucks, G. W.; Schlegel, H. B.; Scuseria, G. E.; Robb, M. A.; Cheeseman, J. R.; Scalmani, G.; Barone, V.; Mennucci, B.; Petersson, G. A.; et al. *Gaussian 09W, Revision C.01*; 2009. Caridi, A.; Kulkarni, S. A.; Di Profio, G.; Curcio, E.; ter Horst, J. H. Template-Induced Nucleation of Isonicotinamide Polymorphs. In *Crystal Growth & Design*, American Chemical Society: 2014; Vol. 14, pp 1135-1141.
13. Aakeröy, C. B.; Beatty, A. M.; Helfrich, B. A.; Nieuwenhuyzen, M. Do Polymorphic Compounds Make Good Cocrystallizing Agents? A Structural Case Study that Demonstrates the Importance of Synthon Flexibility. In *Crystal Growth & Design*, American Chemical Society: 2003; Vol. 3, pp 159-165.

14. Li, J.; Bourne, S. A.; Caira, M. R. New polymorphs of isonicotinamide and nicotinamide. In *Chemical Communications*, The Royal Society of Chemistry: 2011; Vol. 47, pp 1530-1532.
15. Eccles, K. S.; Deasy, R. E.; Fábián, L.; Braun, D. E.; Maguire, A. R.; Lawrence, S. E. Expanding the crystal landscape of isonicotinamide: concomitant polymorphism and co-crystallisation. In *CrystEngComm*, The Royal Society of Chemistry: 2011; Vol. 13, pp 6923-6925.
16. Vicatos, A. I.; Caira, M. R. A new polymorph of the common coformer isonicotinamide. In *CrystEngComm*, The Royal Society of Chemistry: 2019; Vol. 21, pp 843-849.
17. Kerr, H. E.; Softley, L. K.; Suresh, K.; Nangia, A.; Hodgkinson, P.; Evans, I. R. A furosemide–isonicotinamide cocrystal: an investigation of properties and extensive structural disorder. In *CrystEngComm*, The Royal Society of Chemistry: 2015; Vol. 17, pp 6707-6715. Wang, L.; Tan, B.; Zhang, H.; Deng, Z. Pharmaceutical Cocrystals of Diflunisal with Nicotinamide or Isonicotinamide. In *Organic Process Research & Development*, American Chemical Society: 2013; Vol. 17, pp 1413-1418. Dubey, R.; Desiraju, G. R. Structural landscape of the 1 : 1 benzoic acid : isonicotinamide cocrystal. In *Chemical Communications*, The Royal Society of Chemistry: 2014; Vol. 50, pp 1181-1184.
18. Tateiwa, N.; Haga, Y. Evaluations of pressure-transmitting media for cryogenic experiments with diamond anvil cell. In *Review of Scientific Instruments*, American Institute of Physics: 2009; Vol. 80, p 123901.
19. Piermarini, G. J.; Block, S.; Barnett, J. D.; Forman, R. A. Calibration of the pressure dependence of the R1 ruby fluorescence line to 195 kbar. In *Journal of Applied Physics*, American Institute of Physics: 1975; Vol. 46, pp 2774-2780.
20. Inc., B. A. *SAINT*; 2017. Inc., B. A. *APEX3*; 2018.
21. Sheldrick, G. M. *SADABS, Program for Absorption Correction for Data from Area Detector Frames*; 2008.
22. Dolomanov, O. V.; Bourhis, L. J.; Gildea, R. J.; Howard, J. A. K.; Puschmann, H. OLEX2: A complete structure solution, refinement and analysis program. In *Journal of Applied Crystallography*, 2009; Vol. 42, pp 339-341.
23. Groom, C. R.; Bruno, I. J.; Lightfoot, M. P.; Ward, S. C. The Cambridge Structural Database. In *Acta Crystallographica Section B*, 2016; Vol. 72, pp 171-179.
24. Reeves, M. G.; Wood, P. A.; Parsons, S. MrPIXEL: Automated execution of Pixel calculations via the Mercury interface. In *Journal of Applied Crystallography*, 2020; Vol. 53, pp 1154-1162.
25. Gavezzotti, A. Calculation of lattice energies of organic crystals: the PIXEL integration method in comparison with more traditional methods. In *Zeitschrift für Kristallographie - Crystalline Materials*, 2005; Vol. 220, pp 499-510. Gavezzotti, A. Molecular Aggregation: Structure Analysis and Molecular Simulation of Crystals and Liquids. Oxford University Press: Oxford, UK, 2007. Gavezzotti, A. Efficient computer modeling of organic materials. The atom–atom, Coulomb–London–Pauli (AA-CLP) model for intermolecular electrostatic-polarization, dispersion and repulsion energies. In *New Journal of Chemistry*, The Royal Society of Chemistry: 2011; Vol. 35, pp 1360-1368.
26. Macrae, C. F.; Sovago, I.; Cottrell, S. J.; Galek, P. T. A.; McCabe, P.; Pidcock, E.; Platings, M.; Shields, G. P.; Stevens, J. S.; Towler, M.; et al. Mercury 4.0: from visualization to analysis, design and prediction. In *Journal of applied crystallography*, 2020; Vol. 53, pp 226-235.
27. Giordano, N.; Afanasjevs, S.; Beavers, C. M.; Hobday, C. L.; Kamenev, K. V.; O'Bannon, E. F.; Ruiz-Fuertes, J.; Teat, S. J.; Valiente, R.; Parsons, S. The Effect of

Pressure on Halogen Bonding in 4-Iodobenzonitrile. In *Molecules (Basel, Switzerland)*, MDPI: 2019; Vol. 24, p 2018.
28. Gonzalez-Platas, J.; Alvaro, M.; Nestola, F.; Angel, R. EosFit7-GUI: A new graphical user interface for equation of state calculations, analyses and teaching. In *Journal of Applied Crystallography*, 2016; Vol. 49, pp 1377-1382.
29. Harty, E. L.; Ha, A. R.; Warren, M. R.; Thompson, A. L.; Allan, D. R.; Goodwin, A. L.; Funnell, N. P. Reversible piezochromism in a molecular wine-rack. In *Chemical Communications*, The Royal Society of Chemistry: 2015; Vol. 51, pp 10608-10611.
30. Funnell, N. P.; Bull, C. L.; Ridley, C. J.; Capelli, S. Structural behaviour of OP-ROY at extreme conditions. In *CrystEngComm*, The Royal Society of Chemistry: 2019; Vol. 21, pp 4473-4483.
31. Warren, L. R.; McGowan, E.; Renton, M.; Morrison, C. A.; Funnell, N. P. Direct evidence for distinct colour origins in ROY polymorphs. In *Chemical Science*, The Royal Society of Chemistry: 2021; Vol. 12, pp 12711-12718.

Chapter 5

Exploring the thermal behaviour of the solvated structures of nifedipine

5 Exploring the thermal behaviour of the solvated structures of nifedipine

5.1 Abstract

This chapter discusses the crystallisation of solvated structures of the pharmaceutical compound nifedipine, formed from: 1,4-dioxane, morpholine, tetrahydrofuran (THF), pyridine, dimethyl sulfoxide (DMSO), dimethylacetamide (DMA), dimethylformamide (DMF) and methanol. Low-temperature single-crystal X-ray diffraction was used to solve the structures; with a low temperature phase transition observed for DMA resulting in a collection at 173 K. Nifedipine-THF is the only solvate in this study which did not form hydrogen bonds between drug and solvent, with its crystal structure resembling the metastable polymorph, Form C. Desolvation of the solvates was captured using variable temperature X-ray powder diffraction (VT-XRPD). All solvates desolvated to the thermodynamically stable Form A nifedipine, however reflections corresponding to a phase other than Form A were observed during the desolvation of DMF. Nifedipine-methanol also shows interesting behaviour during desolvation, exhibiting negative thermal expansion in the direction of the *b*-axis.

5.2 Introduction

Solid-state characterisation of drug compounds is a fundamental stage in pharmaceutical development that helps to ascertain their physicochemical properties and ultimately the assessment of a drug's efficacy and viability. Solid-state screening of pharmaceutical products allows for a survey and identification of potential solid-state forms, whether they be amorphous or crystalline, single component or multicomponent. This screening process can focus on single-component studies of the crystalline state that are limited to the exploration of polymorphism, the ability of a crystalline material to possess more than one different form without changing the molecular composition, albeit solvates can be observed. Controlling the polymorphic form is important during pharmaceutical manufacturing; preventing problems that could occur downstream, with the example of Ritonavir highlighting the importance of comprehensive solid screening before commercial production.[1] Pharmaceutical company, Abbott, would have incurred considerable costs when an unknown polymorph of the antiretroviral protease inhibitor precipitated out, identified as being the thermodynamically stable form of the two Ritonavir polymorphs. Screening for multicomponent crystals, survey compositions that include the pharmaceutical and a guest molecule in different ratios as well as different crystallisation conditions. These can include salts (if the molecules are charged), co-crystals (where the compounds are in their neutral state) and solvates. The first two solid forms are targeted, that is to say, the choice of guest molecules are based on the molecular properties and how the guests may interact with the pharmaceutical compound. Solvates form when solvent molecules are incorporated into the crystal structure. If the solvent is water, the resultant product is termed a hydrate. On many occasions the isolation of a solvate is a by-product of the solvent screen and unintentional however a judicious choice of solvent can lead to solvates that are targeted. On the whole, however, solvation during the crystallisation process can cause a number of issues within pharmaceutical development. For example, levothyroxine is commercially used in its hydrated form, levothyroxine sodium pentahydrate (LSP), to treat hypothyroidism.[2-4] LSP is susceptible to dehydration to the monohydrate form when stored under elevated temperature and low relative humidity, causing chemical instability.[4] This product has been known to be recalled due to issues with chemical and physical stability, however there is no alternative treatment available hence these issues need to be addressed.[3] The MHRA have previously reported issues with tablet hardness, resulting in a medicines recall,[2] whilst the FDA have issued multiple recalls due to subpotency.[5] Therefore there is a requirement to study and understand the formation and the properties of solvated materials so that the risks of their use can be mitigated against. Additional concern is the toxicity of organic solvents that are not categorised as Class III and not regarded as safe by the International Conference on Harmonisation (ICH) guidelines for limits on residual solvents.[6, 7]

A number of pharmaceutical solvates have been thoroughly investigated, including sorafenib tosylate, ciclesonide, olanzapine, gallic acid and trimesic acid, amongst others.[8, 9, 10] Solvation has been shown to positively impact the dissolution properties of pranlukast, occasionally used in the treatment of asthma.[11] The ethanol solvate was discovered to be 4 times more soluble than the commercial hemihydrate form however it was not stable above 90% relative humidity and transformed to the hemi-hydrate. Other solvated forms (DMF and 1-propanol) were not as stable to these environments. Characterisation of the pranlukast solvates included X-ray powder diffraction, thermogravimetry, differential thermal analysis and dynamic vapour sorption, for a comprehensive study of the solid-state forms. Structural relationships between olanzapine solvates have been extensively studied by Bhardwaj and co-authors.[10] In this study, solution crystallisation and solvent-assisted grinding were employed to obtain 56 solvates, 24 of which were unreported and subsequently solved using single-crystal X-ray diffraction. Calculations of crystal energies determined that olanzapine is not able to form dense packing arrangements, providing space for solvent molecules to reside. 18 of the olanzapine solvates were found to pack identically to the pure thermodynamically stable form; a relationship which gave insight as to why they desolvated to that particular polymorph.[10] These examples highlight that pharmaceutical materials are susceptible to the formation of solvated forms hence it is imperative that we are able to understand their stability and their desolvation pathway so that they may be used. Collective knowledge of these systems can also be used to help develop new pharmaceutical products or processes.

Desolvation is the process by which a solvent is removed from the crystal structure, either mechanically or thermally.[8, 12, 13] Although solvated structures are known to improve physicochemical properties, downstream processes, such as milling, spray-drying and wet granulation, can lead to desolvation, eliminating the improved properties, hence not usually selected for development owing to this risk. Acetonitrile-solvated piroxicam-succinic acid co-crystals were studied by Liu *et al.* in 2019 where they showed that on increase in temperature, the solvated co-crystal broke up to form the alpha polymorph of piroxicam and the piroxicam-succinic acid co-crystal.[14] Interestingly, single crystals showed a change in colour with decrease in temperature, not caused by a major structural transformation, but possibly due to the electronic band structure of the co-crystal Desolvation can provide a way of crystallising out new polymorphs of the host molecule. A study into anti-HIV drug, 2-chloro-4-nitrobenzoic acid, concluded that the desolvation of five solvates did not lead to the polymorph with a crystal structure that most resembled the starting material.[12] 1,4-dioxane, *p*-xylene and mesitylene all formed acid-acid dimers with the drug, but desolvated to Form II, a mixture of Form I and II, and Form I respectively. Minkov *et al.,* also investigated the desolvation of widely known drug furosemide, interestingly noting that large crystals of the dimethylformamide solvate produced the Form III polymorph, whereas the powdered sample desolvated to the Form I polymorph, highlighting the importance of particle size to the polymorphic outcome.[13] Desolvation from larger particles was slow, occurring in two stages over 450 K; first desolvation at the surface of the crystal forming the Form III polymorph, then desolvation occurring in the bulk of the crystal at a higher temperature. The powdered sample desolvated at a quicker rate, with complete desolvation by 375 K to the Form I polymorph. Another problem is the toxicity of the solvents incorporated into these multi-component crystal structure. The solvents used in crystallisations can be harmful if ingested and therefore should be avoided or limited in pharmaceutical formulations.[6] Regulation around the quantity of residual solvent is found in the ICH guideline Q3C (R8).

Nifedipine is an L-type calcium channel antagonist used in the treatment of cardiovascular disease,[15, 16] categorised as a Class II compound using the Biopharmaceutical Classification System i.e. it has poor aqueous solubility but high membrane-permeability (Figure 5.1).[17] Nifedipine has six identified polymorphs. Similar to other pharmaceutical crystal structures, there are inconsistencies in the nomenclature of nifedipine. Form A or α was first solved by Triggle *et al.,* and is the thermodynamically stable form which leads to the amorphous state on melting.[18] Form C (β) is produced from the melt of the amorphous form and was first solved via synchrotron powder data,[15] before the structure was confirmed using single-crystal X-ray diffraction.[19] Gui *et al.,* solved the structures of four further polymorphs of nifedipine in their paper, discussing the role that the nitrophenyl group plays in reversible polymorphic transitions of nifedipine.[20] β' is the high temperature phase (333 K) that is enantiotropically related to the β form. Single-crystals of the β polymorph were grown from the melt and cool of the amorphous form of nifedipine mixed with 10 wt.% TWEEN- used in many biomedical applications. Heating the β form above 333 K led to the transition to β'. These are structurally similar to γ and its high temperature form, γ'. Gui *et al.,* note that the γ' form grows slowly from droplets of the melt of thermodynamically stable polymorph at 373 K, which if cooled below 247 K transitioned to the γ polymorph. Finally, δ was crystallised by seeding the melt of nifedipine with structurally similar compound felodipine, with the resultant structure having ester groups in the cis/cis conformer, not seen in the other polymorphs. Recent work has been carried out on the crystal habit of nifedipine when crystallising from five different solvents.[21] Li *et al.* observed that the change in morphology of the α-polymorph was generally caused by the hydrogen-bond acceptor ability of the solvent. Of particular importance to our study is that despite crystallisation from the solvents there were no solvates found despite the large number of hydrogen-bonding acceptor sites on nifedipine.

Metastable polymorphs of nifedipine have only been discovered from the melt of the amorphous state hence this prompted us to investigate the polymorph landscape of nifedipine via a solvent-screen with the aim to isolate a metastable polymorph of nifedipine directly or through a desolvation pathway. Previous work had shown that it forms solvates with dioxane and DMSO which made it surprising that acetone did not interact favourably in the study of Li *et al.* In this paper we, firstly, isolate seven new solvates of nifedipine and structurally characterise these using single-crystal X-ray diffraction. Then we compare the molecular structures dividing these into cyclic and chain solvents. Finally, we investigate the desolvation of the solvates using a combination of Differential Scanning Calorimetry and powder diffraction to observe the crystal structure changes that occur on loss of solvent.

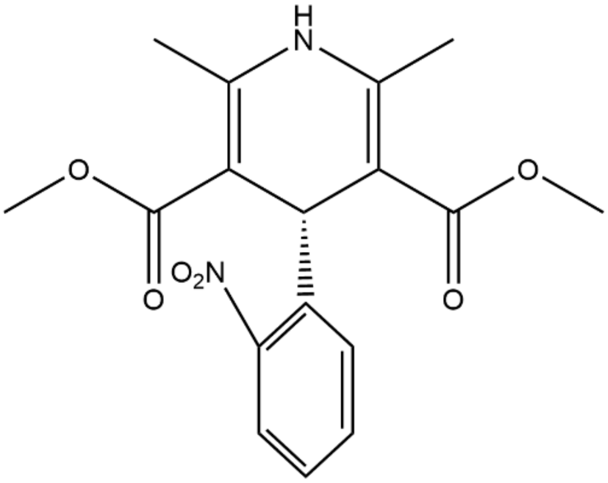

Figure 5.1: Molecular diagram of nifedipine.

5.3 Experimental

5.3.1 Materials

Nifedipine (Alfa Aesar, purity 98%) was slurried in selected solvents (1g/mL) for 24 hours using a magnetic stirrer to agitate the slurry (*ca.* 295 K). A list of solvents used in this study can be found in Table 5.1. Solid material was separated from the solution using a centrifuge and dried between filter paper before analysis. The supernatant solution was filtered using a 0.2 µm PTFE filter into clean glass vials and covered with pierced lids to aid slow evaporation of the solvent and obtain single-crystals for analysis. Nifedipine decomposes when exposed to light, therefore vials were wrapped in aluminium foil to minimise exposure to light and stored in a fumehood until suitable crystals were obtained.

Table 5.1: Solvents used in the solvent screen study of nifedipine.

Solvent	**Grade**	**Supplier**
Acetonitrile	≥99.9%	Fisher
Butyl acetate	≥99.5%	Sigma Aldrich
1,3-dioxane	98.0%	Alfa Aesar
1,4-dioxane	≥99.0%	Alfa Aesar
Dimethylacetamide	≥99.5%	Sigma Aldrich
Dimethylformamide (anhydrous)	99.8%	Sigma Aldrich
Dimethyl sulfoxide	≥99.9%	Sigma Aldrich
Ethanol	99.8%	Fisher
Ethyl Acetate	≥ 99.7%	Sigma Aldrich
Heptane	99.0%	Honeywell
Hexane	≥97.0%	Sigma Aldrich
2-methyltetrahydrofuran	99.0%	Alfa Aesar
Methanol	HPLC	VWR
Morpholine	99.0%	Alfa Aesar
Nitromethane	For synthesis	Merck
2-propanol	ACS Reagent	VWR
Pyridine	≥ 99.0%	Honeywell
Tetrahydrofuran	HPLC ≥ 99.9 %	Honeywell

5.3.2 Single-Crystal X-ray Diffraction

X-ray diffraction data of Nifedipine Form A, recrystallised from ethanol, were collected using a Bruker D8 Venture diffractometer with IμS Microfocus Source (Cu Kα1 – 1.54178 Å) and Photon II CCD detector at 297 K. Data were reduced using Apex 3 software, incorporating SAINT V8.40B. SADABS was used for absorption correction. Samples were cooled using an Oxford Cryosystems Cryostream 800 system. The following solvated structures were collected at 100 K, with the exception of DMA, which was collected at 173 K (due to a phase transition below this temperature): pyridine, morpholine, tetrahydrofuran, dimethylacetamide, dimethylformamide, dimethyl sulfoxide, methanol. Further diffraction data were collected on the methanol solvate on a Bruker Kappa APEX II with IμS Microfocus Source (Mo Kα1 – 0.71073Å) and APEX II CCD detector. Data were reduced using similar procedures as above. Variable temperature data of a single crystal of the methanol solvate were collected in 25 K increments from 100 to 275 K using an Oxford Cryosystems Cryostream 800 system because the solvated structure showed non-linear thermal behaviour at higher temperatures. Diffraction data for the 1,4-dioxane solvate was collected using a Rigaku Synergy-I with Hybrid Pixel Array detector, at 100 K. Data were reduced using CrysAlisPro with SCALE 3 ABSPACK correction implemented.

All structures were solved using ShelXT intrinsic phasing incorporated in the Olex2 software.[22, 23] Refinements were carried out using ShelXL least-squares refinement.[24] Non-hydrogen atoms were anisotropically refined before the addition of hydrogen atoms. Three structures showed disorder in the solvate molecules: tetrahydrofuran, morpholine and dimethylacetamide. To model these, the occupancy of morpholine and tetrahydrofuran atoms were set at 0.5 through the use of the 'Split' function in Olex2.[23] The atoms in the second component were moved to positions where residual electron density were highest. The atoms were being modelled around an inversion centre and so we decided to model the whole molecule at 0.5 occupancy rather than half the molecules at occupancy of 1; this also helped us to create the z-matrix for refinement against our powder diffraction data. The atoms in the dimethylacetamide molecule were split using the same procedure, with atoms refined before fixing the occupancy to 0.85 in molecule one and the remaining molecules occupancy set to 0.15. Distances between atoms were restrained with the SADI atoms, DFIX restraint, and EADP constraints applied. All crystallographic data is located in the supporting information (Table C1 in Appendix C).

5.3.3 X-ray Powder Diffraction

Screening of the solid samples was carried out using a Bruker D8 Advance II powder diffractometer with a multi-well flat plate, Cu X-ray source (Ka1 = 1.5406 Å). An angular range of 4-35° 2θ with 0.017° 2θ step size with 1 second exposure per step was used. Excess solvent was removed from samples using filter paper prior to placing on a 28-well plate constructed from steel with Kapton film backing. Data were collected at ambient temperature. From this data, samples of interest were repeated using capillary X-ray powder diffraction. as described below.

5.3.4 Variable-Temperature X-ray Powder Diffraction

Solid from the slurry experiments were lightly ground to break up any aggregates using an agate pestle and mortar and transferred to 0.7 mm diameter borosilicate glass capillaries. A Bruker D8 Advance diffractometer with Johansson monochromator (Cu Kα1 – 1.5406 λ) was used to collect the data. Samples were heated in 5 K increments (360 K/min) using an Oxford Cryosystems Cryostream 800 system and held at the target temperature for 5 minutes before commencing the data collection (4-35°, 2θ, 0.017° per step, 1 second exposure). For the samples 1,4-dioxane and tetrahydrofuran, the heating process took 30 minutes to increase from 293 K to the next temperature in the series: 343 and 313 K respectively. Material isolated from pyridine and methanol slurries provided XRPD data consistent with that of Form A nifedipine, therefore single crystals of these solvates were grown and ground for capillary XRPD data collection. Unit cell parameters were determined over the range of temperatures for each solvated structure using Rietveld refinement through the Topas software in the batch processing sequential mode (TOPAS Academic V5).[25] The fitting of the patterns near the transition were revisited due to the automated procedures not coping with the multiple phases and the unit cell parameters used in the plots. For the low-temperature phase of the DMA solvate, the structure was solved using DASH using the 100K data.[26] This structure was used in the Rietveld refinement of the low-temperature powder data.

5.3.5 Thermal Analysis

Differential Scanning Calorimetry (DSC) and Thermal Gravimetric Analysis (TGA) was carried out using The STA 449 F1 Jupiter®. Samples (*ca.* 4-6 mg) were loaded into aluminium pans with pierced lids and sealed. The temperature programme was as follows: 20-minute isothermal step (293 K), heat (293-493 K, 10 K/min), cool (493-293 K, 10 K/min) and a final isothermal step for 5 minutes (293 K). Helium was used as a purge and protective gas at a rate of 50 ml/min and 20 ml/min respectively. Data was analysed using NETZSCH Proteus Thermal Analysis 8.0.2. Thermal data can be found in

.

5.3.6 FTIR Spectroscopy

Crystallisation behaviour from methanol and ethanol were different, therefore we used IR to assess the solutions to see if there was any difference using the solutions. The filtered supernatant solution collected after slurrying was analysed prior to crystallisation. FTIR spectra were collected using a Shimadzu IRSpirit Fourier Transform Infrared Spectrophotometer with QATR-S single-reflectance attenuated total reflectance (ATR) probe. Parameters for data collection were transmittance measurement mode and Happ Genzel apodization. Spectra resolution was set to 4 cm^{-1}, with 64 scans per spectrum in the range of 400 to 4000 cm^{-1}. Background scans were conducted on the pure solvent between each sample to remove interference from the sample scans.

5.4 Results and Discussion

Nifedipine is a dihydropyridine compound with multiple functional groups that potentially allow for hydrogen bonding with solvents. Solvents selected for this study were based on the two nifedipine solvates deposited in the Cambridge Structural Database (CSD): 1,4-dioxane (N_{14DIO}) and dimethyl sulfoxide (N_{DMSO}).[16, 27, 28] Seven new solvated structures were discovered in this investigation, providing an expansion of the crystal structure landscape of nifedipine. Solvates were produced from various solvent systems: morpholine, tetrahydrofuran, pyridine, dimethylacetamide (2 polymorphs), dimethylformamide and methanol – in addition to the known 1,4-dioxane and dimethyl sulfoxide structures. The remaining solvents recrystallised the thermodynamically stable Form A nifedipine from slow evaporation and slurry routes (Figure 5.2).

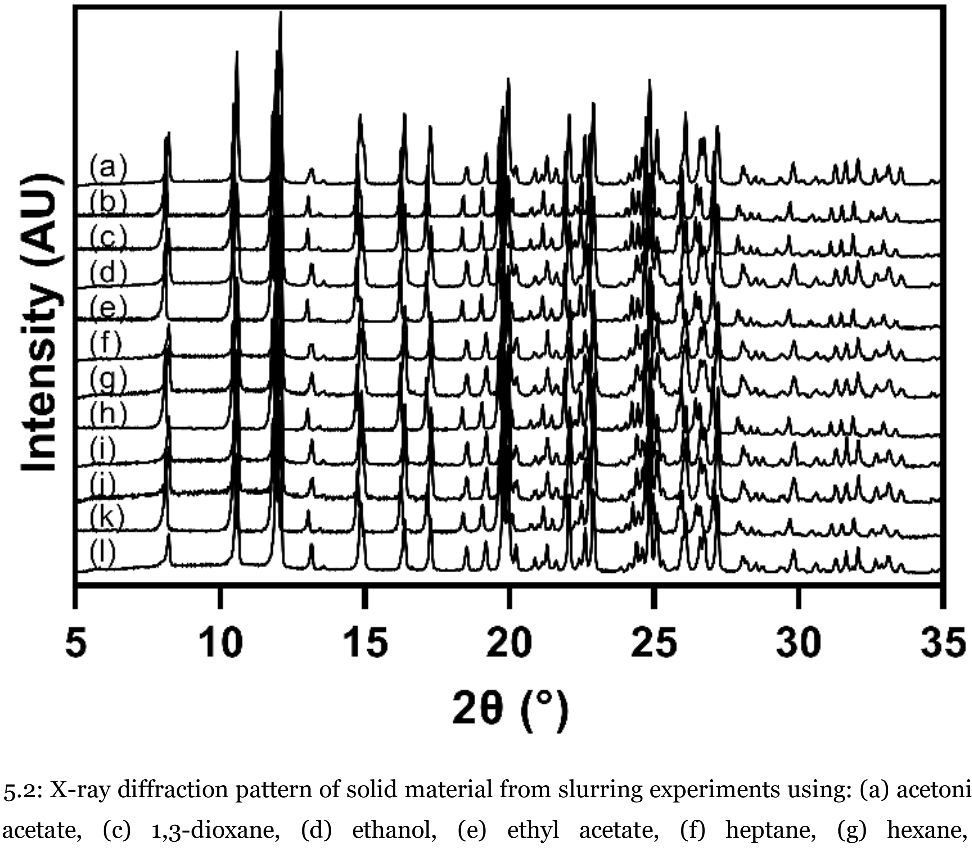

Figure 5.2: X-ray diffraction pattern of solid material from slurring experiments using: (a) acetonitrile, (b) butyl acetate, (c) 1,3-dioxane, (d) ethanol, (e) ethyl acetate, (f) heptane, (g) hexane, (h) 2-methyltetrahydrofuran, (i) nitromethane, (j) 2-propanol, (k) water and (l) Form A nifedipine as supplied from AlfaAesar.

To facilitate the discussion of the solvated phases we will first describe the known phases in more detail. The structure of nifedipine Form A (CSD Refcode: BICCIZ) was first reported by Triggle and co-authors.[18] They showed that the ring structure of dihydropyridine is not planar with displacement of the nitrogen atom (N1) and opposite carbon atom (C3) to the same side of the ring, forming a boat-like orientation. Form A crystallises in monoclinic $P2_1/c$ with one molecule in the asymmetric unit. The amine of the dihydropyridine group acts as a hydrogen bond donor, interacting with the carbonyl group of a neighbouring molecule forming zig-zag chains parallel to the *b*-axis (Figure 5.3b). Nitrophenyl groups alternate their position, pointing into and out of the plane of the page, maintaining the T-motif of the molecules (Figure 5.3a). The 2-fold rotation about the *b*-axis allows chains to stack closely, with van der Waals interactions between layers.

Metastable polymorphs of nifedipine have been discovered from the melt of amorphous nifedipine. Structural determination of Form C (CSD Refcode: BICCIZ02) first came from synchrotron powder diffraction,[15] before determination via single-crystal X-ray diffraction.[19] Form C crystallises in $P1$, with two molecules in the unit cell. Identical hydrogen bonding motifs are observed in both of the mentioned nifedipine polymorphs, but in this case is observed to propagate in the [011] direction. Unlike Form A, these chains consist of the two symmetry-independent molecules forming an ABAB motif. Short-contact interactions are present between the chains, but the zig-zag pattern is not present (Figure 5.3c). Form C is slightly denser than Form A, at ambient temperature, 1.382 and 1.378 g/cm^3 respectively, which gives a reduction in the void space from 18.1% of the unit cell in Form A to 13.5% in Form C.[28]

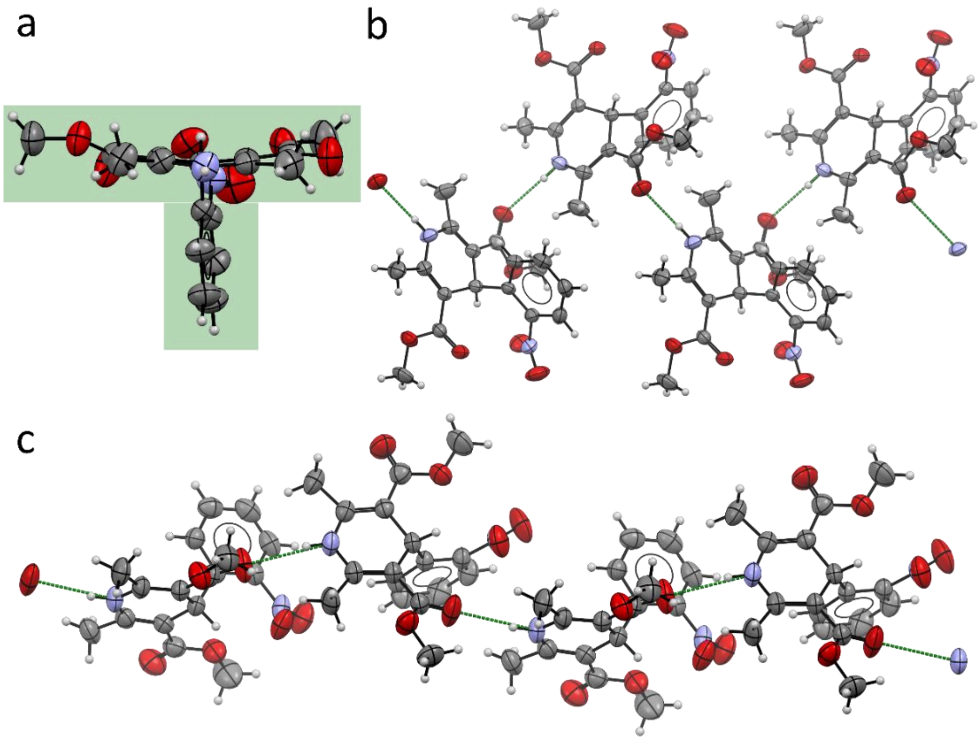

Figure 5.3: a) The molecular structure of NIF showing the T-motif. Structural comparison of NIF chains connected via NH···O hydrogen bonds in (b) Form A (BICCIZ07) and (c) Form C (BICCIZ03). Note the zig-zag-like hydrogen bonding pattern in Form A compared with the more linear pattern in Form C.

Table 5.2: Unit cell parameters of six identified polymorphs of nifedipine.

Form	**α (Form A) 100 K[20]**	**β (Form C) 100 K[19]**	**β' 338 K [20]**	**γ 100 K [20]**	**γ' 250 K [20]**	**δ 100 K [20]**
Refcode[a]	BICCIZ07	BICCIZ 02	BICCIZ08	BICCIZ09	BICCIZ11	BICCIZ12
a (Å)	10.567(3)	9.6661(6)	9.696(2)	19.065(6)	11.435(4)	11.905(4)
b (Å)	10.408(3)	13.7006(8)	14.231(3)	11.506(4)	12.244(4)	10.908(3)
c (Å)	14.788(4)	14.1184(9)	14.463(3)	15.109(5)	12.327(4)	12.779(4)
α (°)	90	61.028(3)	61.90(3)	90	75.535(16)	90
β (°)	95.028(12)	79.631(4)	80.40(1)	108.962(18)	89.055(16)	106.980(9)
γ (°)	90	81.904(4)	81.80(1)	90	84.774(19)	90
Volume (Å^3)	1620.2(8)	1605.89(17)	1731.0(7)	3134.7(18)	1664.2(10)	1587.2(8)
Space Group	$P2_1/c$	$P1$	$P1$	$P2_1/c$	$P1$	$P2_1/n$

[a] Taken from the CSD.[28]

5.4.1 Structural similarity

Our investigation first looked at solvents with ring systems similar to N_{14DIO}. Crystallographic information can be found in Table C1 in Appendix C. Initially, we will provide a brief structural description of the 1,4-dioxane solvate as there is some isostructural behaviour in these systems.

5.4.1.1 N_{14DIO}

The crystal structure of the 1,4-dioxane solvate was first discussed in 2003 by Caira *et al.*,[16] with the hydrogen bond acceptor having the ability to form a hydrogen bond at either side of the molecule; not possible for solvents including pyridine and THF. The asymmetric unit consists of one molecule of nifedipine and half a molecule of 1,4-dioxane leading to a 2:1 solvate. The solvent molecule takes a chair conformation and is bonded to the dihydropyridine group of the nifedipine via a O···HN hydrogen parallel to the *b*-axis. The main body of the nifedipine molecule lies approximately on the (2 1 0) plane with the nitrophenyl group lying perpendicular to this. The main body of the dioxane molecule is orientated perpendicular to the (2 1 0) plane. Figure 5.4 shows how the layers stack perpendicular to the *a*-axis.

5.4.1.2 N_{MORPH}

The structure of the morpholine solvate (N_{MORPH}) is isostructural to N_{14DIO}, triclinic ($P1$) with similar unit cell lengths (Table 5.3). Morpholine is heterocyclic, orientating itself in the chair conformation, possessing one hydrogen bond donor (amine functional group) and two hydrogen bond acceptors, from the oxygen and nitrogen atoms at positions 1 and 4 in the oxazine ring. Like the dioxane solvate, the main body of nifedipine lies on the (2 1 0) plane, with the nitrophenyl roughly perpendicular (87.62°). The orientation of the nitrophenyl group separates the 2:1 (nifedipine: morpholine) molecular unit within the same layer, limiting interaction between them. Layers are connected via weak van der Waals forces in the direction of the *a*-axis. On further comparison, within the bounds of the modelling we note that the position of the 1,4-dioxane molecules overlay well with the symmetry generated molecule. The morpholine molecule does not overlap fully that may indicate that the morpholine molecules reside in slightly different orientations in the crystal leading to a looser packing. This could provide an explanation as to its desolvation and the difference in thermal behaviour of the isostructural solvates. The hydrogen bond donor on morpholine is in close proximity to the nitro group of a neighbouring molecule translated along the *b*-direction via $NH_{(MORPH)}\cdots O_{(NIF)}$, forming a ring within the crystal structure (Figure 5.4d). The torsional angle around the C17-C1-N1-O2 is within standard deviation (-31.14(14) ° N_{DIO} vs -31.75(12) ° N_{MORPH}) which suggests that the torsional angle has no impact on the packing of the solvated crystal structure. Using the CSD hydrogen bond statistics tool, we were able to determine that the hydrogen bonding between nifedipine and morpholine is not unusual. The distance between N_2 (donor) and N3 (acceptor) is 3.02 Å; the mean being 3.2 Å from 249 hits on the database. The second hydrogen bond featuring the oxygen of the morpholine has a distance of 2.98 Å; with the database showing a mean of 3.07 Å calculated using 848 structures.

Table 5.3: Unit cell parameters of nifedipine solvates N_{14DIO} and N_{MORPH}.

	***a* (Å)**	***b* (Å)**	**c (Å)**	**α (°)**	**β (°)**	**γ (°)**
N_{14DIO}	7.5604(10)	11.1362(10)	11.8563(10)	73.606(10)	73.185(10)	75.643(10)
N_{MORPH}	7.5423(6)	11.1513(9)	11.8923(9)	73.997(2)	73.957(2)	75.253(2)

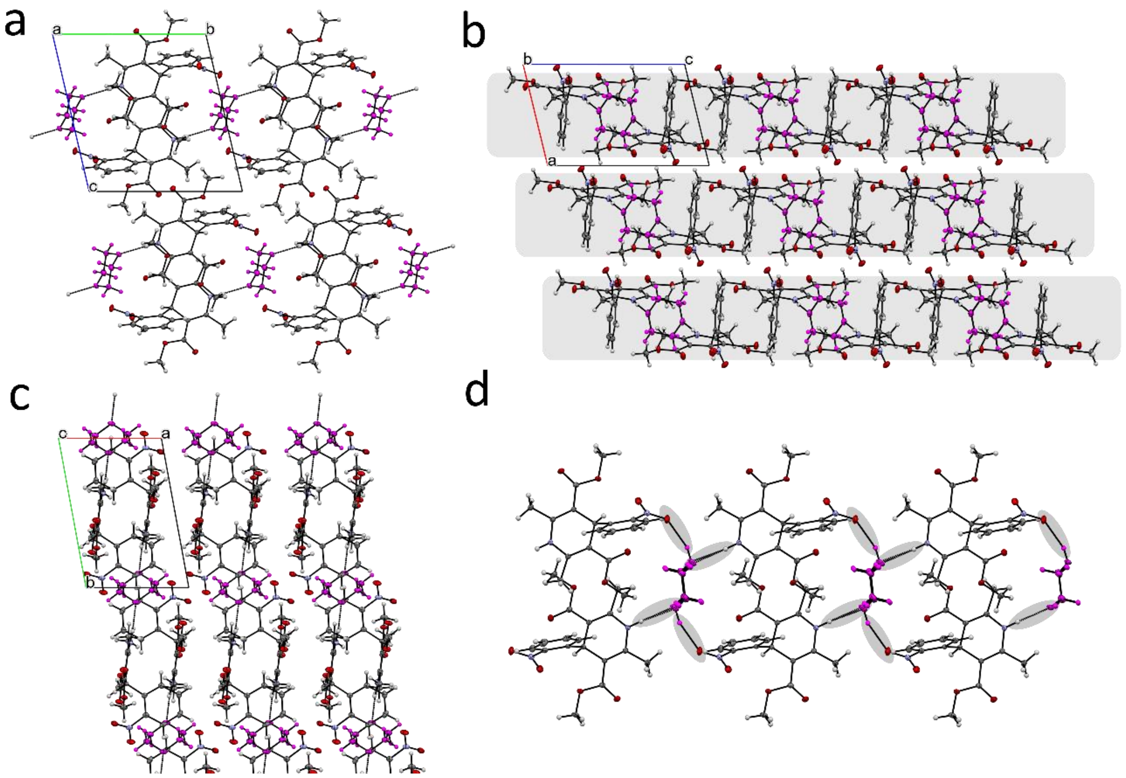

Figure 5.4: Structure of 1,4-dioxane-nifedipine solvate shown down crystallographic a) a-, b) b- and c) c-axis. Layers are seen in the structure, parallel to the c-axis and perpendicular to the a-axis; highlighted in Figure b. Nitrophenyl groups separate the layers that run perpendicular to the a-axis. d) shows the isostructural morpholine solvate within the isostructural solvate in both of the modelled orientations, forming a ring structure. Molecules are rotated slightly rotated with respect to each other, showing movement within the structure.

5.4.1.3 N_{DMSO}

Despite the obvious differences in the molecular structure of the solvent, the next three structures show a significant similarity to the N_{DIO} and N_{MORPH} structures. The structure of N_{DMSO} was previously determined by Klimakow and co-authors.[27] It crystallises in the triclinic space group *P*1 with one nifedipine and one DMSO molecule in the asymmetric unit. The structure is isostructural with N_{14DIO} and N_{MORPH}. At 100K cell lengths, *a, b,* and *c,* are 7.9036(10), 11.8798(15) and 11.9713(15) Å respectively, with angles, α, β and γ of 67.099(3) °, 78.341(3) ° and 79.126(4) ° respectively. Hydrogen bonding connects the two components between the dihydropyridine nitrogen of NIF and oxygen of the DMSO (D···A, N2H2···O7) with a distance of 2.8597(18) Å compared with 2.877(2) Å observed in the ambient structure.[27] The DMSO molecules of neighbouring groups are arranged in an anti-parallel arrangement forming units of two nifedipine and two DMSO. The orientation of the nitrophenyl groups aid the overlap between the nitro and methoxy group of a neighbouring molecule, translated down the *a*-axis.

5.4.1.4 N_{DMA}

N_{DMA} was collected at 173 K due the structure undergoing a transition at low temperature (143 K), which is discussed later. Crystallising with a P1 space group, the cell lengths, *a, b,* and *c, are* 7.6638(10), 11.6006(16) 13.9001(19) Å respectively, with angles α, β and γ, of 65.688(3) °, 76.979(3) ° and 92.932(3) ° respectively. There is one molecule of nifedipine and one molecule of DMA in the asymmetric unit. Hydrogen bonding links nifedipine to the DMA molecule via the NIF pyridine group, as seen in the ring solvate structures, but hydrogen bonding is absent between nifedipine molecules. Packing of N_{DMA} is similar to N_{DMSO}, showing a similar T-

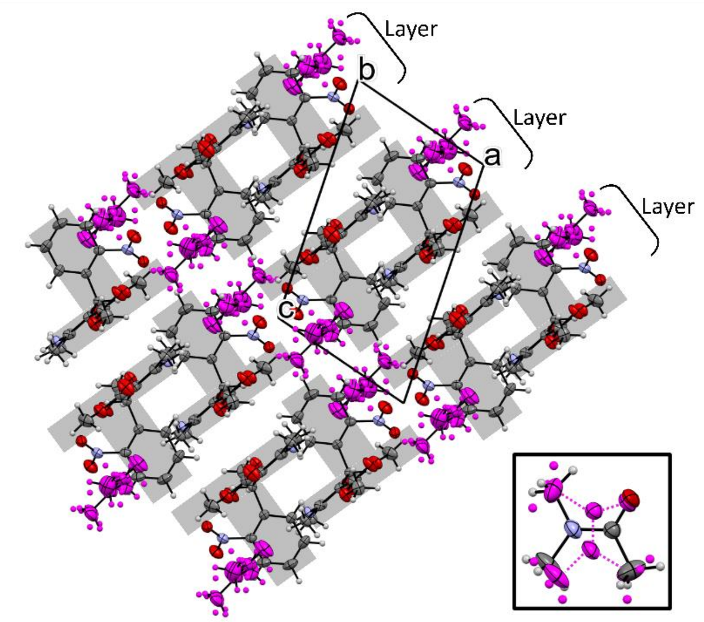

Figure 5.5: Layers in the NDMA structure. Nitrophenyl groups are orthogonal to the main body of the nifedipine, fitting in the opposite chain forming a bilayer, forming a T-motif. DMA molecules are coloured pink for visual ease. Inset shows the two orientations DMA occupies in the structure, coloured in pink and by element.

motif. The main body of the nifedipine molecules sits on (101) plane, with nitrophenyl groups orthogonal to this. The solvent molecules show disorder, occupying two positions in the structure. The structure was also collected at 297 K and did not display any disorder within the structure. DMA molecules sit planar with respect to the dihydropyridine ring (6.80°) of nifedipine and form a channel with the other solvent molecules, with little interaction between them. As shown in Figure 5.5 the main body of the nifedipine molecules align anti-parallel to each other in the unit cell, whilst the nitrophenyl groups are orthogonal and fit into the next layer forming a bilayer. Viewed along the *b*-direction, these bilayers are separated from others on the (101) plane by the solvent channels.

During the low-temperature XRD collection of N_{DMA}, the single crystal was observed to disintegrate at 100 K, turning opaque on cooling under the Cryostream. A sample was loaded into a capillary to investigate whether a structure could be solved from the powder data. Figure 5.6a shows the surface plot of the XRPD data captured every 10K from 293K down to 103 K. The transition was clearly observed at 143 K, and this phase remains stable to lower temperatures. The structure was solved with a stoichiometric ratio of 1:1, identical to that of the structure collected at 173 K, but without disorder in the solvent molecules. Unit cell details are provided in Table 5.4. A shift in molecules is also observed after the transition to the 103K structure. As shown in Figure 5.6b, there is a slight rotation in the nitrophenyl group of the nifedipine. There is also a reduction in unit cell volume when the temperature of the system is decreased, with efficient packing of the molecules. At 173 K, the cell volume is 1082.7(3) Å^3, which decreased to 1047.68 Å^3 at 103 K.

Table 5.4: Data collection parameters and unit cell information for N_{DMA} collected at 103 K and 173 K.

Temperature Collection	**103 K**	**173 K**
Method of Collection	Powder	Single Crystal
Space Group	*P* 1	*P* 1
Cell Lengths (Å)	*a* = 7.48, *b* = 11.36, *c* = 13.87	*a* = 7.6638(10), *b* = 11.6006(16), *c* = 13.9001(19)
Cell Angles (°)	α = 65.13, β = 74.73, γ = 85.87	α = 65.688(3), β = 76.979(3), γ = 92.932(3)
Cell Volume (Å^3)	1047.68	1082.7(3)

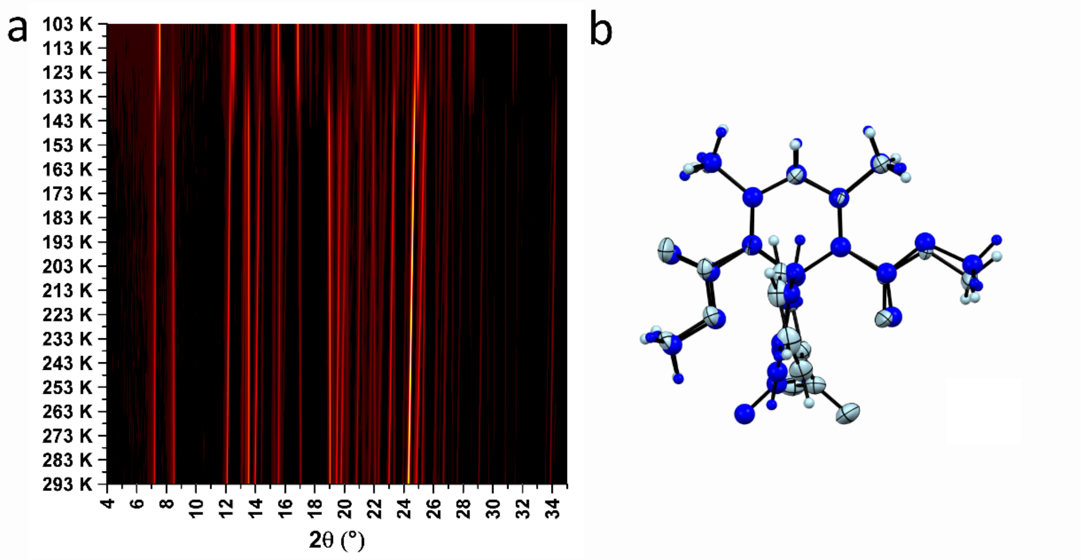

Figure 5.6: Low temperature transition of N_{DMA}; a) Surface plot of XRPD patterns cooling from 293 K to 103 K – temperature is displayed on the y-axis. Structures of the new phase were solved at 103 K. b) Structures of 103 K (dark blue), and 173 K (light blue) are displayed with pyridine groups overlaid.

5.4.1.5 N_{DMF}

The N_{DMF} solvate is isostructural to N_{DMA}, however we note the difference in collection temperature; N_{DMF} was collected at 100 K which results in tighter packing of the molecules. Again, we see hydrogen bonding involving the dihydropyridine of the nifedipine, N2H2···O7 (2.8533(12) Å). The DMF molecules reside in a similar location of the structure to the DMA, but the DMF molecules sit perpendicular with respect to the main body of the nifedipine molecules (65.49°), differing from DMA. The solvent molecules are not disordered and are fixed in one orientation, sitting in channels parallel to the *a*-axis. In this orientation the DMF is able to interact with the methoxyl group of the nifedipine molecules in the layer above and a second symmetry-related molecule interacts from above. The disorder present in DMA could be attributed to the additional methyl group compared to DMF. The additional methyl permits the rotation of molecule without a significant change to the overall space taken up by the solvent. Essentially, the central two carbon atoms of DMA are the only atoms that require additional modelling. A rotation of DMF would require additional space in the N_{DMF} structure leading to inefficiency in packing.

5.4.2 Thermal analysis of structurally similar compounds

Thermal analysis was conducted on the powder recovered from the slurries. We investigated the desolvation of the nifedipine solvates using variable-temperature XRPD. Preliminary data was collected using STA (DSC-TGA), providing an indication of the temperature range of desolvation (Table 5.5). Simulated powder patterns were produced from the single-crystal XRD data and compared to that of the XRPD patterns collected on the slurried samples, confirming their identity. Through the VT-XRPD we were able to follow the desolvation of the crystal structures on increasing temperature to the thermodynamically stable Form A.

Table 5.5: Thermal analysis for nifedipine solvates.

Solvent	**Expected Mass Loss (%)**[a]	**Observed Mass Loss (%)**[b]	**Solvent Loss Temperature Range (K)**	**Boiling point of Solvent (K)**
1,4-dioxane	11.28	8.07	392-402	374
Morpholine	11.17	11.81	379-390	402
Tetrahydrofuran	9.43	9.48	349-361	339
Pyridine	18.59	17.06	304-352	388
Dimethyl sulfoxide	18.41	32.47	293-473	462
Dimethylacetamide	20.10	23.61	369-383	438
Dimethylformamide	17.43	16.98	370-410	426
Methanol	8.47	1.69	329-337	338

[a] Calculated from SC-XRD data. [b] Calculated from TGA data.

5.4.2.1 N_{14DIO}

The behaviour of N_{14DIO} during heating is anisotropic, with greater increase in the *a*-axis which is perpendicular to the layers in the structure and where hydrogen bonding is absent (Figure 5.7b). Desolvation is clean with a clear transition from the solvate to Form A nifedipine beginning at 373 K (Figure 5.7a and c). This is close to the boiling point of 1,4-dioxane at 374 K. Full desolvation to the stable polymorph of nifedipine is complete by 408 K. A rationale for the desolvation process is that the dioxane molecules are located in channels parallel to the *b*-axis, so as heat is applied and the structure expands, solvent molecules can easily escape the structure. Over the timescale of the XRPD run there is no indication of amorphisation before crystallisation and the crystallinity is maintained throughout the transition to thermodynamically stable Form A.

5.4.2.2 N^{MORPH}

N_{MORPH} shows similar behaviour to N_{DIO}. The greatest change is seen in the *a*-axis where hydrogen bonding is absent Figure 5.8b). Morpholine contains an oxygen and nitrogen as opposed to the two oxygen atoms in 1,4-dioxane, making the hydrogen bond between solvent and nifedipine stronger, however the onset of desolvation starts much earlier. Reflections for Form A appear at 358 K, with full desolvation by 388 K which is lower than the boiling point of morpholine, 402 K (Figure 5.8a). Slight changes in orientation in the crystal structure are noted which may indicate slightly different orientations of morpholine, aiding the desolvation by making it easier for the morpholine to escape. Hydrogen bond statistics show that the NH···N (3.02 Å) bond length is slightly longer than NH···O (2.98 Å) and could result in a weaker interaction. In turn, this would ease desolvation of morpholine from the structure. Desolvation has an onset of 379 K and endpoint of 390 K, in the DSC thermograph (Figure 5.8c). The differences seen between VT-XRPD and DSC are due to differences in heating rate and the heat gradient of the capillary used in XRPD.

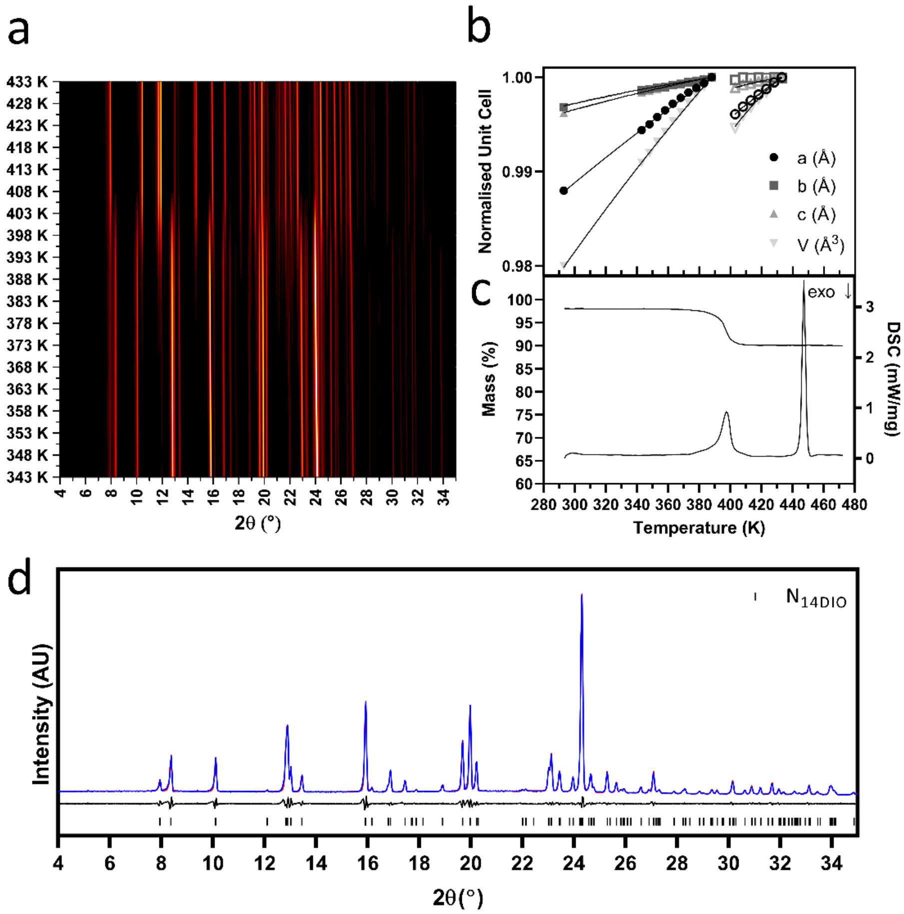

Figure 5.7: Thermal data of N_{14DIO} capturing the desolvation to Form A nifedipine a) Surface plot of VT-XRPD data from 343 K to 433 K. b) Unit cell parameters from Rietveld refinements of each XRPD pattern. Closed symbols represent data for the solvate, open symbols represent data for desolvated structure. c) DSC and TGA trace for N_{14DIO}. d) XRPD pattern for the 1,4-dioxane solvate collected at 293 K. The experimental data is shown in blue, whilst the calculated profile is shown in red. The difference profile is displayed underneath the diffraction pattern showing that they agree. The calculated reflections are based on the single-crystal data collected for N_{14DIO}.

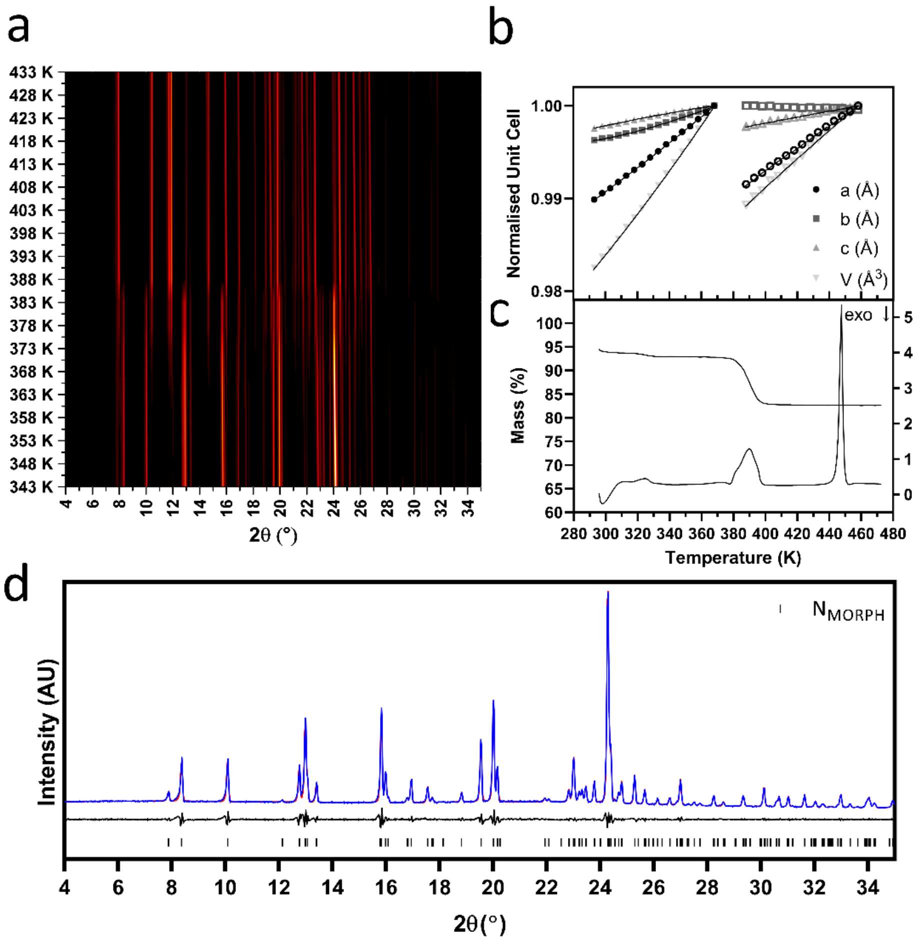

Figure 5.8: Thermal data of Nmorph capturing the desolvation to Form A Nifedipine a) Surface plot of VT-XRPD data from 343 K to 433 K. b) Unit cell parameters from Rietveld refinements of each XRPD pattern. Closed symbols represent data for the solvate; open symbols represent data for desolvated structure. c) DSC and TGA trace for Nmorph. d) XRPD pattern for the morpholine solvate collected at 293 K. The experimental data is shown in blue, whilst the calculated profile is shown in red. The difference profile is displayed underneath the diffraction pattern showing that they agree. The calculated reflections are based on the single-crystal data collected for Nmorph.

5.4.2.3 N_{DMSO}

Thermal behaviour of N_{DMSO} is anisotropic with the greatest expansion in the *a*- and *c*-axis, which both show identical behaviour (Figure 5.9b). Desolvation of N_{DMSO} is considerably different to that of the ring structured solvates previously discussed. DMSO remains present in the crystal structure for a significant amount of time due to the strength of interaction between the solvent and nifedipine, together with its high boiling point (462 K). During STA analysis, we observe a constant mass loss from 293 K which encompasses the melt and decomposition of nifedipine, making desolvation difficult to distinguish (Figure 5.9c). DMSO is known to be difficult to remove from samples,[13] hence why mass loss observed during TGA analysis was 32.47 %, greater than the expected mass loss of 18.41%, calculated from the known stoichiometry (
). DMSO molecules are located within channels in the crystal structure, parallel to the *a*-axis, which according to literature should aid the escape of the solvent,[14] however the boiling point of DMSO is greater than the melting point of the thermodynamically stable polymorph of nifedipine (*ca.* 446 K). VT-XRPD gives us a clearer indication of the desolvation of the structure, with Form A becoming apparent at 363 K (Figure 5.9a). The diffraction patterns from this point are poor quality, with a reduction in reflection intensity and observation of an amorphous background. We speculate that we are observing DMSO being released from the structure, but due to its high boiling point, DMSO does not evaporate from the capillary therefore dissolution of nifedipine is observed prior to the melt. This is also supported by the DSC trace, where no melting endotherm of nifedipine is observed.

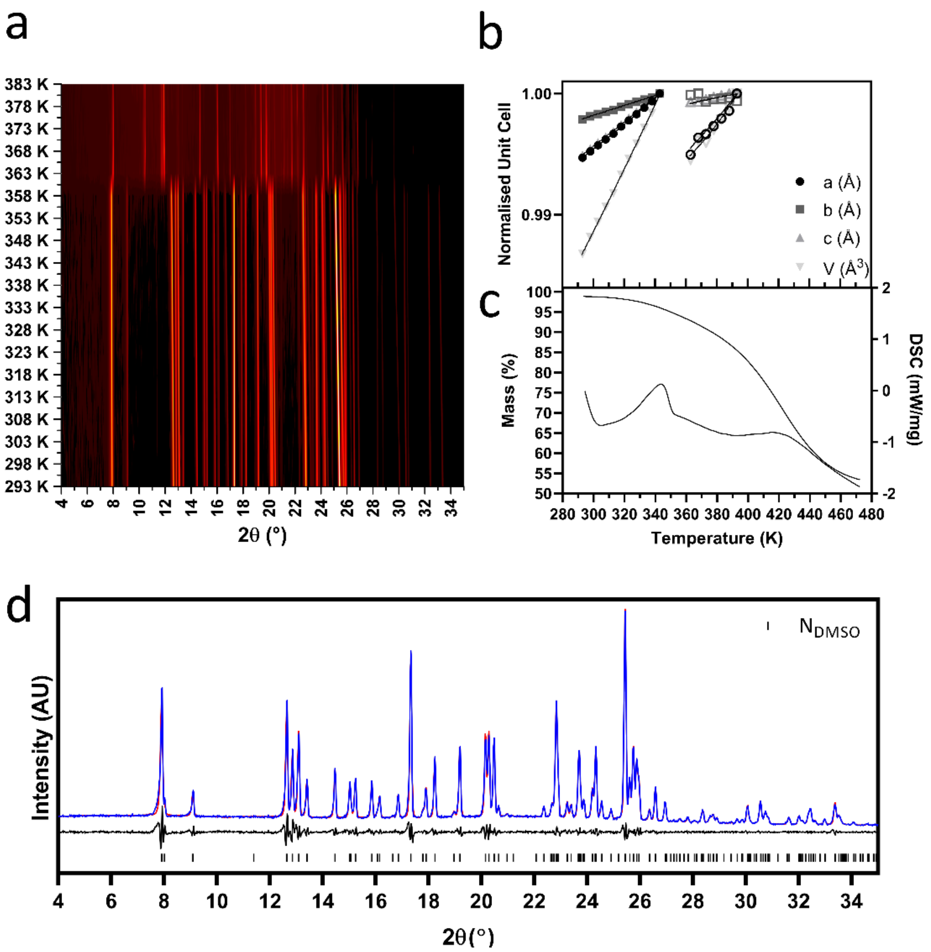

Figure 5.9: Thermal data of N_{DMSO} capturing the desolvation to Form A Nifedipine a) Surface plot of VT-XRPD data from 293 K to 383 K. b) Unit cell parameters from Rietveld refinements of each XRPD pattern. Closed symbols represent data for the solvate; open symbols represent data for desolvated structure. c) DSC and TGA trace for N_{DMSO}. No prominent melting event is witnessed. d) XRPD pattern for the DMSO solvate collected at 293 K. The experimental data is shown in blue, whilst the calculated profile is shown in red. The difference profile is displayed underneath the diffraction pattern. The calculated reflections are based on the single-crystal data collected for N_{DMSO}.

5.4.2.4 N^{DMA}

N_{DMA} shows similar thermal behaviour to N_{DMSO}, with DMA remaining in the crystal structure until 383 K, as shown in the unit cell plot (Figure 5.10b). Greatest expansion in the a-axis, the direction of the layers which are connected via short contacts. The first endothermic event in the DSC trace ends at 383 K, simultaneous with a mass loss of 23.61% which accounts for the removal of DMA (Figure 5.10c, Table 5.5). VT-XRPD confirms this observation, with the solvate present until 383 K (Figure 5.10a). Again, we see differences between the characterisation techniques. STA shows the loss of DMA and subsequent melt of nifedipine at 444 K. VT-XRPD shows that similar to DMSO, DMA is removed from the crystal structure but remains in the capillary, causing the dissolution of nifedipine hence poor-quality diffraction patterns beyond 383 K.

5.4.2.5 N^{DMF}

NDMF is structurally similar to N_{DMA}, with greatest expansion in the same direction, however, this is where the similarities end. The unit-cell parameters for the solvate can be fit up to 348 K, and Form A beyond 363 K (Figure 5.11b). Between this, reflections for another form are observed in the VT-XRPD, between 348 and 363 K, but cannot be fit to either of the solvate or Form A (Figure 5.11a). These reflections may be attributed to the metastable Form C polymorph, or a new phase (Figure 5.12). This change in phase is observed in the DSC showing a sharp endotherm at 365 K, followed by a broad endothermic event that leads to the melt of Form A nifedipine (Figure 5.11c). The TGA confirms two different weight loss events, one corresponding to the loss of the solvent and second, the melt and subsequent slow decomposition of nifedipine. This is not observed in any of the other desolvation experiments which may suggest that either DMF is accelerating the decomposition of nifedipine, or that the additional phase shows chemical instability compared with Form A.

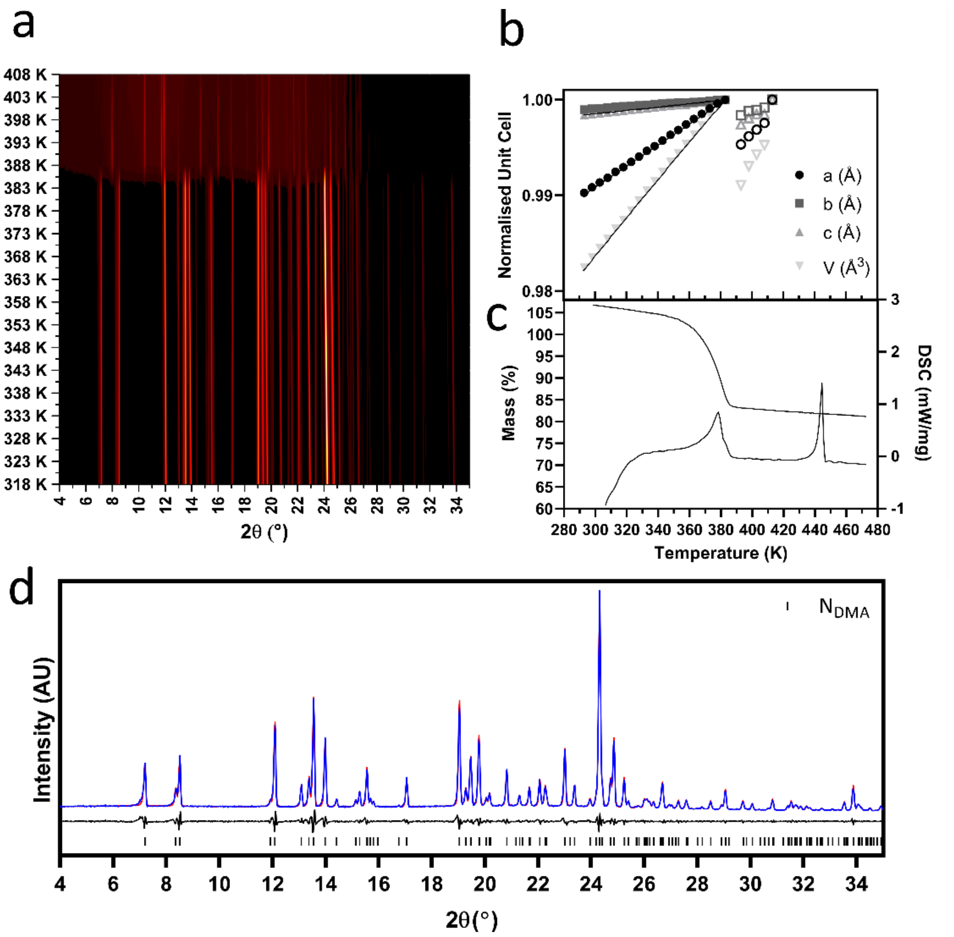

Figure 5.10: Thermal data of N_{DMA} capturing the desolvation to Form A Nifedipine a) Surface plot of VT-XRPD data from 293 K to 403 K. Melt of the sample is captured from 388 K. b) Unit cell parameters from Rietveld refinements of each XRPD pattern. Closed symbols represent data for the solvate; open symbols represent data for desolvated structure. c) DSC and TGA trace for N_{DMA}. d) XRPD pattern for the DMA solvate collected at 293 K. The experimental data is shown in blue, whilst the calculated profile is shown in red. The difference profile is displayed underneath the diffraction pattern. The calculated reflections are based on the single-crystal data collected for N_{DMA}.

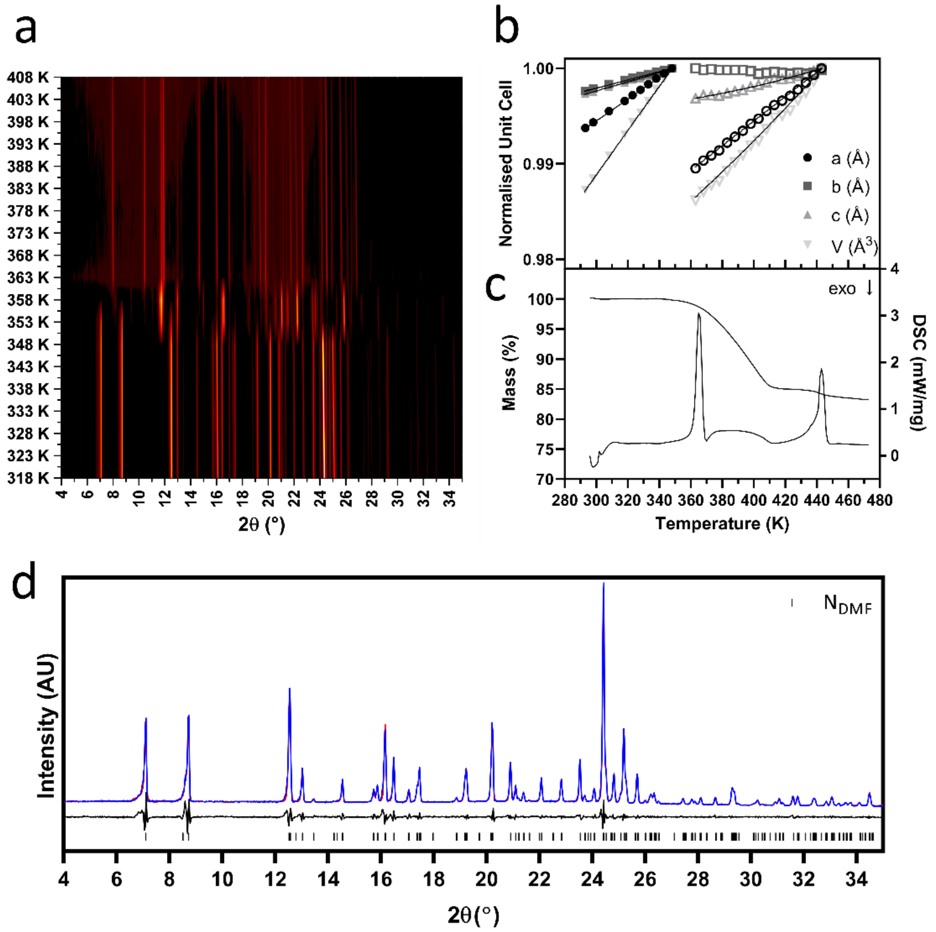

Figure 5.11: Thermal data of N_{DMF} capturing the desolvation to Form A Nifedipine a) Surface plot of VT-XRPD data from 293 K to 363 K. b) Unit cell parameters from Rietveld refinements of each XRPD pattern. Closed symbols represent data for the solvate; open symbols represent data for desolvated structure. c) DSC and TGA trace for N_{DMF}. d) XRPD pattern for the DMF solvate collected at 293 K. The experimental data is shown in blue, whilst the calculated profile is shown in red. The difference profile is displayed underneath the diffraction pattern. The calculated reflections are based on the single-crystal data collected for N_{DMF}.

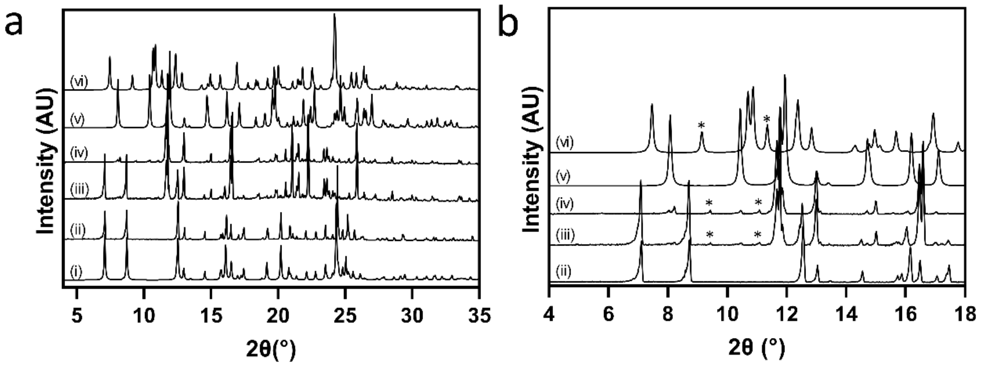

Figure 5.12: XRPD of nifedipine-DMF solvate from 4 to 35°, 2θ. (i) Simulated powder pattern from SC-data. VT patterns at (ii) 293 K; (iii) 353 K and (iv) 358 K. The latter temperatures show the start of desolvation to Form A nifedipine. (vi) Simulated powder pattern of Form A nifedipine from SC-data collected at 297 K and (vi) Powder pattern of Form C nifedipine collected at 296 K (BICCIZ03). b) Expanded view of Figure a, highlighting the region where a form other than Form A appears during desolvation and 353 and 358K. Asterisks indicate reflections that correspond to Form C nifedipine.

5.4.3 Unique solvate structures

5.4.3.1 N_{THF}

Tetrahydrofuran (N_{THF}), a cyclic ether, has the ability to form one hydrogen bond through its oxygen atom. Although collected at 100 K, the modelled structure showed disorder, with the solvent molecules sitting on an inversion centre despite not being centrosymmetric. The crystallographic symmetry opens up the potential for hydrogen bonding in opposite directions. Despite this, the THF is not involved in any hydrogen-bonding interactions at all. NIF molecules form hydrogen bonds between the nitrogen in the dihydropyridine (N2) and the ester carbonyl group of a neighbouring molecule (O6) that resembles the metastable polymorph of NIF, Form C (Figure 5.13). The unit cell parameters and the hydrogen bonding in this structure are similar to Form C but the difference being that the nifedipine molecules are symmetry-equivalent in N_{THF}. The differences between N_{THF} and the Form C polymorph show that there is a translational change in the neighbouring chains that allows the THF to sit in pockets between the chains made by the nitrophenyl rings. There are no opportunities in this pocket for the THF molecules to engage in hydrogen bonding. The addition of the THF into the structure has altered the O2 N1 C1 C2 dihedral angle from 143.29 and 151.77 ° in molecules 1 and 2 of Form C to 133.21° in the N_{THF} structure. Void analysis of the structure indicates a comparable space in each of the forms calculated using a probe radius of 0.5 Å, and approximate grid spacing of 0.2 Å (Form C: 13.5% of the unit cell (217.59 Å^3); N_{THF}: 13% of the unit cell (239.52 Å^3)).

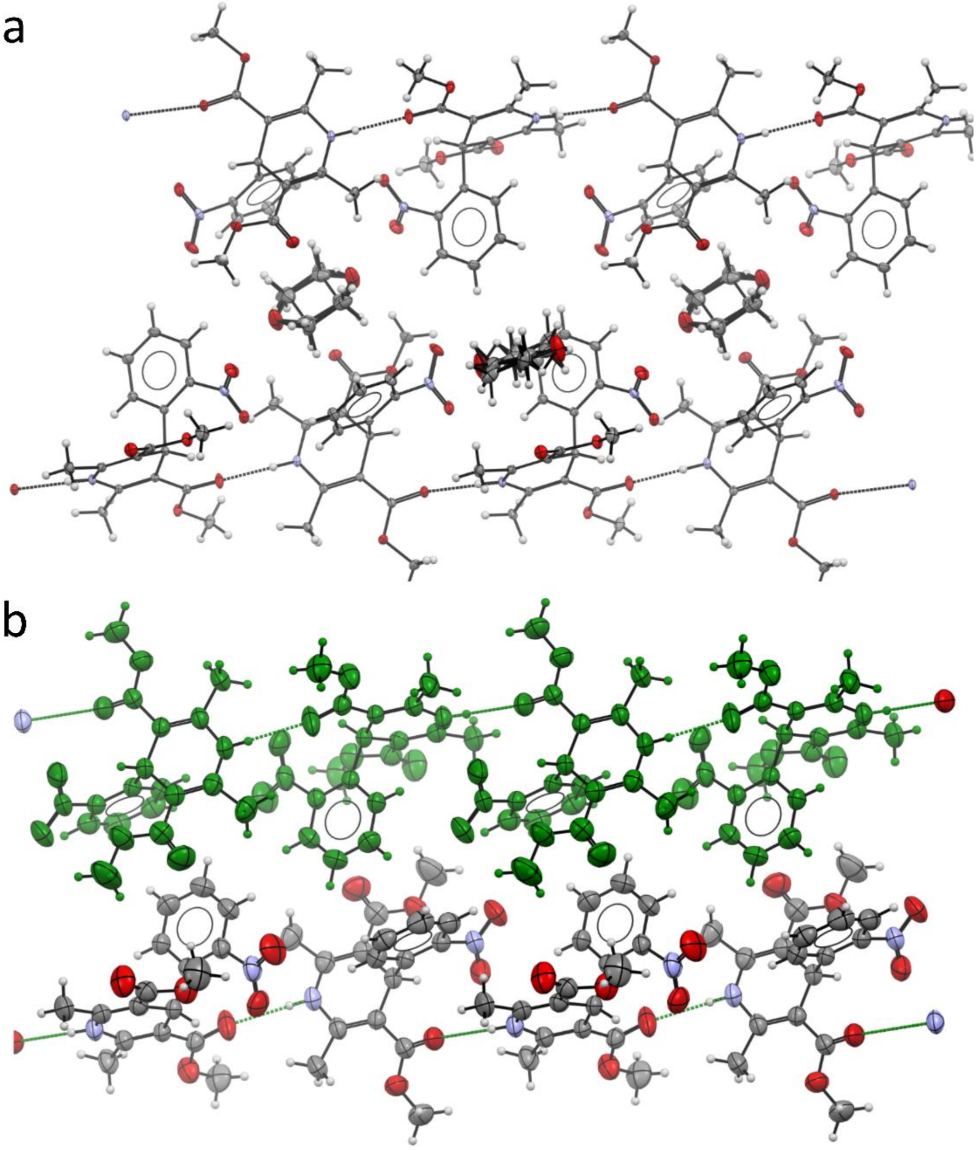

Figure 5.13: The similarities in the hydrogen bonding chains in a) N_{THF} and b) nifedipine Form C indicating the similarity. Neighbouring chains are translated to accommodate the THF molecules in the structure. The green colouring of Form C highlights the neighbouring chain. Both structures were collected at 100 K. The unit cell parameters for Form C have been taken from the CSD (refcode: BICCIZ02) and transformed to equate to the N_{THF} solvate which shows the commonality in the unit cell lengths.[28]

Table 5.6: Unit cell parameters of nifedipine solvate N_{THF} and metastable polymorph Form C. Both structures were collected at 100 K. Form C unit cell parameters have been taken from the CSD (refcode: BICCIZ02).[16] The unit cell lengths are similar if the change in the a- and b-axis are taken into consideration.

	a	***b***	**c**	**α**	**β**	**γ**
N_{THF}	13.9233(14)	9.1421(9)	14.5374(15)	90	96.280(4)	90
Form C Nifedipine	9.6661(6)	13.7006(8)	14.1184(9)	61.028(3)	79.631(4)	81.904(4)

In the THF solvate, there is no hydrogen bonding is present between nifedipine and THF molecules. Expansion of the structure is greatest in the direction of the *a*- and *b*- axis, with both axes exhibiting identical behaviour (Figure 5.14b). This is the direction in which hydrogen bonding between nifedipine molecules is absent. DSC shows us that desolvation takes place between 349 and 361 K, above the boiling point of THF at 339 K. The neat endotherm corresponds to lack of hydrogen bonding present between THF and nifedipine (Figure 5.14c). VT-XRPD shows that desolvation starts to take place as early as 313 K where the Rietveld fit of the XRPD pattern identified the additional peaks to that of Form A nifedipine (Figure 5.14a). The solvate remains in the sample till 348 K, but the unit cell can only be fit till 338 K due to the low level of sample. THF is located within channels of the crystal structure which facilitates an easy route for desolvation. BFDH morphology prediction shows how the THF molecules reside in layers on the largest face of the crystal surfaces that would facilitate the desolvation. Variation in temperature was observed between DSC and VT-XRPD due to experimental differences, i.e., aluminium pan versus borosilicate capillary. Although N_{THF} and Form C nifedipine are structurally similar, we do not see reflections corresponding to Form C during the desolvation. If Form C was crystallised during the desolvation, we should have observed this during the DSC/TGA, but this is not seen. Groof *et al.,* observed that Form C easily converts to thermodynamically stable Form A nifedipine, with increase in temperature from ambient to 120 °C, where an exothermic event was observed.[29] TGA data can also be used to confirm the stoichiometry of the crystal structure that is provided by single-crystal XRD. The calculated ratio of nifedipine to THF is 2:1, with a weight loss of 9.43% after desolvation, which agrees with the experimental data with a weight loss of 9.48% (Table 5.5).

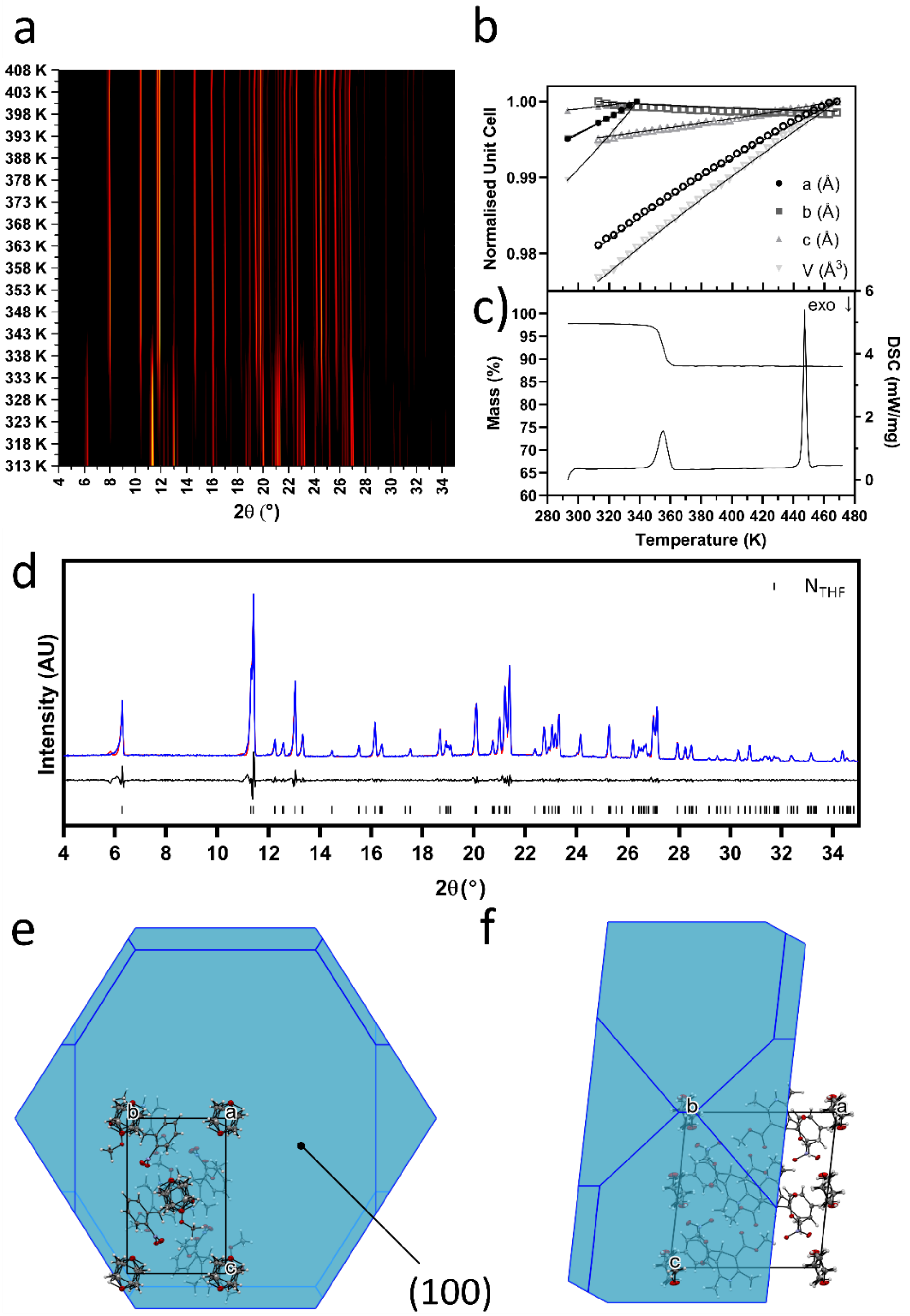

Figure 5.14: Thermal data of NTHF capturing the desolvation to Form A nifedipine a) Surface plot of VT-XRPD data from 313 K to 408 K. b) Unit cell parameters from Rietveld refinements of each XRPD pattern. Closed symbols represent data for the solvate; open symbols represent data for desolvated structure. c) DSC and TGA trace for NTHF. d) XRPD pattern for the THF solvate collected at 293 K. The experimental data is shown in blue, whilst the calculated profile is shown in red. The difference profile is displayed underneath the diffraction pattern showing that they agree. The calculated reflections are based on the single-crystal data collected for NTHF. The BFDH morphology for NTHF along e) a-axis and f) b-axis indicating the placement of the THF molecules with respect to the largest face of the crystal. The location of the THF molecules facilitates the loss on heating.

5.4.4 Pyridine and Methanol

5.4.4.1 N_{PYRI}

N_{PYRI} contains two nifedipine and two pyridine molecules. This solvate crystallises in the $P2_1$ space group with cell lengths of 9.4363(10) Å, 14.4247(14) Å and 15.1387(15) Å for *a*, *b,* and *c* respectively, and a β angle of 96.160(3) °. Similar to the N_{14DIO} and N_{MORPH} structures the hydrogen bond forms between the solvent molecules and nifedipine via the nitrogen acceptor group that is parallel to the c-axis. The main body of the nifedipine molecule and the pyridine lie parallel to one another. This enables van der Waals interactions between the pyridine and neighbouring nifedipine molecules. As we extend out along the *c*-axis, the close contacts between the nitro groups and neighbouring methoxy group become evident. The pyridine molecules are located in small pockets, sandwiched between the methoxy group and ring system of a translated molecule. When viewed down the *c*-axis, the intramolecular structure resembles a T-motif, with the nitrophenyl group perpendicular to the rest of the molecule, as shown in Figure 5.15 (molecule 1 = 86.25 °; molecule 2 = 87.79 °). In this view, the T-motif of sequential molecules along the c-axis are head-to-toe and form a motif that is repeated throughout the structure. These motifs form a herringbone structure with each other. Layers of similarly orientated motifs are parallel to a-c plane.

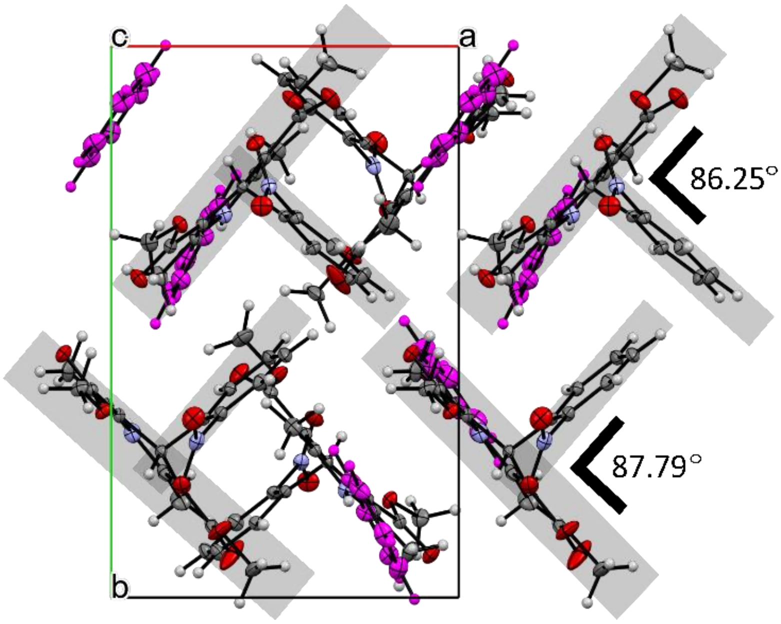

Figure 5.15: Structure of N_{PYRI} viewed down the c-axis. Nifedipine molecules are highlighted in grey indicating the T-motif. The nitrophenyl groups are rotated by 86.25° and 87.79° in molecules 1 and 2 respectively; pyridine molecules are coloured pink for clarity,

The diffraction pattern produced for the pyridine solvate showed the sample to be Form A nifedipine, indicating that the pyridine solvate is likely to be a metastable form. Single crystals of the pyridine solvate, produced by slow evaporation, were ground for analysis, which may have facilitated an increased rate of desolvation due to decreasing the particle size thus increasing surface area. N_{PYRI} shows noticeable expansion in the *b*-axis, the direction perpendicular to the layers within the crystal structure, where there is no hydrogen bonding but π-π interactions between molecules. Unit cell parameters of the solvates could only be determined between 293 and 313 K, therefore with the limited data, it is difficult confirm whether the thermal behaviour is anisotropic (Figure 5.16b). DSC for N_{PYRI} shows desolvation of the system has an onset of *ca.* 304 K and is complete by *ca.* 352 K, below the boiling point of pyridine (388 K). The DSC thermograph shows a complex endotherm, with overlapping peaks observed during desolvation which could be due to the different symmetry-inequivalent pyridine molecules being released at slightly different times (Figure 5.16c). VT-XRPD shows rapid desolvation of the sample, with full conversion to Form A nifedipine by 323 K (Figure 5.16a). This inconsistency between STA and XRPD could be attributed to the differences in experimental conditions.

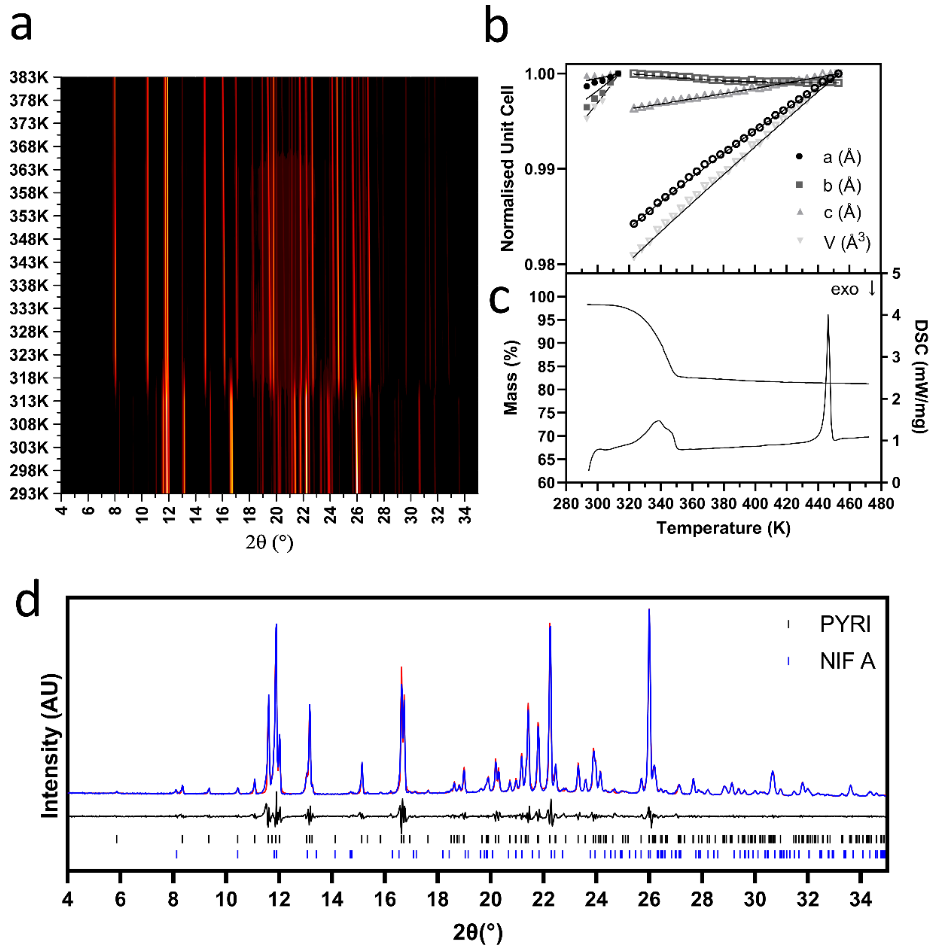

Figure 5.16: Thermal data of NPYRI capturing the desolvation to Form A Nifedipine a) Surface plot of VT-XRPD data from 293 K to 383 K. b) Unit cell parameters from Pawley refinements of each XRPD pattern. Closed symbols represent data for the solvate; open symbols represent data for desolvated structure. c) DSC and TGA trace for NPYRI. d) XRPD pattern for the pyridine solvate collected at 293 K. The experimental data is shown in blue, whilst the calculated profile is shown in red. The difference profile is displayed underneath the diffraction pattern. The calculated reflections are based on the single-crystal data collected for NPYRI and nifedipine Form A.

5.4.4.2 N_{MeOH}

The final structure is N_{MeOH} which was an unexpected solvate, the product of slow evaporation from methanol. This was unlike ethanol which resulted in the recrystallisation of Form A nifedipine, as did the slurry product from methanol. N_{MeOH} is dissimilar to the solvates reported previously; methanol forms two hydrogen bonds via the hydroxyl group, acting as both donor and acceptor to two nifedipine molecules (N2H2···O7, 2.9201(11) Å; and H7O7···O6, 2.7995(10) Å). The ability of the methanol to form two hydrogen bonds leads to a chain structure parallel to the b-axis. This hydrogen-bonded chain structure resembles Form A of nifedipine, which has hydrogen bonds between a carbonyl group and dihydropyridine of neighbouring molecule (Figure 5.17). Chains are linked through an inversion centre with little interaction between layers. Main body of the nifedipine are parallel to the (3 0 -2) plane. As seen in N_{DMA} and N_{DMF}, nitrophenyl groups are orthogonal to the dihydropyridine groups, sitting between the layers.

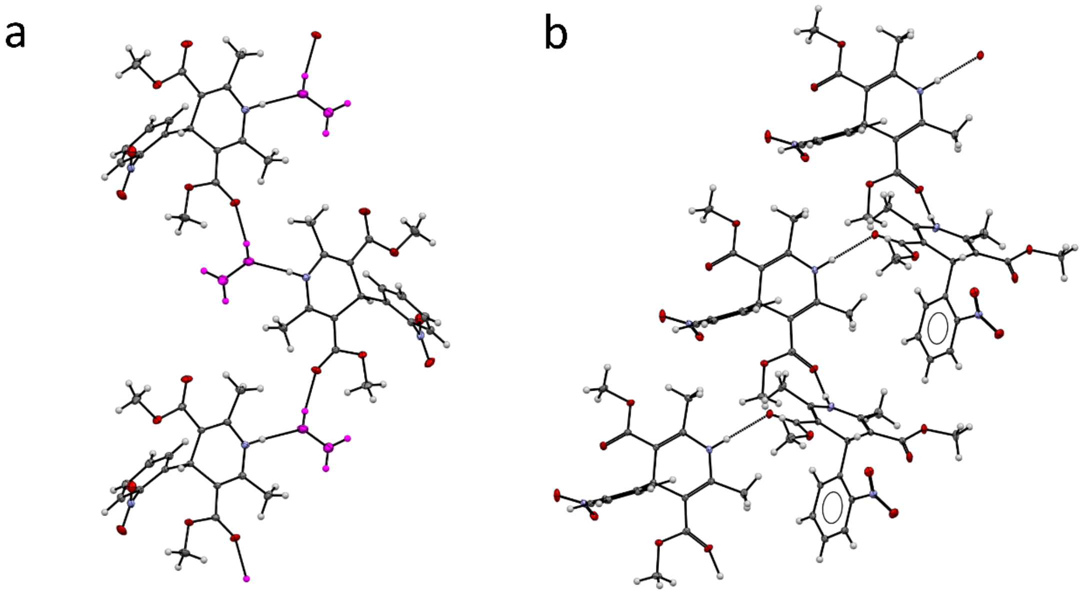

Figure 5.17: The structure of (a) N_{MeOH} and (b) nifedipine Form A showing the similarities in structure between the two forms. The loss of methanol from the structure would enable the NH...O interaction to form without significant change in the packing.

Interestingly, N_{MeOH} displays negative thermal behaviour along its *b*-axis. Negative thermal expansion (NTE) is a mechanism predominantly reported for metal-organic frameworks.[30] Authors describe the mechanism as having a wine-rack expansion; with expansion in one direction causing contraction in a second.[31] Recent publication by van der Lee and Dumitrescu explains how NTE is common amongst organic crystals, but rarely reported.[32] In N_{MeOH}, chains of nifedipine and solvent molecules align in the direction of the *b*-axis, with the hydrogen bonds between methanol and carbonyl group of the nifedipine (O7H7···O6) (Figure 5.19a and d). This is also where short contacts are located between the nitrophenyl ring and methoxy group of the neighbouring molecule. When viewed down the crystallographic *a*-axis, large voids are apparent in the structure between the nifedipine molecules in which the methanol molecules are located, running parallel to the *b*-axis (Figure 5.19d). We speculate that as the temperature increases, escape of solvent molecules from these voids causes nifedipine to bridge the gap and hydrogen bond to stabilise the structure. Hence, the *b*-axis contracts. Slurrying nifedipine in methanol did not result in the conversion of pure nifedipine to the solvate. Instead, single-crystals from the slow evaporation were ground for both VT-XRPD and STA. The pulverisation of single-crystals seems to have induced mechanical desolvation. Form A nifedipine was present in all of the diffraction patterns as small trace quantities, but due to the small quantity could only be fit using Rietveld refinement from 338 K onwards (Figure 5.18a). STA shows us that the onset of desolvation took place prior to analysis; TGA shows a mass loss of 1.69% prior to the melt of Form A, which was calculated to be 8.47 % when using diffraction data (Figure 5.18c,

). This mass loss is simultaneous with an endothermic event in the DSC trace. The sample environment for the XRPD and DSC are very different with the latter being more susceptible to desolvation due to the openness to the environment compared with a solid in a borosilicate capillary which accounts for the difference.

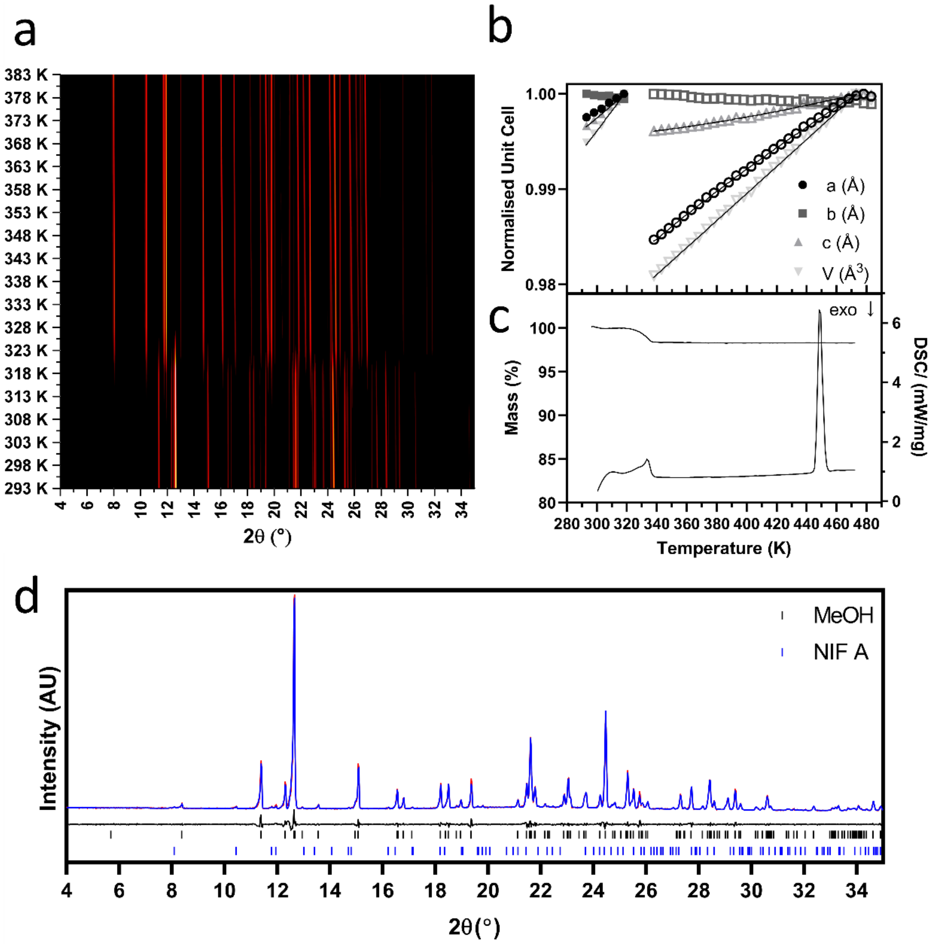

Figure 5.18: Thermal data of N_{MeOH} capturing the desolvation to Form A Nifedipine a) Surface plot of VT-XRPD data from 293 K to 368 K. b) Unit cell parameters from Pawley refinements of each XRPD pattern. Closed symbols represent data for the solvate; open symbols represent data for desolvated structure. c) DSC and TGA trace for N_{MeOH}. d) XRPD pattern for the MeOH solvate collected at 293 K. The experimental data is shown in blue, whilst the calculated profile is shown in red. The difference profile is displayed underneath the diffraction pattern. The calculated reflections are based on the single-crystal data collected for N_{MeOH}.

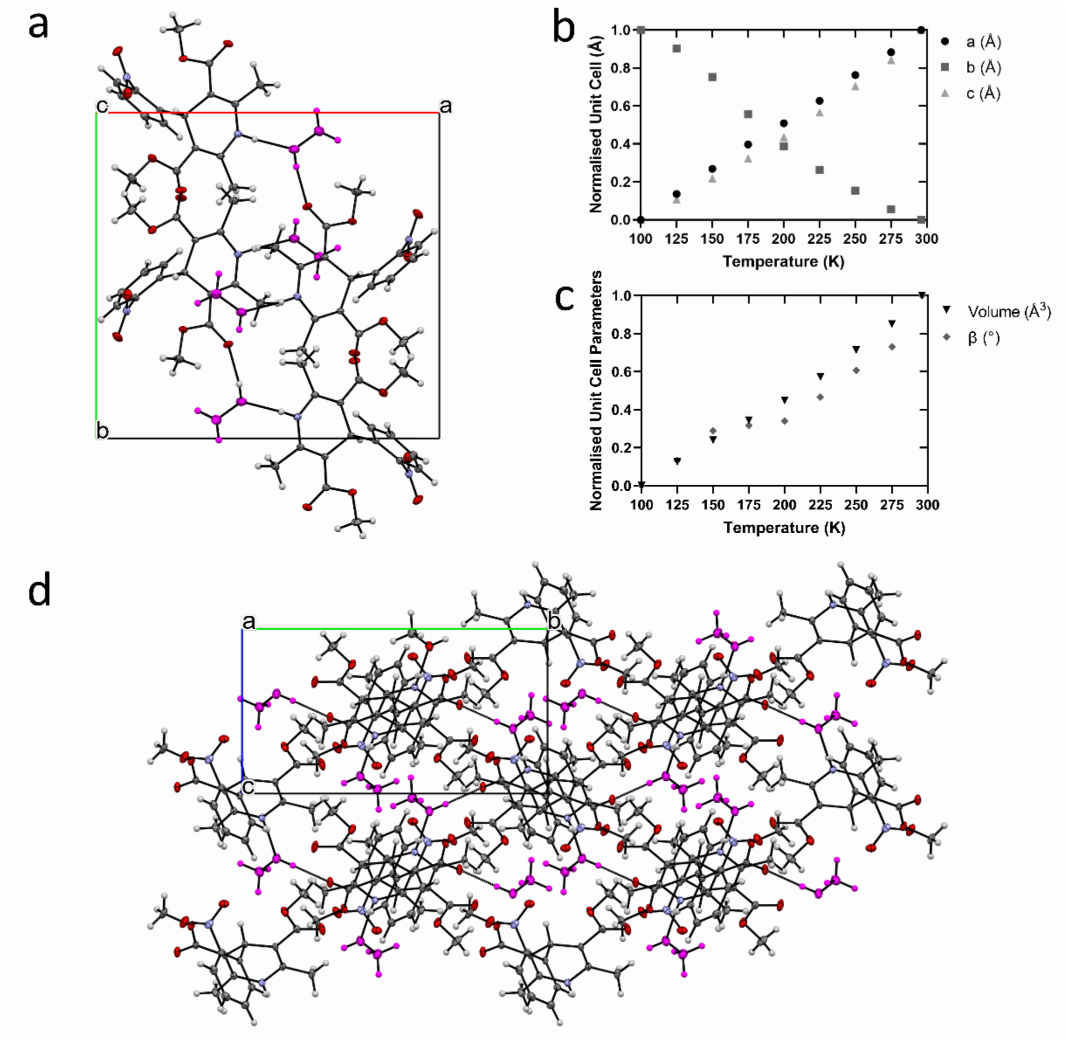

Figure 5.19: N_{MeOH} viewed down the c-axis with methanol molecules displayed in pink. Non-linear thermal behaviour of N_{MeOH} showing the b) decrease in b-axis and c) increase in β angle and volume with increasing temperature. Unit cell parameters were determined using SC-XRD. d) Structure of N_{MeOH} viewed along the a-axis.

Further investigation into the negative thermal expansion was conducted using SC-XRD, at low temperature. A single crystal was collected at 100 K with subsequent collections increasing by 25 K (Figure 5.19b and c). From these data, Pixel calculations have been carried out on the variable-temperature single-crystal structures (100 K to 275 K). Four interactions involving the *b*-axis were evaluated and are provided in Figure 5.20 and Table C2 in Appendix C. Interaction 1 exists between the phenyl group of one molecule and the methoxy group of a neighbouring molecule in an adjacent layer and are predominantly dispersive in nature. The overall energy of this interaction remains relatively consistent with temperature, whilst the centroid distance decreases. Interactions 2 & 4 provide further insight into the thermal behaviour of N_{MeOH} and are located between the methanol molecule and nifedipine and also with another methanol in an adjacent layer (Figure 5.20). The Pixel calculations show that as the temperature increases, the distance between centroids for this interaction decreases. In each of these interactions the overall energy is becoming more stabilising. Interaction 2 indicates that this is achieved via a lowering of the repulsion between the nifedipine and methanol whilst Interaction 4 indicates a slight stabilisation with coulombic and dispersive forces becoming more prevalent (-1 to -1.9 $kJmol^{-1}$). From the calculations there is little information, so another rationale needs to be considered. On lowering the temperature, the molecules in Figure 5.19a rotate around the *a*-axis direction that results in the molecule increasing the length in the *b*-direction as the methoxy group becomes more parallel to the *b*-axis. In addition to this, a minor structural change is that the nitrobenzene ring also rotates from 41.38 to 42.78 ° for the C13-C12-C6-C7 torsion angle which moves it in the direction of being more parallel to the *b*-axis. This rotation is likely to continue to higher temperatures with the negative thermal expansion.

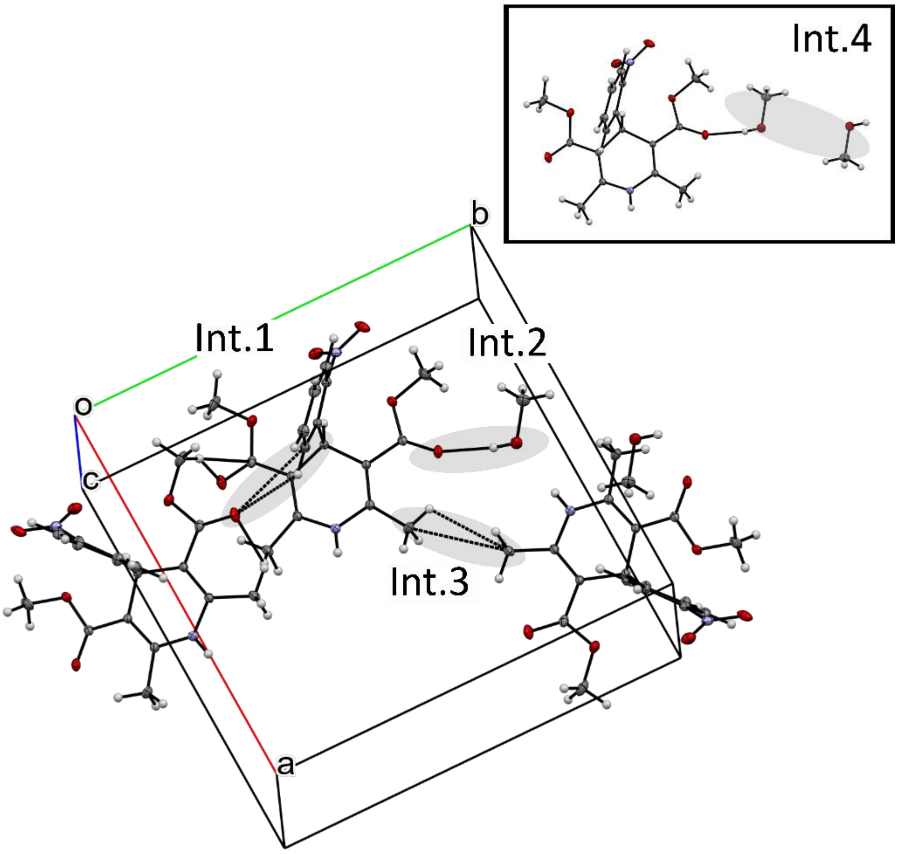

Figure 5.20: Four interactions of solvate N_{MeOH} involving the *b*-axis as calculated by Pixel. The inset shows interaction four, which is partially visible in the main Figure.

5.4.5 Solution Study – Ethanol and Methanol

During the study we observed that nifedipine did not form a solvate with ethanol but did with methanol. To further investigate this, saturated solutions of nifedipine in the two solvents were analysed using FTIR. Figure 5.21a. shows the spectra of the saturated solutions, with the background of the respective solvent removed. The IR of nifedipine was first discussed by Burger and Koller, which aids in our discussion.[33] Solutions were filtered through 0.2 μm PTFE filters prior to analysis, removing any solid crystalline material, in order to look at the behaviour of nifedipine in the solvent. Solubility of nifedipine in methanol and ethanol at 20 °C are 26 mg/mL and 17 mg/mL respectively.[34] The carbonyl region of the spectra is displayed in Figure 5.21b, where differences between nifedipine in the methanol solution and in the ethanol solution are seen. From the IR spectra, there is a significant shift of one of the carbonyl stretches to higher energy that is observed in the methanol solution compared with the ethanol solution. This shift is towards the non-bonded carbonyl stretch of an aromatic ester (~1725 cm^{-1}) which signifies that during solvation only one ester is involved in hydrogen bonding compared with the ethanol solution where the two esters are involved in hydrogen bonding (lowering their stretch). Crystallisation of N_{MeOH} from the slow evaporation of a saturated solution resulted in the solvate interacting though the hydroxyl group of the alcohol and one carbonyl ester in nifedipine but the second is involved in a loose CH···O interaction involving the nitrobenzene. This may signify that in methanol, nifedipine interacts with both methanol and other nifedipine molecules creating a cluster where only one ester is able to hydrogen bond to the solvent.[35]

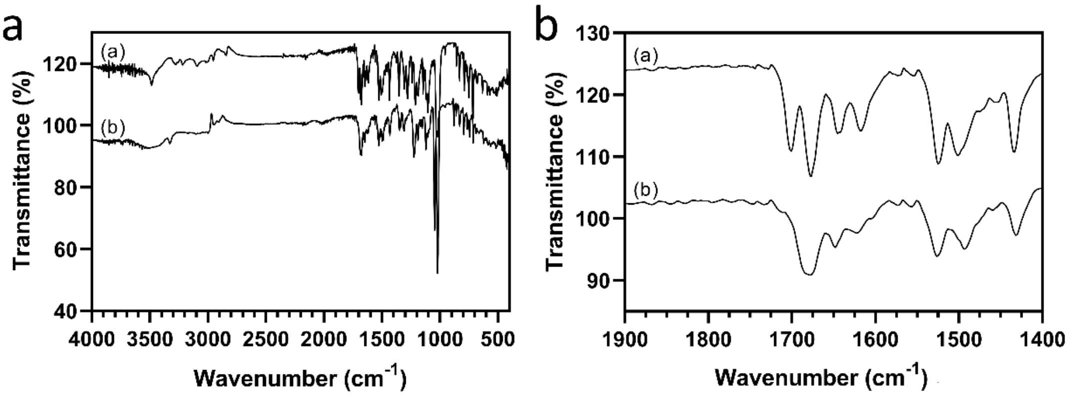

Figure 5.21: FTIR spectra of nifedipine in a) methanol and b) ethanol. The background of the respective solvents was removed to aid in the identification of nifedipine. Figure 20b. highlights the spectra between 1400-1900 cm^{-1}, the region where we see the carbonyl stretch.

5.5 Conclusions

A solvent screen of nifedipine has identified seven new solvates, adding to the structural landscape of this drug as summarised in Figure 5.22. The reported 1,4-dioxane and DMSO solvates led to the choice of solvents we believed would interact favourably with nifedipine, based on similarity in structures. Cyclic solvents morpholine, THF and pyridine, and chain solvents DMA, DMF and methanol. Structures for the new crystal forms were collected using SC-XRD and disorder was observed in the morpholine, THF and DMA structures, collected at 100 K. No hydrogen bonding was observed in the structure containing THF, instead nifedipine molecules orientate themselves similarly to the chain structure of the metastable Form C polymorph whilst THF molecules sit in channels. We also identified the transition of the DMA solvate to a low temperature phase when subjected to 100 K conditions. The disorder that was present in the high temperature phase was frozen out at lower temperature. The VT-XRPD desolvation study of the DMF solvate led to the observation of peaks corresponding to the metastable Form C nifedipine, at 353 and 358 K. Form C was not able to be isolated during the desolvation. Methanol produced another solvate with interesting behaviour, observing negative thermal behaviour on desolvation. Pixel calculations were performed to provide an insight into this behaviour but observing the structure from 100 K to 275 K led to the observation that the methoxy group and nitrophenyl ring rotate, becoming more parallel to the *b*-axis with increasing temperature, thus contracting in length. Thermal desolvation was assessed using VT-XRPD and STA, which led to the transition of all samples to the thermodynamically stable polymorph of nifedipine, Form A.

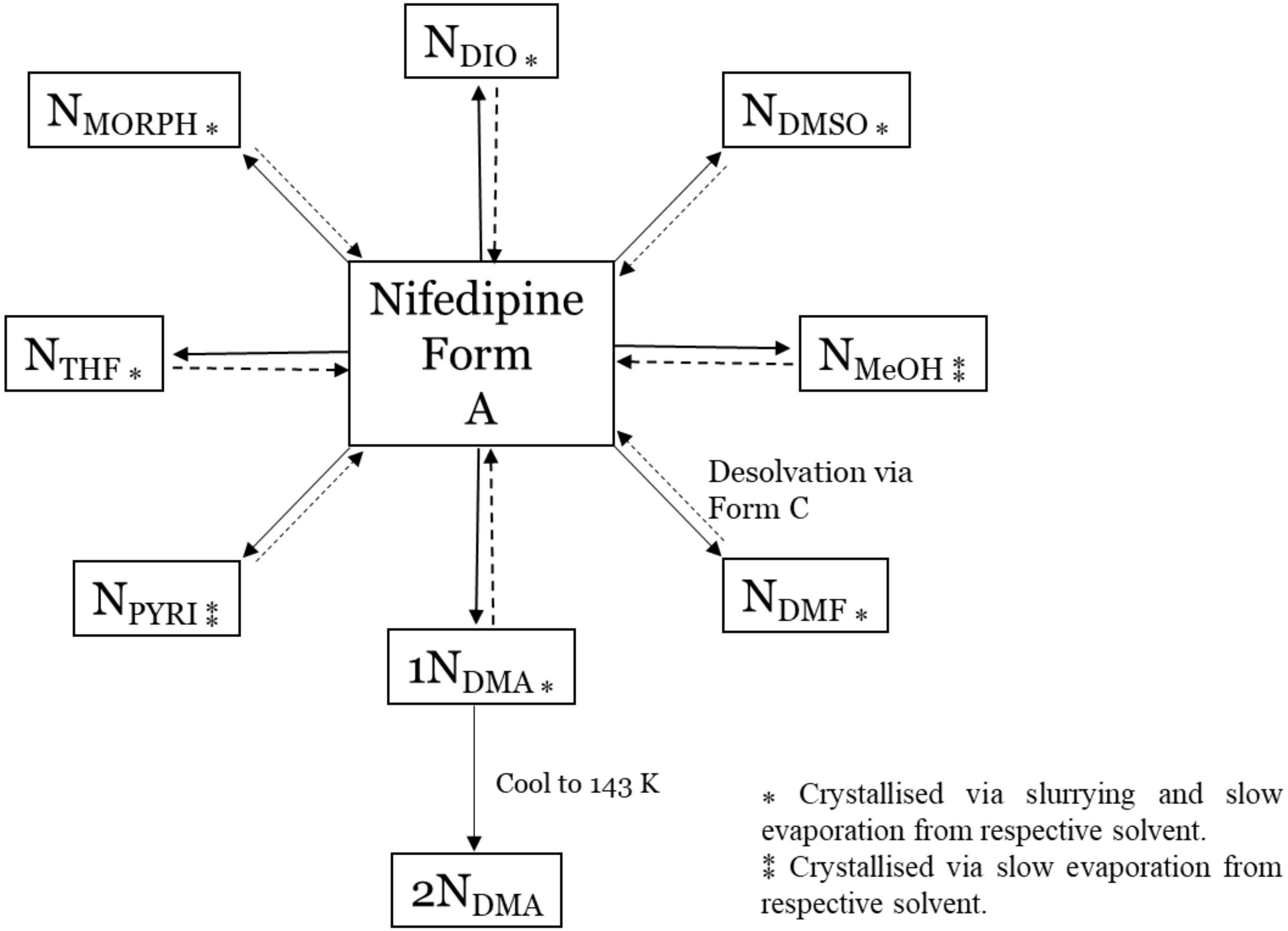

Figure 5.22: Summary of the solid-form landscape of nifedipine. Dashed lines represent desolvation back to the thermodynamically stable Form A Nifedipine.

5.6 References

1. Chemburkar, S. R.; Bauer, J.; Deming, K.; Spiwek, H.; Patel, K.; Morris, J.; Henry, R.; Spanton, S.; Dziki, W.; Porter, W.; et al. Dealing with the Impact of Ritonavir Polymorphs on the Late Stages of Bulk Drug Process Development. In *Organic Process Research & Development*, American Chemical Society: 2000; Vol. 4, pp 413-417.
2. Agency, M. a. H. p. R. Class 2 Medicines Recall: Accord-UK Ltd (Trading style: NorthStar), LEVOTHYROXINE TABLETS BP 50 micrograms EL (21)A/23. In *Medicines recall/notification*, 2021.
3. Kaur, N.; Suryanarayanan, R. Levothyroxine Sodium Pentahydrate Tablets – Formulation Considerations. In *Journal of Pharmaceutical Sciences*, 2021.
4. Shah, H. S.; Chaturvedi, K.; Hamad, M.; Bates, S.; Hussain, A.; Morris, K. New Insights on Solid-State Changes in the Levothyroxine Sodium Pentahydrate during Dehydration and its Relationship to Chemical Instability. In *AAPS PharmSciTech*, 2019; Vol. 20, p 39.
5. FDA. Human Drug Product Recalls Pending Classification. In *Recalls, Market Withdrawals, & Safety Alerts*, 2017.
6. ICH. ICH guideline Q3C (R8) on impurities: guideline for residual solvents. Amsterdam, 2021; pp 1-51.
7. Lee, A. Y.; Erdemir, D.; Myerson, A. S. Crystal Polymorphism in Chemical Process Development. In *Annual Review of Chemical and Biomolecular Engineering*, Annual Reviews: 2011; Vol. 2, pp 259-280.
8. Yang, P.; Qin, C.; Du, S.; Jia, L.; Qin, Y.; Gong, J.; Wu, S. Crystal Structure, Stability and Desolvation of the Solvates of Sorafenib Tosylate. In *Crystals*, 2019; Vol. 9.
9. Zhou, L.; Yin, Q.; Du, S.; Hao, H.; Li, Y.; Liu, M.; Hou, B. Crystal structure, thermal crystal form transformation, desolvation process and desolvation kinetics of two novel solvates of ciclesonide. In *RSC Advances*, The Royal Society of Chemistry: 2016; Vol. 6, pp 51037-51045. Braun, D. E.; Bhardwaj, R. M.; Florence, A. J.; Tocher, D. A.; Price, S. L. Complex Polymorphic System of Gallic Acid—Five Monohydrates, Three Anhydrates, and over 20 Solvates. In *Crystal Growth & Design*, American Chemical Society: 2013; Vol. 13, pp 19-23. Ward, M. R.; Oswald, I. D. H. Hidden Solvates and Transient Forms of Trimesic Acid. In *Crystals*, 2020; Vol. 10. Bodart, L.; Prinzo, M.; Derlet, A.; Tumanov, N.; Wouters, J. Taking advantage of solvate formation to modulate drug–drug ratio in clofaziminium diclofenac salts. In *CrystEngComm*, The Royal Society of Chemistry: 2021; Vol. 23, pp 185-201.
10. Bhardwaj, R. M.; Price, L. S.; Price, S. L.; Reutzel-Edens, S. M.; Miller, G. J.; Oswald, I. D. H.; Johnston, B. F.; Florence, A. J. Exploring the Experimental and Computed Crystal Energy Landscape of Olanzapine. In *Crystal Growth & Design*, American Chemical Society: 2013; Vol. 13, pp 1602-1617.
11. Furuta, H.; Mori, S.; Yoshihashi, Y.; Yonemochi, E.; Uekusa, H.; Sugano, K.; Terada, K. Physicochemical and crystal structure analysis of pranlukast pseudo-polymorphs II: Solvate and cocrystal. In *Journal of Pharmaceutical and Biomedical Analysis*, 2015; Vol. 111, pp 44-50.
12. Aitipamula, S.; Chow, P. S.; Tan, R. B. H. Solvates and polymorphic phase transformations of 2-chloro-4-nitrobenzoic acid. In *CrystEngComm*, The Royal Society of Chemistry: 2011; Vol. 13, pp 1037-1045.
13. Minkov, V. S.; Beloborodova, A. A.; Drebushchak, V. A.; Boldyreva, E. V. Furosemide Solvates: Can They Serve As Precursors to Different Polymorphs of Furosemide? In *Crystal Growth & Design*, American Chemical Society: 2014; Vol. 14, pp 513-522.
14. Liu, X.; Tang, C. C.; Boldyreva, E. V.; Pulham, C. R. Influence of Crystal Packing on the Mechanism of Decomposition of the Acetonitrile-Solvated Cocrystal of Piroxicam and Succinic Acid. In *Crystal Growth & Design*, American Chemical Society: 2019; Vol. 19, pp 7315-7323.

15. Bortolotti, M.; Lonardelli, I.; Pepponi, G. Determination of the crystal structure of nifedipine form C by synchrotron powder diffraction. In *Acta Crystallographica Section B: Structural Science*, 2011; Vol. 67, pp 357-364.
16. Caira, M. R.; Robbertse, Y.; Bergh, J. J.; Song, M.; De Villiers, M. M. Structural Characterization, Physicochemical Properties, and Thermal Stability of Three Crystal Forms of Nifedipine. In *Journal of Pharmaceutical Sciences*, Elsevier: 2003; Vol. 92, pp 2519-2533.
17. Horvat, G.; Pantić, M.; Knez, Ž.; Novak, Z. Encapsulation and drug release of poorly water soluble nifedipine from bio-carriers. In *Journal of Non-Crystalline Solids*, North-Holland: 2017; Vol. 481, pp 486-493.
18. Triggle, A. M.; Shefter, E.; Triggle, D. J. Crystal structures of calcium channel antagonists: 2, 6-dimethyl-3, 5-dicarbomethoxy-4-[2-nitro-, 3-cyano-, 4-(dimethylamino)-, and 2, 3, 4, 5, 6-pentafluorophenyl]-1, 4-dihydropyridine. In *Journal of Medicinal Chemistry*, 1980; Vol. 23, pp 1442-1445.
19. Gunn, E.; Guzei, I. A.; Cai, T.; Yu, L. Polymorphism of nifedipine: Crystal structure and reversible transition of the metastable β polymorph. In *Crystal Growth and Design*, 2012; Vol. 12, pp 2037-2043.
20. Gui, Y.; Yao, X.; Guzei, I. A.; Aristov, M. M.; Yu, J.; Yu, L. A Mechanism for Reversible Solid-State Transitions Involving Nitro Torsion. In *Chemistry of Materials*, American Chemical Society: 2020; Vol. 32, pp 7754-7765.
21. Li, W.; Shi, P.; Du, S.; Wang, L.; Han, D.; Zhou, L.; Tang, W.; Gong, J. Revealing the role of anisotropic solvent interaction in crystal habit formation of nifedipine. In *Journal of Crystal Growth*, 2020; Vol. 552, p 125941.
22. Sheldrick, G. M. SHELXT - Integrated space-group and crystal-structure determination. In *Acta Crystallographica Section A: Foundations of Crystallography*, 2015; Vol. 71, pp 3-8.
23. Dolomanov, O. V.; Bourhis, L. J.; Gildea, R. J.; Howard, J. A. K.; Puschmann, H. OLEX2: A complete structure solution, refinement and analysis program. In *Journal of Applied Crystallography*, 2009; Vol. 42, pp 339-341.
24. Sheldrick, G. M. Crystal structure refinement with SHELXL. In *Acta Crystallographica Section C: Structural Chemistry*, 2015; Vol. 71, pp 3-8.
25. Coelho, A. A. TOPAS and TOPAS-Academic: An optimization program integrating computer algebra and crystallographic objects written in C++: An. In *Journal of Applied Crystallography*, 2018; Vol. 51, pp 210-218.
26. David, W. I. F.; Shankland, K.; van de Streek, J.; Pidcock, E.; Motherwell, W. D. S.; Cole, J. C. DASH : a program for crystal structure determination from powder diffraction data. In *Journal of Applied Crystallography*, International Union of Crystallography: 2006; Vol. 39, pp 910-915.
27. Klimakow, M.; Rademann, K.; Emmerling, F. Toward Novel Pseudo-Polymorphs of Nifedipine: Elucidation of a Slow Crystallization Process. In *Crystal Growth & Design*, American Chemical Society: 2010; Vol. 10, pp 2693-2698.
28. Groom, C. R.; Bruno, I. J.; Lightfoot, M. P.; Ward, S. C. The Cambridge Structural Database. In *Acta Crystallographica Section B*, 2016; Vol. 72, pp 171-179.
29. Grooff, D.; De Villiers, M. M.; Liebenberg, W. Thermal methods for evaluating polymorphic transitions in nifedipine. In *Thermochimica Acta*, 2007; Vol. 454, pp 33-42.
30. Goodwin, A. L.; Kepert, C. J. Negative thermal expansion and low-frequency modes in cyanide-bridged framework materials. In *Physical Review B*, American Physical Society: 2005; Vol. 71, p 140301. Wu, Y.; Kobayashi, A.; Halder, G. J.; Peterson, V. K.; Chapman, K. W.; Lock, N.; Southon, P. D.; Kepert, C. J. Negative Thermal Expansion in the Metal–Organic Framework Material Cu3(1,3,5-benzenetricarboxylate)2. In *Angewandte Chemie International Edition*, John Wiley & Sons, Ltd: 2008; Vol. 47, pp

8929-8932. Lock, N.; Wu, Y.; Christensen, M.; Cameron, L. J.; Peterson, V. K.; Bridgeman, A. J.; Kepert, C. J.; Iversen, B. B. Elucidating Negative Thermal Expansion in MOF-5. In *The Journal of Physical Chemistry C*, American Chemical Society: 2010; Vol. 114, pp 16181-16186.
31. Cliffe, M. J.; Goodwin, A. L. PASCal: A principal axis strain calculator for thermal expansion and compressibility determination. In *Journal of Applied Crystallography*, 2012; Vol. 45, pp 1321-1329.
32. van der Lee, A.; Dumitrescu, D. G. Thermal expansion properties of organic crystals: a CSD study. In *Chemical Science*, The Royal Society of Chemistry: 2021; Vol. 12, pp 8537-8547.
33. Burger, A.; Koller, K. T. Polymorphism and pseudopolymorphism on nifedipine. In *Scientia Pharmaceutica*, 1996; Vol. 64, p Scientia Pharmaceutica.
34. Ali, S. L. Nifedpine. Florey, K., Al-Badr, A. A., Forcier, G. A., Brittain, H. G., Grady, L. T. B. T.-A. P. o. D. S., Eds.; Academic Press: 1990; Vol. 18, pp 221-288.
35. Warzecha, M.; Verma, L.; Johnston, B. F.; Palmer, J. C.; Florence, A. J.; Vekilov, P. G. Olanzapine crystal symmetry originates in preformed centrosymmetric solute dimers. In *Nature Chemistry*, 2020; Vol. 12, pp 914-920.

Chapter 6

Solvent mediated loading of isonicotinamide into porous silica

This chapter was beset by safety and technical issues as well as the shutdown of the department due to COVID-19. This chapter has been included to show the trajectory of the thesis and how the high-pressure and crystallisation chapters would link into the application in mesoporous silica.

6 Solvent mediated loading of isonicotinamide into porous silica

6.1 Abstract

In this chapter, we explore the loading of isonicotinamide into porous silica. Firstly, we have attempted to create silica particles with known pore sizes and characterised these using nitrogen isotherms. During this study, the reproducibility of literature synthetic methods is questioned. We have followed this by loading isonicotinamide using ethanol and chloroform as the solvents under ambient and high-pressure conditions. The analysis of the loaded particles indicates that isonicotinamide is loaded into the pores and is likely to be in an amorphous form.

6.2 Introduction

The discovery of ordered mesoporous materials (OMM) can be traced back to the early 1990's, where a family of uniform pore, silicate-based, mesoporous molecular sieves, named the M41S family (which included MCM-41, MCM-48, and MCM-50), was first reported.[1] This was the result of the efforts of Mobil corporation in the attempt to identify new zeolites that could selectively convert high molecular weight petroleum based molecules. The synthesis of the structures involved the calcination of aluminosilicates in the presence of quaternary ammonium cationic surfactants, giving rise to a uniform array of channels in the range of 16 to 100 Å. The mechanism of formation was called liquid crystal templating (LCT) by analogy to the surfactant-water liquid crystal phases of the alkyltrimethylammonium salts in water (Figure 6.1). Their large surface areas (typically above 700 m^2/g) and large sorption capacity initially prompted great interest in their use as catalysts, although it was soon discovered that their catalytic activity was, in most cases, much weaker than that of zeolites.[2]

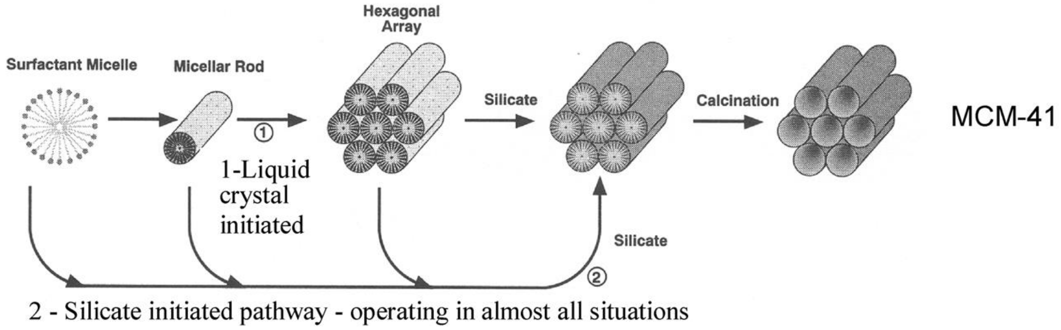

Figure 6.1: Proposed LCT mechanism of formation pathways (Figure adapted from Kresge and Roth).[2]

It was later proposed that an increase in dimensions of the pore structures could be achieved by using amphiphilic polymers of larger molecular weight as organic structure-directing agents. The well-ordered hexagonal mesoporous silica structures obtained in this fashion were named SBA-15 and, unlike the M41S family, displayed very large pores (up to 300 Å) and thicker walls (from 31 to 64 Å). Furthermore, the SBA-15 also displayed greater hydrothermal stability and could be synthesized at lower cost. The versatility of these materials was also apparent in the ability to tune their pore size and silica wall thickness by varying the heating temperature (35 °C to 140 °C) and time of the SBA-15 in the reaction (11 to 72 hours).[3] The morphology of the materials could also be controlled by employing block copolymers, co-surfactants, co-solvents, or the additive of strong electrolytes as structure-directing agents. This approach enabled the selectively of micrometre-sized hard sphere-, fibre-, doughnut-, rope-, and discoid-like mesoporous silica SBA-15.[4] One of the applications that OMMs, in particular MCM-41, soon found interest as a drug delivery system. The disordered network of siloxane bridges and free silanol groups acted as reacting nuclei against an array of guest chemical species. This allowed the MCM-41 material to behave as a matrix for controlled adsorption and release of organic molecules, with no need for pore-wall functionalization,[5] although modifications of the surface of the MCM-41 were later found to impact on the ability to control the delivery rate of drugs.[6] SBA-15 mesoporous silica was also used as a drug delivery system using the drug gentamicin sulphate as model drug.[7] It was further reported that the larger pore size and volume of SBA-15 enabled higher drug loadings and more complete drug release when compared with MCM-41.[8] Ever since, silica-based mesoporous materials have been used to load and release pharmaceutical compounds due to their ability to increase drug dissolution rates,[9] protect from atmospheric moisture,[10] and prevent drug degradation.[11] These effects are thought to be the direct result from the confinement effects of the drug inside the mesopores of the matrices.

This final chapter will build on the previous chapters and the solid-state behaviour of isonicotinamide. The initial investigation of isonicotinamide were focussed on providing baseline information on the behaviour with pressure, as pressure will be used as a potential loading route. We have previously discussed the polymorphic behaviour of isonicotinamide hence it is an interesting test case for confinement. In addition to this the solubility of isonicotinamide is known in a variety of solvents, and the solvent-solute interactions well understood.[12, 13] Due to the literature available, with regards to the interactions between isonicotinamide and a variety of solvents, an adsorption method was chosen to load porous silica. Solvent selection was based on the affinity of isonicotinamide for those solvents. Based on the research carried out by Lynch *et al.,* chloroform has the weakest binding energy due the single weak hydrogen bond that can be formed with isonicotinamide (C–H···O, −24.85 kJ mol^{-1}).[12] This may act in favour of the adsorption method, as isonicotinamide might be released from the interaction in favour of the interaction it could form with the silica particles. Ethanol has a moderate binding energy, with an energy of -39.43 kJ mol^{-1}, based on the interactions via isonicotinamide's carbonyl site. The higher binding energy may not act in favour when it comes down to the adsorption method, however the solubility of isonicotinamide in ethanol is much greater than that in chloroform, which may be advantageous when it comes to characterising the material.

In this chapter we will first characterise the silica mesoporous material before loading the silica using solution-based techniques with the variation in loading pressure. We have focussed our attention on ethanol due to the high solubility and the increased potential for the pores to be loaded with the isonicotinamide solution.

6.3 Experimental

6.3.1 Materials

The following reagents used in the synthesis of silica were purchased from Sigma Aldrich: Ammonium hydroxide (28-30% NH_3 basis); tetraethyl orthosilicate (TEOS, reagent grade 98%); cetyltrimethylammonium chloride solution in water (CTAC, 25% wt.); triethanolamine (TEA, ≥99.5%); 1-octadecene (≥95.0 %) and hexadecyltrimethylammonium p-toluenesulfonate (CTATOS, ≥98.0%).

Isonicotinamide (99% purity) and chloroform (anhydrous ≥99%) were purchased from Sigma Aldrich. Ethanol (99.8%) and methanol (HPLC grade) were purchased from Fisher Scientific. Deuterated isonicotinamide (isonicotinamide-2,3,5,6-d_4) was purchased from CDN isotopes.

SBA-15 (8 nm pore size) and silica gel (9 nm pore size) were purchased from Sigma Aldrich. Silica gel (350-400 m^2/g surface area, 15 nm pore size) was purchased from Alfa Aesar.

6.3.2 Synthesis of porous silica particles

6.3.2.1 Stöber silica

Synthesis of Stöber Silica was adapted and prepared from previously reported methods.[14, 15] Ammonium hydroxide (6 mL) was added to ethanol (100 mL) and stirred under magnetic agitation (400 rpm) for 5 minutes before the addition of TEOS (3 mL). The solution was stirred at 21 °C for 18 hours, followed by centrifugation at 10000 rpm for 30 minutes. The solid material was recovered, then washed in ethanol 3 times before final centrifugation under previously mentioned conditions. The solid material was dried in an oven for 3 days (87 °C).

6.3.2.2 Large-pore silica

Synthesis of large-pore silica was prepared according to methodology by Möller and Bein.[16] CTATOS (0.2695 g), deionised water (13.76 mL) and TEA (75.7 mg) were heated to *ca.* 80 °C in a round-bottomed flask (250 mL) for 20 minutes before the addition of TEOS (2.0410 g). The mixture was magnetically stirred for 2 hours at 1250 rpm, before centrifugation to separate the solid material (10000 rpm for 30 minutes).

Extraction of the porous template was carried out using a solution of ethanol and HCl (5 mL, 90:10 v/v%) at 90 °C under reflux for 45 minutes. The solid material was recovered, once cooled, using centrifugation (10000 rpm, 30 minutes) before the extraction process was repeated for a second time.

Silica particles were washed using a 3-fold washing cycle in ethanol, water, and a final wash with ethanol, for *ca*. 1 hour at each stage. Solid material was collected after each wash using centrifugation as described above. Silica particles were dried overnight at 200 °C.

6.3.2.3 3D dendritic silica

3D dendritic mesoporous silica was prepared according methodology by Shen *et al.*[17] The synthesis was performed in a round-bottomed flask (100 mL) maintained at 60 °C using a water bath and magnetic stirring hot plate (150 rpm). CTAC (24 mL), TEA (0.1625 g) and deionised water (36 mL) were magnetically stirred for 18 hours. The 1-octadecene layer was removed after 18 hours and replaced with a solution of TEOS (4 mL) in decahydronapthalene (16 mL) and stirred for a further 20 hours. After 20 hours, the decahydronapthalene layer was removed and replaced with a solution of TEOS (4 mL) in cyclohexane (16 mL) and stirred for a further 22 hours.

The resultant solid material was collected by centrifugation (10000 rpm for 30 minutes) and the solid pellet washed with ethanol three times, each time centrifuging the slurry using the conditions mentioned above and replacing the supernatant with ethanol. The template was removed in a solution of ammonium nitrate in ethanol (0.6 %wt.) at 60 °C for 6 hours. This extraction was repeated twice in total before the solid material was recovered via centrifugation and dried overnight (200 °C).

6.3.3 Loading of isonicotinamide into porous silica

Silica was conditioned in a vacuum chamber for 24 hours prior to use. Excess isonicotinamide was equilibrated in solvent for 24 hours using magnetic stirring (22 °C). Prior to dosing the porous silica (PSiO) with isonicotinamide solution, excess solids were filtered from the solution using a syringe fitted with PTFE filter (0.2 μm). Deuterated isonicotinamide was used in the high-pressure study of the chloroform samples, due to analysis using neutron diffraction at ISIS Neutron and Muon Source.

Particles loaded at ambient pressure were dosed with the saturated solution containing the isonicotinamide and magnetically stirred for 24 hours to enable wetting of the particles. Silica loaded at an elevated pressure were loaded with the saturated solution of isonicotinamide into a cylindrical PTFE tube, till the entire volume of the tube was filled. The slurry was stirred with a spatula to enable the solution to wet all of the particles, then sealed with PTFE caps and sealing tape. A large volume press was used to apply pressure (6.9 kbar) to the samples for *ca.* 20 hours, which dropped to between 5.8 and 6.4 kbar over the time period.

Subsequent centrifugation of the samples was carried out using a microcentrifuge, till the particles were visible as pellets at the bottom of the tube. The supernatant was removed and filtered through PTFE syringe filter (0.2 μm) for high-performance liquid chromatography (HPLC) analysis. Samples loaded in chloroform were washed in chloroform, whilst samples loaded in methanol were washed using water. Solution from the wash was recovered and filtered for HPLC analysis. The particles were dried in the fume cupboard (22 °C) prior to characterisation.

6.3.4 Characterisation of material

6.3.4.1 Nitrogen Sorption

PSiO particles synthesised according to the previously described methods were characterised using the Quantachrome Autosorb iQ2 instrument. Samples (mass dependent on density) were degassed prior to analysis for *ca.* 18 hours at 300 °C under vacuum to remove any residual moisture from the pores. Measurements were carried out using nitrogen gas as the adsorbate at 77K, with 20 adsorption and 40 desorption points collected per sample.

Data analysis were carried out within the Quantachrome ASiQwin software. Specific surface area was calculated using the Braunauer-Emmett-Teller (BET) equation on adsorption points within the partial pressure range ($P/\ P_o$) of 0.05-0.25 or the linear region of the isotherm. Barrett-Joyner-Halenda (BJH) calculations were used to calculate average pore volume and pore width.

PSiO particles purchased from Sigma Aldrich and Alfa Aesar were characterised at the Chemical Engineering Department, University of Strathclyde by Dr Dave Ashworth prior to loading. Nitrogen sorption analysis was carried out using the Micromeritics ASAP® 2020 BET and Porosimetry instrument. Samples (mass dependent on density) were degassed prior to analysis for *ca.* 18 hours at 300 °C under vacuum. Measurements were carried out using nitrogen gas as the adsorbate at 77 K, with 40 adsorption and 30 desorption points collected per sample. Data analysis were carried out within the ASAP 2420 V2.09 (V2.09 J) software.

6.3.5 X-ray Powder Diffraction (XRPD)

Loaded and unloaded PSiO particles were transferred into 0.7 mm diameter borosilicate glass capillaries. A Bruker D8 Advance diffractometer with Johansson monochromator (Cu $K\alpha 1$ – 1.5406 λ) was used to collect the data from 3-40°, 2θ, 0.018° per step with 10 second exposure.

6.3.6 Thermal Analysis

Differential Scanning Calorimetry (DSC) and Thermal Gravimetric Analysis (TGA) was carried out using The STA 449 F1 Jupiter®. Loaded and unloaded (*ca.* 3-8 mg) were loaded into aluminium pans with pierced lids and sealed. The temperature programme was as follows: 10-minute isothermal step, heat (20-400 °C, 5 °C /min), 10-minute isothermal step, cool (400-20 °C, 20 °C/min) and a final isothermal step for 5 minutes (20 °C). Helium was used as a purge and protective gas at a rate of 50 ml/min and 20 ml/min respectively. Data was analysed using NETZSCH Proteus Thermal Analysis 8.0.2.

6.3.7 Fourier-Transform Infrared Spectroscopy (FTIR)

Analysis was carried out on particles prior to and after loading. FTIR spectra were collected using a Shimadzu IRSpirit Fourier Transform Infrared Spectrophotometer with QATR-S single-reflectance attenuated total reflectance (ATR) probe. Parameters for data collection were transmittance measurement mode and Happ Genzel apodization. Spectra resolution was set to 4 cm^{-1}, with 64 scans per spectra in the range of 400 to 4000 cm^{-1}.

6.3.8 High-Performance Liquid Chromatography

Isonicotinamide content was determined using reverse-phase HPLC analysis. An Agilent 1100 series instrument was used, equipped with degasser, quaternary pump, autosampler, and Variable Wave Detector. A C18 column with 5 µm particle size and dimensions of 150 x 4.6 mm was used as the stationary phase. The mobile phase was composed of methanol and water in a 40:60 ratio respectively at a flow rate of 1 $mLmin^{-1}$. Isonicotinamide was detected using a UV absorbance of 254 nm. The injection volume was 10 µL.

Calibration samples of known concentrations of isonicotinamide were prepared in ethanol and chloroform.

6.4 Results and Discussion

6.4.1 Synthesis of Mesoporous Silica

The premise of this chapter was to synthesise mesoporous silica to be reduced into mesoporous silicon particles via magnesiothermal reduction. As discussed later, the three methods used to synthesis the silica particles failed to produce particles with pores in the mesoporous range (2-50 nm). Safety concerns of our safety team over the reactive nature of the magnesiothermal reduction was significant challenge that ultimately led to the use of the pre-cursor, silica, as the framework for investigation.

The Stöber silica method is the most commonly used method. To produce silica particles, tetraethyl orthosilicate undergoes a hydrolysis reaction using a water/alcohol mixture in the presence of a catalyst which then undergoes a condensation reaction to produce the particles. Reproducible silica particles are produced in a monodisperse suspension. Stöber and Fink reported that they could alter the product of the reaction by changing components in the reaction mixture. For example, increasing the chain length of the silica used, increases the reaction time and particle size.[18] A faster reaction time can be achieved using smaller alkyl silicate molecules i.e. tetramethyl orthosilicate. The presence or absence of ammonia (a commonly used catalyst) influences the spherical shape of the particles. In the presence of ammonia, the particles are spherical however in its absence, irregular shaped particles can be formed.

Figure 6.2 shows the analysis of material synthesised using the Stöber method, involving hydrolysis and condensation reactions.[18] Nitrogen sorption was used to physically characterise the solid material, in particular the porosity of the material. Figure 6.2a, shows the absorption and desorption of the silica. In an ideal situation these should mimic each other with the free flow of nitrogen in and out of the pores with a small hysteresis immediately on desorption. At lower relative pressures the adsorption and desorption should have similar values providing a 'closed' hysteresis loop. In this case, the adsorption data indicate that at relative pressure above 0.8 there is a significant increase in the quantity of nitrogen adsorbed into the silica. On desorption, there is a slight hysteresis, which is desirable however the measurements at lower relative pressures remain higher than the adsorption values. The disparity at these low pressures indicate that our samples are not porous and that the material releases more than was adsorbed which may have been caused by blockage of the pores prior to analysis. The material was subjected to a second cycle of adsorption-desorption analysis to see if the first cycle was able to remove residual solvent or reagents from the pores. This proved to be unsuccessful, exhibiting an isotherm similar to the first cycle shown in Figure 6.2a.

XRD analysis indicates that the solid material synthesised using the Stöber reaction is amorphous, with the diffraction pattern showing an amorphous 'halo', with no diffraction peaks (Figure 6.2b). The FTIR spectrum of the Stöber silica was compared SBA-15 provided by Sigma Aldrich, providing information about the chemical nature of the sample. The only difference seen in the spectra is the additional peak at *ca.* 950 cm^{-1}, which might indicate C-H bending, from residual tetraethyl orthosilicate or an ethoxysilanol reaction by-product. Nonetheless, there are no additional modes around *ca.* 1400 cm^{-1} to support carbon being present in the sample. The additional peak is located next to the prominent Si-O stretch seen at *ca.* 1050 cm^{-1} and could therefore be attributed to the splitting of the Si-O band. Kaya et al. discussed the significant change in IR spectra when silica adsorbs water, in particular the increase in intensity of the shoulder seen at *ca.* 900 cm^{-1}.[19] When water enters the porous silica, the Si-O-Si bonds stretch causing a shift to lower energies, breaking away from the main band. Water is also evident in the material with a broad hydroxyl stretch at *ca.* 3020 cm^{-1} in Figure 6.2c. Residual water in the pores would explain the isotherm seen in in Figure 6.2a, however Stöber silica was degassed under vacuum for 18 hours at 300 °C prior to analysis. The other suggestion is the absence of pores in the silica particles. This has been observed before with a number of groups showing that the Stöber method produces non-porous particles, which explains the lack of hysteresis loop in the adsorption-desorption isotherm.[18, 20]

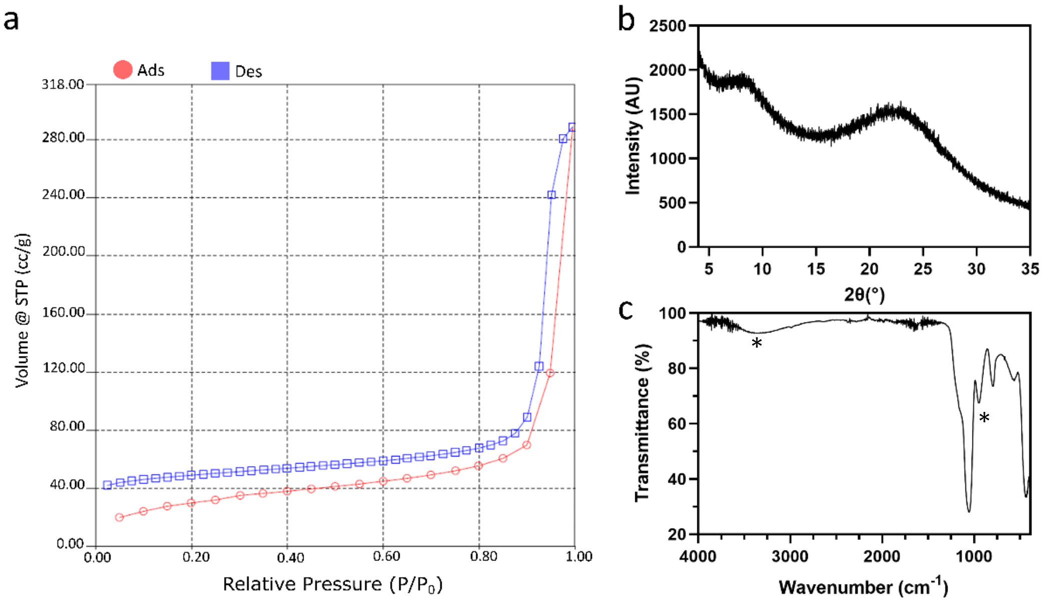

Figure 6.2: Characterisation of Stöber silica by a) nitrogen sorption showing the adsorption and desorption isotherm; b) XRPD and c) FTIR. * Asterisks highlight regions of interest mentioned in the text.

The Stöber silica method has been used as a precursor to various other mesoporous silica synthesis methods, including the large-pore method created by Möller and Bein and used in this study.[16] Surfactants can be used to tune the pore size of mesoporous silica. The surfactant etyltrimethylammonium tosylate (CTATOS) was used in this study to produce a pore size greater than 14 nm. The solid produced was dried using a calcination method at 300 °C for 3 hours to remove the organic material from the silica particles. Figure 6.3 shows the nitrogen sorption analysis of the calcinated samples after the first run (a) and second run (b), both showing near identical isotherms. The sample was analysed twice so that residual moisture from the samples was removed during the first sorption cycle. Consequently, only the data from the second cycle is used in the discussion of the analysis. A surface area of 571 m²/g was calculated using the Brunauer–Emmett–Teller (BET) equation, compared to the 671 m²/g reported. The pore diameters of the calcinated sample were calculated to be 1.66 nm using the BJH method, remarkably less than the 14 nm reported by Möller and Bein.[16]

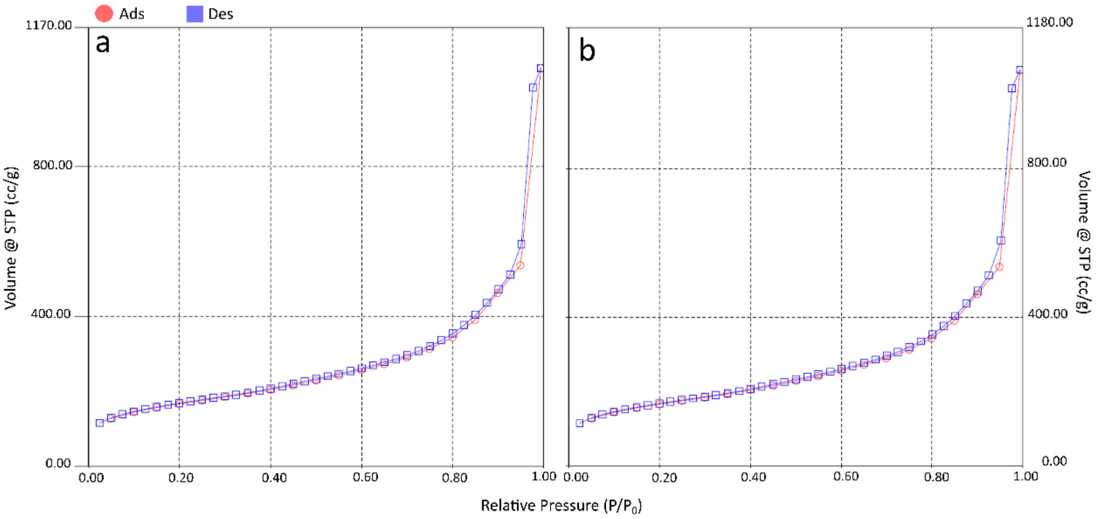

Figure 6.3: Nitrogen sorption isotherm of large-pore silica a) after one cycle and b) after two cycles of nitrogen adsorption-desorption.

The final method that was used in the synthesis of porous silica particles was an oil-water biphase stratification method adapted from Shen et al.[17] Cetyltrimethylammonium chloride (CTAC) was used as the pore template, similar to the previous method, however this method relies on the swelling behaviour of the template in hydrophobic organic solvents to provide the framework for the silica. 1-octadecene was used in the first stage to produce pore sizes of *ca.* 3 nm; decahydronaphthalene was used in the second stage to produce pore sizes of *ca.* 5.5 nm; and the final stage used cyclohexane to produce pores on the outer layer of the silica particles with pores of *ca.* 10 nm. Together, the three stages have been reported to produce mesoporous silica particles with a 'dendritic hierarchical structure'. Figure 6.4 shows the isotherm of material synthesised using the 3D dendritic mesoporous silica method. BET analysis calculates a surface area of 88.769 m^2/g, whilst BJH analysis of the desorption isotherm calculates a pore radius of 1.57 nm. These values are far from the values reported by Shen *et al.*, with their particles having a surface area of *ca.* 647 m^2/g and a final pore size of *ca.* 10 nm.

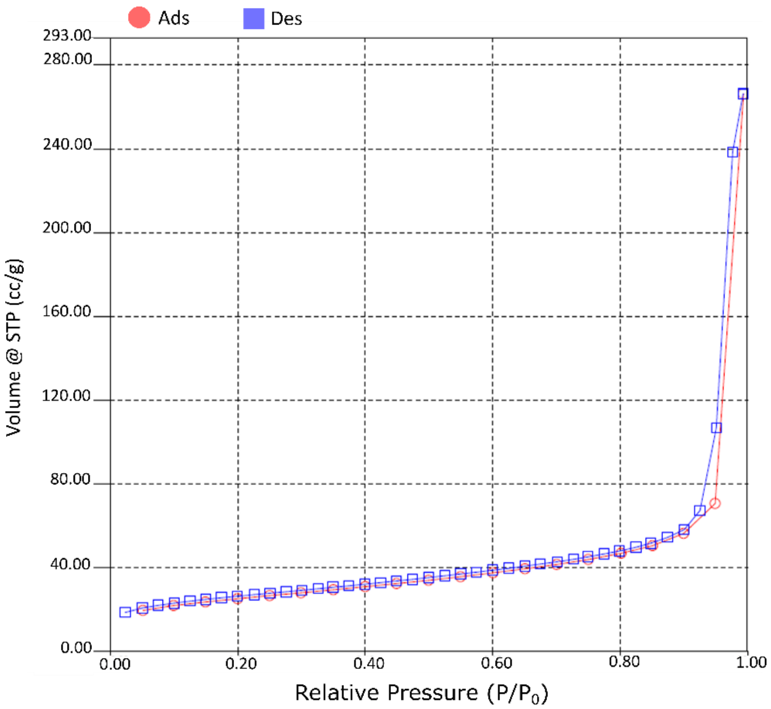

Figure 6.4: Nitrogen sorption isotherm of 3D silica.

We have found that all methods produced particles with a surface area and pore diameter that are inconsistent with the values stated in the literature. For methods that are so well-developed, our inability to replicate these synthesis pathways is intriguing however the concept of reproducibility in science has been subject of a recent article in Nature that highlights a concern in reproducibility however overall the respondents to the survey indicate that observations are generally sound.[21] In our case, there are a number of experimental factors that may have caused this. Notably, the decreased surface area is primarily due to aggregation of the particles during the centrifugation and drying processes. Hübner *et al.,* detailed a method to avoid this where the surface-modification using vinyl groups successfully prevent the agglomeration of particles.[22] Other methods such as changing the dispersion media from ethanol to a water-sodium dodecylsulfate solution enables the formation of a monodisperse suspension of silica particles whilst preventing agglomeration. The dropwise addition of the media with agitation and sonication providing the external pressure to avoid agglomeration. They noted that the fast addition of water created a high local concentration leading to the precipitation and agglomeration of silica particles. The synthesis of silica produced in this chapter did not include the dropwise addition of water, instead adding it all at once which is a contributing factor to the reduced surface area of the particles. Another factor that might have impacted the formation of the particles was the humidity of the laboratory environment the experiments were conducted in. Although water is required in the reaction, it has been reported that it has a significant impact on the synthesis of silica, but due to the complex nature of the reaction it is hard to determine the effect it has.[18] Some papers report conducting the reaction under nitrogen to limit exposure to the surrounding atmosphere. Insufficient removal of the template may have been one factor leading to the small pore diameter and leading to a decreased surface area. Both methods included a template removal stage; the large-pore method utilised calcination to remove CTATOS whilst the 3D method used ammonium nitrate in ethanol at 60 °C. In the first method, the sample is refluxed in hydrochloric acid before heating to 245 °C which is beyond the melting point of CTATOS. In the second 3D method the ammonium nitrate solution enables the cation exchange of the larger CTA^+ cation with the smaller NH_4^+ cation.[23] Transmission emission microscopy (TEM) allows for the visualisation of pores in the nanometre range, and would therefore determine if the pores are blocked.[15, 24] Unfortunately, TEM was not available to us for this study which prohibits us from being able to analyse the silica particles any further.

6.4.2 Loading isonicotinamide into porous silica

The loading of any active pharmaceutical ingredient (API) into porous material requires three stages of characterisation:

- I. Characterisation of the porous material and unconfined API
- II. Concentration analysis of the API solution
- III. Characterisation of the API-loaded particles

I) Characterisation of porous silica and unconfined API

a) Porous silica

The following studies used silica purchased by external sources to avoid the issues faced in the synthesis discussed in the previous section. SBA 15 (proposed pore size 8 nm) and silica gel (proposed pore size of 9 nm) were purchased from Sigma Aldrich. Silica gel with a proposed pore size of 15 nm was purchased from Alfa Aesar. Prior to loading, blank particles were characterised using four techniques: nitrogen sorption, XRPD, FTIR and STA (DSC and TGA). Sorption analysis was used to confirm the physical properties provided by the suppliers, in particular the average pore size (Figure 6.5 and Table 6.1). All samples show characteristic isotherms of mesoporous materials, classified as Type IV (a) isotherms by the International Union of Pure and Applied Chemistry (IUPAC).[25] The closed hysteresis is evident of the uniformity of the pores, which was not seen in the synthesised samples. BJH calculations were used to confirm the pore sizes stated by the suppliers. As displayed in Table 6.1, the average pore widths calculated are different to the values specified by the suppliers, however this is an average value. The product specification of mesoporous SBA-15 (8 nm) states an average pore diameter of 7-9 nm, therefore the values calculated in this study fall within specification. Mesoporous silica with a pore size of 9 nm was not supplied with a product specification, however values determined from N_2 sorption are similar to those for the 8 nm sample. Silica with a stated pore width of 15 nm, was calculated to have an average pore width of 5.22 nm. The product specification provided by Alfa Aesar does not provide any information regarding the pore diameter but does state a surface area of 350-400 m^2/g, which does not compare to 621 m^2/g determined during this study. It is known that particles with smaller pore diameters often have larger surface areas, as observed in Table 6.1.

Whilst the porous nature of the materials is out with the stated values, it is clear that these particles were porous and that we could move forward with the loading of isonicotinamide. Although a high-loading concentration is important for a drug delivery system, the emphasis of this study is on the characterisation of the solid state of isonicotinamide i.e., whether it is crystalline or amorphous. The methods of evaluation utilised are to ensure that isonicotinamide was loaded.

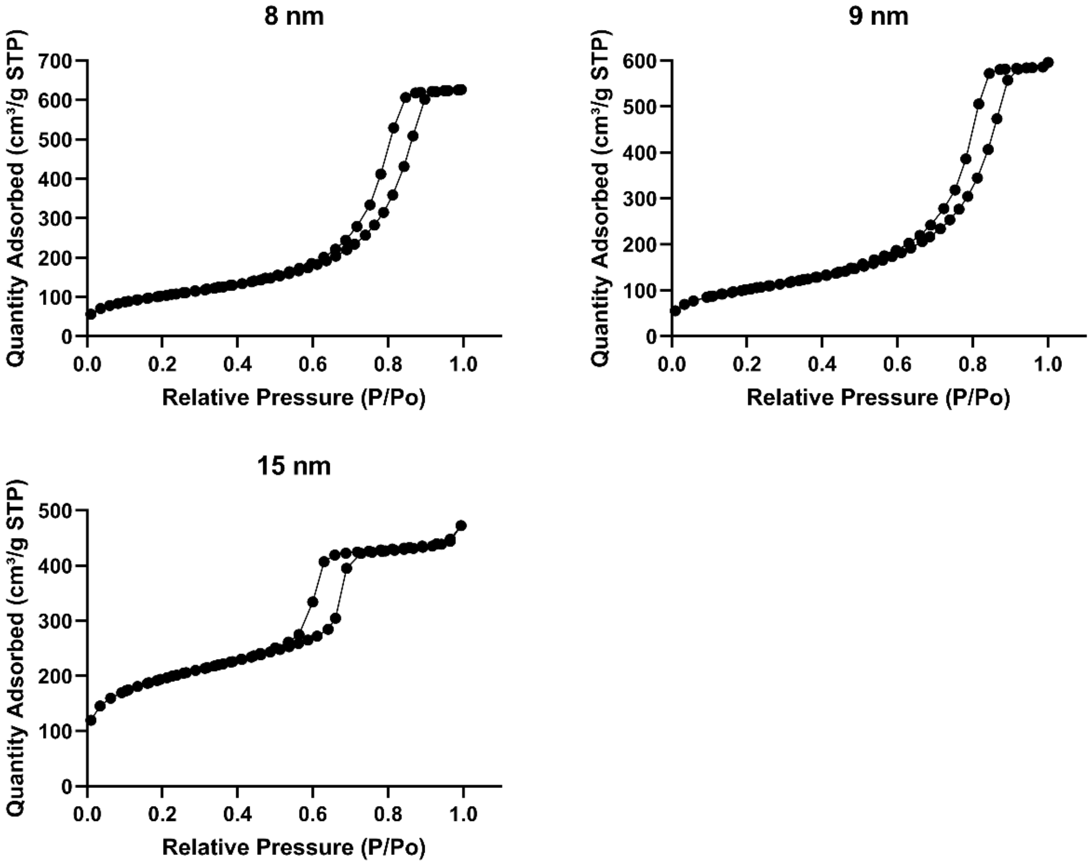

Figure 6.5: N_2 sorption isotherms corresponding to proposed pore sizes from left to right: 8 nm; 9 nm and 15 nm.

Table 6.1: N_2 sorption analysis of blank mesoporous silica.

	8 nm	**9 nm**	**15 nm**
BET Surface Area (m^2/g)	366	362	621
BJH Adsorption average pore width (nm)	8.7	9.8	5.2
Pore volume (cm^3/g)	0.97	0.92	0.73

b) Unconfined API

Prior to the discussion of isonicotinamide loaded in porous silica, it is important to understand the behaviour of the compound in its unconfined state, in particular its thermal behaviour. DSC is an important method to evaluate the location of the API whether it is in the pores or if it has crystallised on the surface as well as determining the crystalline or amorphous nature of the API. The thermograph of Form I isonicotinamide displays minor endotherm at 122.9 °C, followed by the main melting endotherm, with peak at 158.4 °C, followed by decomposition at *ca*. 190 °C evident by the loss of mass observed in the TGA (Figure 6.6).

II) Concentration analysis of the API solution

a) Preparation of isonicotinamide solutions - Calibration curves

To be able to assess the loading of the isonicotinamide in the porous materials, calibration curves for each of the solvents was required. We initially performed calibration curves for three different solvents as well as for a deuterated version of isonicotinamide using HPLC. The latter deuterated sample was chosen as we planned to perform neutron powder diffraction measurements on the sample to identify the recrystallised solid at high pressure. The calibration curves fit the data very well with the R^2 values for all conditions above 0.99 that allows them to be used to quantify the loading of the isonicotinamide into the silica (Figure 6.7).

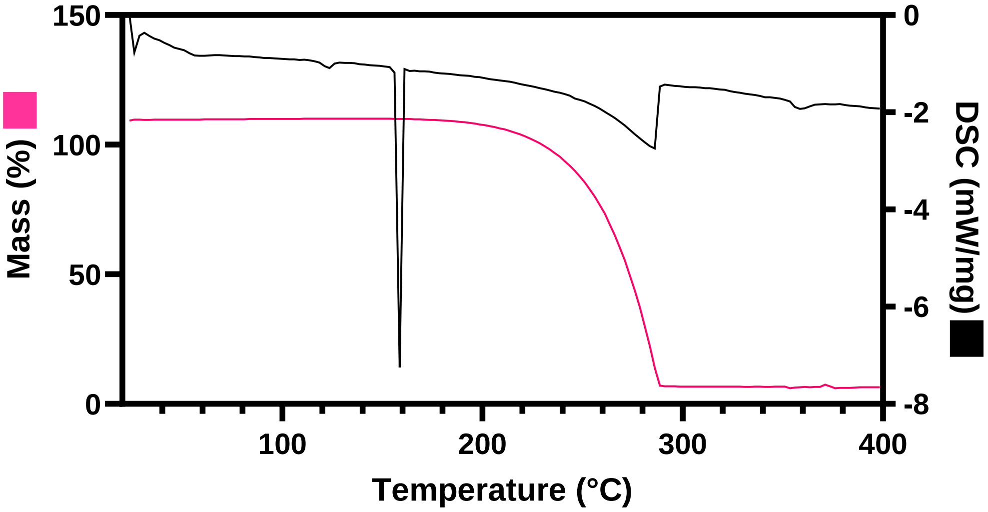

Figure 6.6: DSC (black) and TGA (pink) thermograph of isonicotinamide Form I from 25 to 400 °C.

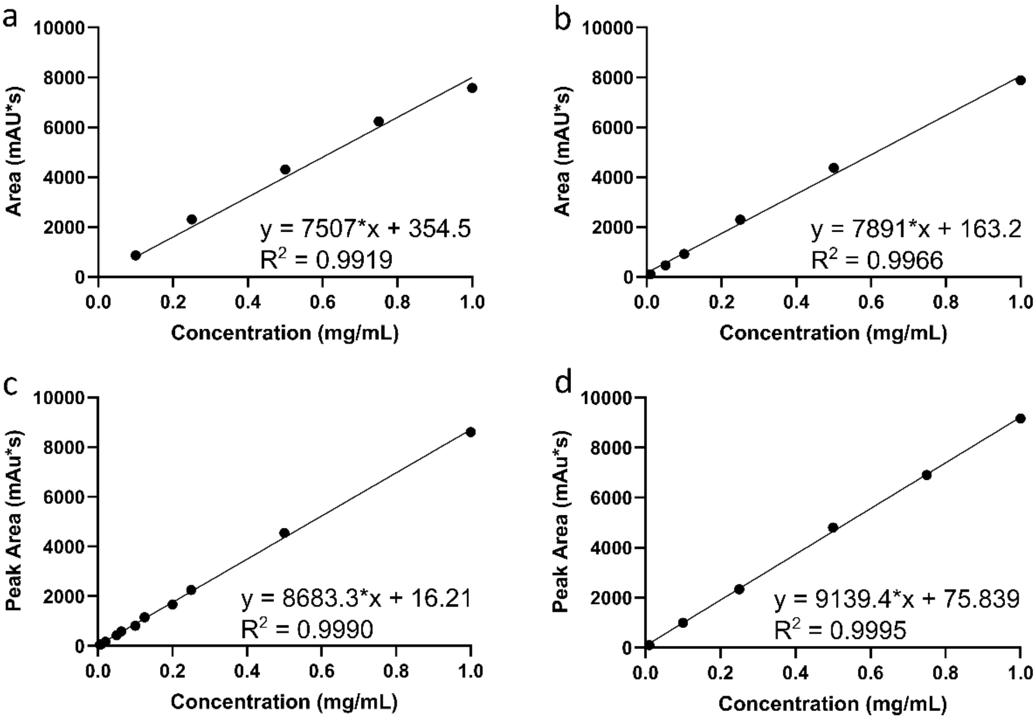

Figure 6.7: HPLC calibration data of isonicotinamide in a) ethanol, b) deionised water, c) deuterated isonicotinamide in chloroform and d) isonicotinamide in chloroform.

b) Sample solution

Our final solutions that were taken forward were ethanol and chloroform. We planned to perform loadings at ambient pressure and at high pressure (~0.8 GPa) hence needed saturated solutions for each of these conditions. Excess isonicotinamide was slurried in ethanol to produce two saturated solutions, the concentrations of which were determined to be 74.82 mg/mL and 65.09 mg/mL for ambient and high-pressure samples respectively. This is a large difference in concentration that may indicate the solution earmarked for the high-pressure experiments may have been undersaturated. This is supported by the study of ter Horst and Cains who determined the concentration to be 72 mg/mL in ethanol.[26] For the chloroform solutions, excess isonicotinamide was slurried for *ca.* 24 hours in chloroform before testing. Concentration determination was carried out using HPLC with ambient and high-pressure loading solutions of 4.13 mg/mL and 3.43 mg/mL respectively. These measurements confirm the high solubility of isonicotinamide in ethanol being over 10 times greater than the solubility in chloroform.

III) Characterisation of the API-loaded particles

a) Loading at ambient pressure – Ethanol

Table 6.2 provides the results from the HPLC analysis of the solutions. The first column indicates the concentration of the solution after the silica has been loaded. From this concentration we are able to calculate the percentage of isonicotinamide that was not loaded into the silica during the loading procedure. Of the three pore sizes, the 9 nm sample appears to have the greater percentage of isonicotinamide loaded whilst the 8 nm has the lowest, 27.23 and 14.07 % respectively; the 15 nm has a percentage loaded of 23.75 %. Using the data from the characterisation of the porous material, the 8 nm silica has a similar surface area and pore volume to the 9nm which would have indicated that it would be able to confine a similar quantity of isonicotinamide, but this is not supported by the HPLC analysis. In addition to this, the wash solution concentration cannot be greater than the loaded value hence we need to turn to diffraction and thermal methods to aid our understanding of what may be going on.

The XRPD, IR, and DSC and TGA measurement can be combined to provide information as to the location of the isonicotinamide – whether it be loaded into the pores or crystallised on the surface of the porous silica. Figure 6.8, Figure 6.9 and Figure 6.10 show the results from blank mesoporous silica, ISO-loaded silica, unwashed and washed. The XRPD for all samples show: that the silica is amorphous; that the washing procedure cleans the samples of any residual crystals that lie on the surface; and that broadly, the remaining solid is largely amorphous with a single weak peak observed (21.5°) in the 8 nm and 9 nm samples. After washing, it is difficult to ascertain the polymorph present, but this peak may be associated with Form III based on the diffraction patterns in Figure 6.11a. The observation of a single peak is odd as there is a further reflection that is equally intense in the predicted pattern at 24° that should also be present, albeit there is a hint of a peak for the 8 nm sample. Preferred orientation of the sample could be present that may account for this observation. The IR suggests the presence of isonicotinamide in the 8 nm sample hence the peak is likely to be from isonicotinamide (Figure 6.8b). Using the unwashed XRPD as a guide, the 9 nm and 15 nm samples indicate that isonicotinamide crystallises as Form III in the 9 nm case whereas it is a mixed phase of Form III with Form II which is identified by the presence of a peak at 15 ° so it would be safe to assume that the peaks in the 8 nm and 9 nm are Form III. Isonicotinamide is known to crystallise concomitantly where Forms I, II and IV can be isolated from the slow evaporation of isonicotinamide in acetone.[27] In this case, porous silica could be acting as a template for the concomitant crystallisation of the isonicotinamide polymorphism the 15 nm case.[28] Intriguingly, the IR spectra for the 9 nm and 15 nm samples do not have a strong signal compared with the 8 nm despite having the highest loadings. The issue with both XRPD and IR is the sensitivity to the sample presence. XRPD will not pick up amorphous forms and the quantity of sample for IR is low. Thermal characterisation methods are more sensitive hence can be used to identify the presence of the isonicotinamide in the silica.

The DSC and TGA results are in panels c-e in each of the Figures. All samples show the removal of water or residual solvent from the samples, evident by a broad endotherm and simultaneous mass loss between 30 and 120 °C, prior to the known melt of isonicotinamide. The melting point of isonicotinamide is between 155 and 157 °C, therefore any crystalline material present in the silica samples should display a sharp melting endotherm in this region (Figure 6.6). When loaded into the mesoporous silica, isonicotinamide shows a reduction in crystallinity, therefore no sharp melting endotherm was observed for any sample. Instead, samples before and after the wash with water show a broad endothermic event between 200 and 300 °C, with a corresponding mass loss between 150 and 300 °C; the temperature of the onset is consistent between samples. The pure silica does not show this event hence it is likely this is the decomposition of isonicotinamide confined in the pores. Previous studies have indicated that confinement of pharmaceutical compounds often leads to the depression of the melting point, according to the Gibbs-Thomson equation.[29] This does not seem to be the case here and there is little evidence to suggest the melting event occurring. Each of the samples show a decrease in mass of approximately 4-9 %. Our diffraction data suggests that the surface crystallisation is washed away during the wash step hence any remaining isonicotinamide must be left in the pores of the silica and is likely to be amorphous in nature. Despite showing the lowest loading in the HPLC method, the 8 nm sample loses the largest proportion of its weight on heating suggesting the greatest loading. A caveat to this is the initial water content, i.e., the initial weight loss due to solvent does change from sample to sample.

Table 6.2: HPLC data of isonicotinamide in ethanol, loaded at ambient and high pressure.

	Pore Size (nm)	**API Loading (mg/mL)**	**API Loading (%)**	**Wash Conc. (mg/mL)**	**API Loading† (mg/mL)**	**API Loading† (%)**
Ambient Pressure	8	10.53	14.07	12.08	-	-
	9	20.46	27.35	12.69	-	-
	15	17.77	23.75	13.24	-	-
High Pressure	8	8.32	12.78	24.57	18.05	24.12
	9	4.28	6.58	12.32	14.02	18.74
	15	-4.21*	-6.47*	9.78	5.52	7.38

* Data shows an increase in isonicotinamide concentration after loading.

† Hypothetical results using 72 mg/mL as the initial saturated solution concentration.

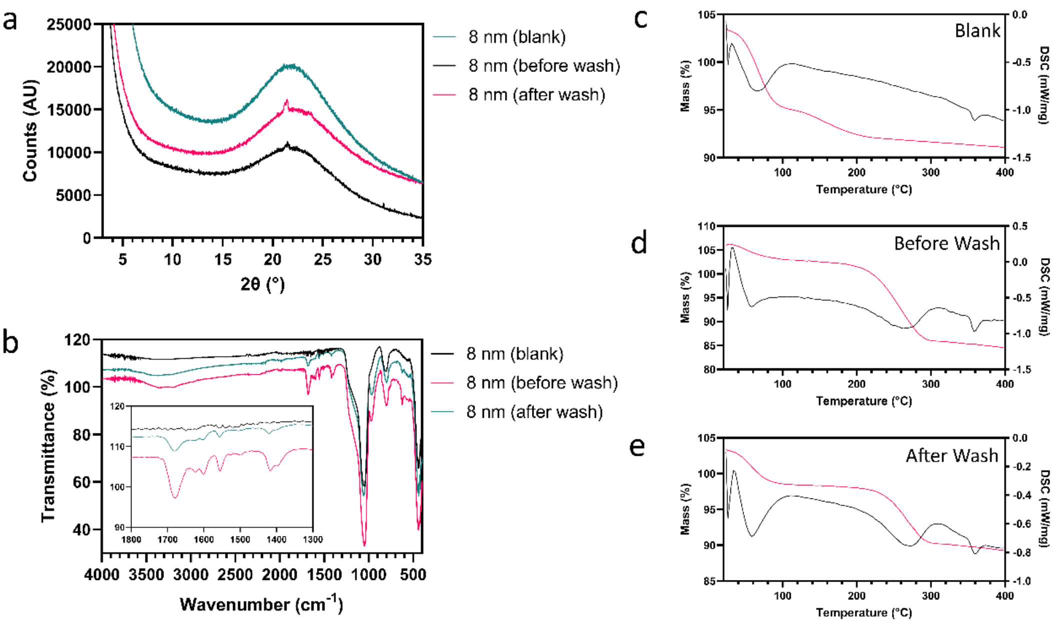

Figure 6.8: 8 nm porous silica loaded using isonicotinamide in ethanol at ambient pressure. a) XRPD of blank, unwashed and washed particles, with crystalline material present in both samples. b) FTIR spectra of blank silica particles and loaded particles between 4000-400 cm^{-1}. Inset shows region of interest between 1800-1300 cm^{-1}. c-e) DSC (black) and TGA (pink) obtained between 20-400 °C at a heating rate of 5 K/min. Blank samples are given for comparison.

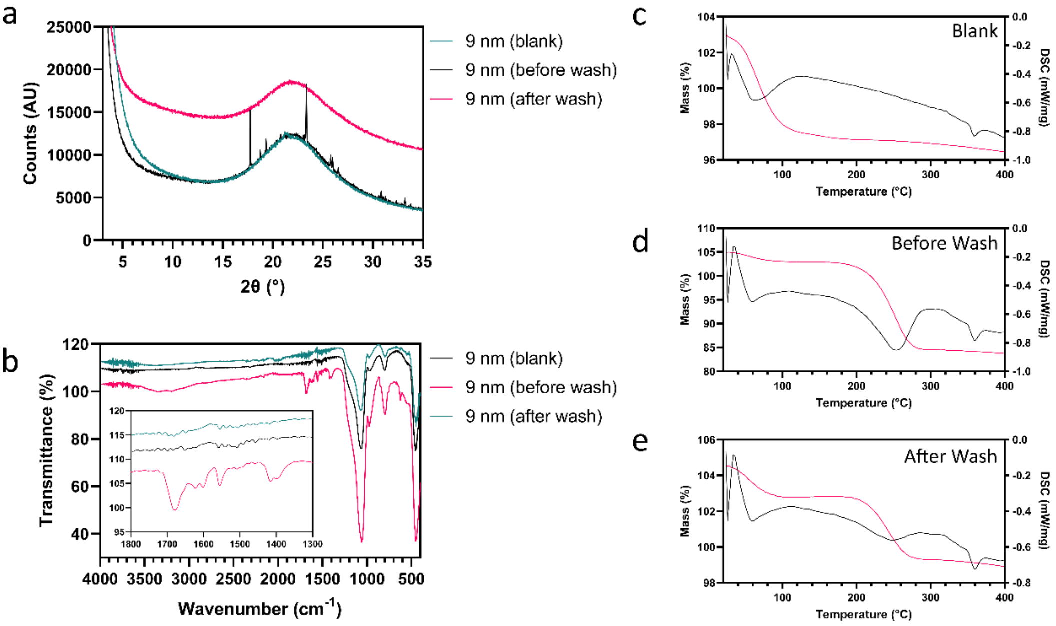

Figure 6.9: 9 nm porous silica loaded using isonicotinamide in ethanol at ambient pressure. a) XRPD of blank, unwashed and washed particles, with crystalline material present in both samples. b) FTIR spectra of blank silica particles and loaded particles between 4000-400 cm^{-1}. Inset shows region of interest between 1800-1300 cm^{-1}. c-e) DSC (black) and TGA (pink) obtained between 20-400 °C at a heating rate of 5 K/min. Blank samples are given for comparison.

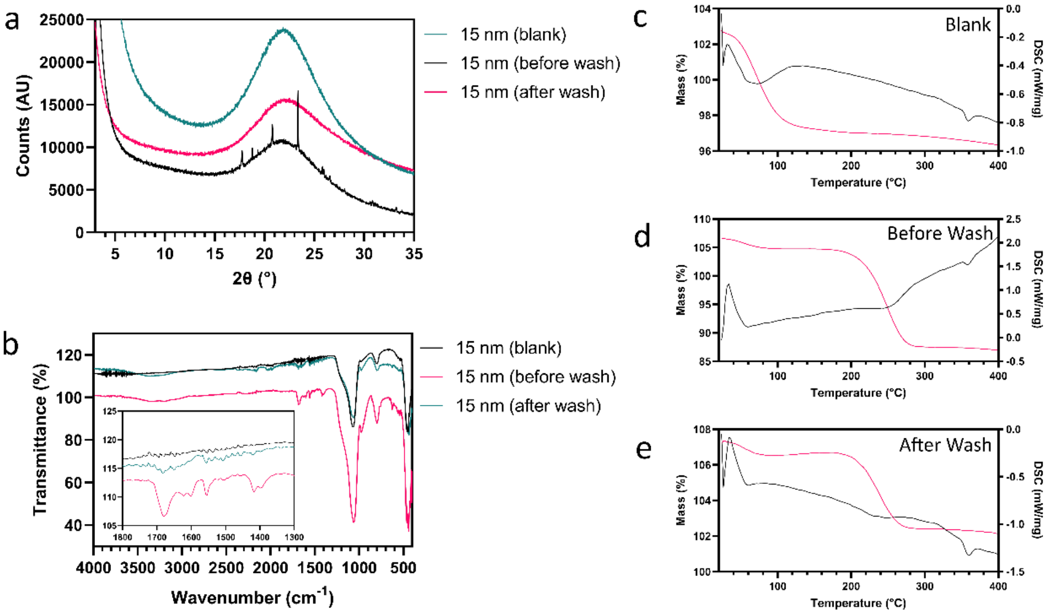

Figure 6.10: 15 nm porous silica loaded using isonicotinamide in ethanol at ambient pressure. a) XRPD of blank, unwashed and washed particles, with crystalline material present in both samples. b) FTIR spectra of blank silica particles and loaded particles between 4000-400 cm^{-1}. Inset shows region of interest between 1800-1300 cm^{-1}. c-e) DSC (black) and TGA (pink) obtained between 20-400 °C at a heating rate of 5 K/min. Blank samples are given for comparison.

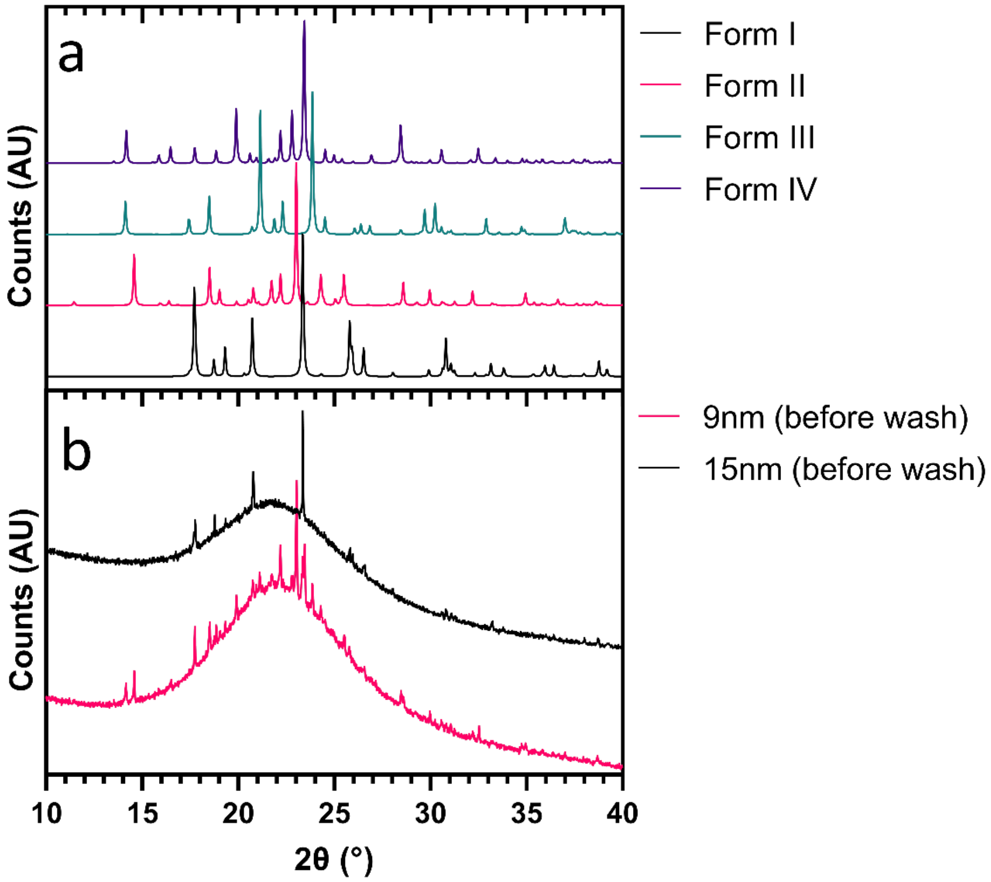

Figure 6.11: XRPD patterns of a) isonicotinamide polymorphs: Form I, II, III and IV and b) isonicotinamide loaded into porous silica using ethanol prior to washing.

b) Loading at high pressure - Ethanol

To caveat the high-pressure loading work, the initial saturated solution concentration was significantly lower than the solution for ambient pressure and literature values (64mg/mL *ca.* 74 mg/mL & 72 mg/mL). The HPLC analysis of the high-pressure shows that the percentage load of isonicotinamide in porous silica at high-pressure is significantly lower than the particles loaded at ambient pressure. Here, porous silica with a stated pore size of 8 nm has the greater percentage loaded, followed by 9 nm (12.78 and 6.58 % of the loading solution respectively). The HPLC data for 15 nm shows an increase in concentration of the loading solution, which is likely due to an error in dilution prior to analysis, therefore the values cannot be used. If we use the hypothetical values for the initial concentration of isonicotinamide (72 mg/mL), the loading is higher than the measured values but still lower than the ambient pressure loading. The XRPD does not show significant crystallisation, with the 8 and 9 nm samples indicating Form III. The DSC traces, perhaps, reflect better why there is a lower loading of isonicotinamide. The proportion of solvent loss in each of the high-pressure loaded samples is substantially higher than the ambient pressure loadings (Table 6.3). This would indicate that more solvent has been pushed into the pores of the silica to the detriment of the isonicotinamide. So, whilst the solvent was required for solubilisation of isonicotinamide and mobility, it has obstructed the interaction between the API and silica. There is still the mass loss associated with the isonicotinamide which indicates that it is present but as a percentage of the total mass, this is much reduced. The neutron powder diffraction experiments did not indicate any crystallisation of isonicotinamide but instead indicated the total collapse of the silica structure (Figure 6.15). This suggests that the quantity of material inside the pores was not substantial enough to provide support for the structure. This may provide some rationale why the loading at pressure was not as high as the ambient pressure loading.

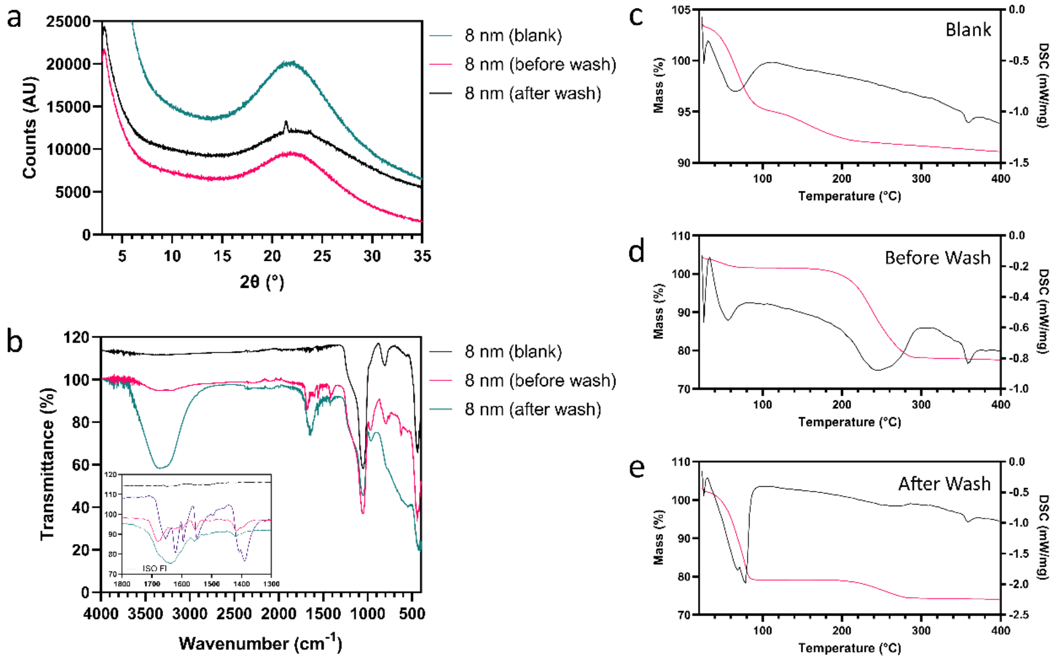

Figure 6.12: 8 nm porous silica loaded using isonicotinamide in ethanol at high pressure. a) XRPD of blank, unwashed and washed particles, with crystalline material present in both samples. b) FTIR spectra of blank silica particles and loaded particles between 4000-400 cm^{-1}. c-e) DSC (black) and TGA (pink) obtained between 20-400 °C at a heating rate of 5 K/min. Blank samples are given for comparison.

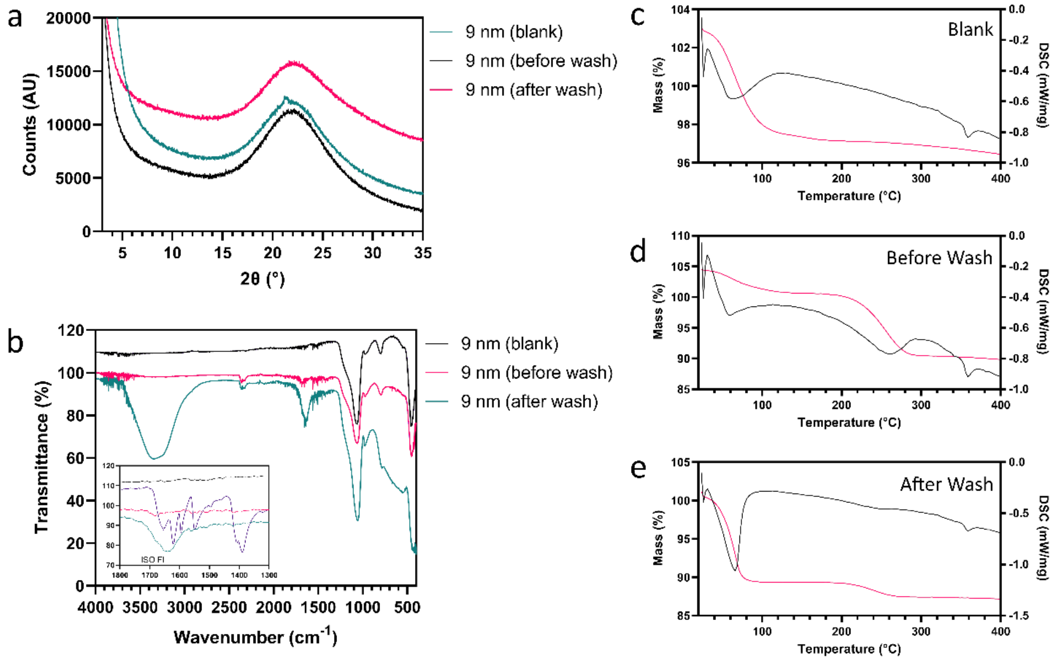

Figure 6.13: 9 nm porous silica loaded using isonicotinamide in ethanol at high pressure. a) XRPD of blank, unwashed and washed particles, with crystalline material present in both samples. b) FTIR spectra of blank silica particles and loaded particles between 4000-400 cm^{-1}. c-e) DSC (black) and TGA (pink) obtained between 20-400 °C at a heating rate of 5 K/min. Blank samples are given for comparison.

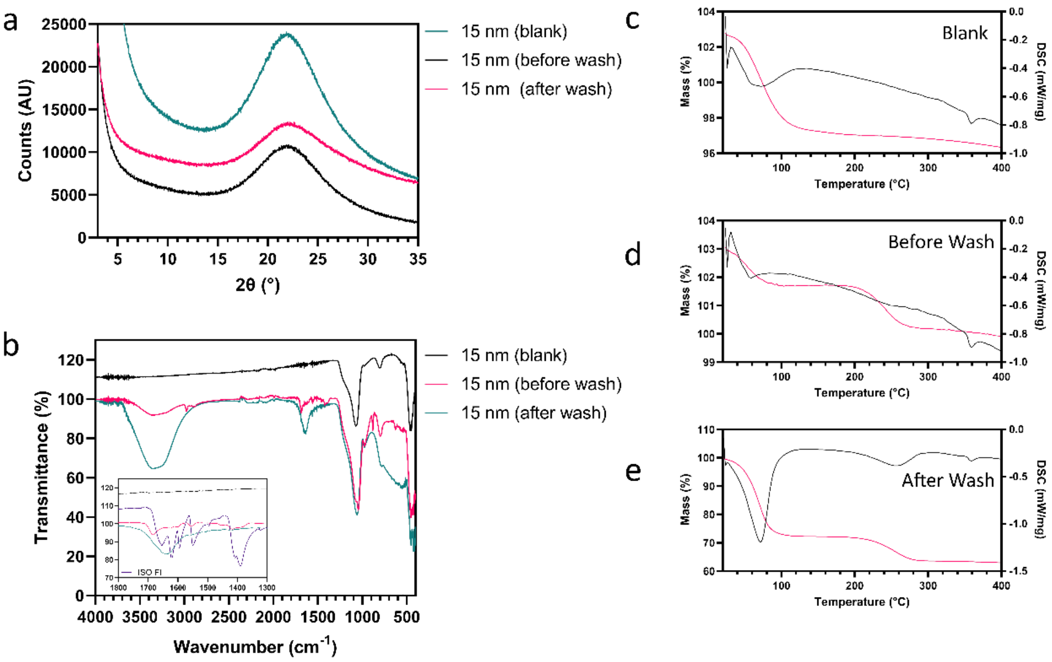

Figure 6.14: 15 nm porous silica loaded using isonicotinamide in ethanol at high pressure. a) XRPD of blank, unwashed and washed particles, with crystalline material present in both samples. b) FTIR spectra of blank silica particles and loaded particles between 4000-400 cm^{-1}. c-e) DSC (black) and TGA (pink) obtained between 20-400 °C at a heating rate of 5 K/min. Blank samples are given for comparison.

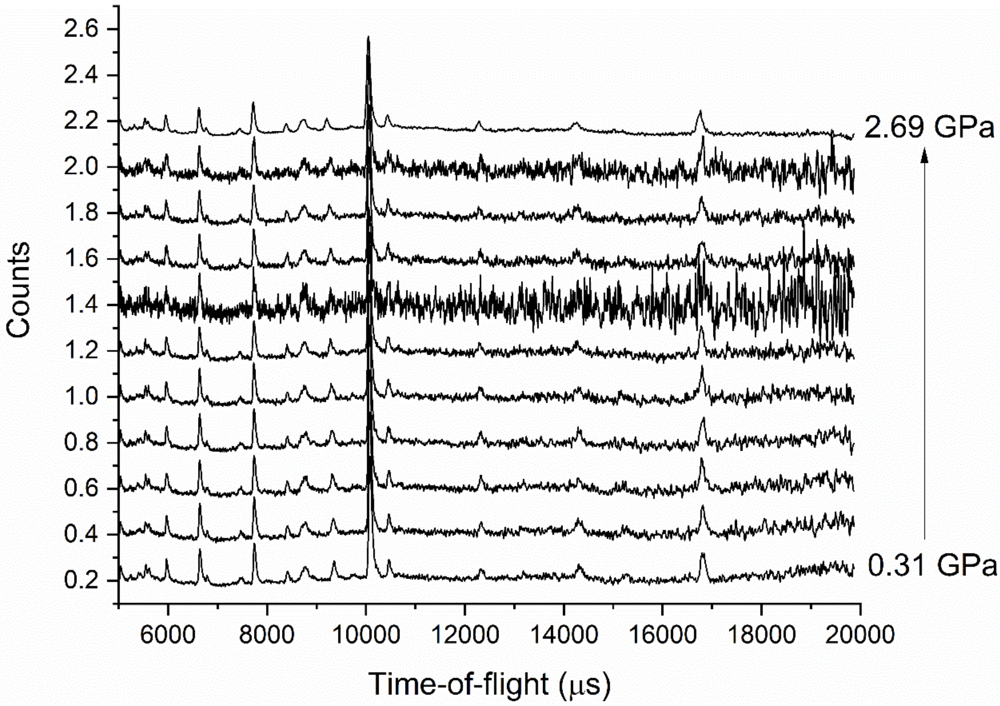

Figure 6.15: Neutron powder diffraction measurements indicating the amorphous nature of silica (absence of diffraction) but presence of lead, alumina and zirconia that are part of the sample environment. No isonicotinamide was present in the sample. The pressure/load curve for this sample indicated the collapse of the silica i.e., the load that was required to achieve the pressure in the sample was significantly higher than a ‘regular’ crystalline solid.

Table 6.3: DSC and TGA data of isonicotinamide in ethanol loaded into porous silica at ambient pressure.

	Sample	**TGA**		**DSC**	
		Mass Loss between 20 and 150 °C (%)	**Mass Loss between 150 and 400 °C (%)**	**Temperature Range (°C)**	**Endotherm Area (J/g)**
8 nm	**Ambient Before Wash**	-3.75	-17.99	227.2 - 295.4	-208.1
	Ambient After Wash	-4.99	-9.08	226.9 - 299.4	-100.3
	HP Before Wash	-2.44	-23.94	206.7 - 292.5	-239.8
	HP After Wash	-23.18	-5.11	213.6-283.6	-40.85
9 nm	**Ambient Before Wash**	-1.8	-19.14	208.9 - 283.4	-196.1
	Ambient After Wash	-1.57	-3.93	203.5 - 268.3	-36.37
	HP Before Wash	-3.64	-10.8	218.4 – 289.0	-77.63
	HP After Wash	-11.2	-2.15	-	-
15 nm	**Ambient Before Wash**	-1.71	-17.75	212.2 – 279.9	-102
	Ambient After Wash	-0.54	-4.53	200.0 – 273.8	-23.99
	HP Before Wash	-27.69	-9.23	210.6 – 287.2	-72.95
	HP After Wash	-1.34	-1.8	-	-

c) Loading using Chloroform solution

Our analysis of the chloroform samples is incomplete due to technical and safety aspects of this chapter as well as the shutdown for COVID-19.

As shown in Table 6.4, chloroform was successfully loaded isonicotinamide into the mesoporous silica particles with greater percentage loaded values, however it is necessary to consider the concentrations of the loading solutions. Ethanol reaches greater concentrations in comparison, with solutions containing *ca.* 18 times more isonicotinamide than chloroform, due for the great difference in affinity as highlighted in the introduction. The loading concentrations in chloroform were of 4.13 mg/mL and 3.43 mg/mL.

The difference with the ethanol solution loading is that, in all cases, the washed samples are amorphous in character. The only sample to show crystalline material is the 8 nm ambient samples prior to washing but after treatment the crystalline sample is removed (presumably form the surface). The DSC traces for each of the samples mimic that seen in the ethanol examples. There is an initial mass loss associated with the solvent before a further loss between 200-300 °C. Of note is the significantly less solvent loss shown in the high-pressure samples. This could be attributed to the higher volatility of chloroform hence there is loss prior to measurement. On the whole however, the isonicotinamide seems to be loaded as an amorphous material as there is no indication of a melting event. Given the paucity of data it is difficult to assess the different modes of loading but one factor that may influence the behaviour is the freezing pressure of the solvents. Ethanol freezes at 1.9 GPa whilst chloroform freezes at a pressure of 0.6 GPa.[30] In terms of loading pressure, this means that the ethanol will still be fluid but the chloroform may have crystallised which would impact the mobility and capillary condensation of isonicotinamide into the pores.

Table 6.4: HPLC data of isonicotinamide in chloroform, loaded at ambient and high pressure.

	Pore Size (nm)	**API Loading (mg/mL)**	**API Loading (%)**	**Wash Conc. (mg/mL)**
Ambient Pressure	8	4.10	99.27	0.12
	15	4.13	100.00	0.04
High Pressure	8	3.14	91.55	0.19
	15	3.42	99.71	0.01

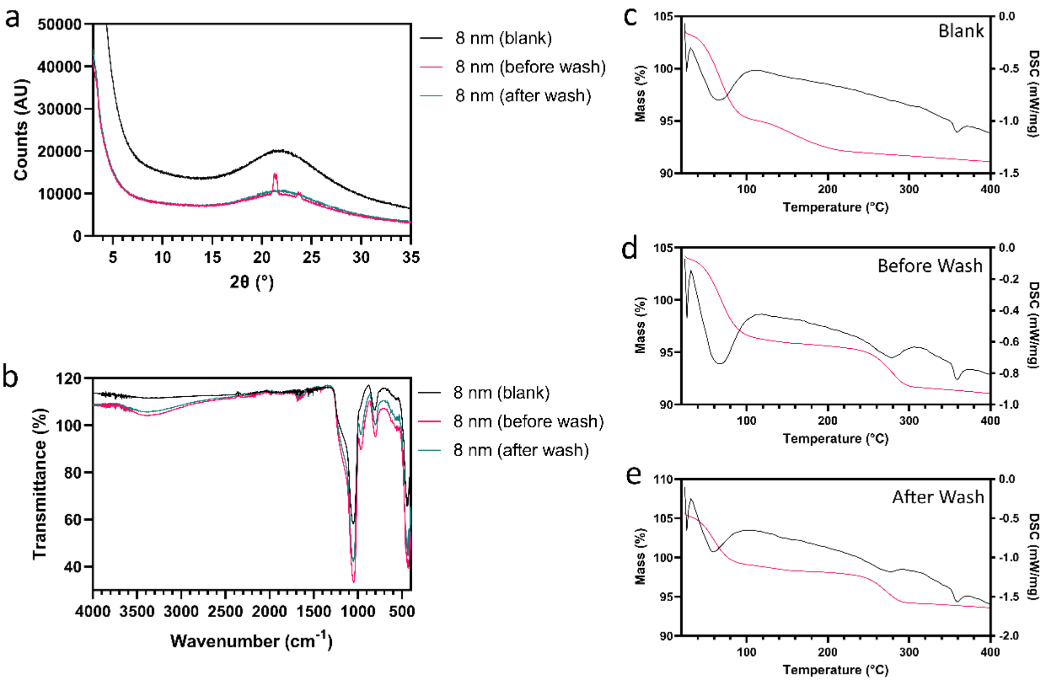

Figure 6.16: 8 nm porous silica loaded using isonicotinamide in chloroform at ambient pressure. a) XRPD of blank, unwashed, and washed particles. b) FTIR spectra of blank silica particles and loaded particles before and after the wash between 4000-400 cm^{-1}. c-e) DSC (black) and TGA (pink) obtained between 20-400 °C at a heating rate of 5 K/min. Blank samples are given for comparison.

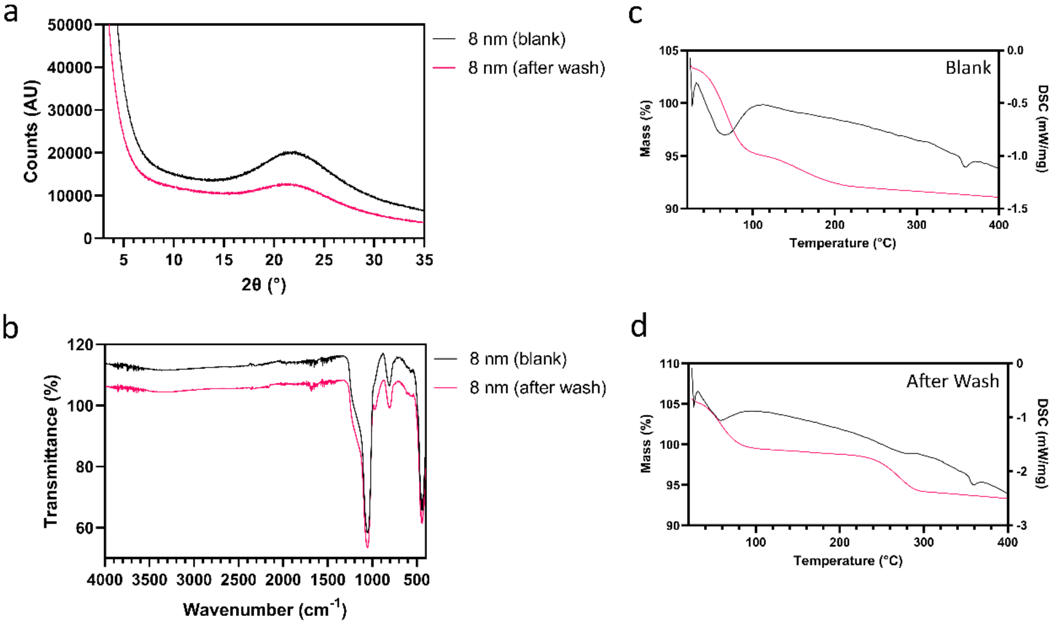

Figure 6.17: 8 nm porous silica loaded using isonicotinamide in chloroform at high pressure. a) XRPD of blank and washed particles. b) FTIR spectra of blank silica particles and loaded particles after the wash between 4000-400 cm^{-1}. c&d) DSC (black) and TGA (pink) obtained between 20-400 °C at a heating rate of 5 K/min. Blank samples are given for comparison.

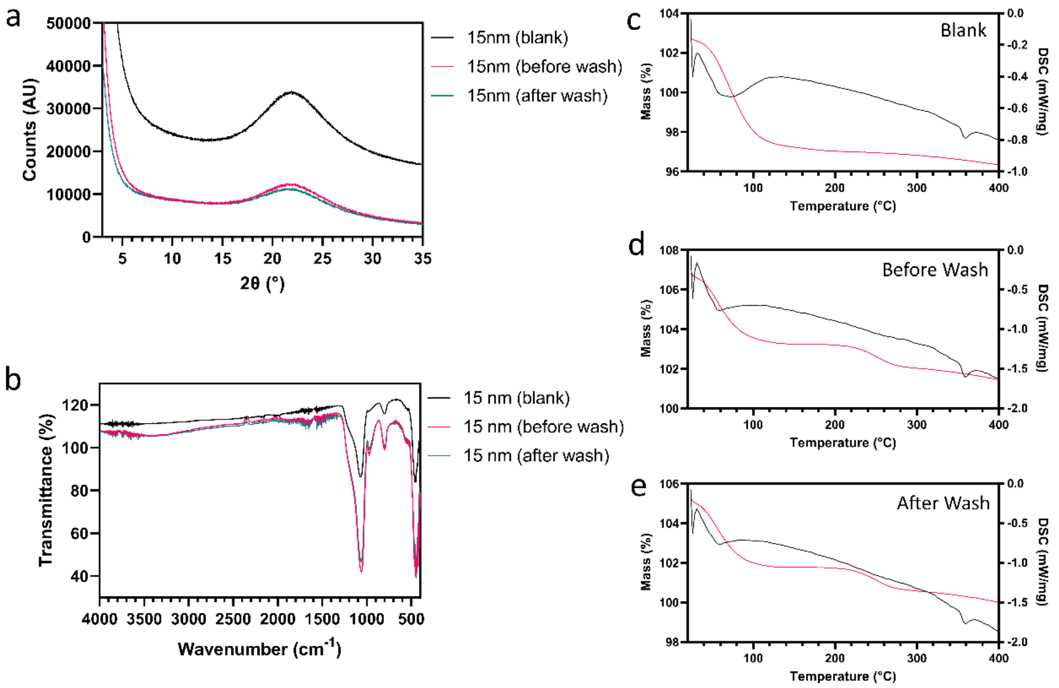

Figure 6.18: 15 nm porous silica loaded using isonicotinamide in chloroform at ambient pressure. a) XRPD of blank, unwashed, and washed particles. b) FTIR spectra of blank silica particles and loaded particles before and after the wash between 4000-400 cm^{-1}. c-e) DSC (black) and TGA (pink) obtained between 20-400 °C at a heating rate of 5 K/min. Blank samples are given for comparison.

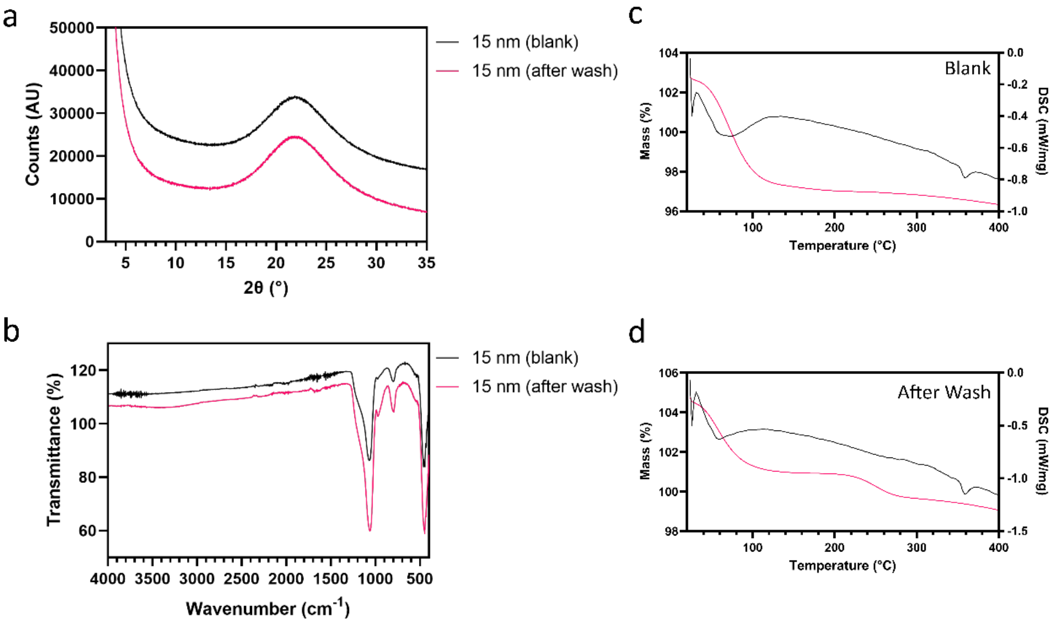

Figure 6.19: 15 nm porous silica loaded using isonicotinamide in chloroform at high pressure. a) XRPD of blank and washed particles. b) FTIR spectra of blank silica particles and loaded particles after the wash between 4000-400 cm^{-1}. c&d) DSC (black) and TGA (pink) obtained between 20-400 °C at a heating rate of 5 K/min. Blank samples are given for comparison.

6.5 Conclusion

In this chapter, we have demonstrated that from our perspective, the methodologies for the preparation of mesoporous silica are not robust. The characterisation of the porous materials indicated that porous materials that pertain to have a particular pore geometry are not necessarily correct. From the scientific perspective, we have been able to successfully load isonicotinamide into the mesoporous materials and that the solid is likely to be amorphous in nature. The different loading methods, i.e., ambient, and high pressure, show differences in the solvent content in the pores. The compression of the solvent in the pores and the potential better interaction of the solvent with the silica may be a reason for the lack of increase of isonicotinamide loading. This is somewhat support by the chloroform measurements where the quantity of solvent left in the pores is insignificant between the ambient and high-pressure loadings.

From the outset this chapter was beset by problems that has prevented the extensive characterisation and the repeats that are necessary to provide a definitive conclusion of the processes that are going on. In particular, the opportunity to refine our silica production was not possible due to time constraints which has impacted the overall study through use of purchased silica. We hoped that we would be able to start to explore the larger molecules, such as nifedipine, which would have been a move towards more complex systems especially given its prolific solvate behaviour.

6.6 References

1. Kresge, C. T.; Leonowicz, M. E.; Roth, W. J.; Vartuli, J. C.; Beck, J. S. Ordered mesoporous molecular sieves synthesized by a liquid-crystal template mechanism. In *Nature*, 1992; Vol. 359, pp 710-713. Kresge, C. T.; Leonowicz, M. E.; Roth, W. J.; Vartuli, J. C. Synthetic Mesoporous Crystaline Material. 1992. Kresge, C. T.; Leonowicz, M. E.; Roth, W. J.; Vartuli, J. C. Composition Of Synthetic Porous Crystalline Material, Its Synthesis. 1992. Beck, J. S.; Vartuli, J. C.; Roth, W. J.; Leonowicz, M. E.; Kresge, C. T.; Schmitt, K. D.; Chu, C. T. W.; Olson, D. H.; Sheppard, E. W.; McCullen, S. B.; et al. A New Family of Mesoporous Molecular Sieves Prepared with Liquid Crystal Templates. In *Journal of the American Chemical Society*, 1992; Vol. 114, pp 10834-10843.
2. Kresge, C. T.; Roth, W. J. The discovery of mesoporous molecular sieves from the twenty year perspective. In *Chemical Society Reviews*, 2013; Vol. 42, pp 3663-3670.
3. Zhao, D.; Feng, J.; Huo, Q.; Melosh, N.; Fredrickson, G. H.; Chmelka, B. F.; Stucky, G. D. Triblock copolymer syntheses of mesoporous silica with periodic 50 to 300 angstrom pores. In *Science*, 1998; Vol. 279, pp 548-552.
4. Zhao, D.; Sun, J.; Li, Q.; Stucky, G. D. Morphological control of highly ordered mesoporous silica SBA-15. In *Chemistry of Materials*, 2000; Vol. 12, pp 275-279.
5. Vallet-Regi, M.; Rámila, A.; Del Real, R. P.; Pérez-Pariente, J. A new property of MCM-41: Drug delivery system. In *Chemistry of Materials*, 2001; Vol. 13, pp 308-311.
6. Muñoz, B.; Rámila, A.; Pérez-Pariente, J.; Díaz, I.; Vallet-Regí, M. MCM-41 organic modification as drug delivery rate regulator. In *Chemistry of Materials*, 2003; Vol. 15, pp 500-503.
7. Doadrio, A. L.; Sousa, E. M. B.; Doadrio, J. C.; Pérez Pariente, J.; Izquierdo-Barba, I.; Vallet-Regí, M. Mesoporous SBA-15 HPLC evaluation for controlled gentamicin drug delivery. In *Journal of Controlled Release*, 2004; Vol. 97, pp 125-132.
8. Heikkilä, T.; Salonen, J.; Tuura, J.; Kumar, N.; Salmi, T.; Murzin, D. Y.; Hamdy, M. S.; Mul, G.; Laitinen, L.; Kaukonen, A. M.; et al. Evaluation of mesoporous TCPSi, MCM-41, SBA-15, and TUD-1 materials as API carriers for oral drug delivery. In *Drug Delivery*, 2007; Vol. 14, pp 337-347.
9. Song, S. W.; Hidajat, K.; Kawi, S. Functionalized SBA-15 materials as carriers for controlled drug delivery: Influence of surface properties on matrix-drug interactions. In *Langmuir*, 2005; Vol. 21, pp 9568-9575. Andersson, J.; Rosenholm, J.; Areva, S.; Lindén, M. Influences of material characteristics on ibuprofen drug loading and release profiles from ordered micro- and mesoporous silica matrices. In *Chemistry of Materials*, 2004; Vol. 16, pp 4160-4167. Mellaerts, R.; Jammaer, J. A. G.; Van Speybroeck, M.; Hong, C.; Van Humbeeck, J.; Augustijns, P.; Van Den Mooter, G.; Martens, J. A. Physical state of poorly water soluble therapeutic molecules loaded into SBA-15 ordered mesoporous silica carriers: A case study with itraconazole and ibuprofen. In *Langmuir*, 2008; Vol. 24, pp 8651-8659.
10. Hong, S.; Shen, S.; Tan, D. C. T.; Ng, W. K.; Liu, X.; Chia, L. S. O.; Irwan, A. W.; Tan, R.; Nowak, S. A.; Marsh, K.; et al. High drug load, stable, manufacturable and bioavailable fenofibrate formulations in mesoporous silica: A comparison of spray drying versus solvent impregnation methods. In *Drug Delivery*, 2016; Vol. 23, pp 316-327.
11. Van Speybroeck, M.; Barillaro, V.; Thi, T. D.; Mellaerts, R.; Martens, J.; Van Humbeeck, J.; Vermant, J.; Annaert, P.; Van Den Mooter, G.; Augustijns, P. Ordered mesoporous silica material SBA-15: A broad-spectrum formulation platform for poorly soluble drugs. In *Journal of Pharmaceutical Sciences*, 2009; Vol. 98, pp 2648-2658. Lee, C. H.; Lo, L. W.; Mou, C. Y.; Yang, C. S. Synthesis and characterization of positive-charge functionalized mesoporous silica nanoparticles for oral drug delivery of an anti-inflammatory drug. In *Advanced Functional Materials*, 2008; Vol. 18, pp 3283-3292.

12. Lynch, M. B.; Lawrence, S. E.; Nolan, M. Predicting Nucleation of Isonicotinamide from the Solvent-Solute Interactions of Isonicotinamide in Common Organic Solvents. In *Journal of Physical Chemistry A*, American Chemical Society: 2018; Vol. 122, pp 3301-3312.
13. Li, B.; Wu, Y.; Zhu, J.; Chen, K.; Wu, B.; Ji, L. Determination and correlation of solubility and mixing properties of isonicotinamide (form II) in some pure solvents. In *Thermochimica Acta*, 2016; Vol. 627-629, pp 55-60.
14. Khanna, L.; Lai, Y.; Dasog, M. Systematic evaluation of inorganic salts as a heat sink for the magnesiothermic reduction of silica. In *Canadian Journal of Chemistry*, 2018; Vol. 96, p 965+.
15. Nozawa, K.; Gailhanou, H.; Raison, L.; Panizza, P.; Ushiki, H.; Sellier, E.; Delville, J. P.; Delville, M. H. Smart Control of Monodisperse Stöber Silica Particles: Effect of Reactant Addition Rate on Growth Process. In *Langmuir*, American Chemical Society: 2005; Vol. 21, pp 1516-1523.
16. Möller, K.; Bein, T. Talented Mesoporous Silica Nanoparticles. In *Chemistry of Materials*, American Chemical Society: 2017; Vol. 29, pp 371-388.
17. Shen, D.; Yang, J.; Li, X.; Zhou, L.; Zhang, R.; Li, W.; Chen, L.; Wang, R.; Zhang, F.; Zhao, D. Biphase Stratification Approach to Three-Dimensional Dendritic Biodegradable Mesoporous Silica Nanospheres. In *Nano Letters*, American Chemical Society: 2014; Vol. 14, pp 923-932.
18. Stöber, W.; Fink, A.; Bohn, E. Controlled growth of monodisperse silica spheres in the micron size range. In *Journal of Colloid and Interface Science*, 1968; Vol. 26, pp 62-69.
19. Kaya, H.; Ngo, D.; Gin, S.; Kim, S. H. Spectral changes in Si–O–Si stretching band of porous glass network upon ingress of water. In *Journal of Non-Crystalline Solids*, 2020; Vol. 527, p 119722.
20. Ghimire, P. P.; Jaroniec, M. Renaissance of Stöber method for synthesis of colloidal particles: New developments and opportunities. In *Journal of Colloid and Interface Science*, 2021; Vol. 584, pp 838-865. Tang, L.; Cheng, J. Nonporous silica nanoparticles for nanomedicine application. In *Nano Today*, 2013; Vol. 8, pp 290-312.
21. Baker, M. 1,500 scientists lift the lid on reproducibility. In *Nature*, 2016; Vol. 533, pp 452-454.
22. Hübner, C.; Fettkenhauer, C.; Voges, K.; Lupascu, D. C. Agglomeration-Free Preparation of Modified Silica Nanoparticles for Emulsion Polymerization—A Well Scalable Process. In *Langmuir*, American Chemical Society: 2018; Vol. 34, pp 376-383.
23. Deekamwong, K.; Wittayakun, J. Template removal by ion-exchange extraction from siliceous MCM-41 synthesized by microwave-assisted hydrothermal method. In *Microporous and Mesoporous Materials*, 2017; Vol. 239, pp 54-59.
24. Boissière, C.; Larbot, A.; van der Lee, A.; Kooyman, P. J.; Prouzet, E. A New Synthesis of Mesoporous MSU-X Silica Controlled by a Two-Step Pathway. In *Chemistry of Materials*, American Chemical Society: 2000; Vol. 12, pp 2902-2913.
25. Thommes, M.; Kaneko, K.; Neimark, A. V.; Olivier, J. P.; Rodriguez-Reinoso, F.; Rouquerol, J.; Sing, K. S. W. Physisorption of gases, with special reference to the evaluation of surface area and pore size distribution (IUPAC Technical Report). In *Pure and Applied Chemistry*, 2015; Vol. 87, pp 1051-1069.
26. Horst, J. H. t.; Cains, P. W. Co-Crystal Polymorphs from a Solvent-Mediated Transformation. In *Crystal Growth & Design*, American Chemical Society: 2008; Vol. 8, pp 2537-2542.
27. Eccles, K. S.; Deasy, R. E.; Fábián, L.; Braun, D. E.; Maguire, A. R.; Lawrence, S. E. Expanding the crystal landscape of isonicotinamide: concomitant polymorphism and co-crystallisation. In *CrystEngComm*, The Royal Society of Chemistry: 2011; Vol. 13, pp 6923-6925.

28. Caridi, A.; Kulkarni, S. A.; Di Profio, G.; Curcio, E.; ter Horst, J. H. Template-Induced Nucleation of Isonicotinamide Polymorphs. In *Crystal Growth & Design*, American Chemical Society: 2014; Vol. 14, pp 1135-1141.
29. Nartowski, K. P.; Tedder, J.; Braun, D. E.; Fábián, L.; Khimyak, Y. Z. Building solids inside nano-space: from confined amorphous through confined solvate to confined 'metastable' polymorph. In *Physical Chemistry Chemical Physics*, The Royal Society of Chemistry: 2015; Vol. 17, pp 24761-24773. Cordeiro, T.; Santos, A. F. M.; Nunes, G.; Cunha, G.; Sotomayor, J. C.; Fonseca, I. M.; Danède, F.; Dias, C. J.; Cardoso, M. M.; Correia, N. T.; et al. Accessing the Physical State and Molecular Mobility of Naproxen Confined to Nanoporous Silica Matrixes. In *The Journal of Physical Chemistry C*, American Chemical Society: 2016; Vol. 120, pp 14390-14401. Talik, A.; Tarnacka, M.; Minecka, A.; Hachuła, B.; Grelska, J.; Jurkiewicz, K.; Kaminski, K.; Paluch, M.; Kaminska, E. Anormal Thermal History Effect on the Structural Dynamics of Probucol Infiltrated into Porous Alumina. In *The Journal of Physical Chemistry C*, American Chemical Society: 2021; Vol. 125, pp 3901-3912. Riikonen, J.; Mäkilä, E.; Salonen, J.; Lehto, V.-P. Determination of the Physical State of Drug Molecules in Mesoporous Silicon with Different Surface Chemistries. In *Langmuir*, American Chemical Society: 2009; Vol. 25, pp 6137-6142.
30. Shimizu, H.; Matsumoto, K. High-pressure Raman study of liquid and molecular crystals at room temperature. 3. Chloroform and chloroform-d. In *The Journal of Physical Chemistry*, American Chemical Society: 1984; Vol. 88, pp 2934-2936.

Chapter 7

Concluding thoughts and future outlook

7 Conclusions and Further Work

Confinement of pharmaceutical compounds can often influence the polymorphic form of the confined compound, or stabilise its amorphous form, often showing improvements in physicochemical properties as a result. Understanding the crystallisation behaviour of a compound prior to its confinement is of great importance and was the aim of the research presented in this thesis, working towards understanding the behaviour of the compounds confined in porous silica. The final chapter of this thesis summarises the findings of this work and offers possibilities for further work.

Chapters 3 and 4 investigated how isonicotinamide polymorphs reacted to high pressure, with the former chapter discussing the reversible pressure-induced superelastic behaviour of thermodynamically stable Form I isonicotinamide. The crystal was observed to undergo a single-crystal to single-crystal transition at 4.98 GPA, to new high pressure phase Form I', captured by SC-XRD and Raman spectroscopy. This enabled the proposal of a possible molecular mechanism by which the transition occurs, rationalised using PIXEL calculations that provided intermolecular energies over the transition to the high-pressure phase. Visual observations of multiple crystals also showed changes to the aspect ratios beyond the phase transition at 4.98 GPa which were reversible on decompression, thus highlighting the superelastic properties of Form I isonicotinamide.

Chapter 4 continued the compression of isonicotinamide, assessing how the differences in hydrogen bonding seen between the polymorphs influenced their behaviour during compression, evaluating three of the metastable forms: Forms II, III and IV. Form II demonstrated a single-crystal-to-single-crystal phase transition at 1.49 GPa. The structure of the high-pressure phase was solved with a lower symmetry and an increase in molecules in the asymmetric unit from two to four. PIXEL calculations showed the stabilisation of dispersive interactions between symmetry independent molecules associated with the transition of Form II. Form III isonicotinamide showed anisotropic compression up to a pressure of 4.27 GPa, with no indication of a phase transition up to this point. An additional hydrogen bond in the chain structure allowed for rotation of the molecules and stabilisation of the structure until the crystal deteriorated and data became unusable. The final polymorph investigated in this series was Form IV isonicotinamide. With a structure similar to that of Form II isonicotinamide, it was expected to behave in a similar manner on compression. XRD data of the single-crystals used deteriorated beyond 2.01 GPa, speculated to be attributable to a phase transition, however this is yet to be confirmed.

Chapter 3 and 4 highlighted the need to crystallise single crystals of a good quality, especially when used in a high pressure study. It was essential that crystals were of a suitable size to produce quality diffraction but small enough to fit within the small dimensions of the DAC and not bridge on compression. The concomitant nature of isonicotinamide also made isolating single-crystals of a particular polymorph challenging. Deterioration of crystals housed in the DAC, prior to the hydrostatic limit of the pressure-transmitting media, was also observed in the study of Form II and Form IV isonicotinamide thus limiting the maximum pressure achieved and the number of data collections. To avoid the issues previously mentioned, crystalline powder can be used when crystallising a suitable single-crystal is not possible. Capabilities of collecting high-pressure X-ray powder diffraction data in-house is limited therefore synchrotron radiation provides the best answer when collecting data. Future beamtime at ISIS Neutron and Muon Source will allow for an in-depth into the structural changes of Forms II, III and IV isonicotinamide, with beamtime at Diamond Lightsource providing complementary data. An aspect of great interest to myself would be to investigate other systems which possess hydrogen bonding through dimer interactions, assessing whether or not these systems also exhibit changes to crystal morphology on compression.

Chapter 5 moved away from using high-pressure and focussed on the use of crystallisation from solvent equilibration and subsequent use of temperature to investigate polymorphism. Seven new solvates of nifedipine were identified, with structures from morpholine, THF, pyridine, DMA, DMF, methanol and known solvates 1,4-dioxane and DMSO collected using X-ray diffraction at 100 K. The nifedipine-THF solvate was the only structure not to possess hydrogen bonding between the solvent and API molecules, instead THF was located in channels, facilitating desolvation. The arrangement of nifedipine molecules resembles the structure of the metastable Form C polymorph but desolvated to form thermodynamically stable Form A. Two polymorphs of the nifedipine-DMA solvate were discovered during the study, with the transition from the ambient-temperature phase to low-temperature phase apparent by VT-XRPD at 143 K. Desolvation from DMF showed diffraction evident of Form C nifedipine between 348 and 363 K. The methanol solvate showed negative linear expansion of the *b*-axis on desolvation, linked back to the winerack-type hydrogen bonding pattern of the nifedipine molecules.

The expanse of work demonstrated in this chapter expands the solid state landscape of nifedipine, however desolvation was only observed to produce thermodynamically stable Form A and did not result in any new polymorphs. Another way to investigate polymorphism, as discussed in Chapter 3 and Chapter 4, is to use high pressure. This could include loading crystals of nifedipine polymorphs into a DAC or recrystallisation from a solution under high pressure – *in situ* crystallisation. This technique has been used to explore high-pressure forms of pharmaceutical compounds including piracetam and paracetamol and proves interesting when investigating nucleation and crystallisation. A further idea to round off this study would be to use variable-temperature synchrotron XRPD, which would allow for quicker collections at 1 full pattern scan per second, capturing phases which may have been missed between data collections and aiding structure solution.

Chapter 6 investigated the crystallisation behaviour of model compound isonicotinamide when confined in porous silica, loading it via an absorption method at both ambient and high pressure. Silica particles were synthesised according to literature methods which were reported to produce monodisperse mesoporous particles, uniform in size and shape. However, Chapter 6 has shown how following the literature methods was not successful and requires additional work to produce well-defined porous particles. For this reason, mesoporous silica was purchased from various suppliers, however characterisation using nitrogen sorption provided data that was not in agreement with the information provided by the suppliers. Further characterisation is required to assess pore size, for example Transmission Electron Microscopy (TEM), capable of capturing images of pores in the mesoporous range providing an average pore diameter. Quantification of isonicotinamide loaded into the porous silica was determined using HPLC, a common technique used to determine concentration due to its sensitivity and ability to adapt methods to suit the analyte. This study used two HPLC methods to determine the concentration of isonicotinamide, however this produced negligible data and provided uncertainty in the amount of isonicotinamide loaded in the pores. Loading solvents were chosen based on the affinity of isonicotinamide for those solvents, with chloroform demonstrating the weakest binding energy of the two. To fully assess the influence of binding energy on loading isonicotinamide via the adsorption method, future studies should aim to further investigate the influence of solvent on the loading of isonicotinamide. Isonicotinamide was successfully loaded into mesoporous silica ranging in pore size. Crystalline material present prior to washing the loaded particles was successfully characterised for when loaded using ethanol into particles with pore sizes of 9 and 15 nm. XRPD identified Form III present for 9n and a mixture of Form III and Form II for 15 nm. Isonicotinamide polymorphs are known to crystallise concomitantly, so this was no surprise. Examining a wider range of pore size may lead to the crystallisation of other polymorphs, and along with a range of solvents would lead to a more comprehensive study of crystallisation behaviour when confined.

In conclusion, the work presented in this thesis has looked in depth at the crystallisation behaviour of two compounds; the effect of compression on isonicotinamide and the influence of solvents on the crystallisation and desolvation of nifedipine. Future research can use these findings to further investigate the compounds behaviour when confined in porous materials and expand their solid-state landscapes.

Appendix A

Table A1: Crystallographic data for the compression study of Form I isonicotinamide from ambient to 2.40 GPa. The Pressure points in bold are from the same crystal.

Pressure/ GPa	Ambient‡	**1.58 ‡**	1.90‡	2.40‡
a, b, c (Å)	10.229 (3), 5.7538 (16), 10.095 (3)	9.599 (2), 5.6979 (4), 9.7492 (7)	9.629 (2), 5.7123 (7), 9.773 (2)	9.528 (5), 5.6786 (15), 9.709 (6)
β (°)	97.277 (18)	103.402 (14)	103.03 (2)	104.08 (5)
V (Å^3)	589.3 (3)	518.68 (12)	523.70 (18)	509.5 (4)
μ (mm^{-1})	0.81	0.11	0.11	0.11
Crystal size (mm)	0.1 × 0.1 × 0.1	0.08 × 0.06 × 0.03	0.17 × 0.11 × 0.05	0.17 × 0.11 × 0.05
Absorption correction	Multi-scan *SADABS2016*/2 (Bruker,2016/2) was used for absorption correction. wR2(int) was 0.0997 before and 0.0633 after correction. The Ratio of minimum to maximum transmission is 0.7213. The λ/2 correction factor is Not present.	Multi-scan *SADABS2016*/2 (Bruker,2016/2) was used for absorption correction. wR2(int) was 0.0877 before and 0.0499 after correction. The Ratio of minimum to maximum transmission is 0.9021. The λ/2 correction factor is Not present.	Multi-scan *SADABS2016*/2 (Bruker,2016/2) was used for absorption correction. wR2(int) was 0.1065 before and 0.0474 after correction. The Ratio of minimum to maximum transmission is 0.8927. The l/2 correction factor is Not present.	Multi-scan *SADABS2016*/2 (Bruker,2016/2) was used for absorption correction. wR2(int) was 0.0761 before and 0.0452 after correction. The Ratio of minimum to maximum transmission is 0.8725. The λ/2 correction factor is Not present.
T_{min}, T_{max}	0.543, 0.753	0.640, 0.745	0.665, 0.745	0.650, 0.745
No. of measured, independent and observed [$I > 2\sigma(I)$] reflections	4398, 1075, 823	2303, 281, 233	2034, 285, 255	999, 259, 233
R_{int}	0.049	0.049	0.030	0.027
θ$_{max}$ (°)	68.395	23.3	23.2	23.3
(sin θ/λ)$_{max}$ (Å^{-1})	0.603	0.556	0.555	0.556
$R[F^2 > 2\sigma(F^2)]$, $wR(F^2)$, S	0.046, 0.118, 1.11	0.035, 0.085, 1.18	0.038, 0.109, 1.08	0.039, 0.107, 1.18
No. of reflections	1075	281	285	259
No. of parameters	82	106	83	82
No. of restraints	0	60	60	60
H-atom treatment	H-atom parameters constrained	All H-atom parameters refined	H-atom parameters constrained	H-atom parameters constrained
Δρ$_{max}$, Δρ$_{min}$ (e Å^{-3})	0.16, −0.22	0.10, −0.10	0.12, −0.13	0.08, -0.11

Cont. Table A1: Crystallographic data from 3.23 to 4.00 GPa.

Pressure/ GPa	3.23‡	**3.46‡**	**3.99‡**	4.00‡
***a*, *b*, *c* (Å)**	9.4148 (10), 5.6817 (4), 9.6396 (12)	9.3656 (17), 5.6791 (3), 9.6213 (6)	9.300 (3), 5.6768 (6), 9.5955 (11)	9.2976 (12), 5.6740 (4), 9.5819 (15)
β (°)	105.208 (11)	105.642 (11)	106.32 (2)	106.290 (13)
V ($Å^3$)	497.58 (9)	492.79 (10)	486.19 (19)	485.19 (11)
μ (mm^{-1})	0.12	0.12	0.12	0.12
Crystal size (mm)	0.17 × 0.11 × 0.05	0.08 × 0.06 × 0.03	0.08 × 0.06 × 0.03	0.17 × 0.11 × 0.05
Absorption correction	Multi-scan *SADABS2016*/2 (Bruker,2016/2) was used for absorption correction. wR2(int) was 0.0703 before and 0.0431 after correction. The Ratio of minimum to maximum transmission is 0.9092. The λ/2 correction factor is Not present.	Multi-scan *SADABS2016*/2 (Bruker,2016/2) was used for absorption correction. wR2(int) was 0.0860 before and 0.0474 after correction. The Ratio of minimum to maximum transmission is 0.8990. The λ/2 correction factor is Not present.	Multi-scan *SADABS2016*/2 (Bruker,2016/2) was used for absorption correction. wR2(int) was 0.0982 before and 0.0541 after correction. The Ratio of minimum to maximum transmission is 0.8104. The λ/2 correction factor is Not present.	Multi-scan *SADABS2016*/2 (Bruker,2016/2) was used for absorption correction. wR2(int) was 0.0978 before and 0.0437 after correction. The Ratio of minimum to maximum transmission is 0.8753. The λ/2 correction factor is Not present.
T_{min}, T_{max}	0.677, 0.745	0.670, 0.745	0.604, 0.745	0.652, 0.745
No. of measured, independent and observed [$I > 2\sigma(I)$] reflections	2101, 270, 249	2165, 271, 211	2132, 261, 192	2056, 265, 237
R_{int}	0.029	0.061	0.078	0.031
θ_{max} (°)	23.3	23.3	23.3	23.3
$(\sin \theta/\lambda)_{max}$ ($Å^{-1}$)	0.556	0.556	0.556	0.556
$R[F^2 > 2\sigma(F^2)]$, $wR(F^2)$, S	0.036, 0.100, 1.20	0.040, 0.110, 1.08	0.047, 0.126, 1.10	0.035, 0.093, 1.14
No. of reflections	270	271	261	265
No. of parameters	82	82	82	82
No. of restraints	60	60	60	60
H-atom treatment	H-atom parameters constrained	All H-atom parameters refined	H-atom parameters constrained	H-atom parameters constrained
$\Delta\rho_{max}$, $\Delta\rho_{min}$ (e $Å^{-3}$)	0.09, -0.12	0.12, −0.13	0.14, −0.15	0.09, −0.14

Cont. Table A1: Crystallographic data from 4.33 to 5.65 GPa.

Pressure (GPa)	**4.33‡**	**4.98‡**	5.65‡
***a*, *b*, *c* (Å)**	9.2314 (19), 5.6679 (4), 9.5601 (6)	13.149 (8), 3.4103 (10), 10.173 (2)	13.177 (9), 3.4083 (19), 10.184 (9)
β (°)	106.813 (12)	93.11 (4)	93.15 (7)
V (Å^3)	478.83 (11)	455.5 (3)	456.7 (6)
μ (mm^{-1})	0.12	0.13	0.13
Crystal size (mm)	0.08 × 0.06 × 0.03	0.06 × 0.03 × 0.02	0.16 × 0.08 × 0.05
Absorption correction	Multi-scan *SADABS2016*/2 (Bruker,2016/2) was used for absorption correction. wR2(int) was 0.0734 before and 0.0457 after correction. The Ratio of minimum to maximum transmission is 0.9046. The λ/2 correction factor is Not present.	Multi-scan *SADABS2016*/2 (Bruker,2016/2) was used for absorption correction. wR2(int) was 0.0927 before and 0.0387 after correction. The Ratio of minimum to maximum transmission is 0.8068. The λ/2 correction factor is Not present.	Multi-scan *SADABS2016*/2 (Bruker,2016/2) was used for absorption correction. wR2(int) was 0.1035 before and 0.0347 after correction. The Ratio of minimum to maximum transmission is 0.6859. The λ/2 correction factor is Not present.
$T_{\min}$, $T_{\max}$	0.674, 0.745	0.601, 0.745	0.511, 0.745
No. of measured, independent and observed [$I > 2\sigma(I)$] reflections	2103, 256, 205	945, 234, 155	591, 238, 119
R_{int}	0.054	0.054	0.061
$\theta_{\max}$ (°)	23.2	22.9	23.3
$(\sin \theta/\lambda)_{\max}$ (Å^{-1})	0.554	0.548	0.555
$R[F^2 > 2\sigma(F^2)]$, $wR(F^2)$, S	0.039, 0.098, 1.15	0.049, 0.129, 1.20	0.045, 0.136, 1.00
No. of reflections	256	234	238
No. of parameters	82	82	82
No. of restraints	60	61	62
H-atom treatment	H-atom parameters constrained	H-atom parameters constrained	H-atom parameters constrained
$\Delta\rho_{\max}$, $\Delta\rho_{\min}$ (e Å^{-3})	0.11, -0.13	0.13, -0.13	0.12, -0.14

Computer programs: SAINT V8.38A1, SHELXT[2], XL [3]

‡ Diffractometer - Bruker *APEX*-II CCD

Table A2: Interactions in the first molecular coordination sphere of Form I isonicotinamide as calculated by MrPIXEL. Each structure was geometry optimised prior to PIXEL calculations to account for any errors in the models derived from the low completeness of the high-pressure datasets.

Pressure (GPa)	Coulombic (kJ mol^{-1})	Polarisation (kJ mol^{-1})	Dispersion (kJ mol^{-1})	Repulsion (kJ mol^{-1})	Total (kJ mol^{-1})
0.0001	-94.4	-33.9	-89.1	103.7	-113.6
1.58	-127.7	-50.2	-122.5	188.7	-111.8
1.9	-122.9	-48.7	-120	179.4	-112.2
2.4	-134	-53.5	-128	206.2	-109.4
3.23	-143.6	-59.2	-136	230.1	-108.6
3.46	-146.9	-61.1	-139.3	240.8	-106.5
3.99	-152.2	-63.4	-144.1	255.6	-104.1
4	-153.8	-64.1	-144.9	258.9	-103.9
4.33	-159.2	-66.5	-149.8	276	-99.5
4.98	-153.6	-68.5	-168	304.4	-85.8
5.65	-152	-68.4	-166.5	300	-86.8

Table A3: Intermolecular interactions during the compression of Form I isonicotinamide, as calculated by MrPIXEL. Each structure was geometry optimised before the PIXEL calculations to account for any errors in the models derived from the low completeness of the high-pressure datasets. Eight significant interactions have been chosen. Energies for Form I' are highlighted in grey.

Pressure (GPa)	Centroid distance (Å)	Coloumbic (kJ mol^{-1})	Polarisation (kJ mol^{-1})	Dispersion (kJ mol^{-1})	Repulsion (kJ mol^{-1})	Total Energy (kJ mol^{-1})
Interaction 1 (Form I and Form I')						
0	7.553	-88.1	-29.2	-19.1	74	-62.4
1.58	7.44	-103.9	-37.2	-21	99.8	-62.3
1.9	7.451	-100.7	-36.4	-20.5	96.4	-61.2
2.4	7.417	-108.2	-39.3	-21.6	107	-62.1
3.23	7.403	-111.1	-40.4	-22	111.1	-62.4
3.46	7.395	-111.8	-40.8	-22.1	113.3	-61.3
3.99	7.387	-112.5	-41.1	-22.3	115.6	-60.3
4	7.385	-113.4	-41.5	-22.3	116.7	-60.6
4.33	7.372	-114	-42.2	-22.7	120.7	-58.1
4.98	7.395	-97.9	-35.4	-21.3	96.3	-58.4
5.65	7.406	-97.6	-36.7	-20.6	93.7	-61.2
Interaction 2 (Form I and Form I')						
0	5.598	-34.3	-12.1	-14	27.1	-33.2
1.58	5.481	-44.1	-18	-18.1	48.6	-31.5
1.9	5.491	-43	-17.3	-17.8	46.8	-31.3
2.4	5.465	-45.4	-18.8	-18.7	51.8	-31.2
3.23	5.444	-48.4	-20.9	-19.3	58.2	-30.5
3.46	5.437	-49	-21.4	-19.6	59.9	-30.1
3.99	5.433	-50.5	-22.2	-20	63.2	-29.6
4	5.427	-51.2	-22.6	-20.1	64.4	-29.6
4.33	5.422	-52.3	-23.1	-20.5	67.5	-28.3
4.98	5.223	-46.7	-19.9	-30	64.3	-32.3
5.65	5.228	-45.7	-19.7	-30	63.7	-31.8

Interaction 3 (Form I and Form I’)						
0	5.403	-3	-2.5	-13.8	5.6	-13.7
1.58	5.177	-7.3	-5.9	-21.4	19	-15.7
1.9	5.186	-6.7	-5.6	-21.1	17.7	-15.7
2.4	5.149	-8.4	-6.7	-22.6	22.1	-15.6
3.23	5.104	-10.2	-7.8	-24.5	27.4	-15.1
3.46	5.092	-10.6	-8	-25.1	29.2	-14.6
3.99	5.062	-11.6	-8.7	-26.3	33.1	-13.6
4	5.059	-11.7	-8.8	-26.4	33.4	-13.6
4.33	5.034	-13	-9.5	-27.6	36.9	-13.3
4.98	6.826	-7.6	-4.2	-11	13.2	-9.6
5.65	6.84	-7.8	-4.2	-10.8	12.7	-10.2
Interaction 4 (Form I and Form I’)						
0	8.073	-9.2	-3.3	-9.7	8.6	-13.6
1.58	7.71	-18.5	-7.8	-15.7	28.7	-13.3
1.9	7.739	-17.5	-7.8	-15.3	26.5	-14.1
2.4	7.658	-19.6	-8.3	-16.5	32.5	-11.8
3.23	7.603	-20.6	-9.3	-17.6	35.8	-11.7
3.46	7.576	-21.8	-10	-18	38.1	-11.6
3.99	7.538	-23	-10.3	-18.8	40.7	-11.5
4	7.533	-23.1	-10.4	-18.9	41.1	-11.3
4.33	7.494	-24.3	-10.8	-19.6	44.3	-10.4
4.98	7.839	-13.2	-5.4	-14	19.6	-13.1
5.65	7.847	-13.2	-5.4	-14.2	19.3	-13.5
Interaction 5 (Form I and Form I’)						
0	7.348	-9.6	-4.1	-11.8	12.9	-12.6
1.58	7.261	-12.1	-5.8	-13.6	20	-11.5
1.9	7.268	-11.4	-5.4	-13.5	18.7	-11.6
2.4	7.248	-12.6	-6.2	-13.9	21.6	-11.3
3.23	7.236	-13.2	-6.7	-14.4	23.4	-10.9
3.46	7.224	-13.6	-7	-14.7	24.6	-10.7
3.99	7.224	-13.7	-7.1	-14.8	25.2	-10.4
4	7.218	-13.8	-7.2	-14.9	25.6	-10.3

4.33	7.206	-14.3	-7.5	-15.2	27.1	-9.9
4.98	7.809	-13.2	-5.8	-11.1	19	-11.2
5.65	7.829	-12.7	-5.5	-10.5	17.7	-11.1
Interaction 6 (Form I and Form I’)						
0	5.754	-3.8	-2	-14.2	7.2	-12.9
1.58	5.698	-6.8	-3.3	-19.3	16.1	-13.4
1.9	5.712	-6.3	-3.1	-18.4	14.6	-13.2
2.4	5.679	-7.8	-4	-20.4	18.6	-13.6
3.23	5.682	-9.2	-5.1	-22	22.8	-13.6
3.46	5.679	-9.8	-5.5	-22.7	24.7	-13.4
3.99	5.677	-11	-5.9	-23.7	27.5	-13.2
4	5.674	-11.2	-6	-23.9	28	-13.1
4.33	5.668	-12.3	-6.4	-24.8	31	-12.5
4.98	3.41	-13.6	-10.3	-52.2	83.1	6.9
5.65	3.408	-13.6	-10.4	-52.1	83.4	7.3
Interaction 7 (Form I)						
0	5.179	0	-1.5	-17.8	9.1	-10.2
1.58	4.802	-4	-2.8	-25	21.1	-10.7
1.9	4.821	-3.9	-2.9	-24.8	20.2	-11.3
2.4	4.76	-5	-3.2	-26	23.2	-11
3.23	4.689	-6.6	-3.8	-28.1	27.2	-11.3
3.46	4.654	-7.2	-4.1	-29.1	29.5	-10.9
3.99	4.616	-7.8	-4.4	-30.1	31.8	-10.4
4	4.615	-7.9	-4.4	-30.1	31.9	-10.5
4.33	4.573	-9.2	-4.8	-31.2	34.7	-10.5
Interaction 8 (Form I’)						
4.98	3.41	-13.6	-10.3	-52.2	83.1	6.9
5.65	3.408	-13.6	-10.4	-52.1	83.4	7.3

Appendix B

Table B1: Crystallographic data for the compression study of Form II isonicotinamide from ambient to 0.78 GPa. The Pressure points in bold are from the same crystal.

Pressure (GPa)	Ambient	**0.39**	**0.50**	0.78
***a*, *b*, *c* (Å)**	16.0124 (6), 8.0021 (3), 9.9382 (3)	15.631 (2), 7.9763 (4), 9.9020 (5)	15.247 (2), 7.9462 (4), 9.8601 (5)	15.072 (7), 7.9277 (18), 9.823 (3)
β (°)	105.308 (2)	105.609 (9)	105.951 (8)	106.22 (2)
V (Å^3)	1228.23 (8)	1189.01 (19)	1148.63 (18)	1127.0 (7)
Z	8	8	8	8
μ (mm^{-1})	0.78	0.10	0.10	0.10
Crystal size (mm)	0.16 × 0.1 × 0.03	0.22 × 0.19 × 0.01	0.22 × 0.19 × 0.01	0.15 × 0.10 × 0.06
Absorption correction	Multi-scan SADABS2016/2 (Bruker,2016/2) was used for absorption correction. wR2(int) was 0.1076 before and 0.0659 after correction. The Ratio of minimum to maximum transmission is 0.8694. The λ/2 correction factor is Not present..	Multi-scan SADABS2016/2 (Bruker,2016/2) was used for absorption correction. wR2(int) was 0.0728 before and 0.0453 after correction. The Ratio of minimum to maximum transmission is 0.8867. The λ/2 correction factor is Not present.	Multi-scan SADABS2016/2 (Bruker,2016/2) was used for absorption correction. wR2(int) was 0.0680 before and 0.0429 after correction. The Ratio of minimum to maximum transmission is 0.8973. The λ/2 correction factor is Not present.	-
T_{min}, T_{max}	0.655, 0.754	0.661, 0.745	0.668, 0.745	-
No. of measured, independent and observed [$I > 2\sigma(I)$] reflections	17001, 2415, 1615	5323, 599, 460	5069, 579, 451	5670, 582, 406
R_{int}	0.072	0.041	0.044	0.101
θ_{max} (°)	72.4	23.3	23.3	23.4
$(\sin \theta/\lambda)_{\text{max}}$ (Å^{-1})	0.618	0.555	0.556	0.558
$R[F^2 > 2\sigma(F^2)]$, $wR(F^2)$, S	0.071, 0.201, 1.04	0.040, 0.096, 1.08	0.044, 0.128, 1.09	0.067, 0.198, 0.82
No. of reflections	2415	599	579	582
No. of parameters	163	163	163	163
No. of restraints	0	228	228	228
H-atom treatment	H-atom parameters constrained	H-atom parameters constrained	H-atom parameters constrained	H-atom parameters constrained
$\Delta\rho_{\text{max}}$, $\Delta\rho_{\text{min}}$ (e Å^{-3})	0.36, -0.24	0.11, -0.08	0.11, -0.09	0.15, -0.16

Cont. Table B1. Crystallographic data from 0.94 to 1.61 GPa.

Pressure (GPa)	**0.94**	1.09	1.49	**1.61**
***a*, *b*, c (Å)**	14.852 (4), 7.9089 (8), 9.8110 (9)	14.90 (1), 7.908 (3), 9.816 (4)	14.706 (7), 7.915 (2), 9.947 (2)	14.455 (3), 7.8900 (16), 9.944 (2)
α, β, γ (°)	106.372 (16)	90, 106.21 (4), 90	91.071 (11), 109.04 (2), 98.53 (3)	91.28 (3), 109.44 (3), 98.33 (3)
V (Å^3)	1105.7 (3)	1110.6 (9)	1079.5 (6)	1055.1 (4)
Z	8	8	8	8
μ (mm^{-1})	0.11	0.10	0.11	0.11
Crystal size (mm)	0.22 × 0.19 × 0.01	0.15 × 0.10 × 0.06	0.15 × 0.10 × 0.06	0.22 × 0.19 × 0.01
Absorption correction	Multi-scan SADABS2016/2 (Bruker,2016/2) was used for absorption correction. wR2(int) was 0.0910 before and 0.0503 after correction. The Ratio of minimum to maximum transmission is 0.7884. The λ/2 correction factor is Not present.	-	-	Multi-scan SADABS2016/2 (Bruker,2016/2) was used for absorption correction. wR2(int) was 0.0764 before and 0.0589 after correction. The Ratio of minimum to maximum transmission is 0.7751. The λ/2 correction factor is Not present.
T_{min}, T_{max}	0.587, 0.745	-	-	0.577, 0.745
No. of measured, independent and observed [$I > 2\sigma(I)$] reflections	3843, 567, 418	5534, 554, 369	4822, 1091, 592	4777, 911, 646
R_{int}	0.051	0.127	0.125	0.070
θ_{max} (°)	23.3	23.2	23.3	23.3
$(\sin \theta/\lambda)_{max}$ (Å^{-1})	0.557	0.555	0.557	0.556
$R[F^2 > 2\sigma(F^2)]$, $wR(F^2)$, S	0.047, 0.139, 1.11	0.073, 0.184, 1.16	0.098, 0.274, 1.22	0.099, 0.266, 1.23
No. of reflections	567	554	1091	911
No. of parameters	163	163	326	325
No. of restraints	228	149	537	536
H-atom treatment	H-atom parameters constrained	H-atom parameters constrained	H-atom parameters constrained	H-atom parameters constrained
$\Delta\rho_{max}$, $\Delta\rho_{min}$ (e Å^{-3})	0.11, -0.11	0.19, -0.17	0.21, -0.19	0.38, -0.29

Computer programs: *SAINT* V8.38A[1], *SHELXT*[2], XL [3]

Table B2: Interactions in the first molecular coordination sphere of Form II isonicotinamide from ambient pressure to 1.09 GPa, as calculated by MrPIXEL. Interactions for 1.49 and 1.61 GPa cannot be calculated due to there being four molecules in the asymmetric unit.

Pressure (GPa)	Coulombic (kJ mol^{-1})	Polarisation (kJ mol^{-1})	Dispersion (kJ mol^{-1})	Repulsion (kJ mol^{-1})	Total (kJ mol^{-1})
0	-88.2	-38.1	-79.5	91.7	-114.1
0.39	-92.0	-40.2	-86.4	103.6	-115.0
0.50	-96.9	-42.9	-94.4	119.7	-114.6
0.78	-99.7	-44.9	-98.9	129.4	-114.1
0.94	-107.3	-48.7	-104.7	144.7	-116.0
1.09	-101.9	-46.2	-102.9	137.7	-113.3
1.49					
1.61					

Table B3: Intermolecular interactions during the compression of Form II isonicotinamide, before the transition, as calculated by MrPIXEL. Twelve significant interactions have been chosen.

Pressure (GPa)	Centroid distance (Å)	Coloumbic (kJ mol^{-1})	Polarisation (kJ mol^{-1})	Dispersion (kJ mol^{-1})	Repulsion (kJ mol^{-1})	Total Energy (kJ mol^{-1})
Interaction 1 Molecule B – Molecule B x, -1+y, z & x, 1+y, z						
0	8.002	-42	-19.2	-12.9	40.6	-33.5
0.39	7.976	-43.6	-20.5	-13.5	44.3	-33.4
0.50	7.946	-46.2	-22.2	-14.1	50.1	-32.3
0.78	7.928	-44.7	-21.4	-13.9	47.9	-32.2
0.94	7.909	-47.8	-23.2	-14.6	53.8	-31.7
1.09	7.908	-46	-22.1	-14.3	50.8	-31.5
Interaction 2 Molecule A – Molecule A x, -1+y, z & x, 1+y, z						
0	8.002	-41.2	-18.7	-12.9	39.7	-33.1
0.39	7.976	-42.4	-19.6	-13.3	42.4	-32.9
0.50	7.946	-44.1	-20.6	-13.8	45.7	-32.8
0.78	7.928	-46.5	-22.3	-14.4	52.4	-30.8
0.94	7.909	-46.6	-22.7	-14.6	53.9	-30
1.09	7.908	-46.5	-22.4	-14.5	53.3	-30.1
Interaction 3 Molecule A – Molecule A x, 0.5-y, -0.5+z & x, 0.5-y, 0.5+z						
0	6.175	-32.7	-12.4	-14.6	28.2	-31.5
0.39	6.139	-34	-13.1	-15.5	30.9	-31.7
0.50	6.094	-33.3	-13	-16.3	31.6	-30.9
0.78	6.07	-33.3	-13.2	-17.2	33.3	-30.4
0.94	6.044	-37.2	-15	-17.9	37.2	-32.9
1.09	6.051	-33	-13.4	-17.5	34.3	-29.5
Interaction 4 Molecule B – Molecule B x, -0.5-y, 0.5+z & x, -0.5-y, -0.5+z						
0	6.18	-31.2	-11.6	-14.1	26.6	-30.4

0.39	6.151	-30.8	-11.7	-14.8	27	-30.3
0.50	6.116	-30.8	-11.8	-15.2	28.2	-29.6
0.78	6.092	-32.6	-12.6	-15.7	30	-31
0.94	6.077	-32.9	-12.7	-16.4	30.9	-31
1.09	6.079	-31.3	-12.2	-15.6	28.9	-30.2
Interaction 5 Molecule A – Molecule A 1-x, 1-y, -z						
0	3.899	0.5	-1.5	-21.4	9.4	-12.9
0.39	3.812	-0.2	-1.9	-23.7	12.3	-13.6
0.50	3.728	-0.8	-2.2	-25.8	15	-13.9
0.78	3.675	-1.6	-2.7	-28	18.6	-13.7
0.94	3.579	-3.3	-3.7	-32.3	27.4	-11.9
1.09	3.642	-1.9	-2.5	-28.4	19.5	-13.2
Interaction 6 Molecule B – Molecule B -x, -y, -z						
0	3.897	0.8	-1.4	-21.3	9.3	-12.5
0.39	3.817	0.3	-1.5	-23.4	11.8	-12.8
0.50	3.731	-0.6	-2	-25.9	15.4	-13.2
0.78	3.679	-1.1	-2.6	-28.2	18.6	-13.4
0.94	3.63	-1.6	-3.1	-29.7	20.9	-13.5
1.09	3.616	-2.1	-3.5	-30.6	23.4	-12.7
Interaction 7 Molecule A – Molecule A 1-x, -0.5+y, 0.5-z & 1-x, 0.5+y, 0.5-z						
0	6.758	-5.4	-2.6	-8.8	5.1	-11.7
0.39	6.711	-5.8	-2.9	-9.3	6	-12
0.50	6.665	-6.5	-3.3	-10.1	7.5	-12.4
0.78	6.619	-6.4	-3.4	-10.5	8.2	-12
0.94	6.585	-8.2	-4.6	-11.7	10.8	-13.6
1.09	6.618	-6.5	-3.4	-10.5	8.4	-12
Interaction 8 Molecule B – Molecule B -x,0.5+y,0.5-z & -x,-0.5+y,0.5-z						
0	6.767	-5.6	-2.7	-8.7	5.3	-11.7
0.39	6.731	-6	-3	-9.3	6.3	-12

0.50	6.689	-6.4	-3.4	-10.2	7.7	-12.3
0.78	6.657	-7.1	-3.9	-10.7	8.9	-12.7
0.94	6.635	-7.5	-4.3	-11.4	10.2	-12.9
1.09	6.622	-8	-4.6	-11.8	11.5	-13
Interaction 9 Molecule A – Molecule B x,0.5-y,-0.5+z & x,0.5-y,0.5+z						
0	4.907	-1.2	-2.7	-16	8.6	-11.3
0.39	4.813	-2	-3.4	-18.2	11.7	-11.9
0.50	4.717	-3.5	-4.5	-21	17.1	-11.9
0.78	4.673	-3.5	-4.6	-21.9	18.1	-12
0.94	4.638	-4	-5.2	-22.9	20.3	-11.8
1.09	4.65	-4.5	-5.2	-23.1	20.6	-12.2
Interaction 10 Molecule A – Molecule B - x,1+y,z & x,-1+y,z						
0	6.021	-1.3	-1.6	-8.3	2.1	-9.2
0.39	5.936	-2.1	-2.1	-9.9	3.4	-10.7
0.50	5.853	-2.9	-2.5	-11.5	5	-11.9
0.78	5.82	-3.1	-2.5	-11.7	5	-12.3
0.94	5.794	-3.6	-3	-12.7	6.7	-12.6
1.09	5.789	-3.8	-3	-12.9	6.6	-13
Interaction 11 Molecule A- Molecule B x, y, z						
0	6.016	4.7	-2.2	-12.6	7.5	-2.6
0.39	5.923	4.6	-2.5	-13.8	9.3	-2.4
0.50	5.828	4	-3.2	-15.9	13	-2
0.78	5.796	3	-3.9	-17.4	16.6	-1.7
0.94	5.755	3.1	-4.3	-17.8	17.8	-1.2
1.09	5.757	3.2	-3.9	-17.7	16.9	-1.6

Table B4: Intermolecular interactions during the compression of Form II isonicotinamide, after the phase transition, as calculated by MrPIXEL. Highlighted interaction shows a greater centroid distance hence why interactions are lower in energy.

Molecule Operator : x, y, z							
Pressure (GPa)	Interaction between:	Centroid distance (Å)	Coloumbic (kJ mol^{-1})	Polarisation (kJ mol^{-1})	Dispersion (kJ mol^{-1})	Repulsion (kJ mol^{-1})	Total Energy (kJ mol^{-1})
1.49	Mol. 1 – Mol. 3	4.456	-4.5	-4.6	-26.3	18.2	-17.2
	Mol. 1 – Mol. 4	4.899	0.6	-2.5	-17	9.8	-9
	Mol. 2 – Mol. 3	9.582	-2.4	-0.1	-0.2	0	-2.7
	Mol. 2 – Mol. 4	4.547	0.7	-4.2	-24	17.5	-10.1
1.61	Mol. 1 – Mol. 3	4.39	-6.2	-5	-28.5	21.7	-18
	Mol. 1 – Mol. 4	4.874	1.9	-3.4	-18.6	12.2	-7.8
	Mol. 2 – Mol. 3	9.528	-2.6	-0.1	-0.2	0	-3
	Mol. 2 – Mol. 4	4.462	-1.7	-6.2	-28.7	27.8	-8.8

Table B5: Crystallographic data for the compression study of Form III isonicotinamide from ambient to 2.64 GPa.

Pressure (GPa)	**Ambient**	**1.40**	**2.28**	**2.64**
a, b, c (Å)	10.1655 (14), 7.4539 (12), 15.9218 (19)	10.0750 (8), 6.793 (2), 15.6034 (12)	10.0246 (7), 6.6326 (16), 15.4928 (11)	10.0087 (8), 6.5806 (19), 15.4565 (13)
V (Å^3)	1206.4 (3)	1067.8 (4)	1030.1 (3)	1018.0 (3)
Z	8	8	8	8
μ (mm^{-1})	0.10	0.11	0.11	0.11
Crystal size (mm)	0.55 × 0.10 × 0.02	0.12 × 0.10 × 0.10	0.12 × 0.10 × 0.10	0.12 × 0.10 × 0.10
Absorption correction	Multi-scan SADABS2016/2 (Bruker,2016/2) was used for absorption correction. wR2(int) was 0.1218 before and 0.0532 after correction. The Ratio of minimum to maximum transmission is 0.7172. The λ/2 correction factor is Not present.	Multi-scan SADABS2016/2 (Bruker,2016/2) was used for absorption correction. wR2(int) was 0.0724 before and 0.0507 after correction. The Ratio of minimum to maximum transmission is 0.8788. The λ/2 correction factor is Not present.	Multi-scan SADABS2016/2 (Bruker,2016/2) was used for absorption correction. wR2(int) was 0.0749 before and 0.0538 after correction. The Ratio of minimum to maximum transmission is 0.8580. The λ/2 correction factor is Not present.	Multi-scan SADABS2016/2 (Bruker,2016/2) was used for absorption correction. wR2(int) was 0.0888 before and 0.0602 after correction. The Ratio of minimum to maximum transmission is 0.8181. The λ/2 correction factor is Not present.
$T_{\min}$, $T_{\max}$	0.535, 0.746	0.655, 0.745	0.639, 0.745	0.609, 0.745
No. of measured, independent and observed [$I > 2\sigma(I)$] reflections	12025, 1841, 1146	3820, 338, 293	3656, 326, 283	3653, 325, 274
R_{int}	0.049	0.041	0.051	0.055
$\theta_{\max}$ (°)	30.6	23.2	23.3	23.3
$(\sin \theta/\lambda)_{\max}$ (Å^{-1})	0.716	0.555	0.556	0.556
$R[F^2 > 2\sigma(F^2)]$, $wR(F^2)$, S	0.046, 0.136, 1.06	0.058, 0.161, 1.09	0.056, 0.169, 1.16	0.062, 0.171, 1.09
No. of reflections	1841	338	326	325
No. of parameters	106	82	82	82
No. of restraints	0	134	134	134
H-atom treatment	All H-atom parameters refined	H-atom parameters constrained	H-atom parameters constrained	H-atom parameters constrained
$\Delta\rho_{\max}$, $\Delta\rho_{\min}$ (e Å^{-3})	0.23, -0.23	0.17, -0.19	0.16, -0.16	0.20, -0.20

Cont. Table B5. Crystallographic data for the compression study of Form III isonicotinamide from 3.01 to 4.27 GPa.

Pressure (GPa)	**3.01**	**4.08**	**4.20**	**4.27**
***a*, *b*, *c* (Å)**	9.9897 (7), 6.5221 (17), 15.4134 (11)	9.9479 (9), 6.383 (2), 15.3052 (13)	9.9384 (13), 6.382 (3), 15.288 (3)	9.9380 (11), 6.369 (3), 15.2920 (17)
V (Å^3)	1004.2 (3)	971.9 (3)	969.7 (5)	968.0 (5)
Z	8	8	8	8
μ (mm^{-1})	0.11	0.11	0.12	0.12
Crystal size (mm)	0.12 × 0.10 × 0.10	0.12 × 0.10 × 0.10	0.12 × 0.10 × 0.10	0.12 × 0.10 × 0.10
Absorption correction	Multi-scan SADABS2016/2 (Bruker,2016/2) was used for absorption correction. wR2(int) was 0.0777 before and 0.0537 after correction. The Ratio of minimum to maximum transmission is 0.8249. The λ/2 correction factor is Not present.	Multi-scan SADABS2016/2 (Bruker,2016/2) was used for absorption correction. wR2(int) was 0.1191 before and 0.0675 after correction. The Ratio of minimum to maximum transmission is 0.8243. The λ/2 correction factor is Not present.	Multi-scan SADABS2016/2 (Bruker,2016/2) was used for absorption correction. wR2(int) was 0.1323 before and 0.0695 after correction. The Ratio of minimum to maximum transmission is 0.7938. The λ/2 correction factor is Not present.	Multi-scan SADABS2016/2 (Bruker,2016/2) was used for absorption correction. wR2(int) was 0.0893 before and 0.0614 after correction. The Ratio of minimum to maximum transmission is 0.7751. The λ/2 correction factor is Not present.
T_{min}, T_{max}	0.615, 0.745	0.614, 0.745	0.591, 0.745	0.577, 0.745
No. of measured, independent and observed [$I > 2\sigma(I)$] reflections	3568, 321, 277	3434, 296, 253	3262, 281, 205	3149, 247, 200
R_{int}	0.046	0.061	0.103	0.069
θ_{max} (°)	23.2	23.3	23.4	23.2
$(\sin \theta/\lambda)_{max}$ (Å^{-1})	0.555	0.556	0.559	0.554
$R[F^2 > 2\sigma(F^2)]$, $wR(F^2)$, S	0.065, 0.180, 1.11	0.065, 0.180, 1.14	0.048, 0.112, 1.07	0.070, 0.190, 1.04
No. of reflections	321	296	281	247
No. of parameters	82	82	82	82
No. of restraints	134	134	134	134
H-atom treatment	H-atom parameters constrained	H-atom parameters constrained	H-atom parameters constrained	H-atom parameters constrained
$\Delta\rho_{max}$, $\Delta\rho_{min}$ (e Å^{-3})	0.21, -0.20	0.22, -0.20	0.13, -0.12	0.19, -0.20

Computer programs: *SAINT* V8.38A[1], *SHELXT*[2], XL [3]

Table B6: Crystallographic data for the compression study of Form IV isonicotinamide from ambient to 0.91 GPa.

Pressure (GPa)	**Ambient**	**0.35**	**0.77**	**0.91**
a, b, c (Å)	11.4132 (6), 8.0036 (4), 10.0234 (5)	10.982 (2), 7.9672 (11), 9.995 (3)	10.712 (9), 7.9259 (19), 9.962 (3)	10.5795 (8), 7.9211 (6), 9.943 (2)
β (°)	94.167 (3)	94.21 (2)	94.11 (4)	94.323 (11)
V (Å^3)	913.18 (8)	872.2 (4)	843.6 (8)	830.87 (19)
Z	6	6	6	6
μ (mm^{-1})	0.78	0.10	0.10	0.10
Crystal size (mm)	0.2 × 0.17 × 0.03	0.19 × 0.17 × 0.01	0.19 × 0.17 × 0.01	0.09 × 0.07 × 0.01
Absorption correction	Multi-scan *SADABS2016*/2 (Bruker,2016/2) was used for absorption correction. wR2(int) was 0.0988 before and 0.0629 after correction. The Ratio of minimum to maximum transmission is 0.7472. The λ/2 correction factor is Not present.	Multi-scan SADABS2016/2 (Bruker,2016/2) was used for absorption correction. wR2(int) was 0.0815 before and 0.0500 after correction. The Ratio of minimum to maximum transmission is 0.8722. The λ/2 correction factor is Not present.	Multi-scan SADABS2016/2 (Bruker,2016/2) was used for absorption correction. wR2(int) was 0.1362 before and 0.0726 after correction. The Ratio of minimum to maximum transmission is 0.7194. The λ/2 correction factor is Not present.	Multi-scan SADABS2016/2 (Bruker,2016/2) was used for absorption correction. wR2(int) was 0.1243 before and 0.0558 after correction. The Ratio of minimum to maximum transmission is 0.8683. The λ/2 correction factor is Not present.
$T_{\min}$, $T_{\max}$	0.563, 0.754	0.650, 0.745	0.536, 0.745	0.647, 0.745
No. of measured, independent and observed [$I > 2\sigma(I)$] reflections	8226, 3085, 2552	3956, 986, 665	2958, 828, 555	3795, 827, 593
R_{int}	0.052	0.078	0.086	0.083
$\theta_{\max}$ (°)	72.1	23.4	23.4	23.3
$(\sin \theta/\lambda)_{\max}$ (Å^{-1})	0.617	0.559	0.558	0.556
$R[F^2 > 2\sigma(F^2)]$, $wR(F^2)$, S	0.046, 0.122, 1.07	0.038, 0.082, 1.06	0.059, 0.167, 1.03	0.039, 0.081, 1.10
No. of reflections	3085	986	828	827
No. of parameters	244	244	244	244
No. of restraints	2	182	404	408
H-atom treatment	H-atom parameters constrained	H-atom parameters constrained	H-atom parameters constrained	H-atom parameters constrained
$\Delta\rho_{\max}$, $\Delta\rho_{\min}$ (e Å^{-3})	0.30, -0.23	0.09, -0.10	0.15, -0.15	0.12, -0.12
Absolute structure	Flack x determined using 899 quotients [(I+)-(I-)]/[(I+)+(I-)]	Flack x determined using 228 quotients [(I+)-(I-)]/[(I+)+(I-)]	Flack x determined using 178 quotients [(I+)-(I-)]/[(I+)+(I-)]	Flack x determined using 232 quotients [(I+)-(I-)]/[(I+)+(I-)]
Absolute structure parameter	0.5 (3)	0.9 (10)	1.8 (10)	-1.0 (10)

Cont. Table B6. Crystallographic data for the compression study of Form IV isonicotinamide from 1.24 to 2.01 GPa.

Pressure (GPa)	**1.24**	**1.40**	**1.62**	**2.01**
***a*, *b*, *c* (Å)**	10.424 (6), 7.9114 (9), 9.9307 (14)	10.329 (7), 7.8901 (10), 9.9083 (15)	10.159 (8), 7.8784 (12), 9.8848 (19)	10.174 (8), 7.8572 (11), 9.8784 (17)
β (°)	94.22 (3)	94.14 (3)	94.32 (4)	94.23 (3)
V ($Å^3$)	816.7 (5)	805.4 (6)	788.9 (7)	787.5 (6)
Z	6	6	6	6
μ (mm^{-1})	0.11	0.11	0.11	0.11
Crystal size (mm)	0.19 × 0.17 × 0.01	0.19 × 0.17 × 0.01	0.19 × 0.17 × 0.01	0.19 × 0.17 × 0.01
Absorption correction	Multi-scan SADABS2016/2 (Bruker,2016/2) was used for absorption correction. wR2(int) was 0.1081 before and 0.0779 after correction. The Ratio of minimum to maximum transmission is 0.7622. The λ/2 correction factor is Not present.	Multi-scan SADABS2016/ 2 (Bruker,2016/ 2) was used for absorption correction. wR2(int) was 0.0798 before and 0.0586 after correction. The Ratio of minimum to maximum transmission is 0.7880. The λ/2 correction factor is Not present.	Multi-scan SADABS2016/2 (Bruker,2016/2) was used for absorption correction. wR2(int) was 0.1014 before and 0.0674 after correction. The Ratio of minimum to maximum transmission is 0.7347. The λ/2 correction factor is Not present.	Multi-scan *SADABS2016*/2 (Bruker,2016/2) was used for absorption correction. wR2(int) was 0.1096 before and 0.0829 after correction. The Ratio of minimum to maximum transmission is 0.7236. The λ/2 correction factor is Not present.
$T_{\min}$, $T_{\max}$	0.568, 0.745	0.587, 0.745	0.547, 0.745	0.539, 0.745
No. of measured, independent and observed [$I > 2\sigma(I)$] reflections	2406, 715, 574	2117, 677, 545	1907, 690, 538	2064, 672, 526
R_{int}	0.079	0.071	0.062	0.081
$\theta_{\max}$ (°)	23.3	23.3	23.3	23.3
$(\sin\theta/\lambda)_{\max}$ ($Å^{-1}$)	0.556	0.556	0.556	0.556
$R[F^2 > 2\sigma(F^2)]$, $wR(F^2)$, S	0.073, 0.188, 1.09	0.062, 0.165, 1.06	0.057, 0.151, 1.07	0.072, 0.190, 1.05
No. of reflections	715	677	690	672
No. of parameters	244	244	244	244
No. of restraints	404	404	404	404
H-atom treatment	H-atom parameters constrained	H-atom parameters constrained	H-atom parameters constrained	H-atom parameters constrained
$\Delta\rho_{\max}$, $\Delta\rho_{\min}$ (e $Å^{-3}$)	0.20, -0.21	0.13, -0.17	0.14, -0.21	0.17, -0.24
Absolute structure	Flack x determined using 232 quotients [(I+)-(I-)]/[(I+)+(I-)]	Flack x determined using 213 quotients [(I+)-(I-)]/[(I+)+(I-)]	Flack x determined using 207 quotients [(I+)-(I-)]/[(I+)+(I-)]	Flack x determined using 208 quotients [(I+)-(I-)]/[(I+)+(I-)]
Absolute structure parameter	2.0 (10)	-2.4 (10)	0.1 (10)	0.5 (10)

Computer programs: *SAINT* V8.38A[1], *SHELXT*[2], XL[3]. Absolute structure Flack determination.[4]

Appendix C

Table C1: Crystallographic data of nifedipine solvates.

	N_{14DIO}	N_{MORPH}	N_{THF}
Formula	$C_{17}H_{18}N_2O_6{\cdot}C_2H_4O$	$2(C_{17}H_{18}N_2O_6){\cdot}C_4H_9NO$	$2(C_{17}H_{18}N_2O_6){\cdot}C_4H_8O$
M_r	390.38	779.79	764.77
Crystal system,	Triclinic, *P* 1	Triclinic, *P* 1	Monoclinic, $P2_1/c$
Temp. (K)	100	100	100
a, b, c (Å)	7.5604 (1), 11.1362 (1), 11.8563 (1)	7.5423 (6), 11.1513 (9), 11.8923 (9)	13.9233 (14), 9.1421 (9), 14.5374 (15)
α, β, γ (°)	73.606 (1), 73.185 (1), 75.643 (1)	73.997 (2), 73.957 (2), 75.253 (2)	96.280 (4)
V (Å^3)	901.54 (2)	906.63 (12)	1839.3 (3)
Z	2	1	2
Radiation type	Cu *K*a	Mo *K*a	Mo *K*a
μ (mm^{-1})	0.93	0.11	0.11
Crystal size (mm)	0.4 × 0.35 × 0.25	0.28 × 0.26 × 0.09	0.32 × 0.13 × 0.07
Diffractometer	XtaLAB Synergy, HyPix3000	Bruker *APEX*-II CCD	Bruker *APEX*-II CCD
Absorption correction	Multi-scan *CrysAlis PRO* 1.171.41.99a (Rigaku Oxford Diffraction, 2021) Empirical absorption correction using spherical harmonics, implemented in SCALE3 ABSPACK scaling algorithm.	Multi-scan *SADABS2016*/2 (Bruker,2016/2) was used for absorption correction. wR2(int) was 0.0990 before and 0.0322 after correction. The Ratio of minimum to maximum transmission is 0.9760. The l/2 correction factor is Not present.	Multi-scan *SADABS2016*/2 (Bruker,2016/2) was used for absorption correction. wR2(int) was 0.1461 before and 0.0550 after correction. The Ratio of minimum to maximum transmission is 0.8622. The l/2 correction factor is Not present.
T_{min}, T_{max}	0.114, 1.000	0.728, 0.746	0.643, 0.746
No. of measured, independent and observed [$I > 2\sigma(I)$] reflections	21224, 3552, 3543	28798, 4676, 4393	73490, 5614, 4987
R_{int}	0.027	0.020	0.036
(sin θ/λ)$_{max}$ (Å^{-1})	0.619	0.685	0.715
$R[F^2 > 2\sigma(F^2)]$, $wR(F^2)$, S	0.036, 0.095, 1.07	0.035, 0.095, 0.97	0.037, 0.102, 1.03
No. of reflections	3552	4676	5614
No. of parameters	257	270	275
No. of restraints	0	6	5
H-atom treatment	H-atom parameters constrained	H atoms treated by a mixture of independent and constrained refinement	H-atom parameters constrained
$\Delta\rho_{max}$, $\Delta\rho_{min}$ (e Å^{-3})	0.29, -0.31	0.43, -0.26	0.45, -0.32
Absolute structure	N/A	N/A	N/A
Absolute structure parameter	N/A	N/A	N/A

Cont. Table C1: Crystallographic data of nifedipine solvates.

	NPYRI	**NDMSO**	**NDMA**
Formula	$C_{17}H_{18}N_2O_6{\cdot}C_5H_5N$	C2H6OS·C17H18N2O6	C17H18N2O6·C4H9NO
M_r	425.43	424.46	433.45
Crystal system,	Monoclinic, $P2_1$	Triclinic, *P* 1	Triclinic, *P* 1
Temp. (K)	100	100	173
a, b, c (Å)	9.4363 (10), 14.4247 (14), 15.1387 (15)	7.9036 (10), 11.8798 (15), 11.9713 (15)	7.6638 (10), 11.6006 (16), 13.9001 (19)
α, β, γ (°)	96.160 (3)	67.099 (3), 78.341 (3), 79.126 (4)	65.688 (3), 76.979 (3), 92.932 (3)
V (Å^3)	2048.7 (4)	1006.5 (2)	1082.7 (3)
Z	4	2	2
Radiation type	Mo *Ka*	Mo Ka	Mo Ka
μ (mm^{-1})	0.10	0.21	0.10
Crystal size (mm)	0.32 × 0.24 × 0.09	0.16 × 0.05 × 0.01	0.4 × 0.25 × 0.11
Diffractometer	Bruker *APEX*-II CCD	Bruker APEX-II CCD	Bruker APEX-II CCD
Absorption correction	Multi-scan *SADABS2016*/2 (Bruker,2016/2) was used for absorption correction. wR2(int) was 0.0794 before and 0.0352 after correction. The Ratio of minimum to maximum transmission is 0.9609. The l/2 correction factor is Not present.	Multi-scan SADABS2016/2 (Bruker,2016/2) was used for absorption correction. wR2(int) was 0.1110 before and 0.0630 after correction. The Ratio of minimum to maximum transmission is 0.7017. The l/2 correction factor is Not present.	Multi-scan SADABS2016/2 (Bruker,2016/2) was used for absorption correction. wR2(int) was 0.1470 before and 0.0676 after correction. The Ratio of minimum to maximum transmission is 0.8046. The l/2 correction factor is Not present.
T_{min}, T_{max}	0.717, 0.746	0.524, 0.746	0.600, 0.746
No. of measured, independent and observed [$I > 2\sigma(I)$] reflections	54023, 11054, 10804	13422, 5156, 3963	36418, 6605, 5213
R_{int}	0.020	0.054	0.043
$(\sin\theta/\lambda)_{max}$ (Å^{-1})	0.706	0.705	0.715
$R[F^2 > 2\sigma(F^2)]$, $wR(F^2)$, S	0.029, 0.079, 1.04	0.045, 0.110, 1.02	0.045, 0.130, 1.04
No. of reflections	11054	5156	6605
No. of parameters	567	269	309
No. of restraints	1	0	13
H-atom treatment	H-atom parameters constrained	H-atom parameters constrained	H-atom parameters constrained
$\Delta\rho_{max}$, $\Delta\rho_{min}$ (e Å^{-3})	0.30, -0.17	0.38, −0.56	0.31, −0.23
Absolute structure	Flack x determined using 4948 quotients [(I+)-(I-)]/[(I+)+(I-)] (Parsons, Flack and Wagner, Acta Cryst. B69 (2013) 249-259).	N/A	N/A
Absolute structure parameter	0.20 (9)	N/A	N/A

Cont. Table C1: Crystallographic data of nifedipine solvates.

	N_{DMF}	**N_{MeOH}**
Formula	$C_{17}H_{18}N_2O_6\cdot C_3H_7NO$	$C_{17}H_{18}N_2O_6\cdot CH_4O$
M_r	419.43	378.37
Crystal system,	Triclinic, P 1	Monoclinic, P21/c
Temp. (K)	100	100
a, b, c (Å)	7.4526 (13), 11.647 (2), 13.559 (2)	15.6780 (15), 14.4816 (14), 8.0842 (8)
α, β, γ (°)	70.741 (5), 97.785 (5), 73.470 (5)	104.112 (4)
V (Å^3)	1030.4 (3)	1780.1 (3)
Z	2	4
Radiation type	Mo Ka	Mo Ka
μ (mm^{-1})	0.10	0.11
Crystal size (mm)	0.34 × 0.15 × 0.08	0.40 × 0.23 × 0.08
Diffractometer	Bruker APEX-II CCD	Bruker APEX-II CCD
Absorption correction	Multi-scan SADABS2016/2 (Bruker,2016/2) was used for absorption correction. wR2(int) was 0.1093 before and 0.0513 after correction. The Ratio of minimum to maximum transmission is 0.9140. The l/2 correction factor is Not present.	Multi-scan SADABS2016/2 (Bruker,2016/2) was used for absorption correction. wR2(int) was 0.1274 before and 0.0492 after correction. The Ratio of minimum to maximum transmission is 0.9302. The l/2 correction factor is Not present.
T_{min}, T_{max}	0.682, 0.746	0.694, 0.746
No. of measured, independent and observed [$I > 2\sigma(I)$] reflections	35697, 5888, 5050	101200, 5484, 5006
R_{int}	0.038	0.032
(sin θ/λ)$_{max}$ (Å^{-1})	0.718	0.717
$R[F^2 > 2\sigma(F^2)]$,	0.037, 0.098, 1.03	0.037, 0.105, 1.03
No. of reflections	5888	5484
No. of parameters	278	254
No. of restraints	0	0
H-atom treatment	H-atom parameters constrained	H atoms treated by a mixture of independent and constrained refinement
Δρ$_{max}$, Δρ$_{min}$ (e Å^{-3})	0.40, −0.27	0.46, -0.39

Computer programs: SAINT,[1] *CrysAlis PRO* 1.171.41.99a, [5]SHELXT,[2] SHELXL,[3] Olex2 1.3 [6]

Table C2: Intermolecular interactions during temperature study of solvate N_{MeOH}, as calculated by MrPIXEL Four significant interactions have been chosen.

Temperature (K)	Centroid distance (Å)	Coloumbic (kJ mol^{-1})	Polarisation (kJ mol^{-1})	Dispersion (kJ mol^{-1})	Repulsion (kJ mol^{-1})	Total Energy (kJ mol^{-1})
Interaction 1 (x,0.5-y,0.5+z and x,0.5-y,-0.5+z) Nifedipine – Nifedipine						
100	8.485	-9.1	-6.1	-29.9	20.4	-24.7
125	8.476	-9.1	-6	-29.8	20.3	-24.7
150	8.468	-7	-5.9	-29	19.1	-22.9
175	8.459	-9.8	-6.5	-30.2	22.1	-24.4
200	8.451	-9.7	-6.5	-30.2	22.1	-24.3
225	8.447	-8.5	-5.6	-28.1	17.8	-24.5
250	8.446	-8.9	-6	-29.1	19.8	-24.3
275	8.444	-8.8	-5.9	-28.9	19.4	-24.2
Interaction 2 (x,y,z) Nifedipine - Methanol						
100	6.315	-38.4	-14.6	-15.1	44.9	-23.1
125	6.329	-37.9	-14.1	-14.8	43.7	-23.2
150	6.338	-37.4	-13.8	-14.6	42.6	-23.2
175	6.346	-36.8	-13.7	-14.4	42	-23
200	6.353	-36.8	-13.6	-14.2	41.1	-23.5
225	6.359	-35.9	-13.4	-14.2	39.5	-23.9
250	6.366	-36.5	-13.5	-14.2	39.9	-24.2
275	6.375	-36.5	-13.2	-14	38.7	-25
Interaction 3 (1-x,0.5+y,1.5-z and 1-x,-0.5+y,1.5-z) Nifedipine – Nifedipine						
100	11.208	-7.7	-1.3	-8.5	6.2	-11.3
125	11.223	-7.4	-1.3	-8.4	6.1	-11
150	11.234	-7.7	-1.5	-9.1	6.6	-11.8
175	11.247	-7.3	-1.4	-8.4	6.3	-10.7
200	11.257	-7.2	-1.4	-8.4	6.3	-10.7
225	11.268	-7.7	-1.7	-9	6.7	-11.6

250	11.281	-7	-1.3	-7.9	5.7	-10.4
275	11.292	-6.9	-1.3	-7.9	5.7	-10.4
Interaction 4 (1-x,2-y,1-z) Methanol – Methanol						
100	4.669	-0.1	-0.2	-0.8	0	-1
125	4.623	-0.1	-0.2	-0.8	0	-1.1
150	4.587	-0.1	-0.2	-0.9	0	-1.2
175	4.554	-0.1	-0.2	-0.9	0	-1.3
200	4.527	-0.2	-0.2	-1	0	-1.4
225	4.512	-0.3	-0.2	-1	0	-1.5
250	4.489	-0.4	-0.2	-1.1	0	-1.7
275	4.471	-0.5	-0.2	-1.1	0	-1.9

References

1. Inc., B. A. *SAINT*; 2017.
2. Sheldrick, G. M. SHELXT - Integrated space-group and crystal-structure determination. In *Acta Crystallographica Section A: Foundations of Crystallography*, 2015; Vol. 71, pp 3-8.
3. Sheldrick, G. M. Crystal structure refinement with SHELXL. In *Acta Crystallographica Section C: Structural Chemistry*, 2015; Vol. 71, pp 3-8.
4. Parsons, S.; Flack, H. D.; Wagner, T. Use of intensity quotients and differences in absolute structure refinement. In *Acta Crystallographica Section B*, 2013; Vol. 69, pp 249-259.
5. Diffraction, R. O. *CrysAlis PRO*; Rigaku Corporation, 2021.
6. Dolomanov, O. V.; Bourhis, L. J.; Gildea, R. J.; Howard, J. A. K.; Puschmann, H. OLEX2: A complete structure solution, refinement and analysis program. In *Journal of Applied Crystallography*, 2009; Vol. 42, pp 339-341.